JARNAS

Journal of Advanced Research in Natural and Applied Sciences

ISSN: 2757-5195 Volume: **11** Issue: **2** Year: **2025**

Journal of Advanced Research in Natural and Applied Sciences (abbreviated as J. Adv. Res. Nat. Appl. Sci. or JARNAS) is an international, peer-reviewed, and open-access journal.

J. Adv. Res. Nat. Appl. Sci. is a science journal focusing on new theories and their applications.

JARNAS was founded in 2015, and its first issue was published on 29 Dec 2015.

Language: As of 2024, JARNAS accepts contributions in American English only.

Frequency: 4 Issues Per Year

Publication Dates: March, June, September, and December

e-ISSN: 2757-5195

Editor-in-Chief: Hüseyin Çavuş

Email: jarnas.journal@gmail.com

Publisher: Çanakkale Onsekiz Mart University

APC: JARNAS incurs no article processing charges.

Review Process: Single-Blind Peer Review

DOI Numbers: The published papers are assigned DOI numbers.

Journal Boards

Physical Sciences

Fahri Aliçavuş
fahrialicavus@comu.edu.tr
Çanakkale Onsekiz Mart University, Türkiye

Statistics

Burcu Mestav
burcumestav@comu.edu.tr
Çanakkale Onsekiz Mart University, Türkiye

Bioengineering

Zikriye Özbek
zikriye@comu.edu.tr
Çanakkale Onsekiz Mart University, Türkiye

Chemical Engineering

Uğur Cengiz
ucengiz@comu.edu.tr
Çanakkale Onsekiz Mart University, Türkiye

Civil Engineering

Mehmet Özgür
mehmetozgur@comu.edu.tr
Çanakkale Onsekiz Mart University, Türkiye

Electrical & Electronics Engineering

Özgür Turay Kaymakçı
okaymakci@comu.edu.tr
Çanakkale Onsekiz Mart University, Türkiye

Environmental Engineering

Çiğdem Öz Yaşar
cigdem.oz@comu.edu.tr
Çanakkale Onsekiz Mart University, Türkiye

Food Engineering (Food Sciences)

Nükhet Nilüfer Zorba
dnukhet@comu.edu.tr
Çanakkale Onsekiz Mart University, Türkiye

Geological Sciences and Engineering

Deniz Şanlıyüksel Yücel
denizsyuksel@comu.edu.tr
Çanakkale Onsekiz Mart University, Türkiye

Geomatic Engineering

Mehmet Ali Yücel
aliyucel@comu.edu.tr
Çanakkale Onsekiz Mart University, Türkiye

Azime Gökçe
azimegokce@gmail.com
Ege University, Türkiye

Müge Teker Yıldız
mugeteker.mt@gmail.com
Çanakkale Onsekiz Mart University, Türkiye

Gamze Turgay İzzetoğlu
gamze.turgay@ege.edu.tr
Ege University, Türkiye

Chemistry

Serkan Karakaya
skarakaya@comu.edu.tr
Çanakkale Onsekiz Mart University, Türkiye

Eda Gökırmak Söğüt
edagokirmak@yyu.edu.tr
Van Yüzüncü Yıl University, Türkiye

Nusret Genç
nusret.genc@gop.edu.tr
Tokat Gaziosmanpaşa University, Türkiye

Kıymet Berkil Akar
kiymet.berkilakar@gop.edu.tr
Tokat Gaziosmanpaşa University, Türkiye

Kübra Zenkin
kubrazenkin@gmail.com
Düzce University, Türkiye

Arianit A. Reka
arianit.reka@unite.edu.mk
University of Tetova, Republic of North Macedonia

Cecilia Georgescu
cecilia.georgescu@ulbsibiu.ro
Lucian Blaga University of Sibiu, Romania

Mathematics

Ebutalib Çelik
e.celik@comu.edu.tr
Çanakkale Onsekiz Mart University, Türkiye

İsmail Faruk Durmuş
ifarukdurmus@gmail.com
Yeni Yüzyıl University, Türkiye

Ali Övgün
ali.ovgun@emu.edu.tr
Eastern Mediterranean University, KKTC

Statistics

Canan Güneş
canangunes@comu.edu.tr
Çanakkale Onsekiz Mart University, Türkiye

Duygu Sıddıkoğlu
sduygu@comu.edu.tr
Çanakkale Onsekiz Mart University, Türkiye

Yener Ünal
uyener@cumhuriyet.edu.tr
Cumhuriyet University, Türkiye

Kadir Karakaya
kkarakaya@selcuk.edu.tr
Selçuk University, Türkiye

Berrin Gültay
berringultay@comu.edu.tr
Çanakkale Onsekiz Mart University, Türkiye

Aynur Yonar
aynursahin@selcuk.edu.tr
Selçuk University, Türkiye

Chemical Engineering

Lütfi Erden
lutfi.erden@comu.edu.tr
Çanakkale Onsekiz Mart University, Türkiye

Ömür Aras
omur.aras@manas.edu.kg
Bursa Technical University, Türkiye

Özgün Yücel
ozgun@gtu.edu.tr
Gebze Technical University, Türkiye

Hikmet Okkay
hokkay@yalova.edu.tr
Yalova University, Türkiye

Aygül Can
aygul.can@gibtu.edu.tr
Gazi̇antep Islamic Science and Technology University, Türkiye

Melik Öksüz
melik.oksuz@omu.edu.tr
Ondokuz Mayıs University, Türkiye

Salih Özbay
salihozbay@sivas.edu.tr
Sivas University of Science and Technology, Türkiye

İkrime Orkan Uçar
ikrimeucar@duzce.edu.tr
Düzce University, Türkiye

Hasan Arslanoğlu
hasan.arslanoglu@comu.edu.tr
Çanakkale Onsekiz Mart University, Türkiye

Civil Engineering

İlknur Dalyan
ilknur.dalyan@comu.edu.tr
Çanakkale Onsekiz Mart University, Türkiye

Fevziye Ayça Saraçoğlu
favarol@comu.edu.tr
Çanakkale Onsekiz Mart University, Türkiye

Fatih Yonar
fatihyonar@comu.edu.tr
Çanakkale Onsekiz Mart University, Türkiye

Selen Aktan
saktan@comu.edu.tr
Çanakkale Onsekiz Mart University, Türkiye

Muhammet Gökhan Altun
muhammetgokhan.altun@comu.edu.tr
Çanakkale Onsekiz Mart University, Türkiye

Electrical & Electronics Engineering

Environmental Engineering

Food Engineering

Murat Zorba
murat_zorba@comu.edu.tr
Çanakkale Onsekiz Mart University, Türkiye

Filiz İçier
filiz.icier@ege.edu.tr
Ege University, Türkiye

Seval Dağbağlı
seval.dagbagli@cbu.edu.tr
Manisa Celal Bayar University, Türkiye

Onur Güneser
onur.guneser@usak.edu.tr
Uşak University, Türkiye

Yavuz Cokal
ycokal@bandirma.edu.tr
Bandırma Onyedi Eylül University, Türkiye

Cengiz Caner
ccaner@comu.edu.tr
Çanakkale Onsekiz Mart University, Türkiye

Seda Özdikmenli Tepeli
sedaozdikmenli@comu.edu.tr
Çanakkale Onsekiz Mart University, Türkiye

Müge İşleten Hoşoğlu
mugehosoglu@gtu.edu.tr
Gebze Teknik University, Türkiye

Mehmet Seçkin Aday
mseckinaday@comu.edu.tr
Çanakkale Onsekiz Mart University, Türkiye

Burak Altınel
burak.altinel@ege.edu.tr
Ege University, Türkiye

Mechanical Engineering

Emine Feyza Şükür
efeyza.sukur@samsun.edu.tr
Samsun University, Türkiye

Ferhat Yıldırım
ferhatyildirim@comu.edu.tr
Çanakkale Onsekiz Mart University, Türkiye

Yusuf Şahin
ysahin@ohu.edu.tr
Niğde Ömer Halis Demir University, Türkiye

Adem Yar
ademyar@bingol.edu.tr
Bingöl University, Türkiye

Hatice Sinem Şaş Çaycı
haticesas@sabanciuniv.edu
Sabancı University, Türkiye

Okan Demir
odemir@ktun.edu.tr
Konya Teknik University, Türkiye

Murat Koyunbakan
murat.koyunbakan@dpu.edu.tr
Kütahya Dumlupınar University, Türkiye

Mining Engineering

Abdullah Fişne
fisnea@itu.edu.tr
İstanbul Technical University, Türkiye

Orhan Özdemir
orhanozdemir@itu.edu.tr
İstanbul Technical University, Türkiye

Mustafa Çınar
mcinar@comu.edu.tr
Çanakkale Onsekiz Mart University, Türkiye

CONTENTS

Journal of Advanced Research in Natural and Applied Sciences
dergipark.org.tr/en/pub/jarnas
Open Access

ISSN: 2757-5195 | 11 (2) (2025) 95-106 | doi.org/10.28979/jarnas.1645815

Caffeic Acid's Influence on the Viability and Apoptosis of a Diverse Array of Cancer Cell Lines

Merve Sezer Kürkçü[1], Deniz Genç[2], Bekir Çöl[3]

Article Info
Received: 24 Feb 2025
Accepted: 22 Apr 2025
Published: 30 Jun 2025
Research Article

Abstract − Natural phytochemicals, such as caffeic acid (CA), are emerging as promising candidates for cancer therapy due to their bioactive properties. This study investigated the cytotoxic potential of CA across ten cancer cell lines—HuH7 (hepatocellular carcinoma), PC3 (prostate adenocarcinoma), HeLa (cervical carcinoma), CaCo2 and HT29 (colorectal adenocarcinoma), SW48 (colon carcinoma), MG63 (osteosarcoma), A673 (Ewing's sarcoma), 2A3 (pharyngeal squamous cell carcinoma), and CARM-L12-TG3 (lung carcinoma)—alongside the healthy HMC3 (microglial) cell line. Cell viability was evaluated via MTT assays, while apoptosis induction and cell cycle modulation in CA-treated CaCo2 cells were analyzed using flow cytometry. Results revealed heightened sensitivity to CA in HT29, 2A3, and A673 cells, which exhibited reduced viability at lower concentrations than other cancer and healthy cell lines. CA induced apoptosis and inhibited proliferation in CaCo2 colorectal cells, with pronounced effects observed in cancer types directly exposed to dietary components (e.g., colon and pharynx) and bone-related malignancies (Ewing's sarcoma and osteosarcoma). This study provides novel insights into CA's efficacy against less-studied cancers, such as pharyngeal squamous cell carcinoma (2A3) and Ewing's sarcoma (A673). These findings underscore CA's potential as a targeted cytotoxic agent, particularly for diet-associated and bone cancers. Further research is warranted to elucidate its mechanisms, optimize therapeutic applications, and validate safety and efficacy in preclinical and clinical settings, positioning CA as a viable candidate for preventive and adjunctive cancer therapies.

Keywords − *Caffeic acid, cancer cell lines, cytotoxicity, apoptosis, phytochemicals*

1. Introduction

Cancer persists as a leading cause of global mortality, driving the urgent need for novel therapeutic strategies that circumvent the adverse effects of conventional treatments like chemotherapy and radiotherapy. In recent years, the interplay between diet and cancer pathogenesis has emerged as a critical area of investigation, with phytochemicals—naturally occurring bioactive compounds in plant-based foods—garnering attention for their potential to mitigate cancer risk and progression [1-4]. Among these compounds, phenolic acids, particularly caffeic acid (CA), have demonstrated significant biological activity, including anti-inflammatory, immunomodulatory, and anticancer properties [5-8]. CA, a hydroxycinnamic acid derivative, is ubiquitously distributed in plant tissues (e.g., leaves, seeds, and fruits) and is notably abundant in coffee, one of the world's

[1]mervesezer@mu.edu.tr; [2]denizgenc@mu.edu.tr; [3]bcol@mu.edu.tr (Corresponding Author)
[1]Research and Application Center for Research Laboratories, Muğla Sıtkı Koçtaman University, Muğla, Türkiye
[1,3]Biotechnology Research Center, Muğla Sıtkı Koçman University, Muğla, Türkiye
[2]Department of Pediatric Health & Diseases, Faculty of Health Sciences, Muğla Sıtkı Koçman University, Muğla, Türkiye
[2]Immunology and Stem Cell Laboratory, Research Laboratories Center, Muğla Sıtkı Koçman University, Muğla, Türkiye
[3]Department of Biology, Faculty of Science, Muğla Sıtkı Koçman University, Muğla, Türkiye

most consumed beverages [9-11]. Its esterified forms are present in cereals such as barley, rice, oats, and herbs like oregano and sage [2,9]. Epidemiological studies associate moderate coffee consumption with reduced cancer incidence and mortality, particularly in postmenopausal women, underscoring CA's potential role in these protective effects [12-16]. While 95% of ingested CA is absorbed in the small intestine, its bioavailability and bioactivity depend on factors such as dietary source, brewing methods, and intestinal metabolism [11,17]. Beyond its antioxidative effects, CA has been shown to modulate DNA methylation, reduce genotoxicity, and inhibit tumorigenic pathways, positioning it as a multifaceted candidate for cancer therapy [13,18,19].

Despite these advances, gaps persist in understanding CA's cell-type-specific cytotoxicity, particularly in cancers affecting anatomical regions directly exposed to dietary components (e.g., colon, pharynx) and bone-related malignancies. To address this, we evaluated CA's cytotoxic effects across ten cancer cell lines representing diverse malignancies—including colorectal adenocarcinoma (CaCo2, HT29), pharyngeal squamous cell carcinoma (2A3), Ewing's sarcoma (A673), and others—alongside healthy HMC3 microglial cells. Using MTT assays, we determined IC50 values (the concentration required for 50% growth inhibition) and further investigated CA's mechanism of action via apoptosis and cell cycle analysis in CaCo2 cells.

2. Materials

2.1. Chemicals, Reagents, and Kits

Caffeic acid (CA) was purchased from Sigma Aldrich (#C0625). CA was dissolved in ethanol (50 mg/ml) and then diluted with the medium. DMEM (Dulbecco's modified Eagle's medium) (#DMEM-HA), RPMI 1640 (Roswell Park Memorial Institute) (#RPMI-A) medium, and Dulbecco's phosphate-buffered saline (dPBS) (#PBS-1A) were purchased from Capricorn Scientific. 3-(4,5-Dimethylthiazol-2)-yl)-2,5-diphenyl (MTT) (#M2128) and Trypan blue (#T8154-20ML) were purchased from Sigma. Penicillin and streptomycin (#PS-B), as well as fetal bovine serum (FBS) (#10500-064), were purchased from GIBCO. Trypsin–EDTA (#P10-019100) and sodium pyruvate (#P04-43100) were purchased from PANbiotech. Dimethyl sulfoxide (DMSO) (#1264ML500) was purchased from Neofroxx GmbH. The Annexin V apoptosis detection kit with 7-AAD (#30060) was purchased from Biotium.

2.2. Cancer Cell Lines and Culture Conditions

In vitro cell culture studies used a laminar flow cabinet from Nüve (Nüve, Turkiye). Ten cancer cell lines and one healthy cell line were tested. Human liver hepatocellular carcinoma cells (HuH7) were obtained from Thermo Fisher Scientific. Human prostate cancer cells (PC3 #CRL-1435), human cervical carcinoma cells (HeLa #CRM-CCL-2), colorectal adenocarcinoma cells (Caco2 #HTB-37™; HT29 #HTB-38; SW48 #CCL-231), osteosarcoma cells (MG63 #CRL-1427™), Ewing's sarcoma cells (A673, #CRL-1598), pharynx carcinoma squamous cells (2A3 #CRL-3212), and microglial health cells (HMC3 CRL-3304™), and malignant mesothelioma cells (CARM-L12-TG3) were obtained from ATCC® (American Type Culture Collection, Manassas, VA, USA). Complete DMEM (cDMEM, 10% fetal bovine serum (FBS), 2 mM L-glutamine, and 1% sodium pyruvate) was used to cultivate all cell lines. The environment was humidified with 5% CO2 and maintained at 37°C for the cells.

3. Methods

3.1. Determination of Cytotoxicity by MTT Assay

CA was dissolved in ethanol before use. In 96-well plates, cancer cells were seeded at a density of 4,000 cells per well. The cells were incubated for 48 and 72 hours, respectively, in media with a higher CA concentration following a 24-hour initial incubation. Additionally, cells were cultured in media containing caffeic acid dissolved in ethanol and increasing amounts of doxorubicin for control. Each well was incubated for four hours

with an MTT solution (0.5 mg/ml) added after 48 and 72 hours at 37°C. Due to the reaction, the viable cell mitochondrial dehydrogenases reduced MTT to a purple formazan product. The quantity of MTT formazan product was determined by measuring its absorbance at 570 nm using a microplate reader after dissolving it in DMSO.

3.2. Flow Cytometry Analysis

The cells intended for apoptosis analysis by flow cytometry were seeded into 24-well tissue culture plates. Following a 24-hour incubation period, the culture media were aspirated and replaced with fresh media containing CA. The cells were then allowed to incubate for an additional 48 hours. For analysis, cells were detached from the plate by trypsinization and harvested. In accordance with the manufacturer's guidelines for the apoptosis kit, the cells were centrifuged to separate them from the medium and subsequently stained with FITC Annexin V and 7-AAD. Flow cytometry was used to examine at least 30.000 cells immediately following staining for each measurement.

3.3. Statistical Analysis

Cytotoxicity experiments were conducted in triplicate, and the IC50 values were determined using the GraphPad Prism software program (GraphPad Software, San Diego, USA). The mean ± standard deviations (SD) of the experiments were determined. To assess significant differences among the IC50 values of the cells, a one-way analysis of variance (ANOVA) was performed, with statistical significance defined at $p < 0.05$.

4. Results

4.1. Cytotoxic Effects of Caffeic Acid (CA) Across Cell Lines

Cell viability dose-response curves for PC3 (Figure 1A), HeLa (1B), HuH7 (1C), CaCo2 (1D), MG63 (1E), HT29 (1F), A673 (1G), SW48 (1H), 2A3 (1I), CARM-L12-TG3 (1J), and healthy HMC3 (1K) cells treated with caffeic acid (CA) for 48 and 72 hours are shown in Figure 1. Curves were generated using GraphPad Prism to determine IC50 values across the tested cell lines.

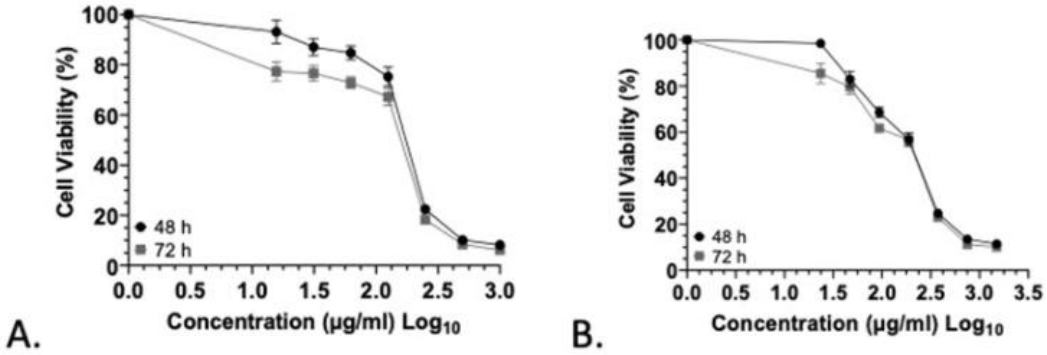

Figure 1. Dose- and time-dependent effects of CA on cell viability. A) Viability percentages of PC3 cells, B) Hela cells – exposed to different CA concentrations ranging from 23.44-1500 µg/ml (0 - 3.5 Log10) for 48 hours and 72 hours

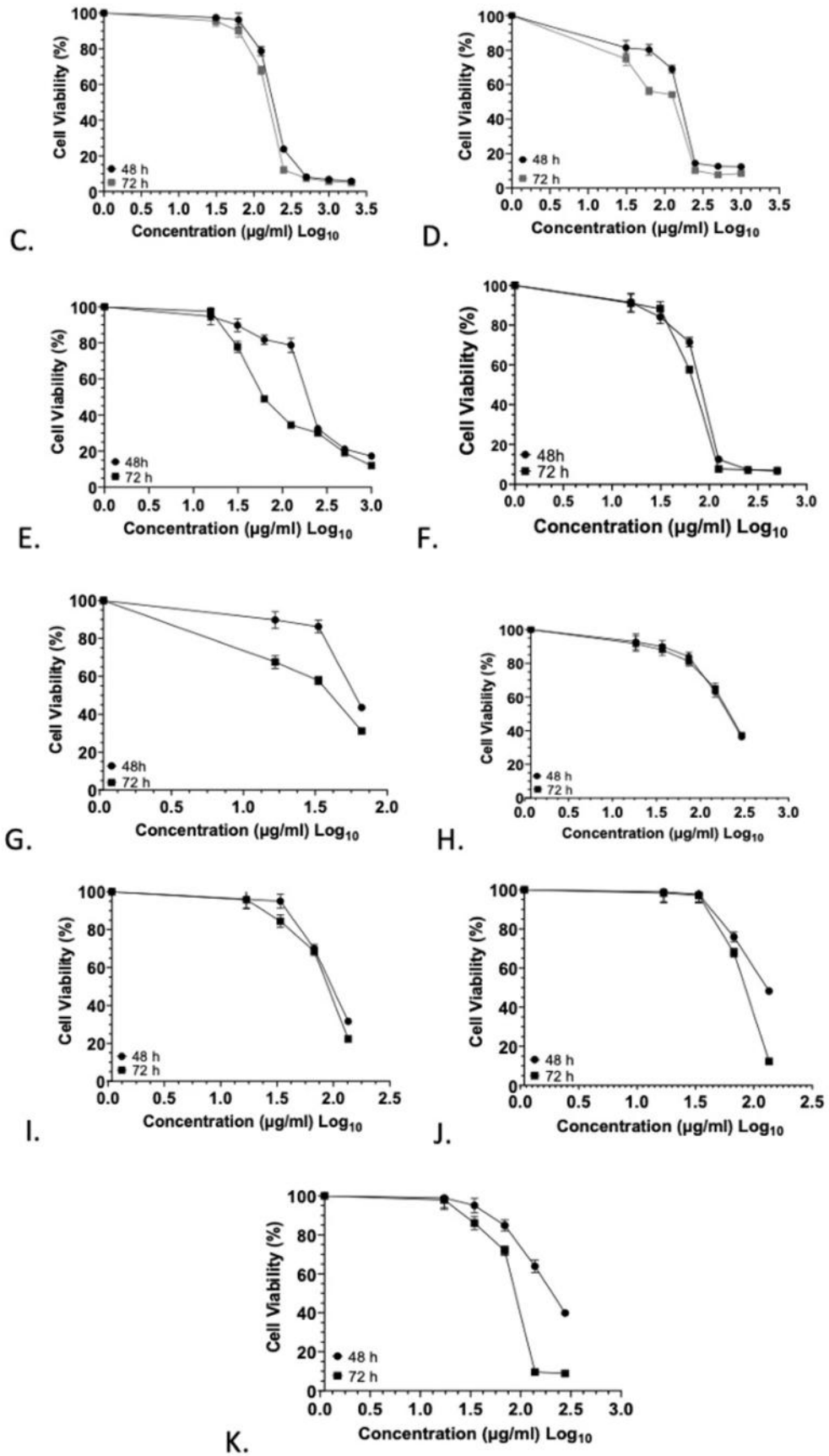

Figure 1. (Continued) Dose- and time-dependent effects of CA on cell viability. C) HUH7 cells, D) CaCo2 cells, E) MG63 cells, F) HT29 cells, G) A673 cells, H) SW48 cells, I) 2A3 cells, J) CARM-L12-TG3, K) HMC3 health cells – exposed to different CA concentrations ranging from 23.44-1500 µg/ml (0 - 3.5 Log10) for 48 hours and 72 hours

IC_{50} values were calculated for each cancer cell line at specified treatment durations, ranked by sensitivity, and compiled in Table 1.

Table 1. IC_{50} values of caffeic acid (CA) on different cell lines

Tissue Sources	Cell Lines	IC_{50} value ± SD (mg/ml)	
		48 h	72 h
Ewings sarcoma	A673	59.21 ± 0.71	45.36 ± 1.07
Colorectal adenocarcinoma	HT29	81.05 ± 4.92	67.63 ± 4.10
Pharynx carcinoma	2A3	93.52 ± 1.66	88.64 ± 1.19
Malign mesothelioma	CARM-L12-TG3	120.16 ± 3.36	82.53 ± 0.86
Osteosarcoma	MG63	215.02 ± 13.92	75.86 ± 4.72
Colorectal adenocarcinoma	CaCo2	152.24 ± 10.38	97.19 ± 5.92
Liver hepatocellular carcinoma	HUH7	177.06 ± 9.12	141.17 ± 5.96
Prostate cancer	PC3	188.35 ± 11.17	150.25 ± 12.34
Colorectal adenocarcinoma	SW48	183.26 ± 8.56	193.71 ± 8.39
Cervical cancer	HeLA	195.4 ± 17.22	176.65 ± 16.12
Health microglial cell	HMC3	185.98 ± 10.52	77.52 ± 2.35

Cancer cells were treated with various concentrations (23.3 – 1500 µg/ml) of CA and assessed for cell viability using the MTT assay at 48 and 72 hours. The IC50 values were calculated using GraphPad Prism 5 software. The IC_{50} values for CA against each cell line represent the means of three independent experiments (n=3) and are presented as mean ± SD.

Significant decreases in cell viability were observed in the HT29, A673, 2A3, and CARM-L12-TG3 cell lines with increasing CA concentrations. When these cell lines are compared with the healthy cell line HMC3, it is evident that the CA concentration, which does not affect the healthy cell line, exerts a cytotoxic effect on these cancer cell lines (Figure 2).

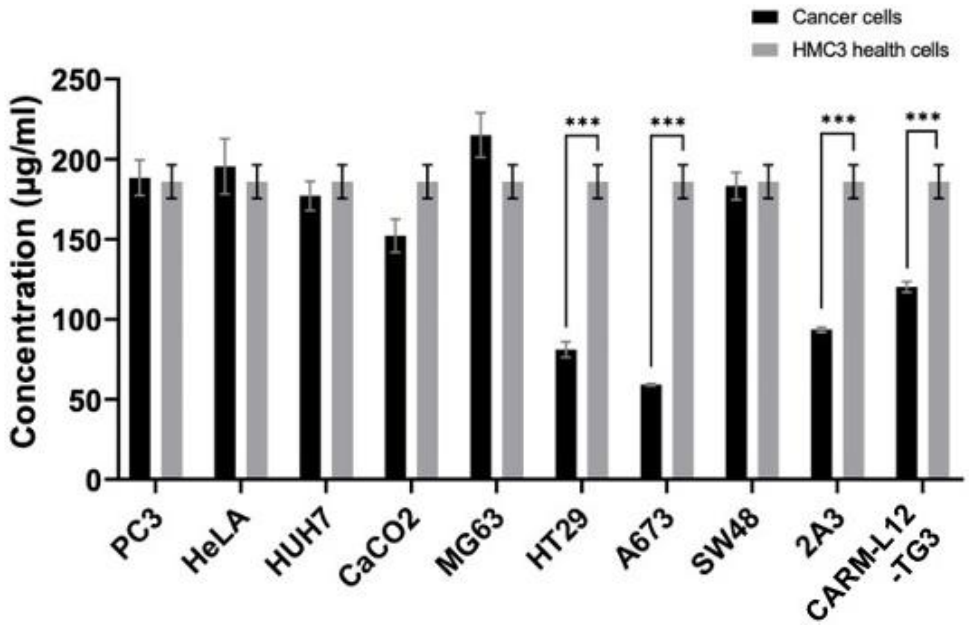

Figure 2. Comparative analysis of CA cytotoxicity in cancer versus healthy cells. IC50 values of caffeic acid (CA) across cancer cell lines (PC3, HeLa, HUH7, CaCo2, MG63, HT29, A673, SW48, 2A3, CARM-L12-TG3) and the healthy HMC3 cell line are indicated by graphical representation with statistically significant differences in IC50 (***$p < 0.05$).

4.2. CA Induces Apoptosis in CaCo2 Colorectal Cancer Cells

We evaluated the early apoptotic, late apoptotic, and necrotic effects of caffeic acid (CA) using flow cytometry after staining with Annexin V and 7-AAD. Annexin V staining was observed in both early and late stages of apoptosis, while 7-AAD staining was present only in cells at the late apoptosis stage. This differentiation allowed us to distinguish late apoptotic or necrotic cells from those in early apoptosis. Flow cytometry analysis represented early apoptotic cells as positive for Annexin V and negative for 7-AAD in the lower right quadrant, while late apoptotic cells were positive for both Annexin V and 7-AAD in the upper right quadrant. As depicted in Figure 3, negative area (Figure 3A), the control group without CA exhibited 14.6%±1.8% for early apoptosis and 1.3%±0.3% for late apoptosis (Figure 3B), following treatment with 125 µg/ml of caffeic acid (CA) for 48 hours, the percentage of early and late apoptotic CaCo2 cells was 37.0%±3.8% and 32.8%±2.9%, respectively (Figure 3C). When treated with doxorubicin for 48 hours and used as a drug control, the percentage of early and late apoptotic CaCo2 cells was 26.9%±2.6% and 29.9%±2.1% (Figure 3D).

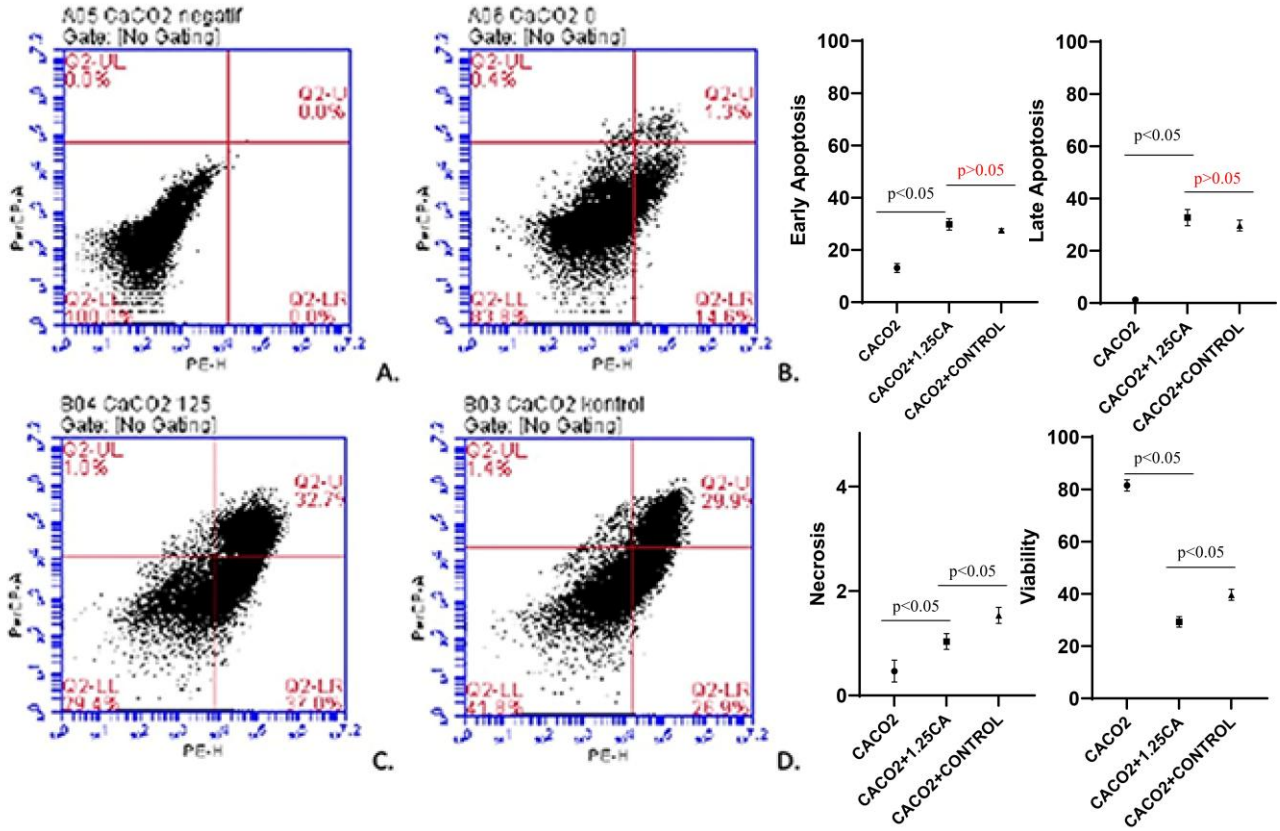

Figure 3. Flow cytometry apoptosis assay following Annexin V fluorescein isothiocyanate/7-AAD staining. CaCo2 cells were treated with CA (125 µg/ml) (C), doxorubicin (drug control) (D), without CA (B) for 48 h, and negative area (A). Representative scatter plots of 7-AAD (y-axis) vs. Annexin V (x-axis)

Statistical analysis revealed that untreated CaCo2 cells exhibited significantly higher cell viability compared to cells treated with 125 µg/mL caffeic acid (CA) or doxorubicin (positive control) ($p<0.05$). Furthermore, untreated cells displayed elevated necrosis levels relative to CA- and doxorubicin-treated groups ($p< 0.05$). CA and doxorubicin treatments robustly induced apoptosis: early and late apoptosis rates were significantly higher in treated cells than in untreated controls ($p<0.05$). Notably, CA-treated cells showed greater necrosis ($p<0.05$) but lower overall viability ($p<0.05$) compared to doxorubicin-treated cells, underscoring CA's potent cytotoxic activity.

5. Discussion

Cancer remains one of the leading causes of mortality worldwide, despite significant advances in medical science. Current research is focused on discovering novel compounds with enhanced therapeutic efficacy and reduced side effects compared to conventional treatments [20-23]. Caffeic acid (CA), a naturally occurring polyphenol found in various dietary sources, has garnered attention due to its potential anticancer properties. In our study, we evaluated the cytotoxic effects of CA on 10 different cancer cell lines representing seven distinct cancer types.

Caffeic acid is a prominent bioactive component of coffee, one of the most widely consumed beverages worldwide. Coffee is a pharmacologically active beverage nearly ubiquitous in daily life [24]. The influence of coffee consumption on health has been the subject of extensive research. Coffee's impact on human health has been extensively studied, with evidence suggesting both beneficial and adverse effects. The majority of these studies have indicated that coffee consumption has a beneficial impact on various aspects of health [25,26]. Recent meta-analyses have reinforced the potential protective effects of coffee consumption against various cancers, including colorectal and liver cancer, due to its antioxidant and anti-inflammatory properties [27] and metabolic disturbances [28,29]. The presence of bioactive compounds such as CA in coffee has been proposed as one of the contributing factors to these effects.

In our study, we analysed the cytotoxic impact of CA on multiple cancer cell lines and compared these findings to a healthy cell line (HMC3). The HT29, A673, 2A3, and CARM-L12-TG3 cell lines exhibited statistically significant differences in viability compared to the healthy cell line (Table 2). In particular, CA demonstrated a pronounced effect on the HT29 colon cancer cell line, reducing its viability by 50% at a concentration of 81.05 µg/ml, which did not adversely affect the healthy cell line. This finding aligns with recent research highlighting the anticancer potential of CA and other phenolic acids in colorectal cancer models [21, 30-32].

Table 2. Listing significant changes by statistically comparing the IC50 values of cancer cell lines versus healthy cell lines against caffeic acid (CA)

	Significant Differences	***P* value**	**Mean of Group A**	**Mean of Group B**	**Difference**	**SE of difference**	**t ratio**	**df**	**q value**
PC3	No	0.803	188.30	186.00	2.367	8.860	0.267	4	0.48635
HeLA	No	0.464	195.40	186.00	9.426	11.650	0.809	4	0.35133
HUH7	No	0.330	177.10	186.00	-8.917	8.040	1.109	4	0.28534
CaCo2	No	0.017	152.20	186.00	-33.740	8.531	3.955	4	0.02029
MG63	No	0.045	215.00	186.00	29.040	10.070	2.883	4	0.04533
HT29	Yes	0.000	81.05	186.00	-104.900	6.704	15.650	4	0.00023
A673	Yes	0.000	59.21	186.00	-126.800	6.087	20.820	4	0.00019
SW48	No	0.746	183.30	186.00	-2.722	7.829	0.348	4	0.48635
2A3	Yes	0.000	93.52	186.00	-92.450	6.149	15.040	4	0.00023
CARM-L12-TG3	Yes	0.000	120.20	186.00	-65.810	6.376	10.320	4	0.00075

Their digestive systems come into direct contact with food components. Therefore, it can be expected that cells in these systems would be the most affected by changes in diet. Colon cancer cells are directly influenced by dietary components, making them particularly susceptible to bioactive compounds. Prior studies have demonstrated that phenolic acids such as 3-O-methylgallic, gallic, p-coumaric, and ferulic acid can reduce cell viability, induce apoptosis, and regulate cell cycle progression in colon cancer models [33-36]. Our results corroborate these findings, reinforcing that dietary polyphenols like CA may exert chemopreventive effects by modulating key cellular pathways. In this study, we observed a similar effect on colon cancer cell lines. Specifically, we evaluated and compared three different colon cancer cell types in our research. Among these

three colon cancer cell lines, it was found that CA had the most significant impact on the HT29 cell line. At a CA concentration of 81.05 µg/ml, which did not affect the HMC3 healthy cell line, the viability of the HT29 colon cancer cell line decreased by 50% (Figure 4).

Beyond the digestive tract, bioactive food components interact with cells in the oral cavity, tongue, and esophagus. Syringic acid, another phenolic compound, has been reported to induce cell cycle arrest and promote apoptosis in cervical, tongue, and mouth carcinomas [9, 37]. Consistent with these observations, our study identified the 2A3 pharynx cancer cell line as one of the most responsive to CA treatment, suggesting a potential therapeutic application in upper gastrointestinal cancers (Figure 2).

Additionally, we found that the Human Ewing's sarcoma A673 cell line exhibited the greatest sensitivity to CA exposure, with IC50 values of 59.21 ± 0.7 mg/ml at 48 hours and 45.36 ± 1.07 mg/ml at 72 hours (Figure 2). These findings expand on prior research indicating that phenolic compounds, including CA, may disrupt sarcoma cell proliferation via oxidative stress modulation and apoptosis induction [37,38].

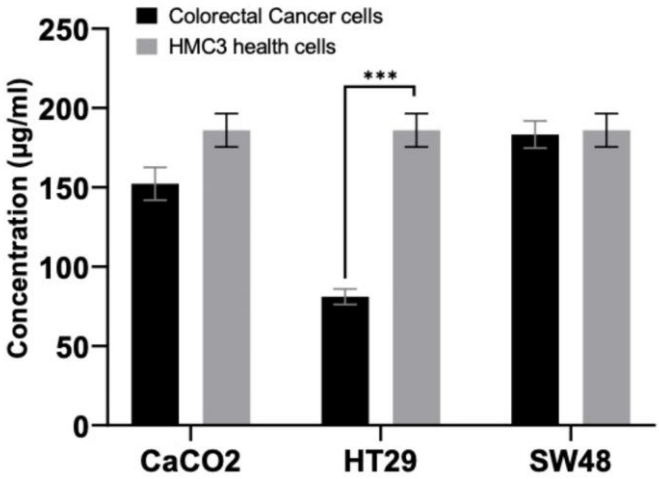

Figure 4. Comparison of CaCo2, HT29, SW48 IC50 caffeic acid (CA)concentrations of colon cancer cells and IC50 caffeic acid (CA) concentrations of HMC3 healthy cell line.

Lastly, diet plays a pivotal role in bone health, with studies indicating that coffee consumption may influence bone mineral density. Hirata et al. [39,40] previously reported positive effects of coffee intake on lumbar spine bone density . Recent investigations [41,42] have further elucidated the relationship between polyphenol-rich diets and osteoporosis risk reduction, emphasizing the potential osteoprotective effects of CA and other coffee-derived compounds .

Overall, our study contributes to the growing body of evidence supporting the anticancer properties of CA. However, further research is warranted to elucidate its precise mechanisms of action and to determine its potential for clinical applications. Future studies should focus on in vivo models and combinatorial approaches with existing chemotherapeutic agents to enhance therapeutic efficacy while minimizing toxicity.

6. Conclusion

Caffeic acid (CA) demonstrated significant cytotoxic effects on various cancer cell lines, particularly those associated with body regions directly exposed to bioactive food components, such as the colon, pharynx, and bone. CA exhibited selective cytotoxicity toward cancer cells while sparing healthy cells, suggesting its potential as a targeted treatment for specific cancer types. Different cancer cell lines displayed varying sensitivities to CA, with some cell lines, like HT29, A673, 2A3, and CARM-L12-TG3, being more affected by CA concentrations that did not impact healthy cells. This study underscores the potential of phytochemicals, such as CA, found in commonly consumed foods and coffee, as natural and effective treatments for certain cancers. It suggests that dietary components may play a role in cancer prevention and treatment. The paper

compiled by Pavlíková in 2023 highlighted studies demonstrating that caffeic acid possesses anticancer properties across various cancer types [43]. The review reveals that the mechanisms of action of CA vary depending on the cancer type, emphasizing the need for further research to fully understand its effectiveness and safety in cancer prevention and treatment. Our study also focused on cancer cell lines that had not been previously explored in the literature, offering new insights into how caffeic acid affects cancer cells in anatomical regions directly influenced by its bioactive properties. The study emphasizes the need for additional research to investigate the underlying mechanisms of CA's cytotoxic effects, its potential as a complementary therapy, and its safety and efficacy in clinical applications. Future studies should consider incorporating additional experiments, such as survival assays and wound healing assays, to further validate the findings and enhance the robustness of the study. These supplementary analyses could provide deeper insights into the underlying mechanisms and strengthen the overall conclusions. Overall, the findings suggest that CA holds promise as a cytotoxic agent against specific cancer types and warrants further investigation as a potential therapeutic option in cancer treatment.

Author Contributions

The author read and approved the final version of the paper. They all read and approved the final version of the paper.

Conflict of Interest

All the authors declare no conflict of interest.

Ethical Review and Approval

No approval from the Board of Ethics is required.

Acknowledgment

We would like to thank the Biotechnology Research Center and the Proteogenome Technologies Research Laboratory at Muğla Sıtkı Koçman University Research Laboratories Center (ALM research building) for their support.

References

[1] K. A. Onat, M. Sezer, B. Çöl. *Some biological activities of phenolic compounds cinnamic acid, caffeic acid and P-coumaric acid*, Journal of the Institute of Science and Technology 11 (4) (2021) 2587–2598.

[2] L. S. Rosa, N. J. A. Silva, N. C. P. Soares, M. C. Monteiro, A. J. Teodoro. *Anticancer properties of phenolic acids in colon cancer – A review*, Journal of Nutrition and Food Sciences 06 (02) (2016) 468–274.

[3] M. Abotaleb, A. Liskova, P. Kubatka, D.Büsselberg. *Therapeutic potential of plant phenolic acids in the treatment of cancer*, Biomolecules 10 (2) (2020) 221–229.

[4] E. M. Brown, C. I. R. Gill, G. J. McDougall, D. Stewart. *Mechanisms underlying the anti-proliferative effects of berry components in in vitro models of colon cancer*, Current Pharmaceutical Biotechnology 13 (1) (2012) 200–209.

[5] V. Lobo, A. Patil, A. Phatak, N. Chandra. *Free radicals, antioxidants and functional foods: Impact on human health*, Pharmacognosy Reviews 4 (8) (2010) 118–126.

[6] K. Aslıhan Onat-Taşdelen, H. Öztürkel-Kabakaş, E. Yüksektepe, Ş. Serter Çatav, G. Güzel, B. Çöl, H. Kim, Y. Kee Chae, E. Sonay Elgin. *Functional groups matter: Metabolomics analysis of Escherichia coli exposed to trans-cinnamic acid and its derivatives unveils common and unique targets*, World Journal of Microbiology and Biotechnology 40 (2) (2024) 47–58.

[7] H. Öztürkel Kabakaş, M. Sezer Kürkçü, K. A. Onat Taşdelen, B. Çöl. *The cytotoxic effect of benzoic acid on ten different cancer cell lines*, Eskişehir Technical University Journal of Science and Technology A - Applied Sciences and Engineering 25 (1) (2024) 66–77.

[8] B. Açıkalın, N. Sanlier. *Coffee and its effects on the immune system*, Trends in Food Science & Technology 114 (2021) 819–830.

[9] S. Cheemanapalli, R. Mopuri, R. Golla, A. C.M., S. Kumar Chitta. *Syringic acid (SA)–a review of its occurrence, biosynthesis, pharmacological and industrial importance*, Biomedicine & Pharmacotherapy 108 (2018) 547–557.

[10] C. Magnani, V. Isaac, M.A. Correa, H.R.N. Salgado. *Caffeic acid: a review of its potential use in medications and cosmetics*, Anal. Methods 6 (2014) 3203–3210.

[11] G. Williamson, F. Dionisi, M. Renouf. *Flavanols from green tea and phenolic acids from coffee: critical quantitative evaluation of the pharmacokinetic data in humans after consumption of single doses of*, Mol Nutr Food Res 55 (6) (2011) 864–873.

[12] S. Schmit, H. Rennert, G. Rennert, S.B. Gruber. *Coffee consumption and the risk of colorectal cancer*, Cancer Epidemiol Biomarkers 25 (4) (2016) 634–639

[13] N. J. Frost-Meyer, J.V. Logomarsinho. *Impact of coffee components on inflammatory markers: A review*, Journal of Functional Foods 4 (4) (2012) 819–830.

[14] R. Poole, O. J. Kennedy, P. Roderick, J. A. Fallowfield, P. C. Hayes, J. Parkes. *Coffee consumption and health: umbrella review of meta-analyses of multiple health outcomes*, Umbrella review of meta-analyses of multiple health outcomes 359 (2017) 5024.

[15] M. J. Gunter, N. Murphy, A. J. Cross, L. Dossus, L. Dartois, G. Fagherazzi, R. Kaak, T. Kühn, H. Boein, K. Aleksandrova, A. Tjonneland, A. Olsen, K. Overvad, S. C. Larsen, M. L. Redondo Cornejo, A. Agudo, M. J. Sánchez Pérez, J. M. Altzibar, C. Navarro, E. Ardanaz, K. Khaw, A. Butterworth, K. E. Bradbury, A. Trichopoulou, P. Lagiou, D. Trichopoulos, D. Palli, S. Grioni, P. Vineis, S. Panico, R. Tumino, B. Bueno-de-Mesquita, P. Siersema, M. Leenders, W. J Beulens, C. U. Uiterwaal, P. Wallström, L. M. Nilsson, R. Landberg, E. Weiderpass, G. Skeie, T. Braaten, P. Brennan, I. Licaj, D. C. Muller, R. Sinha, N. Wareham, E. Riboli. *Coffee Drinking and Mortality in 10 European Countries*, Annals of Internal Medicine 167 (4) (2017) 236–247.

[16] L.F. Andersen, D.R. Jacobs Jr, M.H. Carlsen, R.Blomhoff. *Consumption of coffee is associated with reduced risk of death attributed to inflammatory and cardiovascular diseases in the Iowa Women's Health Study*, American Journal of Clinical Nutrition 83 (5) (2018) 1039–1046.

[17] M.R. Olthof, P.C.H. Hollman, M.B. Katan.*Chlorogenic acid and caffeic acid are absorbed in humans*, J Nutr 131 (1) (2001) 66–71.

[18] L.C. Hernandes, A. R. Thomazela Machado, K. Tuttis, D. Luís Ribeiro, A. Ferro Aissa, P. Pícoli Dévoz, L. M. Greggi Antunes. *Caffeic acid and chlorogenic acid cytotoxicity, genotoxicity and impact on global DNA methylation in human leukemic cell lines*, Genetics and Molecular Biology 43 (3) (2020).

[19] R. J. Bułdak, T. Hejmo, M. Osowski, Ł. Bułdak, M. Kukla, R. Polaniak, E. Birkner. *The impact of coffee and its selected bioactive compounds on the development and progression of colorectal cancer in vivo and in vitro*, Molecules 23 (12) (2018) 3309.

[20] B. Çöl, M. Sezer Kürkçü, A. Sorucu. *Okaliptus balının PC3, CaCO2, HeLa ve HuH7 Kanser Hücre Hatları Üzerindeki Sitotoksisitesinin Değerlendirilmesi*, International Journal of Innovative Approaches in Science Research 5 (4) (2021) 195–206.

[21] F. Xing, N. Liu, C. Wang, X. D. Wang. *Caffeic acid phenethyl ester promotes oxaliplatin sensitization in colon cancer by inhibiting autophagy*, Scientific Reports 14 (1) (2024) 1–10.

[22] E. Dibek, A. Babayeva, E. S. Elgin, M. S. Kürkçü, B. Çöl. *Genome-wide screen of Escherichia coli Keio mutant line identifies genes related to propolis effect*, European Food Research and Technology 251 (3) (2024) 429–448.

[23] K. A. Onat-Taşdelen, H. Öztürkel-Kabakaş, E. Yüksektepe, Ş. S. Çatav, G. Güzel, B. Çöl, H. Kim, Y. K. Chae, E. S. Elgin. *Functional groups matter: metabolomics analysis of Escherichia coli exposed to trans-cinnamic acid and its derivatives unveils common and unique targets*, World Journal of Microbiology and Biotechnology 40 (2) (2024).

[24] J.V. Higdon, B.Frei. *Coffee and health: A review of recent human research*, Critical reviews in food science and nutrition 46 (2) (2007) 101–123.

[25] K. Socała, A. Szopa, A. Serefko, E. Poleszak, P. Wlaz. *Neuroprotective effects of coffee bioactive compounds: a review*, WlaźInternational journal of molecular sciences 22 (1) (2020) 107.

[26] B.B. Gökcen, N. Şanlier. *Coffee consumption and disease correlations*, Critical reviews in food science and nutrition 59 (2) (2017) 336–348.

[27] W. Y. Long, G. hua Zhao, Y. Wu, Y. Liu. *Gallic acid inhibits Kaposi's Sarcoma-associated herpesvirus lytic reactivation by suppressing RTA transcriptional activities*, Food Science and Nutrition 9 (2) (2021) 847–854.

[28] M. F. Mendoza, R. M. Sulague, T. Posas-Mendoza, C. J. Lavie. *Impact of coffee consumption on cardiovascular health*, Ochsner J. 23 (2) (2023) 152–158.

[29] K. Nieber. *The Impact of Coffee on Health*, Planta Medica 83 (16) (2017) 1256–1263.

[30] L. Budisan, D. Gulei, A. Jurj, C. Braicu, O. Zanoaga, R. Cojocneanu, L. Pop, L. Raduly, A. Barbat, A. Moldovan, C. Moldovan, A. B. Tigu, C. Ionescu, A. G. Atanasov, A. Irimie, I. Berindan-Neagoe. *Inhibitory effect of CAPE and kaempferol in colon cancer cell lines—possible implications in new therapeutic strategies*, International Journal of Molecular Sciences 20 (5) (2019) 1199.

[31] A. Esmeeta, S. Adhikary, V. Dharshnaa, P. Swarnamughi, Z. Ummul Maqsummiya, A. Banerjee, S. Pathak, A. K. Duttaroy. *Plant-derived bioactive compounds in colon cancer treatment: An updated review*, Biomedicine and Pharmacotherapy 153 (2022) 113384.

[32] S. C. Lim, T. B. Lee, S. I. Han. *Caffeic Acid Enhances Anticancer Drug-induced Apoptosis in Acid-adapted HCT116 Colon Cancer Cells*, Anticancer Research 44 (6) (2024) 2587–2595.

[33] S. C. Forester, Y. Y. Choy, A. L. Waterhouse, P. I. Oteiza. *The anthocyanin metabolites gallic acid, 3-O-methylgallic acid, and 2,4,6-trihydroxybenzaldehyde decrease human colon cancer cell viability by regulating pro*, Mol Carcinog 53 (6) (2014) 432–439.

[34] B. Janicke, G. Önning, S. M. Oredsson. *Differential effects of ferulic acid and p-coumaric acid on S phase distribution and length of S phase in the human colonic cell line Caco-2*, Journal of Agricultural and Food Chemistry 53 (17) (2005) 6658–6665.

[35] B. Janicke, C. Hegardt, M. Krogh, G. Önning, B. Åkesson, H. M. Cirenajwis, S. M. Oredsson. *The antiproliferative effect of dietary fiber phenolic compounds ferulic acid and p-coumaric acid on the cell cycle of Caco-2 cells*, Nutrition and Cancer 63 (4) (2011) 611–622.

[36] M. R. Islam, S. Akash, M. M. Rahman, F. T. Nowrin, T. Akter, S. Shohag, A. Rauf, A. S. M. Aljohani, J. Simal-Gandara. *Colon cancer and colorectal cancer: Prevention and treatment by potential natural products*, Chemico-Biological Interactions 368 (2022) 110170.

[37] B. Abijeth, D. Ezhilarasan. *Syringic acid induces apoptosis in human oral squamous carcinoma cells through mitochondrial pathway*, Journal of Oral and Maxillofacial Pathology 24 (1) (2020) 40–45.

[38] R. M. T. de Lima, A. C. dos Reis, J. V. de Oliveira Santos, J. R. de Oliveira Ferreira, J. W. G. de Oliveira Filho, A. C. Soares Dias, A. A. P. M. de Menezes, A. M. O. F. da Mata, M. V. O. B. de Alencar, T. de Jesus Aguiar dos Santos Andrade, M. F. C. Jardim Paz, D. C. do Nascimento Rodrigues, P. M. P. Ferreira, J. M. de Castro e Sousa, S. K. Mishra, M. T. Islam, A. A. de Carvalho Melo-Cavalcante. *Antitumoral effects of [6]-gingerol [(S)-5-hydroxy-1-(4-hydroxy-3-methoxyphenyl)-3-decanone] in sarcoma 180 cells through cytogenetic mechanisms*, Biomedicine and Pharmacotherapy 126 (2020) 110004.

[39] H. Hirata, K. Kitamura, T. Saito, R. Kobayashi, M. Iwasaki, A. Yoshihara, Y. Watanabe, R. Oshiki, T. Nishiwaki, K. Nakamura. *Association between dietary intake and bone mineral density in Japanese postmenopausal women: The Yokogoshi cohort study*, Tohoku Journal of Experimental Medicine 239 (2) (2016) 95–101.

[40] T. M. Alfaro, R. A. Monteiro, R. A. Cunha, C. R. Cordeiro. *Chronic coffee consumption and respiratory disease: A systematic review*, Wiley Online Library 12 (3) (2018) 1283–1294.

[41] S. Yang, Y. Sun, L. Kapilevich, X. Zhang, Y. Huang. *Protective effects of curcumin against osteoporosis and its molecular mechanisms: a recent review in preclinical trials*, Frontiers in Pharmacology 14 (2023) 1249418.

[42] K. Wang. *The potential therapeutic role of curcumin in osteoporosis treatment: based on multiple signaling pathways*, Frontiers in Pharmacology 15 (2024) 1446536.

[43] N. Pavlíková. *Caffeic Acid and Diseases-Mechanisms of Action*, International Journal of Molecular Sciences 24 (1) (2023) 588–598.

Journal of Advanced Research in Natural and Applied Sciences
dergipark.org.tr/en/pub/jarnas
Open Access

ISSN: 2757-5195 | 11 (2) (2025) 107-116 | doi.org/10.28979/jarnas.1650045

Investigation of Mineralogy and Ceramic Technology Properties of Sivrihisar Kurtşeyh Sepiolites (Türkiye)

Kağan Kayacı[1], Şengül Can Genç[2], Mehmet Uğur Taşkıran[3], Hasan Poçan[4], Mehmet Mert Doğu[5], Semih Yüksel[6], Yıldız Yıldırım[7]

Article Info
Received: 03 Mar 2025
Accepted: 20 May 2025
Published: 30 Jun 2025
Research Article

Abstract − In this study, the geology, mineralogy, and potential uses of the Sivrihisar sepiolite and dolomitic sepiolites of the Eskişehir region (Türkiye) for ceramic wall tiles were investigated. A geological map of the open pits in the village of Kurtşeyh and generalized stratigraphic sections are presented. Samples taken from the pit sequences were characterized in terms of their mineralogy by XRD (X-ray diffraction). Chemical and Thermal analysis of the raw materials was determined by XRF (X-ray fluorescence), Thermal analysis (TA), and Differential Thermal analysis (DTA). Besides these studies, the thermal properties and shrinkage (%), water absorption (%), and color (L, a, b) of the fired wall tile bodies were investigated to determine their technological properties. In light of all the analysis results, alternative body formulations were created, and these recipes were fired under wall tile conditions. The fired phases were then mineralogically characterized, and the physical and technological properties of the different bodies were studied. As a sum, 10% dolomitic sepiolite usage instead of İstanbul clays is suitable for manufacturing wall tiles.

Keywords − *Sepiolite, whitewares, geology, ceramic, mineralogy*

1. Introduction

Our country's ceramic sector supplies 90% of the plastic clays it uses in production from the Şile (Istanbul) region. In addition, it imports high-strength and colored fired clays from Ukraine, which it also uses in its recipes. Recently, there has been news that the area permitted for mining in the Şile region by the Ministry of Forestry and the General Directorate of Forestry has been reduced to 1/3 of the current amount. If this restriction is realized, the clay reserve, estimated to be approximately 250 million tons, will have decreased to 80-90 million tons. Only 30% of this is suitable clay for ceramics production.

Due to this limited situation and the state of war in Ukraine, ceramic producers have difficulty obtaining clay and are resorting to alternative solutions. For this purpose, the use of carbonated sepiolitic clays, known to exist in the area extending from Sivrihisar and its vicinity in the south of Eskişehir in inner NW (Northwest) Anatolia and towards Polatlı, Ankara, has been brought to the agenda. The main objectives of this study are to investigate the geology of the region in question, to reveal the geology of different types of rock assemblages that form the basis of sepiolitic clays and the geological features of the Neogene basin that developed on this

[1]kagankayaci@kale.com.tr; (Corresponding Author); [2]scangenc@itu.edu.tr; [3]ugurtaskiran@kale.com.tr; [4]pocan18@itu.edu.tr, [5]dogum18@itu.edu.tr, [6]asal.semih@gmail.com, [7]yildizyildirim@kale.com.tr
[1,3,7]Kaleseramik Research-Development Center, Çan, Çanakkale, Türkiye
[2,5]Department of Geological Engineering, Faculty of Mines, Istanbul Technical University, İstanbul, Türkiye
[4]Ozifin Mining Ltd., Ankara, Türkiye
[6]Turkish Petroleum International Co., Ankara, Türkiye

basis and include clays, to determine the sedimentary deposits in the basin, to investigate which zones are suitable for ceramic production, to reveal the clay mineralogy, and to compare whether the clays of the Eskişehir region can be an alternative with the clays of the Şile region in Istanbul.

Sepiolite occurs in two different polymorphic structures in nature. The first of these is α-sepiolite, which is amorphous, compact, and in the form of massive nodules and is known as meerschaum in German because its external appearance resembles sea foam; the second is β-sepiolite, which occurs in the form of small, flat, and round particles or amorphous aggregates [1]. Sepiolite is formed due to the decomposition of serpentine as a secondary mineral. It has high sorption power by holding water up to 200-250 times its weight. The pH value suitable for its formation is 8-8.5, and when it is heated above 300ºC, its structure changes and pores deteriorate [2]. Sepiolite, formed in layers due to sediment deposition, mostly has an earthy, fine-grained, and slippery appearance. This type of sepiolite contains 90% sepiolite mineral, and the remaining percentage is generally dolomite and smectite group clays, magnesite, palygorskite, and detrital minerals [2].

The Sivrihisar region lies within the tectonic unit known in Turkish geology as the Tavşanlı zone. This zone, which represents the northern part of the Anatolid-Torid block, underwent high-pressure, low-temperature metamorphism in the Late Cretaceous [3-5]. The Tavşanlı Zone consists of three main tectonic units. These are the ophiolite, the Cretaceous-aged accretionary complex, and the Orhaneli passive continental margin metamorphic stack [6]. This complex basement is cut by Late Paleocene-Eocene aged granitic rocks, and on top of this composite basement are the Neogene-aged sedimentary rocks known as the Sakarya and Porsuk formations, which are equivalent to each other and separated by an uplift [7-9]. These sedimentary rocks, known by two different names, consist of dolomitic carbonates at the bottom, gypsiferous clays at the top, milky-brown sepiolites, dolomitic sepiolites, sepiolitic dolomites, montmorillonitic clays, and finally fossiliferous micritic limestones and porcelain-like dolomites at the top (Figure 1).

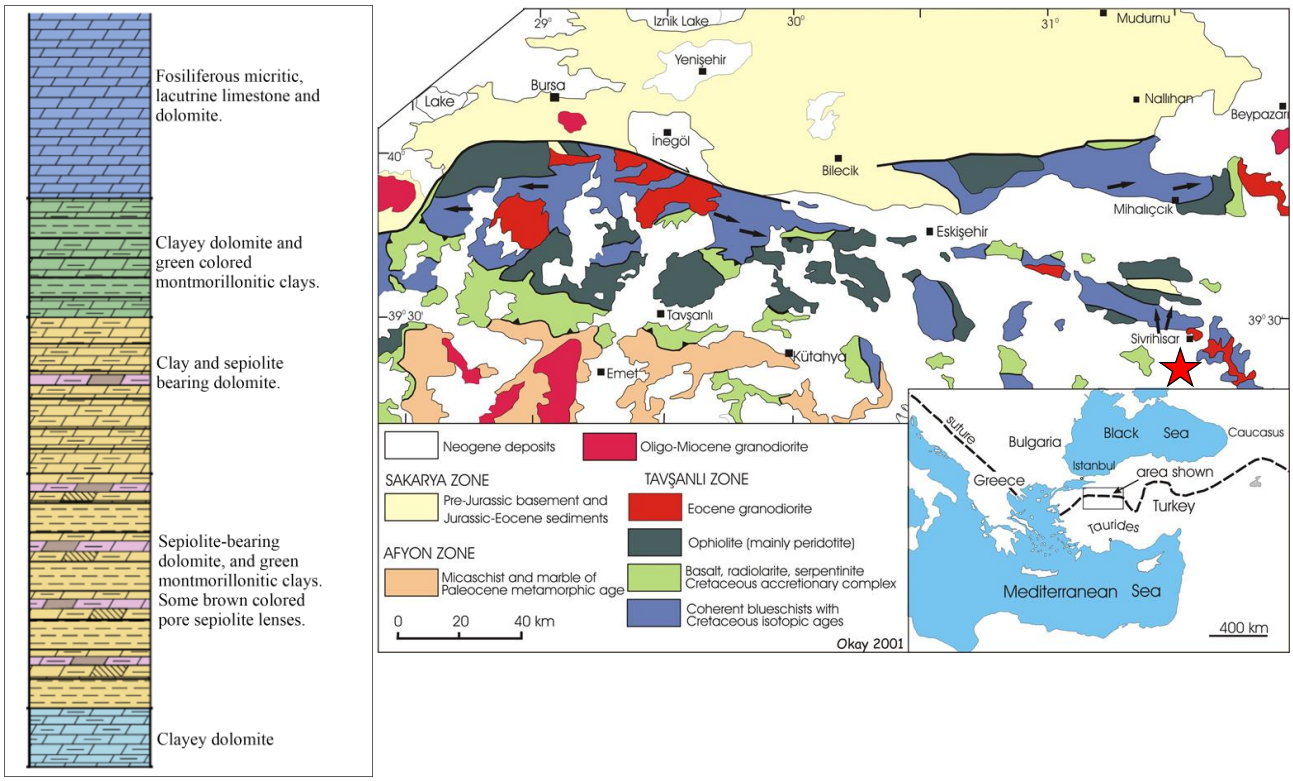

Figure 1. Generalized geology map of the Bursa, Eskişehir, and Kütahya provinces [5] and generalized stratigraphic section of the Sakarya-Porsuk formations around the Kurtşeyh area (red star indicates the study area)

Sepiolites also developed within these lacustrine beds. The age of the Sakarya Formation was determined to be Miocene in studies by Karakaş [10] based on the gastropod and ostracod fossils in the unit. However, later studies by Kadir et al. [7, 8] indicated that the age of the unit is Early Pliocene.

The Neogene deposits in the Kurtşeyh region of the Sakarya Formation, terrestrial deposits formed in a shallow lacustrine environment within the Central Anatolian Neogene Basin, were formed in a playa (alkaline) lake environment and are therefore rich in sepiolite (Figure 1). The brown sepiolite unit, which is rich in organic matter, was formed in anoxic marshes in the center of the playa lake, while the dolomite sepiolite was formed in small ponds of the playa lake, Kadir et al. [8]. Sepiolite, derived from Mg-silicate and dolomitic precursors, is formed in shallow-lacustrine, alkaline (pH: 8.0-9.5), low-salinity, and anaerobic areas [11].

Wall tiles are a mixture of clay, Kaolin, and calcite, which are known as internal decoration materials. The Wall tiles, which may have very different dimensions and thickness, are fired between 1120 C and 1160 C. In general, the wall tile body formulation is used min. 45-40% clay materials to obtain eligible strength values [12]. Sümer [13] obtained the density of sepiolite as 2.08 g/cm3 and its porosity as 37.5% due to some experimental studies on Eskişehir sepiolite used in ceramic production, dimension determination, and chemical analysis. In light of this information, it was observed that up to 40% of sepiolite material could be used in tile ceramics; with sepiolite addition, the density of the ceramic changed from 1.9 g/cm^3 to 2.3 g/cm^3, the water absorption rate changed from 9% to 7.8%, the bending strength changed from 170 kg/cm^2 to 196 kg/cm^2, the heat expansion coefficient changed from 8×10^6 to 5×10^6; the experimental tiles produced had good shock resistance and were mainly in compliance with the standard TSE-4037.

There are many studies on the region in question due to the economic importance of sepiolite and the complex geological structure of the Sivrihisar region. Kayacı and Genç [14] investigated using clay minerals and granites in ceramic bodies and examined this issue with physical-chemical experiments and analyses. Various studies have been conducted for the phases required in ceramic production.

Işık [15] examined the sepiolite formations in the region between Türkmentokat and Karatepe in Eskişehir, performed geochemical analyses of meerschaum (nodular sepiolite), and determined that the meerschaum found in the Sarısu region was genuine. Whitney et al. [16] defined the Sivrihisar Massif, defined the metamorphic rocks in the region, and suggested that it underwent Barrovian-type metamorphism. The formation of metamorphics and their relationship with granites were modeled, and it was determined that metamorphism occurred during the Eocene period. The large-scale study by Okay et al. [17] also included the Günyüzü Pluton. As a result of new datings from granitoids, they determined that the granitoids were Late Paleocene-Early Eocene. It was suggested that the formation of granites was related to subduction and occurred simultaneously with the collision. This study investigated the geology, mineralogy, and ceramic technological properties of sepiolite in the Eskişehir region, and their usability in ceramic bodies was discussed.

2. Materials and Methods

XRF is an analysis method in which the main element oxides are determined from the samples. The sample preparation processes were carried out in the Kaleseramik R&D Laboratory. First, the samples were broken one by one using a tungsten carbide Fritsch pulverized 1 model jaw crusher. In order to ensure homogeneity of the broken samples, sampling was done using the quadrupling method. To remove the samples' moisture, they were dried in a laboratory-type oven at 105°C for 1 day. The dried samples were passed through a 2 mm sieve and ground in a laboratory-type electric mortar. Pellets were prepared from the samples passed through a 63-micron sieve, and primary oxide element analyses were carried out with a Panalytical Axios brand-type XRF device.

Some samples passed through a 63-micron sieve during XRF studies were separated for XRD analysis. Powder samples were taken with a metal spoon and placed in a Pyrex container; a few drops of water were added, mixed, and turned into a paste. The prepared pastes were applied to glass coverslip sections. After drying, they

were placed in the PANalytical X'Pert Pro MPD Diffractometer CuKα radiation brand type device in R&D for XRD shootings. The peaks obtained were evaluated with HighScore Plus software.

In order to determine the thermal properties of the samples determined to be dolomitic sepiolite as a result of XRF and XRD studies, Differential Thermal Analysis (DTA), Thermogravimetric Analysis (TG), and dilatometer methods were used in Kaleseramik R&D. The samples, which were dried at 25°C and turned into powder, were analyzed with the Seteram brand Labysy EVO model DTA-TG-DSC device.

Thermal and optical experiments were conducted to determine the physical-mechanical properties of clay samples from the field. 300 grams of the crushed and quartered samples were taken and placed one by one into ceramic ball containers with a spoon, then 700 grams of water, 1.5 grams of glass water, and 0.6 grams of sodium tripolyphosphate (STPP) were added. The reason for adding these materials is to facilitate the separation of grains in acidic environments. Ceramic containers were placed in a laboratory-type mill device and left to rotate for 10 minutes.

The clay samples passing through the 63-micron sieve were placed on trays by spreading them homogeneously and put in the oven for 24 hours to dry. The samples from the oven were ground by rotating in an agate electric mortar. To gain plasticity, the powdered sample was given 15% of its weight in homogeneous moisture; a 25 g sample was taken and placed in a laboratory-type hydraulic press. Tablets were pressed by applying 36 bar pressure, and the lengths of the pressed tablets were measured using tape.

The prepared tablets were fired at 1125°C for 40 minutes, the wall tile condition in a Sacmi model roller kiln of the Kaleseramik Factory. The length (%), shrinkage (%), and water absorption tests of the samples brought from the furnace were performed according to ISO-EN 10545-3. Color values (L, a, b) were measured with a Minolta brand 3600d Colorimeter device.

3. Results and Discussion

3.1. Mineralogical and Chemical Analysis of Clays in the Kurtşeyh Region

32 samples were collected from the sepiolite-bearing succession of the Kurtşeyh region. Their XRF analysis was carried out to determine the chemical characteristics. The compositional ranges, average chemical compositions of 30 samples, and the two typical samples (SEP-A and SEP-B) are shown in Table 1. In dolomitic sepiolite materials, there is an increase in CaO, MgO, and a decrease in SiO_2. The SiO_2 amount is low for dolomite samples, and CaO and MgO are high and equal in proportion. The other chemical feature is the high LOI, as expected from the carbonaceous rocks. The XRF results combined with the XRD results predicted that the samples studied were sepiolite, dolomitic sepiolite (SEP–B), sepiolitic dolomite (SEP–A), clayey (and siliceous), and common dolomite.

Table 1. XRF results for the samples

SAMPLE	LOI	SiO_2	Al_2O_3	TiO_2	Fe_2O_3*	CaO	MgO	Na_2O	K_2O	MnO	P_2O_5	SO_3
Min-Max	13.50-43.29	3.31-43.12	0.31-12.4	0.04-0.72	0.09-4.98	7.77-37.36	3.12-24.26	0.03-0.47	0.08-2.94	Nd	0.08-0.19	0.12-0.48
Average	34.97	19.22	2.98	0.22	1.13	22.14	18.15	0.19	0.59	Nd	0.12	0.16
SEP-A	21.48	43.12	7.90	0.62	2.61	8	14.22	0.26	1.43	Nd	0.11	0.15
SEP-B	33.71	24.68	1.74	0.20	0.44	15.6	23.04	0.12	0.18	Nd	0.13	0.21

Compositional ranges of the 30 samples, averages, and XRF analysis for the SEP-A and SEP-B samples. LOI: loss on ignition. Here, * denotes total iron. Nd: below detection limits. SEP-A and SEP-B are from [18]

This classification was made for predictive purposes only and does not fully reflect the real character of the material. To more clearly estimate the character of 32 samples that were thought to have a composition that could be used for ceramic production due to XRF analysis, powdered samples were subjected to XRD analysis.

As a result of the examinations, the maximum peak of the sepiolite mineral was determined at 12.5 Å. In addition, sepiolite mineral peaks at 4.4 Å and 4.2 Å. The maximum peak was determined at 2.88 Å for dolomite. Calcite was encountered at 3.03 Å peaks. For quartz, 4.26 Å and 3.34 Å peaks were used for identification purposes.

Table 2 shows some of the rheological properties of the SEP-A, SEP-B, and İstanbul clays. Slip viscosity, flow rate, and thixotropic aspects of SEP-A and SEP-B increase due to their complex structure with needle-shaped fiber agglomerates [19]. The anisotropic structure of sepiolite provides an advantage in the presence of its layered and fibrous structures.

Table 2. The rheological properties of the SEP-A, SEP-B, and İstanbul clays.

Material	Weight volume (gr/lt)	Flow rate (sn)	Viscosity (cp)	Tixotrophic aspect (sn)
İstanbul clay	1650	25	400	32
SEP-A	1660	98	1800	127
SEP-B	1650	89	1700	120

3.2. DTA and TG Tests

As a result of XRF and XRD studies, DTA and TG experiments were performed on a sample suitable for ceramic production. The purpose of this experiment is to characterize the material with thermal processes. The temperature of the sample is gradually increased during the experiment, and the mass change in response to heat is measured. The purpose of the DTA and TGA experiments is to find the temperature at which the physical and chemical water in the raw material decomposes and obtain information about phase or crystal transformations and structure decompositions.

The DTA-TG curves of the sepiolitic dolomite samples (SEP-A, SEP-B) are illustrated in Figures 2a and 2b, respectively. Four weight loss events (peak) are seen in the curves, which occur at around 105°C, 300°C, 650°C, and 800°C. The first endothermic peaks concern the evaporation of residual water. The second weight loss occurs probably due to aluminum and iron hydroxyl hydroxylation. The third and final weight loss is related to the decomposition of $CaCO_3$ and $MgCO_3$. The loss of water and dehydration of clay minerals involve the mass loss of samples.

According to the study, it was concluded that the material is suitable for use in real ceramic recipes. This is because, after 830°C, the material starts to remain stable; that is, the material begins to behave precisely like clay. Before 830°C, the deformation in the crystal structure was visible. The abundance of sepiolite shows that it is in accordance with the prescription.

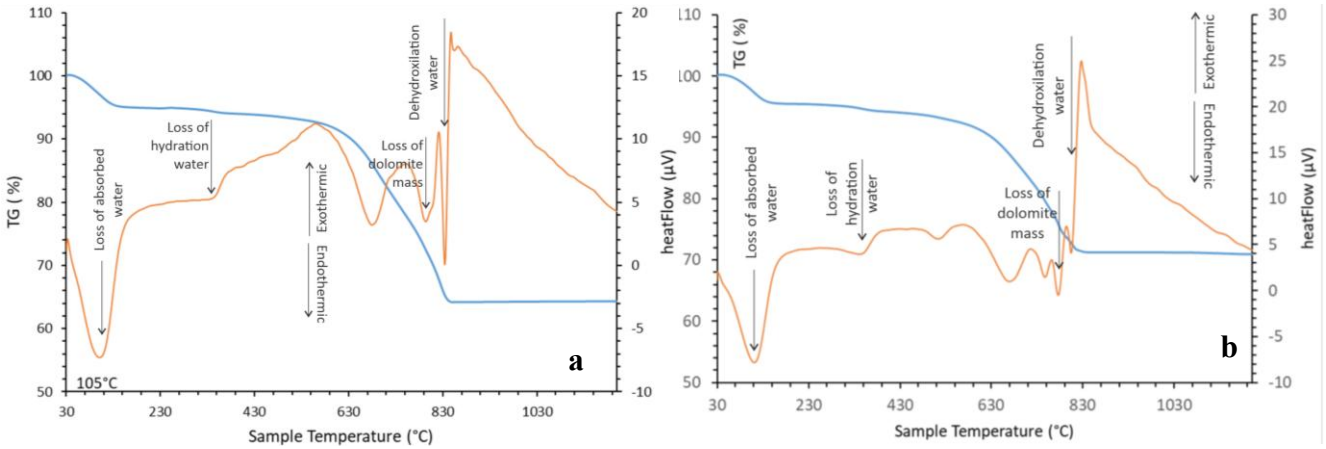

Figure 2. DTA-TG analysis graph of Kurtşeyh dolomitic sepiolite (SEP-A and SEP-B) ground for 60 min

3.3. Thermal and Optical Behaviors

In order to test the suitability of different samples taken from the Kurtşeyh region for use in ceramic production, the changes that occur after firing were determined. The firing temperature of the tablet samples was determined as °C, firing time (min), shrinkage (%), water absorption (%), and color change values L (whiteness), a (yellowness), b (redness) (not shown here). The Sepiolite A sample sintered later than the Sepiolite B sample due to its high SiO_2 and low MgO content. In Figure 3, the % shrinkage and % water absorption values of Sepiolite A and B at different % utilization rates support this conclusion. The results of these tests, samples SEP-A and SEP-B, were chosen to appear very suitable for ceramic tile production and are shown in Figures 3a and 3b. As can be seen, SEP-A and SEP-B for wall tiles shrank by nearly 1% compared to their initial state after being fired at 1125°C for 40 minutes. Usually, the shrinkage value is expected to be between 4-6% for clays, but it is pretty low for this material. This shrinkage value indicates that the raw material is suitable for high amounts in the recipe.

The water absorption value was determined to be 25-32%, which is relatively high compared to normal clays. This value indicates that the material creates visible porosity. The L value was measured between 77 to 92. This shows that the material is highly white, a desired color in ceramic production.

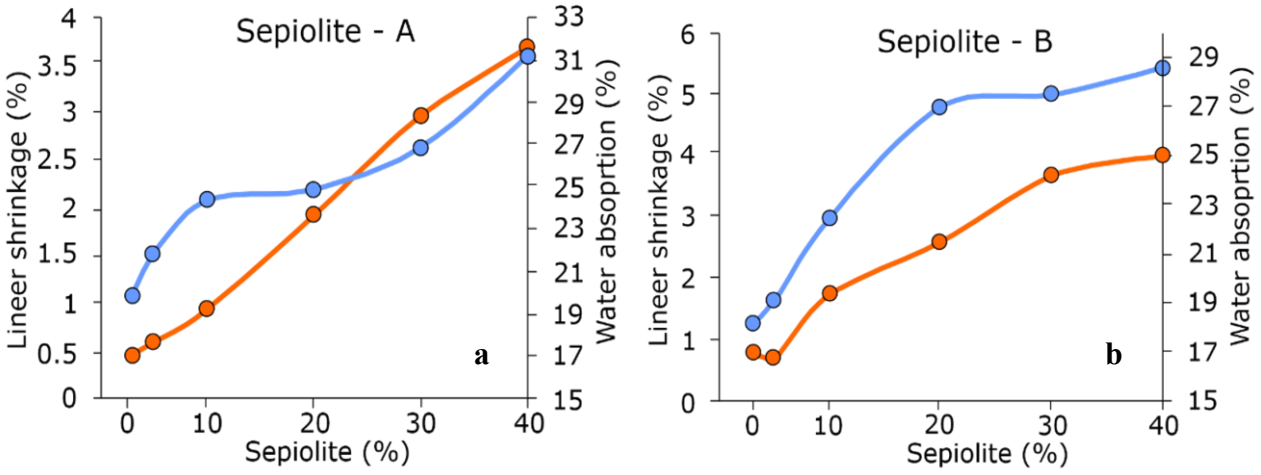

Figure 3. Thermal and water absorption test results of the SEP-A and SEP-B samples taken from the Kurtşeyh region (the blue lines show the linear shrinkage, and the orange ones are water absorption curves).

3.4. The Use of Kurtşeyh Sepiolite in Ceramic Recipes

As a result of the XRF, XRD, thermal, mechanical, and optical experiments, samples that could be used as alternatives to clay minerals in ceramic recipes were determined. Two (SEP-A and SEP-B) were selected and used for the real ceramic recipes. First, the question of what ratio of dolomitic sepiolite should be added instead of clay minerals in the recipe should be understood to obtain more efficiency. Tables 3 and 4 show the chemical and proportional aspects of the components of newly prepared recipes. As can be seen in Table 4, 40% dolomitic sepiolite was used instead of clay minerals.

Table 3. XRF results of the recipe components

	L.O.I.	SiO_2	Al_2O_3	TiO_2	Fe_2O_3	CaO	MgO	Na_2O	K_2O
Marble	44.02	0.65	0.34	0.01	0.05	55.02	1.06	0.05	0.04
Kaolin	9.26	65.38	23.23	0.78	0.32	0.24	0.03	0.02	0.37
Clay	8.78	56.70	24.23	1.05	2.34	0.69	1.04	1.19	2.04

Marble comes from Çanakkale marble/calcites, and Kaolin and clay are from Şile and Ukraine. For SEP-A and SEP-B, see Table 1. Partly after [17]

Table 4. Body formulations by adding dolomitic sepiolites (SEP-A and SEP-B) in varying proportions instead of clay (after [17])

Raw Material	STD	A-3	B-3	A-5	B-5	A-10	B-10	A-20	B-20	A-30	B-30	A-40	B-40
SEP-A		3		5		10		20		30		40	
SEP-B			3		5		10		20		30		40
Marble/Calcite	12	12	12	12	12	12	12	12	12	12	12	12	12
Kaoline	38	38	38	38	38	38	38	38	38	38	38	38	38
Clay	50	47	47	45	45	40	40	30	30	20	20	10	10

Later, these different recipes were again subjected to optical and thermal experiments, and the extent to which the structures changed was examined. Results are shown in Tables 5, 6. We have compared the linear thermal expansion values of the Standard wall tile with the formulations of A-40 and B-40 (Tables 5 and 6). The Linear thermal expansion (20-400°C) value for the Standard wall tile decreased from 66.45 to 63.34 and 62.17 for A-40 and B-40 formulations, respectively. At the same time, moisture expansion values decreased from 0.034% to 0.016% and 0.014%. From non-contact optical dilatometer curves, it was determined that the fastest temperature values at which sintering occurs are 1006°C in the standard body, 970 and 861°C in the bodies with sepiolite addition (Figures 4a and 4b). As the amount of dolomitic sepiolite increases, improvements in thermal properties are observed, and the degree of whiteness also increases.

Table 5. Thermal and optical behaviors of the SEP-A added bodies at various rates

SEP-A Recipe	STD	A-3	A-5	A-10	A-20	A-30	A-40
Linear thermal expansion (20-400°C)	66.45	66.22	65.45	64.98	63.43	62.45	62.34
Moisture expansion (%)	00.34	0.031	0.026	0.022	0.024	0.018	0.016
L	75.23	77.50	77.29	78.80	83.46	88.92	92.56
a	6.16	4.83	3.91	3.98	2.26	1.07	0.65
b	18.41	16.70	17.54	16.14	13.36	9.36	6.17

Table 6. Thermal and optical behaviors of the SEP-B added bodies at various rates

SEP-B Recipe	STD	B-3	B-5	B-10	B-20	B-30	B-40
Linear thermal expansion (20-400°C)	66.45	66.10	65.22	64.67	63.33	62.21	62.17
Moisture expansion (%)	0.034	0.028	0.022	0.019	0.017	0.016	0.014
L	75.23	75.56	75.05	77.49	82.09	83.91	84.99
a	6.16	4.99	4.91	3.63	1.71	1.45	1.25
b	18.41	18.07	20.35	15.31	13.17	11.73	10.86

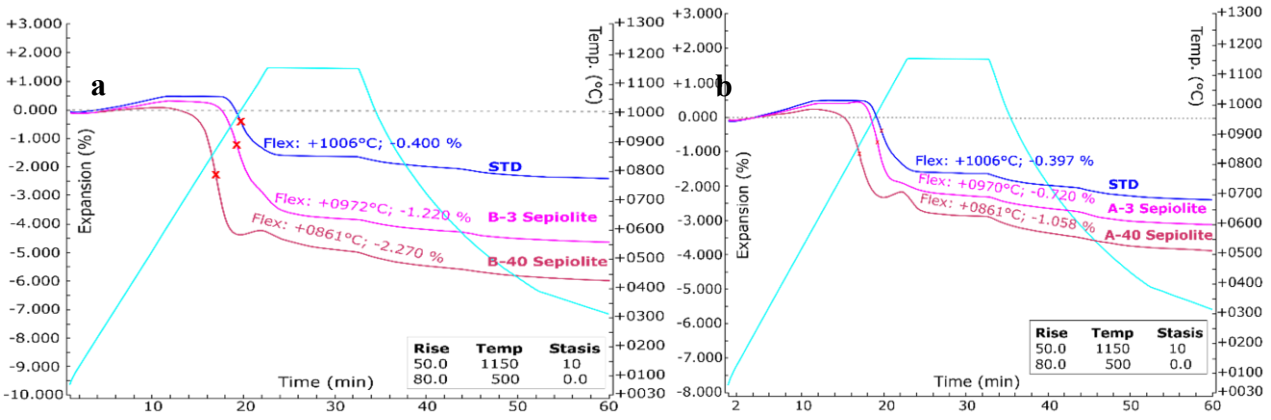

Figure 4. Non-contact optical dilatometer curves for the standard (STD), Recipe-A (A-3, A-40), and Recipe-B (B-3, B-40)

XRD analysis was done on the different fired bodies to understand the new mineral phases. Figures 5a and 5b display the quartz (COD: 96-101-1173), anorthite (COD: 96-901-1632), and enstatite (COD 96-900-1179) phases on the XRD graph. As a result of the increase in dolomitic sepiolite instead of clay, quartz phases decrease, and anorthite and enstatite phases are formed [18]. The decrease in quartz means an increase in crystallization, which is a positive result of using dolomitic sepiolite instead of clay. The enstatite phase indicates the importance of the usability of dolomitic sepiolite compared to clay as an element that increases strength and durability. Anorthite is an indispensable phase for wall tiles regarding porosity and dimensional stability. Sivrihisar dolomite-bearing sepiolites possibly transformed to enstatite at 845°C and amorphous silica at 862°C. This transformation can be formulated as follows [20, 21]:

$$Si_{12}O_{30}Mg_8(OH)_4 \text{ --> } 4Mg_2Si_2O_6 + 4SiO_2 + 2H_2O$$

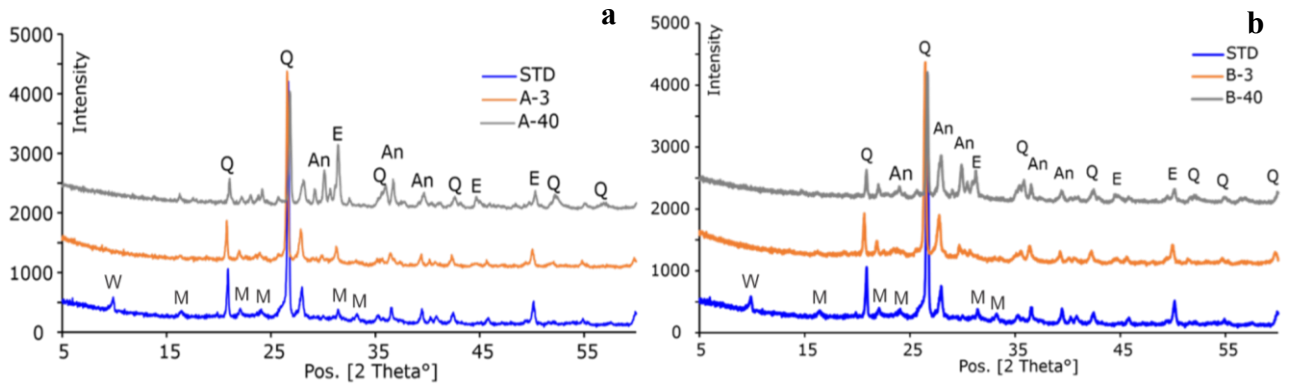

Figure 5. Mineral phases of the fired bodies by XRD (Q: Quartz, An: Anorthite, E: Enstatite, W: Wollastonite, M: Mullite, after [18])

4. Conclusion

In the literature, sepiolite minerals are not commonly used as alternatives to clay minerals used in ceramic recipes. The main reasons for this are that, because of the physical properties of sepiolite, appropriate results cannot be obtained in ceramic recipes (especially since it creates rheological problems), and its reserve is quite low compared to other clay minerals in the world and our country. These physical properties' shrinkage and water absorption values are not considered suitable for recipes. The water absorption value and shrinkage were quite high compared to the clays. This study observed that dolomitic sepiolites processed from the Kurtşeyh region are suitable for use in ceramic production based on XRF, XRD, and other physical and optical tests. This is because dolomite accompanying the sepiolite mineral changes the material's physical, optical, and thermal properties. Sepiolite was transformed into enstatite through dolomite, which positively affected the test results.

Author Contributions

All the authors equally contributed to this work. They all read and approved the final version of the paper.

Conflict of Interest

The author declares no conflict of interest.

Ethical Review and Approval

No approval from the Board of Ethics is required.

References

[1] K. Sarıiz, İ. Nuhoğlu. Endüstriyel hammadde yatakları ve madenciliği, Anadolu University Publications, 1992.

[2] E. Sabah, M. S. Çelik. *Removal of pollutants from wastewater using sepiolite*, Journal of Clay Science and Technology 1 (1) (2006) 55–72.

[3] S. Sherlock, S. Kelley, S. Inger, N. Harris, A. I. Okay. *40 Ar-39 Ar and Rb-Sr geochronology of high-pressure metamorphism and exhumation history of the Tavsanlı Zone, NW Turkey*. Contributions to Mineralogy and Petrology, 137 (1999) 46-58.

[4] P. B. Davis, D. L. Whitney, *Petrogenesis of lawsonite and epidote eclogite and blueschist, Sivrihisar Massif, Turkey.* Journal of Metamorphic Geology 24 (9) (2006) 823-849.

[5] A. I. Okay, *Tavşanlı zone: The northern subducted margin of the Anatolide-Tauride block.* Bulletin of the Mineral Research and Exploration 142 (2011) 191-221.

[6] A. Plunder, P. Agard, C. Chopin, A. Pourteau, A. I. Okay. *Accretion, underplating and exhumation along a subduction interface: From subduction initiation to continental subduction (Tavşanlı zone, W. Turkey)* Lithos 226 (2015) 233-254.

[7] S. Kadir, H. Erkoyun, M. Eren, J. Huggett, N. Önalgil. *Mineralogy, geochemistry, and genesis of sepiolite and palygorskite in Neogene lacustrine sediments, Eskişehir Province, west-central Anatolia, Turkey.* Clays and Clay Minerals 64 (2) (2016) 145-166.

[8] S. Kadir, M. Eren, T. İrkeç, H. Erkoyun, T. Külah, N. Önalgil, J. Huggett. *An approach to genesis of sepiolite and palygorskite in lacustrine sediments of the Lower Pliocene Sakarya and Porsuk Formations in the Sivrihisar and Yunusemre-Biçer regions (Eskişehir), Turkey.* Clays and Clay Minerals 65(5) (2017) 310-328.

[9] K. Sarıiz. *The geology, mineralogy, and occurrence of bedded sepiolite deposits in the Akçayır-Yürükakçayır (Eskişehir) lacustrine basin, central Turkey*. Exploration and Mining Geology 9 (2000) 265-275.

[10] Z. Karakaş, Ö. Karakaş, B. Varol, *Mineralogical investigation of claystone in the Neogene (Miocene Pliocene) lacustrine basin of the Sazak Biçer area (NE of Sivrihisar),* Geological Bulletin of Turkey 50 2 (2007) 57-69.

[11] Ü. Özbaş, *Origin and diagenetic evolution of sepiolite-palygorskite formations in Turkey,* Doctoral Dissertation Dokuz Eylül University (2008) İzmir.

[12] K. Kayacı, *Effect of fluxing raw materials on moisture expansion of monoporosa wall tile bodies,* Journal of Thermal Analysis and Calorimetry 146 (1) (2020) 1603–1611.

[13] G. Sümer, *İstanbul Bölgesi döküm kilinin özellikleri ve seramik döküm çamurunda kullanılma imkanlarının araştırılması,* in: M. Ç. Karakaya, N. Karakaya, (Eds.), 10. Ulusal Kil Sempozyumu, Konya, (2001) pp. 532.

[14] K. Kayacı, S. C. Genç¸, *Sintering behaviour of albite and microgranite containing porcelain stoneware bodies*, Industrial Ceramic 29 (2009) 91–99.

[15] C. E. Işık, M. Beyarslan, *Mineralogy and charectarizations of nodular sepiolite (meerschaum) of Türkmentokat-Karatepe district (Eskişehir)*, Science and Engineering Journal of Fırat University 28 (2) (2016) 73-82.

[16] D. L. Whitney, C. Teyssier, E. Toraman, N. C. Seaton, A. K. Fayon, *Metamorphic and tectonic evolution of a structurally continuous blueschist-to-barrovian terrane, Sivrihisar Massif,* Turkey Journal of Metamorphic Geology 29 (2010) 193–212.

[17] A. I. Okay, O. Monod, P. Monié, *Triassic blueschists and Eclogites from Northwest Turkey: Vestiges of the Paleo-Tethyan subduction,* Lithos 64 (2002) 155–178.

[18] K. Kayacı, Ş. C. Genç, Y. Yıldırım. *Mineralogical and technological properties of the Eskişehir sepiolite (Turkey), and its usage possibilities as enstatite-based wall tile production*, Qualicer 22 (2022) 1-2.

[19] E. S. Sabah, M.S. Çelik *Sepiyolit Oluşumu, Özellikleri, Kullanım Alanları.* (1998), 172.

[20] R. L. Frost, Z. Ding, *Controlled rate thermal analysis and differential scanning calorimetry of sepiolites and palygorskites*, Thermochimica Acta 397 (2003) 119-128.

[21] H. Nagata, S. Shimoda, T. Sudo, *On dehydration of bound water of sepiolite*, Clays and Clay Minerals, 22 (1974) 285-293.

Journal of Advanced Research in Natural and Applied Sciences
dergipark.org.tr/en/pub/jarnas
Open Access

ISSN: 2757-5195 | 11 (2) (2025) 117-131 | doi.org/10.28979/jarnas.1652484

Comparative Study of Surface Roughness in Upskin and Downskin Regions of Conformal Cooling Channel Sections Fabricated with AlSi10Mg, Ti64, 316L in AM-LPBF

Cemal İrfan Çalışkan[1]

Article Info
Received: 06 Mar 2025
Accepted: 13 Apr 2025
Published: 30 Jun 2025
Research Article

Abstract − Conformal cooling channel (CCC), used in many industries such as aviation, molding, biomedical, and robotics, refers to functional fluid channels that provide mass or energy transfer. CCC, which can be produced in limited forms where liquid flow cannot be fully achieved in traditional production technologies, is among the areas where additive manufacturing (AM) offers design freedom. However, in design-integrated CCC productions, sagging and deformation in the pipe section caused by the AM production process and design parameters can cause a decrease in the performance expected from the CCC and cause unpredictable flow problems. The producible CCC section from research constitutes the scope of this study. In this study, the production of cylindrical test specimens with eleven channel cross-sections between 0,4 mm and 9 mm using laser powder bed fusion (LPBF) technology using AlSi10Mg, 316L, and Ti64 materials and the roughness measurements of the upskin and downskin regions and the scanning electron microscope (SEM) examination are comparatively discussed. Inconsistent results were obtained in the surface roughness measurements of the 0,4 mm and 0,5 mm diameter holes considered within the scope of the research due to the diameter being below the production limits. This research shows that surface roughness in the upskin parameter region is more acceptable in all material types. In the laboratory measurements obtained, it is seen that the downskin region surface roughness value in the holes produced with AlSi10Mg is higher than other materials, and it is lower in the holes produced with Ti64 than other materials.

Keywords − *Additive manufacturing, laser powder bed fusion, AlSi10Mg, 316L, Ti64, conformal cooling channels*

1. Introduction

AM is the formalized generic term for the technology popularly known as 3D Printing, also called rapid prototyping [1]. The term is used in various industries to describe rapidly creating a part representation before the final product or commercialization [2]. In other words, creating a physical part directly from digital model data has been widely used to describe technologies that develop prototypes. Nowadays, rapid prototyping technologies are not only used to create models. However, they were initially designed to expand the range of situations tested in the prototyping process. Still, with the advantages of certain materials, it is now possible to create finished products [3]. American Society for Testing and Materials International (ASTM) has defined additive manufacturing as combining materials in layers to produce objects from Computer Aided Design (CAD) model data [4]. While Additive Manufacturing (AM) has existed as a method of processing materials for over three decades, it is now emerging as an essential commercial manufacturing technology.

[1]cemalirfancaliskan@gmail.com (Corresponding Author)
[1]Department of Industrial Design, Faculty of Architecture, Istanbul Technical University, İstanbul, Türkiye

AM, which has been the focus of research since the 1980s, has created new design areas in many industrial areas with its new perspective. One of these innovative areas is the manufacturability of complex internal geometries, functional fluid channels [5]. Various studies on these functional flow channels [6] and complex internal geometries are encountered in areas such as electronic cooling [7], biomedical [8], heat exchangers [9], and molds [10,11].

Research on functional flow channels produced by AM and aimed at regulating cooling performance is referred to in the literature as conformal cooling channels (Figure 1). Various studies in the AM field show that Conformal Cooling Channel (CCC) [12] is a good solution to control thermal stresses, improve the quality of the final product, and reduce cycle time [13].

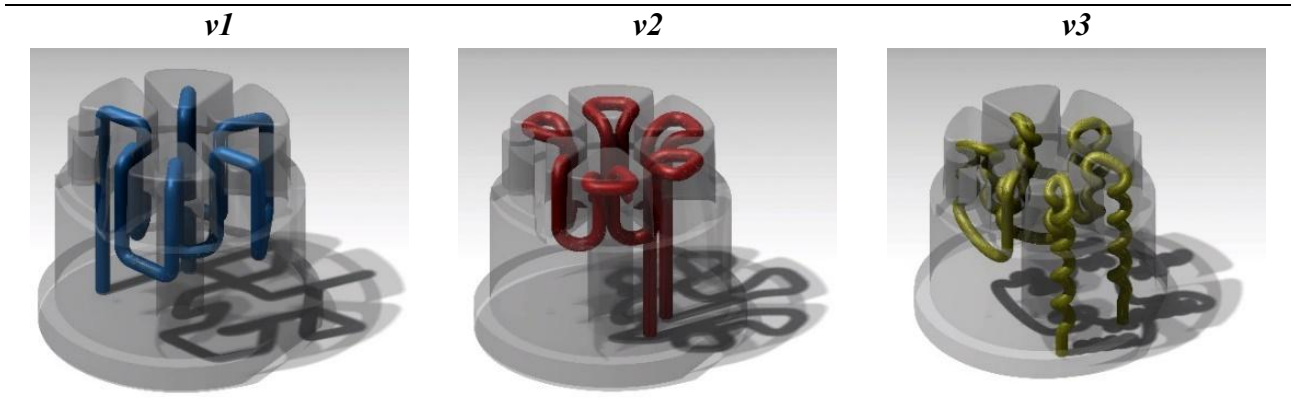

Figure1. Various CCC designs [14]

These systems have a promising future in replacing conventional cooling systems as they can provide more efficient cooling effects and contribute significantly to production quality [15] and efficiency [16]. Some studies indicate that the cycle time is shortened by 30% [17] and 40% in injection systems where CCC-applied molds are used [14]. Some studies on this subject report that production cycle time can be reduced by up to 70%, and shape deviations can be prevented [18]. The diameter of the Conformal Cooling (CC) channels and the ability to manufacture the channel cross-section [19] that does not obstruct the coolant flow play an essential role in cooling and production efficiency in molds and part quality [20]. Some research results show that CC channel-applied eco-friendly molds shorten the cooling time by 45% [21].

The different efficiency values obtained in the research are directly related to the mold size, CCC geometry diameter of this size, the manufacturability of the channel section, and the channel's inner surface roughness. The surface roughness factor is essential in evaluating the CCC channels' liquid pressure drop [22]. It is known that some post-processing, known as abrasive flow machining, is performed to eliminate the unpredictable and inhomogeneous surface roughness in the channel cross-section of 1 to 2 mm diameter channels produced with Laser Powder Bed Fusion (LPBF) [23].

There are not many studies in the literature about the channel cross-sectional form and upskin and downskin regions in the holes of CCC geometries, which are generally known to provide advantages such as increased production quality [24], increased production time [25], energy saving, and efficiency [26].

Our previous studies on channel geometries produced without support determined that some sagging or deformations occurred on the upper surface of the hole where the downskin parameter was effective [27]. In another study we conducted in this context, since the actual surface roughness of the upskin and downskin regions within the channel could not be determined in the channel cross-sections examined with imaging methods such as Computed Tomography (microCT) and Scanning Electron Microscope (SEM) [28], a comparative study was conducted on the surface roughness, which is known to be effective in flow quality in the upskin and downskin regions, with the method presented in this study. Since the probe measurement method of the roughness measuring devices requires the surface to be open from the top, each hole sample was produced in two pieces, and precise vertical surface roughness measurements were completed. Three

roughness values taken from each hole sample are shared comparatively in this research using AlSi10Mg, 316L, and Ti64 materials. In addition, SEM examination was included to show that the sagging effect, which is more intense in hole diameters smaller than 2 mm and where the downskin parameter is effective, is not very effective in larger diameters.

2. Materials

Considering the basic design criteria (Table 1), the LPBF technology manufacturer provided support-free production that can be carried out in channel sections between 0,5 mm and 8 mm.

Table 1. LPBF design parameters [29,30]

The ratio between the section and height of the object to be produced should not be more than 8:1	The outside-to-outside dimensions of the design should not be larger than the platform size	Alternative geometries should be used for sizes larger than 8mm, which are desired to be produced without support
The minimum hole diameter in the design should not be less than 0,5 mm	The maximum hole diameter to be produced without support should be 8mm	The minimum diameter for the cylinder geometry used in the design should not be less than 1 mm
Unsupported angles should not be less than 30-45 degrees. Angle evaluation varies depending on the material used.	Part dimensional tolerance: +,- 0,1 mm	The minimum producible wall thickness should not be less than 0,4mm

Therefore, the hole diameters determined in this research were preferred in this range (Figure 2). Hole test sample designs in the determined range were completed in the Catia V5 part design module, and the research continued with the production process.

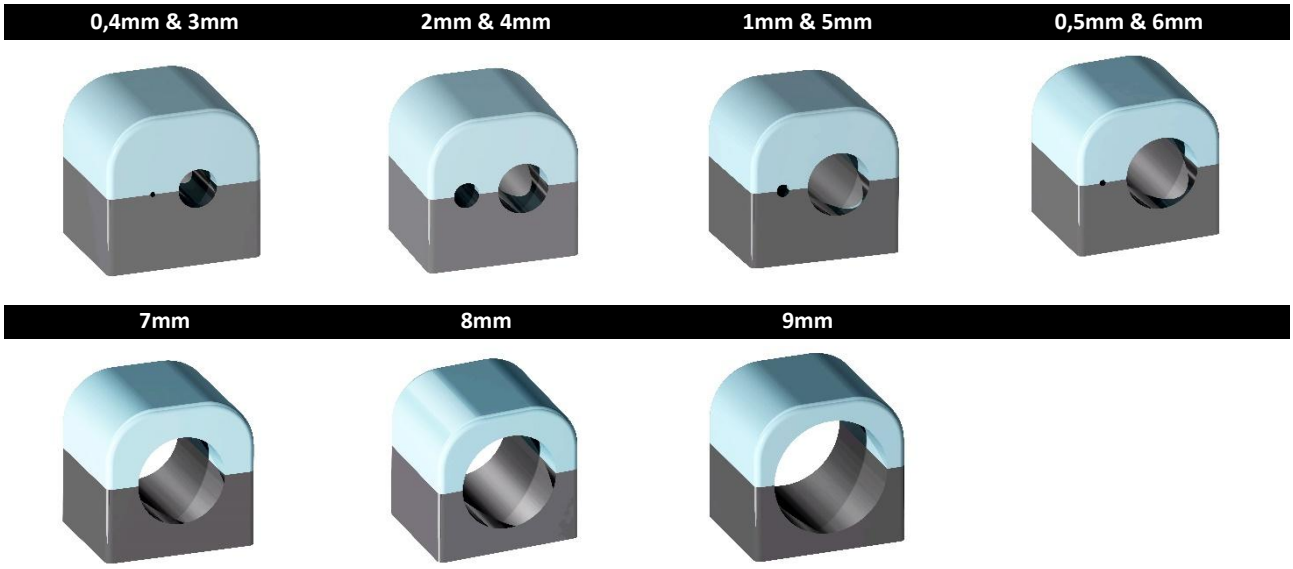

Figure 2. CAD images of the two-piece test samples designed with Catia V5 within the scope of the study

The hole test samples in Figure 2 were designed in two pieces to be able to measure from the bottom and top surfaces of the hole. In this context, some hole diameters were placed in the same sample due to their scale (0,4 mm & 3 mm), and surface roughness measurements were made with three repetitions for each diameter value.

The productions made within the scope of this research were carried out with EOS M290 using AlSi10Mg, 316L, and Ti64 materials. The prevalence of use in the sector was considered in the material selection. In this direction, AlSi10Mg, which is used intensively in electronic cooling, thermal fields, and AM productions, stainless steel 316L used in CCC integrated molding applications, and Ti64, which is a biocompatible material within the scope of CCC's use in the biomedical field, were preferred.

LPBF production technology uses a special parameter set called upskin when the surface faces upwards and downskin when it faces downwards in some sensitive areas of internal geometries. The region and scanning strategy where the upskin and downskin parameters used in the hole samples produced in this study are visualized in Figure 3.

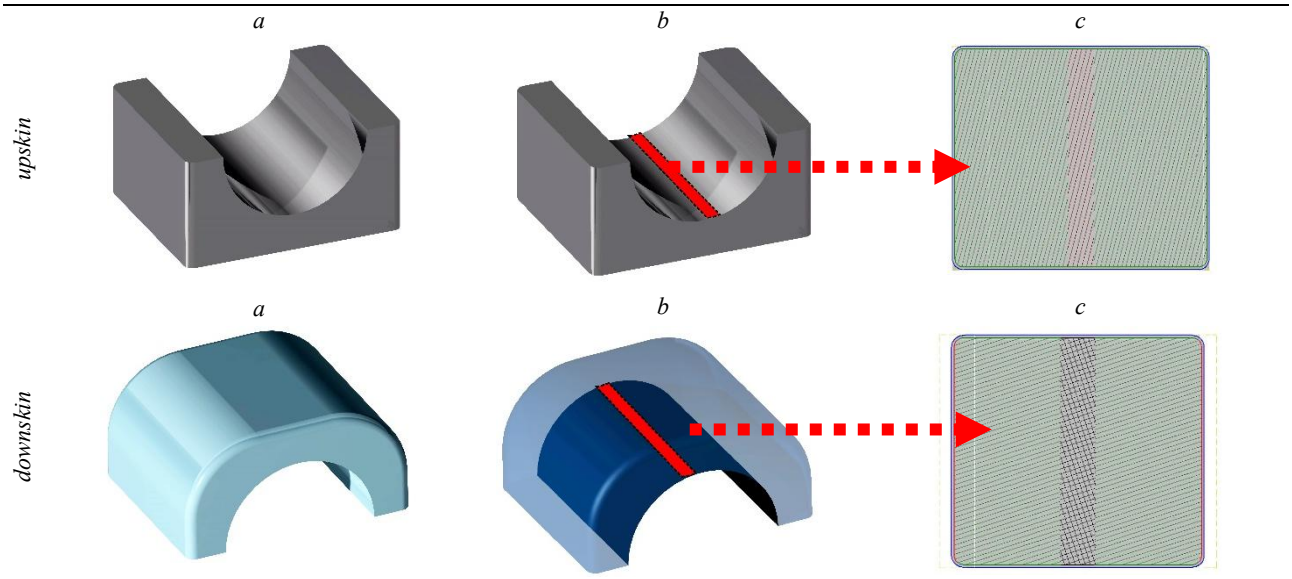

Figure 3. a.Test sample lower and upper CAD, b.upskin & downskin scanning area, c.upskin & downskin scanning area in the EOS print software

The following energy formula (2.1), expressing the balance between the parameters, is used in the research on the process parameter changes. In parameter optimization research to solve the sagging problem of the downskin region, these parameters can be used in production by equalizing the value of the formula [31].

$$E = \frac{P}{vht} \tag{2.1}$$

In this formula, E represents energy, P represents laser power, v represents laser scanning speed, h represents scanning distance, and t represents layer thickness. Upskin and downskin default parameter sets were used in sample production, with three different materials used within the scope of this study (Table 2).

Table 2. EOS upskin and downskin parameters of AlSi10Mg, 316L, and Ti64 materials

	parameters	**upskin**	**downskin**
AlSi10Mg	*hatchdistance:*	0,21 mm	0,21 mm
	scanning speed:	1000 mm/s	1150 mm/s
	laser power:	360 W	340 W
	thickness:	0,09 mm	0,06 mm
	scanning strategy:	X-Y-Alternating	X-Y
316L	*hatchdistance:*	0,09 mm	0,1 mm
	scanning speed:	800 mm/s	1000 mm/s
	laser power:	135 W	80 W
	thickness:	0,04 mm	0,06 mm
	scanning strategy:	X-Y-Alternating	X-Y-Alternating
Ti64	*hatchdistance:*	0,04 mm	0,1 mm
	scanning speed:	1200 mm/s	1000 mm/s
	laser power:	280 W	120 W
	thickness:	0,09 mm	0,06 mm
	scanning strategy:	X-Y	X-Y

3. Methods

3.1. AM Fabrication

Within the scope of the study, the LPBF production phase was started after the CAD design phase. The chemical composition of the materials used in production, AlSi10Mg, 316L, and Ti64, is shared in Table 3.

Table 3. Chemical composition of AlSi10Mg (DIN EN 1706) [32], 316L (ASTM F138) [33] and Ti64 (ASTM F1472 and ASTM F2924) [34]

AlSi10Mg	*Al*	*Si*	*Fe*	*Cu*	*Mn*	*Mg*	*Generic particle size distribution*
	balance	% 9,0-11	% 0,55	% 0,05	% 0,45	% 0,25-0,45	
	Ni	*Zn*	*Pb*	*Sn*	*Ti*		
	% 0,05	% 0,10	% 0,05	% 0,05	% 0,15		25 - 70 µm
316L	*Fe*	*Cr*	*Ni*	*Mo*	*C*	*N*	20 – 65 µm
	balance	%17-19	%13-15	%2,25-3	%0,03	%0,10	
Ti64	*Al*	*V*	*O*	*N*	*C*	*H*	20 – 80 µm
	% 5,50-6,75	%3,50-4,50	%0,20	%0,05	%0,08	%0,015	
	Fe	*Y*	*Ti*	*other, each*	*other, total*		
	%0,30	%0,005	balance	%0,10	%0,40		

During the production phase, the CAD data of the hole sample set exported in STL format was placed in the magics software, and the supports were determined (Figure 4a). In order to use the upskin and downskin parameters, the upper and lower surfaces of the holes were positioned in the orientation of the test samples produced in two pieces, preserving their positions. The production file, which was layer-controlled with the EOS print software, was sent to the production system, and the process was started. The images of the test samples coming out of production are shared in Figures 4b and c.

a *b* *c*

Figure 4. a. Orientation and support of test samples in Magics software, b. LPBF production of test samples, c. Completed test samples

3.2. Laboratory Studies

After the production, the upskin and downskin regions of the 1 mm and 4 mm diameter samples were imaged with the SEM device without any post-processing other than removing the supports from the parts (Figure 5).

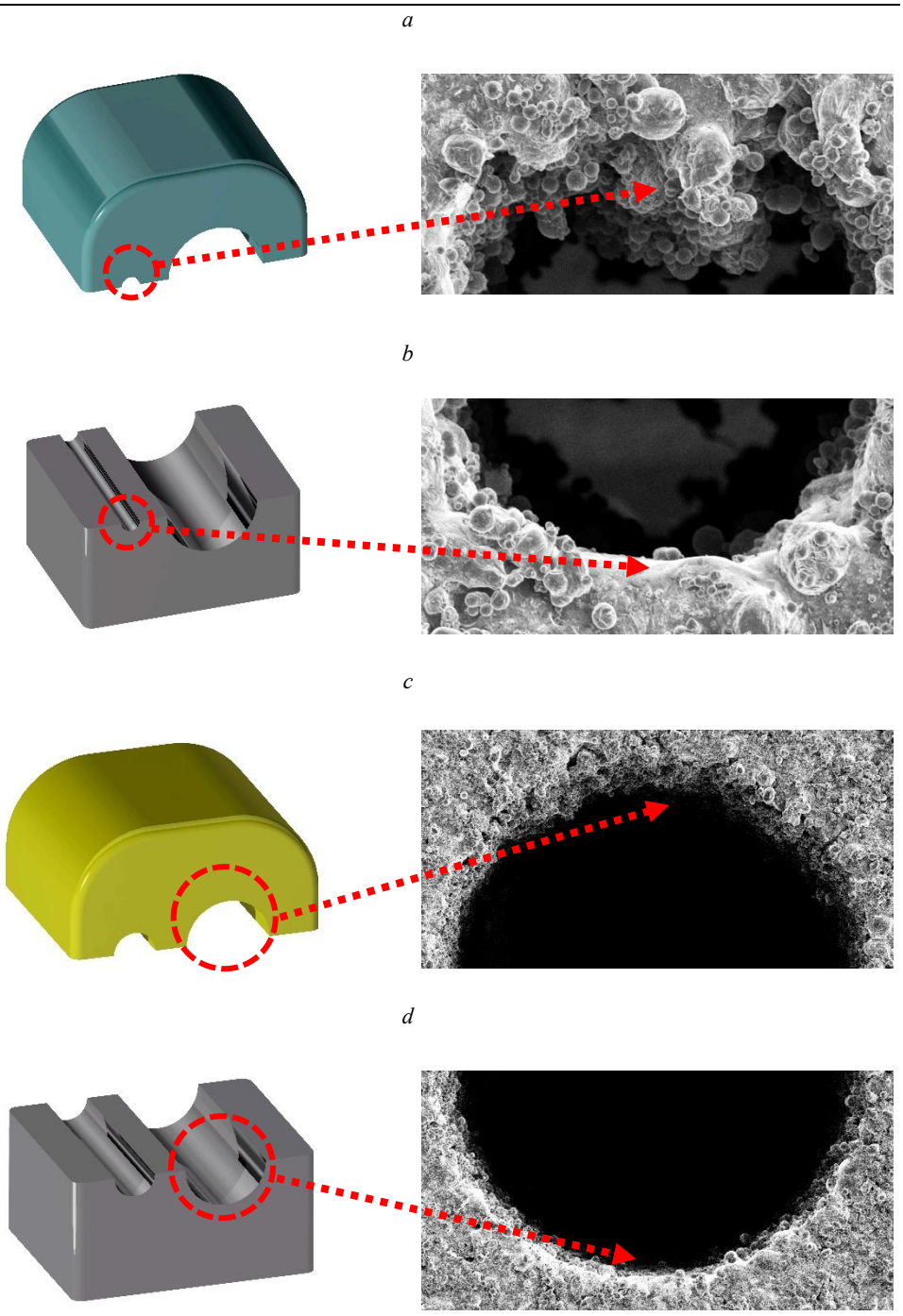

Figure 5. Sem images and CADs. a.1 mm diameter CCC section in the downskin region, b. 1 mm upskin region, c. 4 mm downskin region, d. 4 mm upskin region

In SEM images, which support the data obtained in previous studies in this field [19], the sagging problem in the downskin region (Figure 5a) is seen, especially in low diameters. According to the SEM examination, the hole cross-section form can be produced with higher quality in large diameters. It is known that SEM examinations give results comparable to CAD in in-hole measurements. However, separately measuring the surface roughness values in the upskin and downskin regions is essential for performing functional channel geometries. In this context, the data obtained from surface roughness measurements made with Mitutoyo SJ-500 will be included in the results section as the top and bottom surfaces. The roughness measurements (Figure 6), the average of three measurements taken linearly in the upskin and downskin regions according to the sample size, were taken.

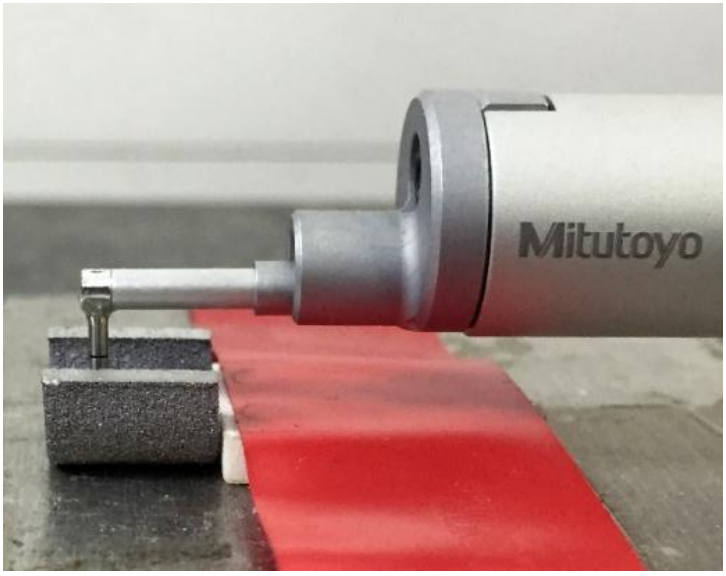

Figure 6. Mitutoyo SJ-500 surface roughness measurement

4. Results and Discussion

The hole diameter range determined within the scope of the research is between 0,4 mm and 9 mm. Accordingly, the test samples produced include hole diameters of 0,4 and 0,5 mm. However, in making small-diameter LPBF circular forms, the distortion of the hole geometry due to sagging and its transformation into an elliptical form led to inconsistent results in surface roughness measurements. Considering the requirement that hole diameters be greater than 0,5 mm in the design criteria shared by the LPBF manufacturer, it can be said that it is normal to obtain inconsistent surface roughness values from hole diameters in this range. In addition, it is considered acceptable that using circular probes in surface roughness measurement devices gives inconsistent results in measuring small-diameter circular forms that are deteriorated by sagging.

The data of surface roughness measurements made in the upskin parameter regions of hole test samples produced with AlSi10Mg, 316L, and Ti64 materials are shared in Figure 7.

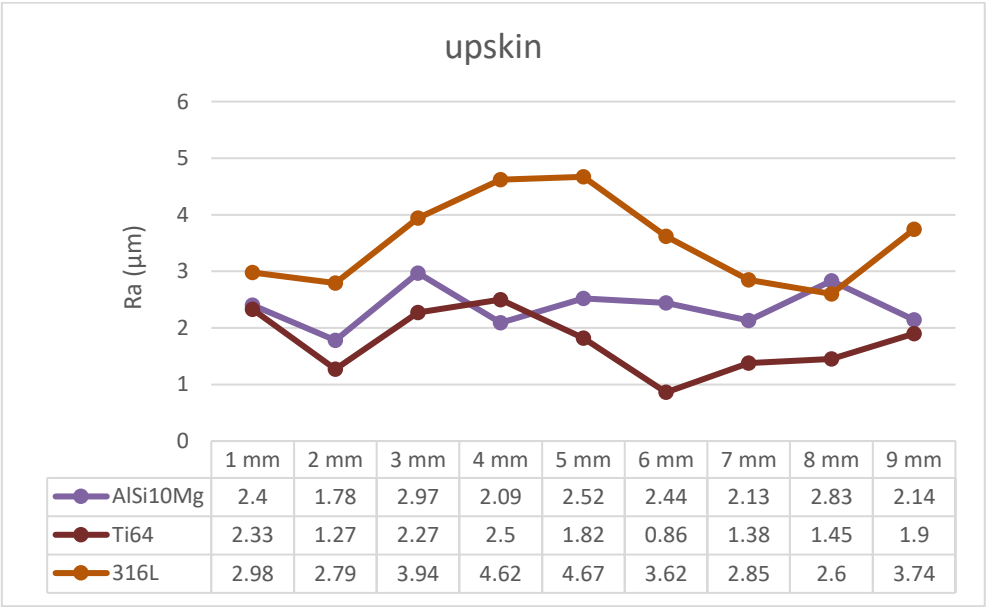

	1 mm	2 mm	3 mm	4 mm	5 mm	6 mm	7 mm	8 mm	9 mm
AlSi10Mg	2.4	1.78	2.97	2.09	2.52	2.44	2.13	2.83	2.14
Ti64	2.33	1.27	2.27	2.5	1.82	0.86	1.38	1.45	1.9
316L	2.98	2.79	3.94	4.62	4.67	3.62	2.85	2.6	3.74

Figure 7. Surface roughness values in the upskin parameter region of hole sections with 1-9 mm diameters produced with AlSi10Mg, 316L, and Ti64 materials

According to Figure 7, the surface roughness values in the upskin region of the holes produced with 316L are higher than those produced with AlSi10Mg and Ti64 in all holes. It can be stated that the upskin surface roughness values of the holes produced with AlSi10Mg are at an average level compared to the other two materials. In the measurements made in the upskin parameter region, it is seen that the lowest roughness values are obtained with Ti64 material. In the evaluation of Figure 7, it can be stated that the 316L and Ti64 upskin surface roughness graphs exhibit a similar change between the holes, although they are in different value ranges. However, it is seen that the graph obtained from the measurement of test samples produced with AlSi10Mg is quite different from the graphs of the other two materials, and that the surface roughness values between the holes give very close results in this material. The results obtained with 316L and Ti64 materials show that while the roughness values between the holes give close values at 2 and 6 mm, this distance widens considerably at 3, 4, 5, 8, and 9 mm (Figure 7).

This situation is thought to be directly related to the technology manufacturer's development process and material properties of the upskin parameter set.

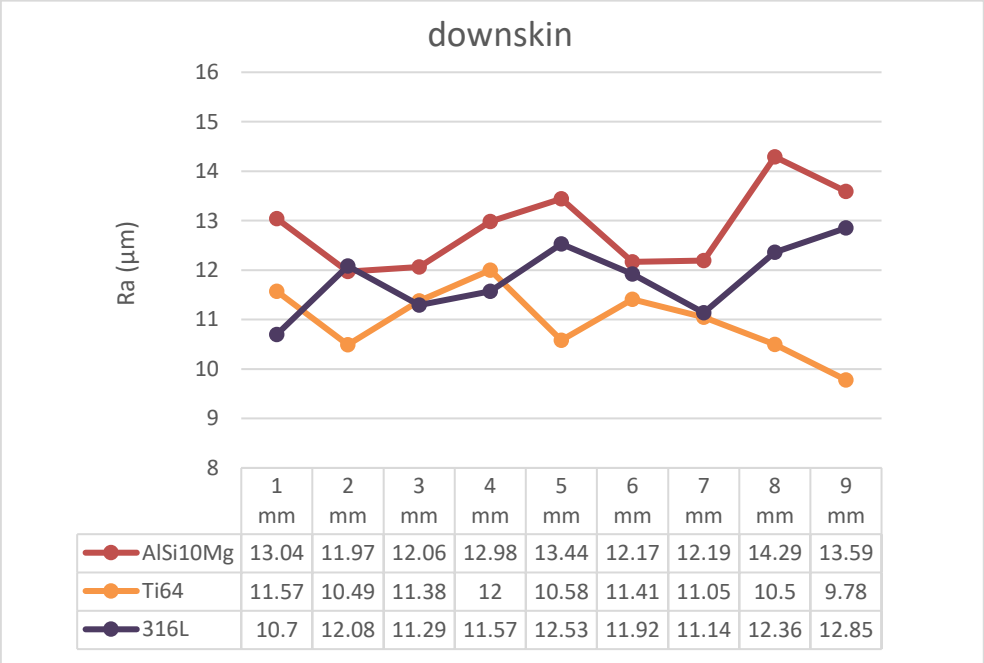

	1 mm	2 mm	3 mm	4 mm	5 mm	6 mm	7 mm	8 mm	9 mm
AlSi10Mg	13.04	11.97	12.06	12.98	13.44	12.17	12.19	14.29	13.59
Ti64	11.57	10.49	11.38	12	10.58	11.41	11.05	10.5	9.78
316L	10.7	12.08	11.29	11.57	12.53	11.92	11.14	12.36	12.85

Figure 8. Surface roughness values in the downskin (where the sagging effect is seen) parameter region of hole sections with 1-9 mm diameters produced with AlSi10Mg, 316L, and Ti64 materials.

The surface roughness values measured from the downskin region of the test samples with hole diameters of 1-9 mm produced with LPBF are shared in Figure 8. According to Figure 8, the roughness value of the downskin region in the holes produced with AlSi10Mg is higher than in other materials. According to this graphic data, sagging will be more intense in the upper region of the holes produced with AlSi10Mg. It is seen that the surface roughness value of the downskin region in the holes produced with Ti64 is generally lower than in other materials. It can be stated that the roughness values taken from the downskin surface parameter region of the holes produced with 316L material are generally higher than Ti64 and lower than AlSi10Mg. However, it can be stated that this situation is out of generalization in some hole measurements, such as 1 mm and 4 mm.

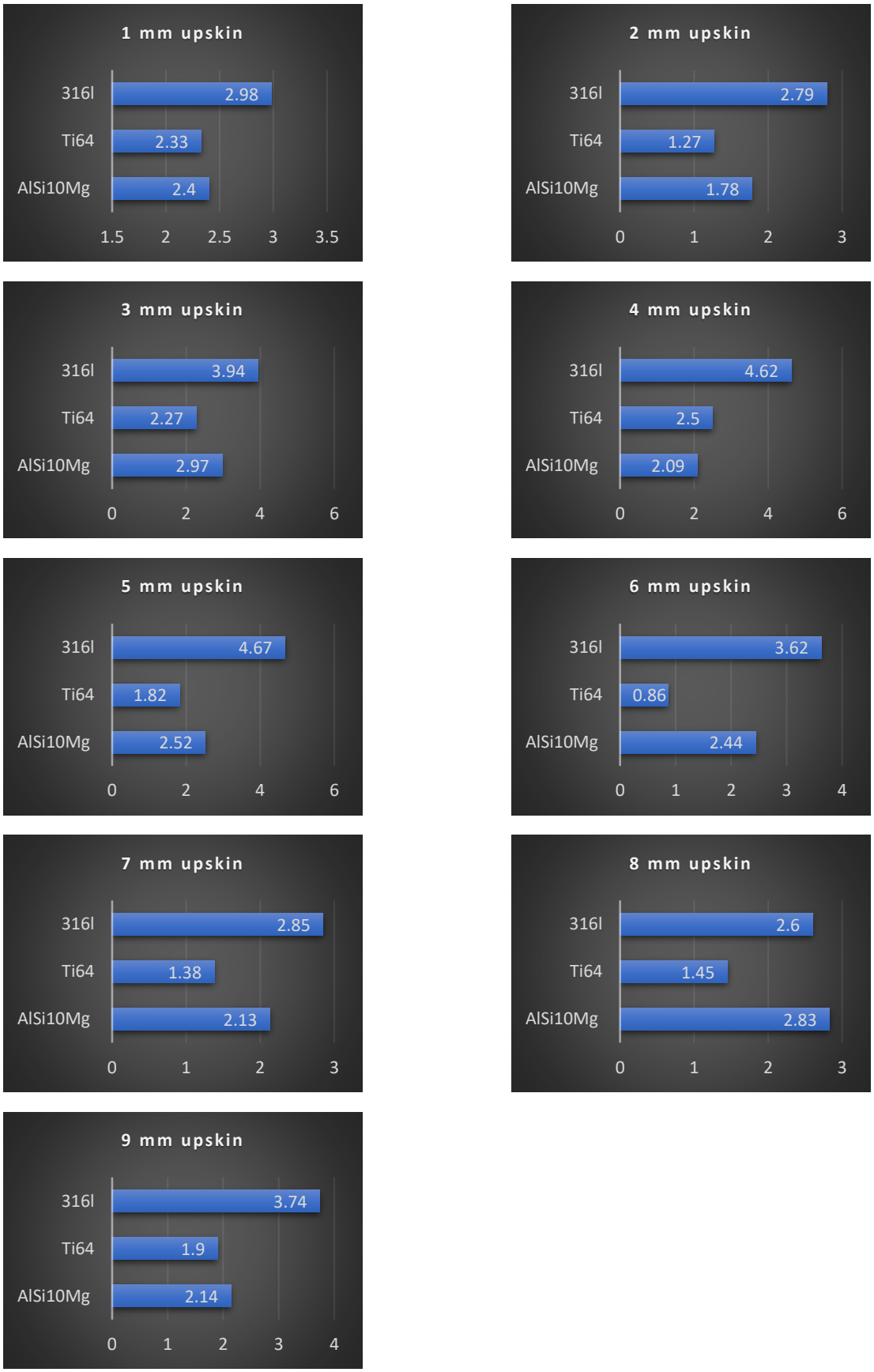

Figure 9. Surface roughness values from the upskin regions with each hole comparison

If we consider the surface roughness values from the upskin regions with each hole comparison (Figure 9) in terms of the three materials within the scope of this research, the following can be stated:

Upskin region surface roughness measurements represent the values taken from the lower arc ce. Figure 9 shows that the surface roughness values obtained from the holes produced with 316L material are 2,6 – 4,67 µm. In this value range, which represents the average of the surface roughness measurements made in three repetitions for each hole, the lowest value of 2,6 µm is seen in the 8 mm hole; the highest value of 4,67 µm is seen in the 5 mm hole. In general, it is seen that the 316L material gives the highest roughness values when compared with the other two materials. The hole is cylindrical.

According to the surface roughness measurements taken from the upskin parameter region of the productions made with Ti64, it is seen that all measurement values are in the range of 0,86 – 2,5 µm. It can be stated that this range is the lowest surface roughness value range for the three materials for upskin measurements. However, in the measurements taken only over 4 mm, it is seen that the roughness value of Ti64, which is 2,5 µm, is 2,09 µm in AlSi10Mg.

According to Figure 9, it can be stated that the upskin measurement results made with AlSi10Mg are in the range of 1,78 – 2,97 µm. It is seen that the lowest roughness value of 1,78 µm belongs to the 2 mm hole upskin measurement; the highest roughness value of 2,97 µm belongs to the 3 mm hole upskin measurement. Although it is an unexpected situation that two extreme values were taken in the roughness measurement of two very close hole diameters, considering that both values and the surface roughness values of all holes produced with AlSi10Mg are very close to each other, it is thought that this situation may be due to unforeseen layer shifting during the production process.

In the general evaluation to be made, it is seen that there is a difference of 2,07 µm between the highest and lowest surface roughness values obtained from holes produced with 316L material; this difference is 1,64 µm in surface roughness measurements taken from the upskin parameter region of productions made with Ti64; and 1,19 µm in AlSi10Mg. In light of this information, when all materials and hole diameters are compared, it is seen that the upskin parameter gives the least variable values in terms of surface roughness obtained in hole productions made with AlSi10Mg material; 316L has the most variable value range. It can be stated that this situation is due to the parameter set development process of the technology manufacturer and the material difference. However, it is thought that it would be correct to investigate the subject with different analysis and test methods in future studies.

Suppose we consider the surface roughness values from the downskin regions with each hole comparison (Figure 10) in terms of the three materials within the scope of this research. The following can be stated: The average of three surface roughness values measured from the downskin parameter region of hole test samples fabricated using AlSi10Mg, 316L, and Ti64 materials is shared graphically for each hole in Figure 10.

According to Figure 10, the surface roughness values measured from the downskin region of the productions made using 316L material are 10,70 – 12,85 µm. The 10,70 µm value is the surface roughness value measured from the downskin region of the 1 mm diameter hole, and the 12,85 µm surface roughness value is the surface roughness value measured from the 9 mm diameter. In the test sample productions made using Ti64 material, it is seen that the surface roughness values measured from the downskin region are in the range of 9,78 - 12 µm. Figure 10 shows that the 9,78 µm value belongs to the 9 mm hole, and the 12 µm measurement belongs to the 4 mm hole. It is seen that the maximum and minimum measurement values of AlSi10Mg downskin are in the range of 11,97 – 14,29 µm. It can be stated that the lowest roughness value of 11,97 µm belongs to the 2 mm hole, and the highest value of 14,29 µm belongs to the 8 mm hole (Figure 10).

Considering that the differences between the maximum and minimum measurements in downskin measurements are 2,15 µm in 316L material, 2,22 µm in Ti64 material, and 2,32 µm in AlSi10Mg, it is seen that the measurement range in all materials develops at similar rates around 2 µm.

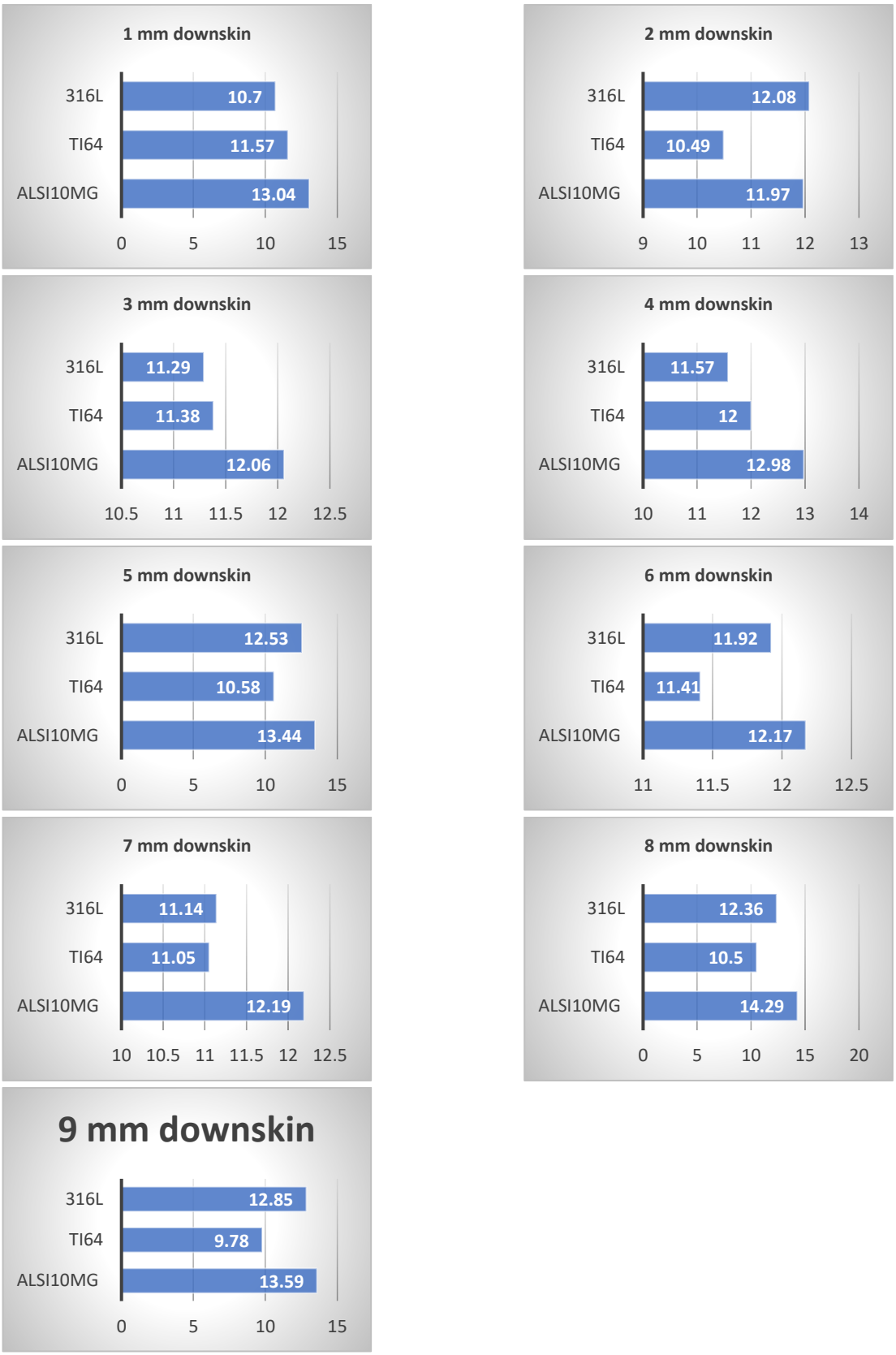

Figure 10. Surface roughness values from the downskin regions with each hole comparison

5. Conclusion

Within the scope of this study, upskin and downskin surface roughness measurements were made on hole test samples produced in AM-LPBF using AlSi10Mg, 316L, and Ti64 materials. The results obtained were compared in the context of the parameter region where the measurement was made, the three materials used in production, and the different holes. In this context, the following can be stated in light of the obtained data:

i. The measurements made within this research's scope show significant differences between the surface roughness values measured from the upskin and downskin parameter regions. In the measurements made in this context, it is seen that the surface roughness values measured from the upskin region, regardless of the material difference, are in the range of 0,86 – 4,67 μm, while the measurements taken from the downskin region are in the range of 9,78 – 14,29 μm. In this context, future research may focus on the downskin region for better channel flow efficiency.

ii. In the surface roughness measurements of the 0,4 mm and 0,5 mm diameter holes considered within the scope of the research, inconsistent results were obtained due to the standard probe measurement method of the roughness measuring devices and the hole diameter being smaller than the measuring device probe. Considering that the LPBF manufacturer's hole diameters must have a manufacturability range greater than 0.5 mm, 1 mm and above should be preferred in CCC designs.

iii. It can be said that the surface roughness in the upskin parameter region is more acceptable in terms of maintaining the flow pressure in the channels; however, it is thought that the measurements in the downskin parameter region in the upper hole region will be effective in the channel pressure drop with higher surface roughness values. In future research and analysis studies, the surface roughness in the upskin and downskin regions should be considered within the scope of the flow pressure performance of these two regions and examined in more detail.

iv. The surface roughness values in the upskin region of the holes produced with 316L are higher than those produced with AlSi10Mg and Ti64 in all hole diameters. It can be said that the upskin surface roughness values of the holes produced with AlSi10Mg are at an average level compared to the other two materials. In the measurements made in the upskin parameter region, it is seen that the lowest roughness values are obtained with Ti64 material. Considering that the surface roughness measurements in the upskin region are lower than the measurements in the downskin region, it is thought that this low roughness obtained with Ti64 will not provide significant advantages in terms of flow in the CC channels. Still, the subject should be investigated with analysis studies in the new research.

v. The roughness value of the downskin region in the holes produced with AlSi10Mg is observed to be higher than that of other materials. In this context, it can be stated that sagging will be more intense in the upper region of the holes produced with AlSi10Mg. In light of this information, it can be noted that if AlSi10Mg is used in CCC applications, the flow performance will be lower than the other two materials considered in this research.

vi. In holes produced with Ti64, it is seen that the surface roughness value of the downskin region is lower than in other materials. Therefore, in the evaluation to be made within the scope of flow pressure in CCC applications where this material is used, it is thought that the efficiency will be better than the other two materials.

vii. The surface roughness values measured from the downskin surface parameter region of the holes produced with 316L material are observed to be higher than Ti64 and lower than AlSi10Mg. It can be stated that 316L material is more efficient than AlSi10Mg and acceptable compared to Ti64 for CCC applications.

Table 4. NOMENCLATURE

AM	*Additive manufacturing*
LPBF	*Laser powder bed fusion*
DMLS	*Direct Metal Laser Sintering (LPBF Production System by EOS)*
CCC	*Conformal Cooling Channel*
ASTM	*American Society for Testing and Materials International*
CAD	*Computer-Aided Design*
CT	*Computed Tomography*
SEM	*Scanning Electron Microscope*
CC	*Conformal Cooling*
Ra	*Surface Roughness*
E	*Energy*
P	*Laser Power*
v	*Laser Scanning Speed*
h	*Scanning Distance*
t	*Layer Thickness*

Author Contributions

The author read and approved the final version of the paper.

Conflict of Interest

The author declares no conflict of interest.

Ethical Review and Approval

No approval from the Board of Ethics is required.

References

[1] I. Gibson, D. Rosen, B. Stucker, M. Khorasani, D. Rosen, B. Stucker, M. Khorasani. Additive Manufacturing Technologies, 17 (2021).

[2] C. İ. Çalışkan, Ü. Arpacıoğlu. *Additive manufacturing on the façade: functional use of direct metal laser sintering hatch distance process parameters in building envelope*, Rapid Prototyping Journal 28 (9) (2022) 1808–1820.

[3] K. V Wong, A. Hernandez. *A review of additive manufacturing*, International Scholarly Research Notices 2012 (1) (2012) 208760.

[4] W. E. Frazier. *Metal additive manufacturing: a review*, Journal of Materials Engineering and Performance 23 (2014) 1917–1928.

[5] C. Zhang, S. Wang, J. Li, Y. Zhu, T. Peng, H. Yang. *Additive manufacturing of products with functional fluid channels: A review*, Additive Manufacturing 36 (2020) 101490.

[6] B. B. Kanbur, Y. Zhou, S. Shen, K. H. Wong, C. Chen, A. Shocket, F. Duan. *Metal additive manufacturing of plastic injection molds with conformal cooling channels*, Polymers 14 (3) (2022) 424.

[7] Y. Li, S. Roux, C. Castelain, Y. Fan, L. Luo. *Design and optimization of heat sinks for the liquid cooling of electronics with multiple heat sources: A literature review*, Energies 16 (22) (2023) 7468.

[8] V. K. Lee, D. Y. Kim, H. Ngo, Y. Lee, L. Seo, S.-S. Yoo, P. A. Vincent, G. Dai. *Creating perfused functional vascular channels using 3D bio-printing technology*, Biomaterials 35 (28) (2014) 8092–8102.

[9] S. A. Niknam, M. Mortazavi, D. Li. *Additively manufactured heat exchangers: A review on opportunities and challenges*, The International Journal of Advanced Manufacturing Technology 112 (3) (2021) 601–618.

[10] S. Feng, A. M. Kamat, Y. Pei. *Design and fabrication of conformal cooling channels in molds: Review and progress updates*, International Journal of Heat and Mass Transfer 171 (2021) 121082.

[11] D. Tomasoni, S. Colosio, L. Giorleo, E. Ceretti. *Design for additive manufacturing: Thermoforming mold optimization via conformal cooling channel technology*, Procedia Manufacturing 47 (2020) 1117–1122.

[12] B. B. Kanbur, S. Suping, F. Duan. *Design and optimization of conformal cooling channels for injection molding: A review*, The International Journal of Advanced Manufacturing Technology 106 (7) (2020) 3253–3271.

[13] G. S. Phull, S. Kumar, R. S. Walia. *Conformal cooling for molds produced by additive manufacturing: A review*, International Journal of Mechanical Engineering and Technology 9 (1) (2018) 1162–1172.

[14] C. İ. Çalışkan, G. Özer, E. Koç, U. S. Sarıtaş, C. F. Yıldız, Ö. Y. Çiçek. *Efficiency research of conformal channel geometries produced by additive manufacturing in plastic injection mold cores (inserts) used in automotive industry*, 3D Printing and Additive Manufacturing 10 (2) (2023) 213–225.

[15] D. Li, H. Wang, N. Dai. *A novel design model of flow channel paths for additive manufacturing*, Rapid Prototyping Journal 30 (6) (2024) 1230–1248.

[16] C. İ. Çalışkan, A. Koca, G. Özer, Ö. Akbal, S. Bakır. *Efficiency comparison of conformal cooling channels produced by additive and subtractive manufacturing in automotive industry plastic injection moulds: A hybrid application*, The International Journal of Advanced Manufacturing Technology 126 (9) (2023) 4419–4437.

[17] Y. Wang, C. Lee. *Design and optimization of conformal cooling channels for increasing cooling efficiency in injection molding*, Applied Sciences 13 (13) (2023) 7437.

[18] S. Feng, A. M. Kamat, Y. Pei. *Design and fabrication of conformal cooling channels in molds: Review and progress updates*, International Journal of Heat and Mass Transfer 171 (2021) 121082.

[19] C. İ. Çalışkan, G. Özer, M. Coşkun, E. Koç. *Investigation of direct metal laser sintering downskin parameters' sagging effect on microchannels*, The International Journal of Advanced Manufacturing Technology 114 (2021) 2567–2575.

[20] C. Tan, D. Wang, W. Ma, Y. Chen, S. Chen, Y. Yang, K. Zhou. *Design and additive manufacturing of novel conformal cooling molds*, Materials and Design 196 (2020) 109147.

[21] W. Heogh, S. M. Yeon, D.-S. Kang, S. Park, S. Park, K. Ryu, J. Sun, L. Ji, Y. Son, K. Choi. *The design and additive manufacturing of an eco-friendly mold utilized for high productivity based on conformal cooling optimization*, Materials and Design 222 (2022) 111088.

[22] T. Bulsiewicz, P. Łapka. *Effects of additive manufacturing on convective heat transfer in 3D-printed micro/mini-channels and fluid passages with micro/mini structures–The review*, International Communications in Heat and Mass Transfer 159 (2024) 108057.

[23] Y. Zhu, D. Li, C. Zhang, F. Lin, M. Wu, Y. Chen. *Abrasive flow machining of laser powder bed fusion fabricated mini-channels: Modelling and verification*, Journal of Manufacturing Processes 141 (2025) 36–47.

[24] X. Xu, E. Sachs, S. Allen, M. Cima, *Designing conformal cooling channels for tooling*, in: D.L.Bourell, J.Beaman, R.Crawford, H. L. Marcus, J.W. Barlow (Eds.), International Solid Freeform Fabrication Symposium, Texas, 1998, pp. 131–146.

[25] Z. Shayfull, S. Sharif, A. M. Zain, M. F. Ghazali, R. M. Saad. *Potential of conformal cooling channels in rapid heat cycle molding: A review*, Advances in Polymer Technology 33 (1) (2014) 21381.

[26] S. Feng, A. M. Kamat, Y. Pei. *Design and fabrication of conformal cooling channels in molds: Review and progress updates*, International Journal of Heat and Mass Transfer 171 (2021) 121082.

[27] C. İ. Çalışkan, G. Özer, M. Coşkun, E. Koç. *Investigation of direct metal laser sintering downskin parameters' sagging effect on microchannels*, The International Journal of Advanced Manufacturing Technology 114 (2021) 2567–2575.

[28] C. İ. Çalışkan, M. Coşkun, G. Özer, E. Koç, T. A. Vurkır, G. Yöndem. *Investigation of manufacturability and efficiency of micro channels with different geometries produced by direct metal laser sintering*, The International Journal of Advanced Manufacturing Technology 117 (11) (2021) 3805–3817.

[29] Crucible Industrial Design. Crucible, Design Guidelines for DMLS (2014), https://www.scribd.com/document/506752344/A-M-Guidelines-Metal, Accessed 05 Mar 2025.

[30] EOS Electro Optical Systems, Design Rules for DMLS (2004), https://www.eos.info/content/blog/how-to-create-differently-with-dmls, Accessed 05 Mar 2025.

[31] N. Shamsaei, A. Yadollahi, L. Bian, S. M. Thompson. *An overview of direct laser deposition for additive manufacturing; Part II: Mechanical behavior, process parameter optimization and control*, Additive Manufacturing 8 (2015) 12–35.

[32] EOS GmbH Electro Optical Systems, EOS Aluminium AlSi10Mg Material Data Sheet (2022), https://www.eos.info/var/assets/03_system-related-assets/material-related-contents/metal-materials-and-examples/metal-material-datasheet/aluminium/material_datasheet_eos_aluminium-alsi10mg_en_web.pdf, Accessed 05 Mar 2025.

[33] EOS GmbH Electro Optical Systems, StainlessSteel 316L Material Data Sheet (2022), https://www.eos.info/var/assets/03_system-related-assets/material-related-contents/metal-materials-and-examples/metal-material-datasheet/stainlesssteel/material_datasheet_eos_stainlesssteel_316l_en_web.pdf,Accessed 05 Mar 2025.

[34] EOS GmbH Electro Optical Systems, Titanium Ti64 Material Data Sheet (2022) https://www.eos.info/var/assets/03_system-related-assets/material-related-contents/metal-materials-and-examples/metal-material-datasheet/titan/ti64/eos_ti64_9011-0014_9011-0039_m290_mds_06-22_en.pdf, Accessed 05 Mar 2025.

Journal of Advanced Research in Natural and Applied Sciences
dergipark.org.tr/tr/pub/jarnas
Open Access

ISSN: 2757-5195 11 (2) (2025) 132-143 doi.org/10.28979/jarnas.1656567

Evaluating Additional Observations of the Same Units to Estimate Misclassification Probabilities in Measurement System Analysis

Sümeyra Sert[1], Coşkun Kuş[2]

Article Info
Received: 12 Mar 2025
Accepted: 10 Jun 2025
Published: 30 Jun 2025
Research Article

Abstract— Measurement System Analysis evaluates the accuracy and precision of measurement processes; in the literature, part variability and measurement error are typically assumed to follow normal distributions, and we adopt this convention. We derive closed-form formulas for Types I and II misclassification probabilities using univariate and bivariate normal cumulative distribution functions, avoiding numerical integration and enabling efficient computation (e.g., in R). Building on these results, we derive explicit maximum likelihood estimates of misclassification probabilities for both the classical approach based on measurements from different parts and the repeated-measurement approach using multiple measurements on the same part at different times. A Monte Carlo study shows that incorporating repeated measurements reduces bias and mean squared error. A brief numerical example with simulated data demonstrates practical implementation.

Keywords — *Monte Carlo simulation, maximum likelihood estimation, measurement system analysis, misclassification probabilities, quality control*

1. Introduction

Statistical Quality Control (SQC) is essential for ensuring product consistency by monitoring process variations and minimizing defects. A fundamental component of SQC is Measurement System Analysis (MSA), which evaluates the accuracy and reliability of measurement processes. One of the key tools in MSA is Gage Repeatability and Reproducibility (Gage R&R), which quantifies measurement variability by analyzing repeatability and reproducibility. To assess the capability of a production process, statistical indices such as the process capability index and the process performance index are utilized. These indices ensure that process variation remains within defined specification limits. For a comprehensive discussion on Gage R&R analysis, we refer to several key studies, including [1–10]. Similarly, for process capability indices, we refer to recent contributions from [11–18].

MSA also aims to provide critical insights into process variation and measurement reliability by distinguishing the variation between the measured items from the errors inherent in the measurement system. Two types of probabilities are associated with the misclassification of an item, which are analogous to Type-I and Type-II errors in hypothesis testing. According to [19], the α probability represents the combined probability of incorrectly failing an item that meets specifications (referred to

[1]sumeyra.sert@selcuk.edu.tr (Corresponding Author); [2]coskun@selcuk.edu.tr
[1,2]Department of Statistics, Faculty of Science, Selçuk University, Konya, Turkey

as a false failure or producer's risk), while the β probability refers to the probability of incorrectly accepting an item that does not meet specifications (also called a missed fault or consumer's risk). These risks guide manufacturers in determining whether the measurement system is adequate or needs improvement.

Under the assumption that both parts and measurement errors follow a normal distribution, several studies have evaluated the misclassification probabilities α and β. Notable contributions in this context include the following: [20] discussed the probabilities associated with the misclassification of items due to measurement variability. [21] used a case study to assess the probabilities of misclassifying items due to measurement variability in the case of multiple sources of product variability. [22] presented methods for expanding the univariate MSA to the multivariate cases, and evaluated the performances of the production test process through misclassification probabilities. [23] presented the generalized inference method for constructing confidence intervals for misclassification probabilities in a Gage R&R study. [24] proposed a bootstrap method to construct confidence intervals for misclassification probabilities in MSA and compared its performance with the generalized inference method. [25] developed a robust method to evaluate misclassification probabilities under the two-component measurement error model. Recently, [26] presented a novel statistical methodology to improve the estimation process for misclassification probabilities, while also constructing uncorrected likelihood ratio confidence intervals for misclassification probabilities in MSA.

In this study, closed-form expressions for misclassification probabilities are derived under a normal distribution framework, providing a more computationally efficient approach than integral-based methods. The maximum likelihood estimation of these misclassification probabilities is also discussed using the methodology presented by [26]. Furthermore, a comprehensive simulation study is conducted to evaluate the performance of this methodology, assessing its accuracy in different scenarios. The remainder of this paper is organized as follows: Section 2 introduces both the classical model and the closed-form expressions for misclassification probabilities. The Maximum Likelihood Estimators (MLEs) of model parameters and misclassification probabilities are discussed in Section 3. A comprehensive simulation study is conducted, considering in-control stages, with the results presented in Section 4. To illustrate the proposed methodologies, a numerical example is provided in Section 5. Finally, Section 6 presents the conclusion of the study.

2. Model Setup

In this paper, we study a model of the form

$$Y = X + M \tag{2.1}$$

where X and M are independent random variables following $\mathcal{N}(\mu_{\text{part}}, \sigma^2_{\text{part}})$ and $\mathcal{N}(0, \sigma^2_{\text{measure}})$, respectively. Then, the random variable $Y = X + M$ following $Y \sim \mathcal{N}\left(\mu_{\text{part}},\, \sigma^2_{\text{part}} + \sigma^2_{\text{measure}}\right)$. Moreover, the misclassification probabilities, denoted as α and β, for lower and upper specification limits L and U is defined by [21]:

$$\begin{aligned} \alpha &= P\left(L < X < U,\, (Y < L \vee Y > U)\right) \\ &= \int_{-\infty}^{L}\int_{L}^{U} f(x,y)\,dx\,dy + \int_{U}^{\infty}\int_{L}^{U} f(x,y)\,dx\,dy \end{aligned} \tag{2.2}$$

and

$$\begin{aligned}\beta &= P\left(L < Y < U, (X < L \vee X > U)\right) \\ &= \int_{-\infty}^{L}\int_{L}^{U} f(x,y)dydx + \int_{U}^{\infty}\int_{L}^{U} f(x,y)dydx \end{aligned} \tag{2.3}$$

where the joint pdf of X and Y is given in (2.4).

$$f_{X,Y}(x,y) = \frac{1}{2\pi\sigma_{\text{part}}\sigma_{\text{measure}}} \exp\left(-\frac{(x-\mu_{\text{part}})^2}{2\,\sigma_{\text{part}}^2} - \frac{(y-x)^2}{2\,\sigma_{\text{measure}}^2}\right) \tag{2.4}$$

[26] did not provide closed-form expressions for the integrals in (2.2) and (2.3). In this paper, closed-form solutions for these integrals are derived based on one-dimensional and two-dimensional normal cumulative distribution functions. Consider the following facts [27], which can be used to obtain explicit expressions for misclassification probabilities:

$$\int_{-\infty}^{z} \Phi\left(c - d\,u\right)\phi(u)\,du = \Phi_2\left(z, \frac{c}{\sqrt{1+d^2}}; \frac{d}{\sqrt{1+d^2}}\right)$$

and

$$\int_{-\infty}^{z} \Phi\left(c + du\right)\phi(u)\,du = \Phi_2\left(z, \frac{c}{\sqrt{1+d^2}}; -\frac{d}{\sqrt{1+d^2}}\right)$$

where, $\phi(\cdot)$ and $\Phi(\cdot)$ denote the probability density function (PDF) and cumulative distribution function (CDF) of the standard normal distribution, respectively. The function $\Phi_2(\cdot,\cdot;\rho)$ represents the CDF of a bivariate normal distribution with mean vector $\mu = \begin{bmatrix}0\\0\end{bmatrix}$ and covariance matrix $\Sigma = \begin{bmatrix}1 & \rho\\ \rho & 1\end{bmatrix}$ where ρ is the correlation coefficient. These functions are readily available in the `stats` and `mvtnorm` packages in R. The standard normal PDF can be computed using `dnorm(x)`, while the CDF is given by `pnorm(x)`. For the bivariate normal CDF, the `pmvnorm(lower, upper, mean, sigma)` function from the `mvtnorm` package can be used. These functions allow for efficient numerical evaluation of probability distributions, making it easy to verify theoretical results.

Let $z = \frac{x-\mu_{part}}{\sigma_{part}}$. By substituting (2.4) into (2.2), we obtain the explicit form of the misclassification probability α as

$$\begin{aligned}\alpha &= \Phi_2\left(b, \frac{\gamma_1}{\sqrt{1+d^2}}; \frac{d}{\sqrt{1+d^2}}\right) - \Phi_2\left(a, \frac{\gamma_1}{\sqrt{1+d^2}}; \frac{d}{\sqrt{1+d^2}}\right) \\ &\quad + \Phi_2\left(b, \frac{\gamma_2}{\sqrt{1+d^2}}; -\frac{d}{\sqrt{1+d^2}}\right) - \Phi_2\left(a, \frac{\gamma_2}{\sqrt{1+d^2}}; -\frac{d}{\sqrt{1+d^2}}\right)\end{aligned}$$

where $a = \frac{L-\mu_{\text{part}}}{\sigma_{\text{part}}}, b = \frac{U-\mu_{\text{part}}}{\sigma_{\text{part}}}, d = \frac{\sigma_{\text{part}}}{\sigma_{\text{measure}}}$, $\gamma_1 = \frac{L-\mu_{\text{part}}}{\sigma_{\text{measure}}}$, and $\gamma_2 = \frac{\mu_{\text{part}}-U}{\sigma_{\text{measure}}}$.

Similarly, by substituting (2.4) into (2.3), the explicit form of another misclassification probability, β, is also obtained as

$$\begin{aligned}\beta &= \Phi_2\left(a, \frac{\gamma_3}{\sqrt{1+d^2}}; \frac{d}{\sqrt{1+d^2}}\right) - \Phi_2\left(a, \frac{\gamma_4}{\sqrt{1+d^2}}; \frac{d}{\sqrt{1+d^2}}\right) + \Phi\left(\frac{\gamma_3}{\sqrt{1+d^2}}\right) \\ &\quad - \Phi_2\left(b, \frac{\gamma_3}{\sqrt{1+d^2}}; \frac{d}{\sqrt{1+d^2}}\right) - \Phi\left(\frac{\gamma_4}{\sqrt{1+d^2}}\right) + \Phi_2\left(b, \frac{\gamma_4}{\sqrt{1+d^2}}; \frac{d}{\sqrt{1+d^2}}\right)\end{aligned}$$

where $\gamma_3 = \frac{U-\mu_{\text{part}}}{\sigma_{\text{measure}}}$ and $\gamma_4 = \frac{L-\mu_{\text{part}}}{\sigma_{\text{measure}}}$.

3. Statistical Inference

Let the measurements $Y_1, Y_2, \ldots, Y_n$ represent daily routine measurements collected on the product, where Y_i (for $i = 1, \ldots, n$) follow $\mathcal{N}\left(\mu_{part},\, \sigma^2_{part} + \sigma^2_{measure}\right)$. Hence, the log-likelihood expression based on sample $Y_1, Y_2, \ldots, Y_n$ is

$$\ell_Y(\boldsymbol{\delta_1}) \propto -\frac{n}{2}\log\left(\sigma^2_{part} + \sigma^2_{measure}\right) - \frac{1}{2(\sigma^2_{part} + \sigma^2_{measure})}\sum_{i=1}^{n}(y_i - \mu_{part})^2 \tag{3.1}$$

where $\boldsymbol{\delta_1} = (\mu_{part}, \sigma_{part}, \sigma_{measure})$, and $\widehat{\boldsymbol{\delta_1}} = (\widehat{\mu}_{part}, \widehat{\sigma}_{part}, \widehat{\sigma}_{measure})$. Then, the associated gradients are found to be:

$$\frac{\partial \ell_Y(\boldsymbol{\delta_1})}{\partial \mu_{part}} = \frac{1}{\left(\sigma^2_{part} + \sigma^2_{measure}\right)}\sum_{i=1}^{n}(y_i - \mu_{part}) = 0 \tag{3.2}$$

$$\frac{\partial \ell_Y(\boldsymbol{\delta_1})}{\partial \sigma_{part}} = \frac{\sigma_{part}}{(\sigma^2_{part} + \sigma^2_{measure})^2}\left(\sum_{i=1}^{n}(y_i - \mu_{part})^2 - n\left(\sigma^2_{part} + \sigma^2_{measure}\right)\right) = 0 \tag{3.3}$$

$$\frac{\partial \ell_Y(\boldsymbol{\delta_1})}{\partial \sigma_{measure}} = \frac{\sigma_{measure}}{(\sigma^2_{part} + \sigma^2_{measure})^2}\left(\sum_{i=1}^{n}(y_i - \mu_{part})^2 - n\left(\sigma^2_{part} + \sigma^2_{measure}\right)\right) = 0 \tag{3.4}$$

The MLEs of parameters can be obtained by solving these equations simultaneously, but only the solution for $\widehat{\mu}_{part}$ can be obtained analytically. Since (3.3) and (3.4) do not provide explicit solutions, they can be solved by using an iterative algorithm to obtain the MLEs of $\boldsymbol{\delta_1}$.

$$\widehat{\mu}_{part} = \frac{\sum_{i=1}^{n} Y_i}{n} \tag{3.5}$$

The solutions of σ_{part} and $\sigma_{measure}$ in (3.3) and (3.4) cannot be obtained in closed form because the total variance of the measurement system, σ^2, involves both σ^2_{part} and $\sigma^2_{measure}$, i.e., $\sigma^2 = \sigma^2_{part} + \sigma^2_{measure}$. Consequently, using data from a single source alone makes it impossible to separate σ_{part} and $\sigma_{measure}$ uniquely, and therefore, there is no single solution. An analytical solution to these equations is only possible if either σ_{part} or $\sigma_{measure}$ is known in advance. Although the `optim` function in R may appear to obtain MLE estimates, changing the optimization method and initial values can lead to different results. For example, we generate data from the $\mathcal{N}\left(\mu_{part},\, \sigma^2_{part} + \sigma^2_{measure}\right)$, where $\mu_{part} = 5$, $\sigma_{part} = 0.2$, and $\sigma_{measure} = 0.05$. The generated data is $4.7409, 4.9212, 5.0696, 4.6897, 5.0527, 5.0081, 5.0229, 5.3006, 4.6718, 5.3412$, and the results are illustrated with Table 1.

Table 1. An illustrative example using different estimation methods in `optim` function

$n = 10$	Initial Value	Method	$\widehat{\mu}_{part}$	$\widehat{\sigma}_{part}$	$\widehat{\sigma}_{measure}$	$\ell\left(\widehat{\boldsymbol{\delta_1}}\right)$
	(5,0.2,0.05)	BFGS	4.9818	0.2211	0.0007	−0.900035
		Nelder-Mead	4.9818	0.1976	0.0990	−0.900035
	(5,1,1)	BFGS	4.9818	0.1563	0.1563	−0.900035
		Nelder-Mead	4.9818	0.1831	0.1238	−0.900035

Table 1 shows that although the value of the log-likelihood function remains identical between different optimization methods, the estimates are different. This demonstrates a classical case of non-identifiability: while the total variance $\sigma^2 = \sigma^2_{part} + \sigma^2_{measure}$ is estimable from the data, its individual components cannot be uniquely separated without additional assumptions or external information. As seen in Table 1, multiple combinations of $(\sigma_{part}, \sigma_{measure})$ can yield the same log-likelihood value, leading to different MLEs depending on the optimization method. This flat likelihood surface, often

referred to as a *ridge*, indicates that the parameter space contains infinitely many equally likely solutions. Therefore, the model is overparameterized and non-identifiable in its current form.

In practice, although the random variable Y in (2.1) can be observed, its components X and M cannot be directly measured. However, following the methodology in [26], by repeatedly measuring a specific product at different times, denoted as $Z_1, Z_2, \ldots, Z_r$, independently and identically distributed (iid) normal random variables with a nuisance mean μ_{nui} and variance $\sigma^2_{measure}$ can be observed. Here, μ_{nui} represents the uninterested mean of the repeatedly measured product, and $\sigma^2_{measure}$ is the variance of M. Thus, additional information about the variance $\sigma^2_{measure}$ of the measurement system is collected, which is expected to improve the estimate of $\sigma^2_{measure}$. It is important to emphasize that the results are derived assuming that the repeated measurements taken by the operator on the same unit are independent. Several strategies can be implemented to ensure that repeated measurements on the same sample remain as independent as possible. First, randomizing the order of measurements and including filler samples can help prevent the operator from realizing that the same item is being measured repeatedly. Second, keeping the product's identity hidden from the operator (i.e., blinding) can reduce the risk of conscious or subconscious bias. Third, allowing sufficient time between measurements can disrupt short-term memory and reduce correlations that might arise from immediate recall. Finally, maintaining a consistent measurement protocol while incorporating minor random variations can minimize residual patterns or habits, strengthening the independence assumption between repeated measurements.

The measurements $Z_1, Z_2, \ldots, Z_r$ can be observed as follows: A previously manufactured product is sent to the laboratory daily along with newly produced products, disguised as a new product. However, the operator will not know it is a previously measured product. Let Z denote the daily measurement for this product. Parameter estimates can be obtained using the following methodology, assuming that the variance of the Z measurements equals the variance of the measurement error.

Let $Y_1, Y_2, \ldots, Y_n$ be iid production measurements and $Z_1, Z_2, \ldots, Z_r$ are iid measurements from daily monitoring of the measurement system. Then, the log-likelihood function is given by

$$\begin{aligned} \ell_{Y,Z}(\boldsymbol{\delta_2}) \;\; &\propto \;\; -\frac{n}{2}\log\left(\sigma^2_{part}+\sigma^2_{measure}\right) - \frac{1}{2(\sigma^2_{part}+\sigma^2_{measure})}\sum_{i=1}^{n}(y_i-\mu_{part})^2 \\ &- \;\; \frac{r}{2}\log\left(\sigma^2_{measure}\right) - \frac{1}{2\sigma^2_{measure}}\sum_{j=1}^{r}(z_j-\mu_{nui})^2 \end{aligned} \tag{3.6}$$

where $\boldsymbol{\delta_2} = (\mu_{part}, \sigma_{part}, \sigma_{measure}, \mu_{nui})$, $\widetilde{\boldsymbol{\delta_2}} = (\widetilde{\mu}_{part}, \widetilde{\sigma}_{part}, \widetilde{\sigma}_{measure}, \widetilde{\mu}_{nui})$, and μ_{nui} is a nuisance parameter. It can be considered a truly measured value of the previously manufactured product. However, it is not used to compute the misclassification probabilities, our goal. The gradients for μ_{part}, σ_{part}, $\sigma_{measure}$, and μ_{nui} are found to be

$$\frac{\partial \ell_{Y,Z}\left(\boldsymbol{\delta_2}\right)}{\partial \mu_{part}} = \frac{1}{\left(\sigma^2_{part}+\sigma^2_{measure}\right)}\sum_{i=1}^{n}(y_i-\mu_{part}) = 0$$

$$\frac{\partial \ell_{Y,Z}\left(\boldsymbol{\delta_2}\right)}{\partial \sigma_{part}} = \frac{\sigma_{part}}{(\sigma^2_{part}+\sigma^2_{measure})^2}\left(-\,n\,(\sigma^2_{part}+\sigma^2_{measure}) \;+\; \sum_{i=1}^{n}(y_i-\mu_{part})^2\right) = 0$$

$$\begin{aligned}\frac{\partial \ell_{Y,Z}(\boldsymbol{\delta_2})}{\partial \sigma_{measure}} &= -\frac{n\,\sigma_{measure}}{\sigma^2_{part}+\sigma^2_{measure}} + \frac{\sigma_{measure}}{(\sigma^2_{part}+\sigma^2_{measure})^2}\sum_{i=1}^{n}(y_i-\mu_{part})^2 \\ &- \frac{r}{\sigma_{measure}} + \frac{1}{\sigma^3_{measure}}\sum_{j=1}^{r}(z_j-\mu_{nui})^2 = 0\end{aligned}$$

and

$$\frac{\partial \ell_{Y,Z}(\boldsymbol{\delta_2})}{\partial \mu_{nui}} = -\frac{r}{2}\log(2\pi\sigma^2_{measure}) - \frac{1}{2\sigma^2_{measure}}\sum_{j=1}^{r}(z_j-\mu_{nui})^2 = 0$$

respectively. The maximum likelihood estimators are obtained by solving the above equations, and can be explicitly derived as follows:

$$\widetilde{\mu}_{part} = \frac{\sum_{i=1}^{n} Y_i}{n} \tag{3.7}$$

$$\widetilde{\sigma}_{part} = \sqrt{\frac{1}{n}\sum_{i=1}^{n}(Y_i-\widetilde{\mu}_{part})^2 - \frac{1}{r}\sum_{j=1}^{r}(Z_j-\widetilde{\mu}_{nui})^2} \tag{3.8}$$

$$\widetilde{\sigma}_{measure} = \sqrt{\frac{1}{r}\sum_{j=1}^{r}(Z_j-\widetilde{\mu}_{nui})^2} \tag{3.9}$$

and

$$\widetilde{\mu}_{nui} = \frac{\sum_{j=1}^{r} Z_j}{r}$$

respectively. Then, the MLEs of α and β probabilities can be easily obtained by the invariance property of MLEs.

Remark 3.1. Incorporating the Z observations alongside the Y data permits closed-form expressions for the MLEs (see (3.7)–(3.9)). This approach fully resolves the identifiability problem inherent in the likelihood function of (3.1), which relies exclusively on the Y data.

Remark 3.2. Let r denote the number of independent observations $Z_1, Z_2, \ldots, Z_r \sim \mathcal{N}(\mu_\nu, \sigma^2_{measure})$. Then, as $r \to \infty$, MLE of $\sigma_{measure}$, denoted by $\widetilde{\sigma}_{measure}$, converges in probability to the true value $\sigma_{measure}$; that is,

$$\widetilde{\sigma}_{measure} \xrightarrow{p} \sigma_{measure}$$

Consequently, as $r \to \infty$, the full maximum likelihood estimation procedure that uses both Y and Z converges to the estimation procedure in which $\sigma_{measure}$ is treated as known and fixed. In particular, the estimator $\widetilde{\sigma}_{part}$ derived from the full dataset (including Z) asymptotically behaves like the estimator obtained without access to Z, under the assumption that $\sigma_{measure}$ is known.

4. Simulation Study

In this section, we perform a simulation study to evaluate the performance of the estimation method considered in Section 3. Specifically, the parts are assumed to follow a normal distribution with $\mu_{part} = 13$ and $\sigma_{part} = 3$. Additionally, measurement errors are assumed to be normally distributed with a mean of 0 and a standard deviation of $\sigma_{measure} = 1.5$. Also, $\mu_{nui} = 15$ is pre-determined. The simulation study is designed for different combinations of sample sizes (n, r) for $n = 50, 100, 250$ and $r = 5, 10, 25, 50, 100, 250, 500, 1000, 2000$ by considering in control stages. In this regard, L and U are determined such that 90% of the true values of the products (X) fall between L and U. In this case, for $\mu_{part} = 15$ and $\sigma_{part} = 3$ it is predetermined that 90% of the products fall within this range when

$L = 11.15$ and $U = 27.82$. 50000 trials are used in the simulation, and the performance of the MLEs for the model parameters and misclassification probabilities are evaluated using mean squared error (MSE) and bias criteria. The results for $\widetilde{\boldsymbol{\delta_2}}$, $\widetilde{\alpha}$ and $\widetilde{\beta}$ are presented in Figures 1-10.

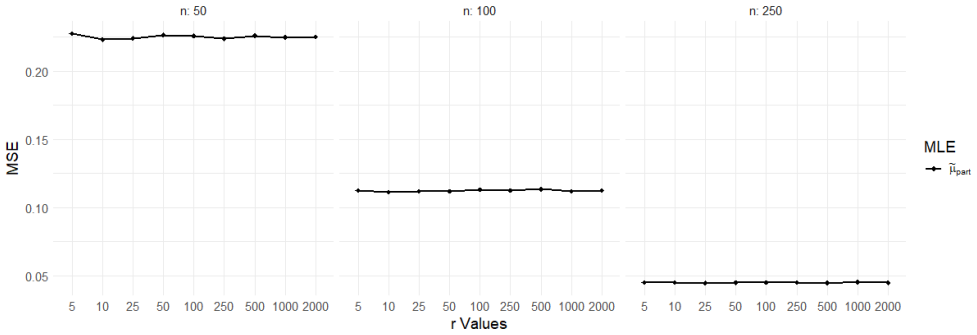

Figure 1. MSE values in $\widetilde{\mu}_{part}$ for different n and r values

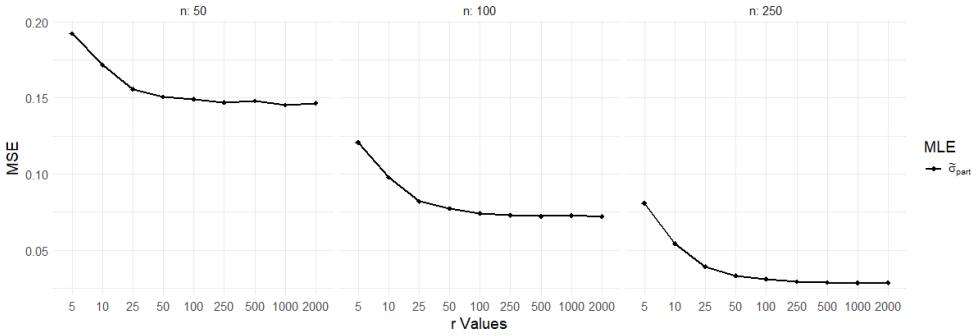

Figure 2. MSE values in $\widetilde{\sigma}_{part}$ for different n and r values

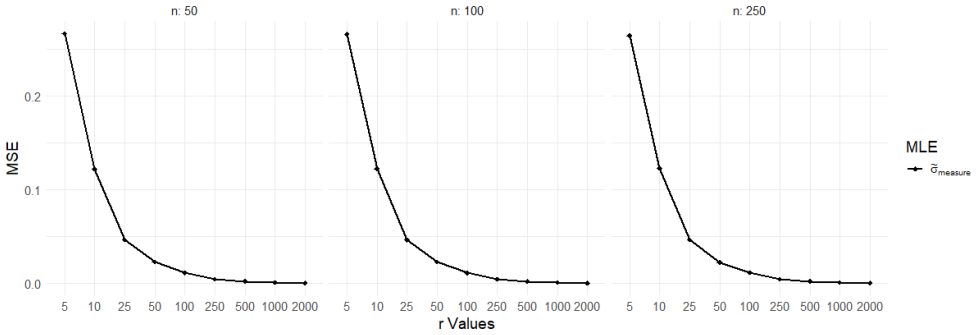

Figure 3. MSE values in $\widetilde{\sigma}_{measure}$ for different n and r values

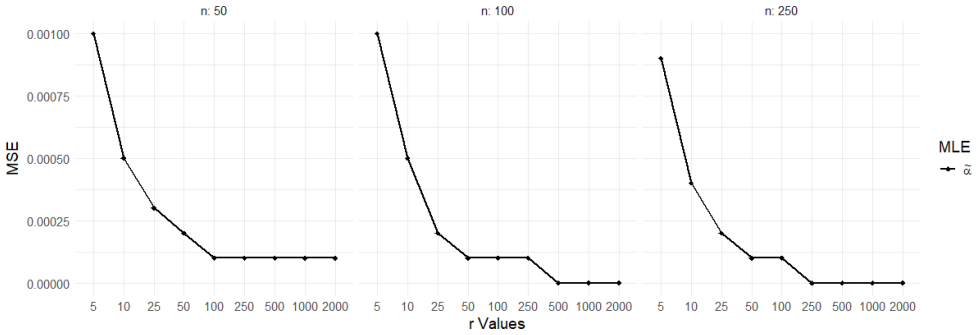

Figure 4. MSE values in $\widetilde{\alpha}$ for different n and r values

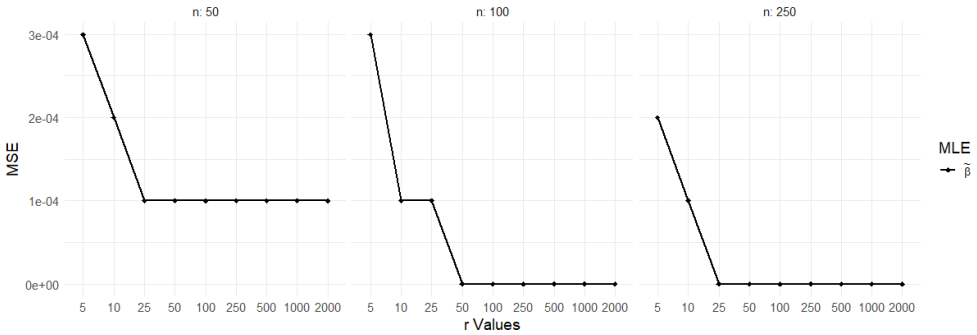

Figure 5. MSE values in $\widetilde{\beta}$ for different n and r values

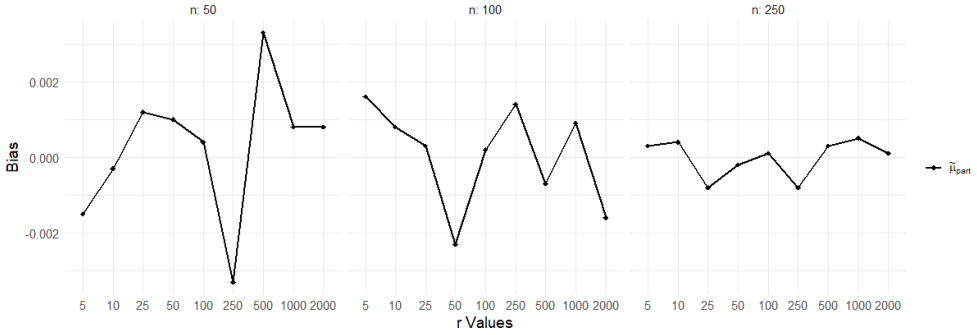

Figure 6. Bias values in $\widetilde{\mu}_{part}$ for different n and r values

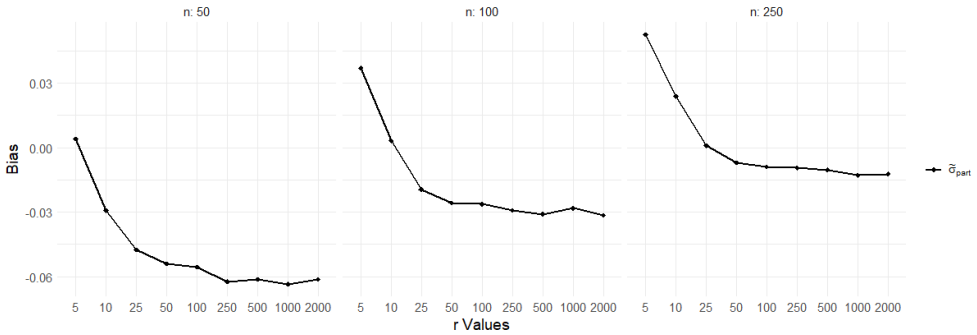

Figure 7. Bias values in $\widetilde{\sigma}_{part}$ for different n and r values

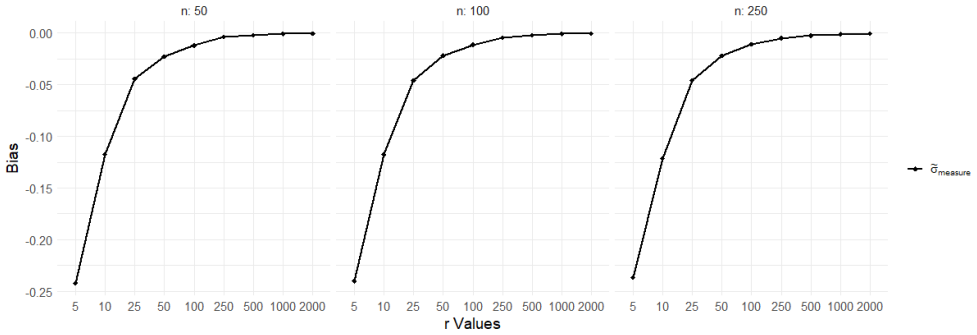

Figure 8. Bias values in $\widetilde{\sigma}_{measure}$ for different n and r values

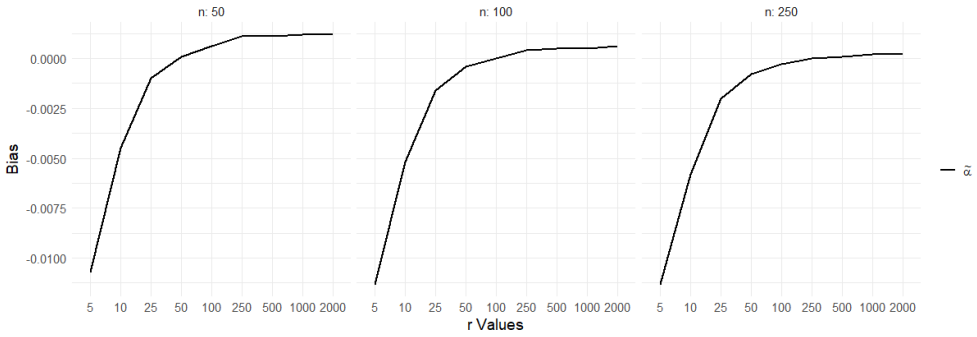

Figure 9. Bias values in $\widetilde{\alpha}$ for different n and r values

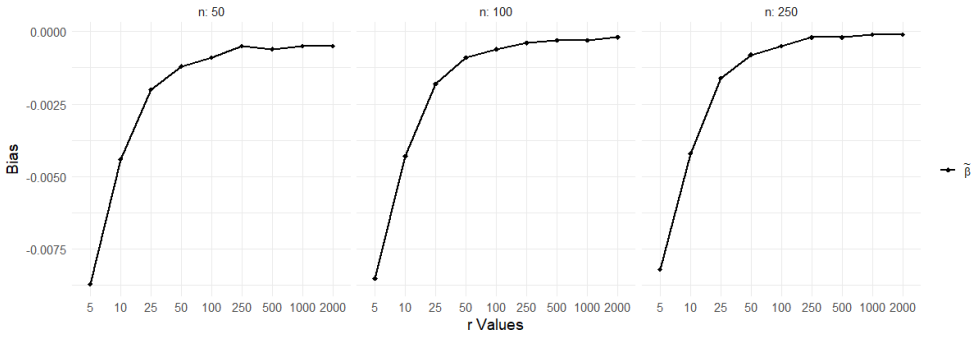

Figure 10. Bias values in $\widetilde{\beta}$ for different n and r values

According to Figures 1–10, several key observations can be made. Firstly, as expected, since μ_{part} is primarily identified from the Y data, the inclusion of additional Z observations does not significantly affect its estimation. As expected, the MSE and bias of all MLEs for each model parameter, as well as the MLEs of the misclassification probabilities α and β, tend to zero as both the sample size n and the number of repeated measurements r increase. Moreover, as r increases (i.e., as the number of repeated measurements for the same subject increases), there is a positive effect on the MSEs of all estimators.

5. Illustrative example

In this section, a simulated data set is used for illustration purposes. This data set is generated assuming parts are distributed normally with parameters $\mu_{part} = 20$ and $\sigma_{part} = 0.3$, and measurement errors are assumed to be distributed normally with mean zero and standard deviation 0.05. Then, the measurements are generated using (2.1) and by fixing `set.seed(1)`. 20 parts are measured, with an extra $r = 10$ observations collected. The measurements (Y) and the additional observations (Z) are obtained as follows:

Measurements (Y):
19.8094, 20.0558, 19.7458, 20.4851, 20.1002, 19.7504, 20.1482, 20.2245, 20.1751, 19.9071,
20.4597, 20.1185, 19.8110, 19.3264, 20.3421, 19.9863, 19.9950, 20.2870, 20.2497, 20.1806.
Extra Observations (Z):

20.6479, 20.5748, 20.5993, 20.5773, 20.5111, 20.5592, 20.5602, 20.5770, 20.6350, 20.6181,

where $\mu_{nui} = 20.58$ is pre-determined. It is also assumed that the manufacturer has specified the specification limits as $L = 19.7$ and $U = 20.4$. Measurements including measurement errors are displayed in Figure 11, where the dashed lines indicate the lower and upper specification limits.

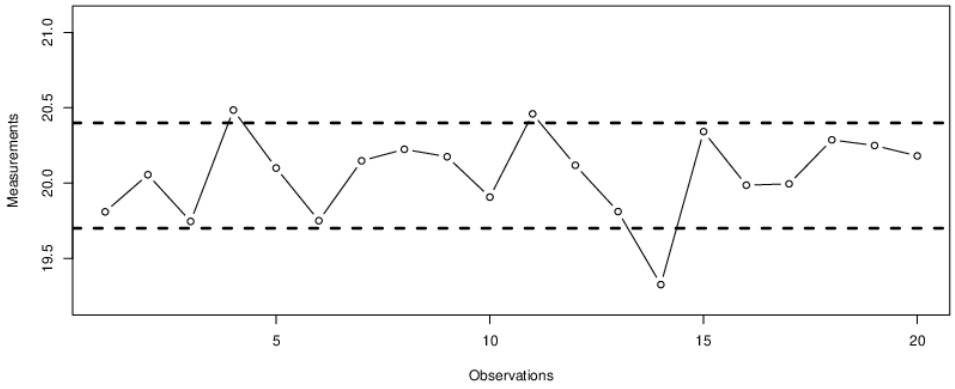

Figure 11. Measurements

The MLEs of model parameters and misclassification probabilities based on the above data are given in Table 2.

Table 2. MLEs of model parameters and misclassification probabilities for the numerical example

Parameter	n	r	μ_{part}	σ_{part}	$\sigma_{measure}$	μ_{nui}	α	β
True Values	20	-	20	0.3	0.05	20.58	0.0302	0.0239
$\widehat{\boldsymbol{\delta}_1}$	20	-	20.0579	0.1727	0.2085	-	0.1699	0.0165
$\widehat{\boldsymbol{\delta}_2}$	20	10	20.0579	0.2669	0.0453	20.5733	0.0262	0.0199

Table 2 illustrates that incorporating additional observations into the measurement system enhances the accuracy of estimating σ_{part} and $\sigma_{measure}$, even in cases with small sample sizes, and consequently improves the estimation of the misclassification probabilities α and β.

6. Conclusion

MSA plays a critical role across various fields including manufacturing, engineering, and reliability of measurement systems. One of the main problems in MSA is the presence of measurement errors, which may lead to misclassification, specifically Type I and Type II errors. This study provides closed-form expressions for misclassification probabilities, which are derived based on one-dimensional and two-dimensional normal CDFs. The proposed analytical approach offers a computationally efficient alternative, especially in platforms like `R`. In addition to the classical sample, the study investigates the impact of repeated measurements by the same operator on the same part, highlighting the positive effects of these additional observations on the MLEs of misclassification probabilities in MSA. Overall, the findings indicate that incorporating repeated measurements via Z leads to notable improvements in both the estimation of model parameters—by reducing MSE and bias—and the estimation of misclassification probabilities α and β, thereby enhancing the overall accuracy of the measurement system. Finally, a numerical illustration using simulated data confirms the practical applicability and effectiveness of the proposed approach. The primary limitation of this study is the assumption of normally distributed part variation and measurement errors, as well as the use of a single-operator measurement structure. In future studies, new estimators can be proposed, and their properties can be analyzed under the assumption that more than one operator is involved and that their measurements are dependent rather than independent.

Author Contributions

All the authors equally contributed to this work. This paper is derived from the first author's doctoral dissertation supervised by the second author. They all read and approved the final version of the paper.

Conflicts of Interest

All the authors declare no conflict of interest.

Ethical Review and Approval

No approval from the Board of Ethics is required.

Acknowledgment

This work was supported by the Office of Scientific Research Projects Coordination at Selçuk University, Grant number: 23111006.

References

[1] R. K. Burdick, G. A. Larsen, *Confidence intervals on measures of variability in R&R studies*, Journal of Quality Technology 29 (3) (1997) 261–273.

[2] K. K. Dolezal, R. K. Burdick, N. J. Birch, *Analysis of a two-factor R&R study with fixed operators*, Journal of Quality Technology 30 (2) (1998) 163–170.

[3] R. K. Burdick, A. E. Allen, G. A. Larsen, *Comparing variability of two measurement processes using R&R studies*, Journal of Quality Technology 34 (1) (2002) 97–105.

[4] R. K. Burdick, C. M. Borror, D. C. Montgomery, *A review of methods for measurement systems capability analysis*, Journal of Quality Technology 35 (4) (2003) 342–354.

[5] B. P. Weaver, M. S. Hamada, S. B. Vardeman, A. G. Wilson, *A Bayesian approach to the analysis of gauge R&R data*, Quality Engineering 24 (4) (2012) 486–500.

[6] J. Quiroz, R. Baumgartner, Interval Estimations for Variance Components: A Review and Implementations, Taylor & Francis, 2019.

[7] D. C. Montgomery, Introduction to statistical quality control, John Wiley & Sons, 2019.

[8] A. Shirodkar, S. Rane, *Evaluation of coordinate measuring machine using gage repeatability & reproducibility*, International Journal of System Assurance Engineering and Management 12 (1) (2021) 84–90.

[9] W. O. S. Soares, R. S. Peruchi, R. A. V. Silva, P. Rotella Junior, *Gage R&R studies in measurement system analysis: A systematic literature review*, Quality Engineering 34 (3) (2022) 382–403.

[10] J. Plura, D. Vykydal, F. Tošenovskỳ, P. Klaput, *Graphical tools for increasing the effectiveness of gage repeatability and reproducibility analysis*, Processes 11 (1) (2022) 1.

[11] M. Croquelois, C. Ferraris, M. Achibi, F. Thiebaut, *Process capability indices with student mixture models applied to aircraft engines GD&T*, Journal of Manufacturing Science and Engineering 144 (10) (2022) 101008.

[12] M. Saha, *Applications of a new process capability index to electronic industries*, Communications in Statistics: Case Studies, Data Analysis and Applications 8 (4) (2022) 574–587.

[13] M. Saha, S. Dey, *Uses of a new asymmetric loss-based process capability index in the electronic industries*, Communications in Statistics: Case Studies, Data Analysis and Applications 9 (2) (2023) 135–151.

[14] M. Saha, A. Devi, P. Pareek, *Applications of process capability indices for suppliers selection problems using generalized confidence interval*, Communications in Statistics: Case Studies, Data Analysis and Applications 9 (3) (2023) 270–286.

[15] K. Karakaya, *Inference on process capability index S_{pmk} for a new lifetime distribution*, Soft Computing 28 (19) (2024) 10929–10941.

[16] K. Karakaya, I. Kınacı, Y. Akdoğan, B. Saraçoğlu, C. Kuş, *Statistical inference on process capability index cpyk for inverse Rayleigh distribution under progressive censoring*, Pakistan Journal of Statistics and Operation Research 20 (1) (2024) 37–47.

[17] K. Karakaya, *A general novel process capability index for normal and non-normal measurements*, Ain Shams Engineering Journal 15 (6) (2024) 102753.

[18] W. A. Hamdi, Y. Akdoğan, T. Erbayram, M. Alqawba, A. Z. Afify, *Statistical inference of the generalized process capability index for the discrete lindley distribution*, Scientific Reports 15 (1) (2025) 6776.

[19] D. C. Montgomery, Introduction to statistical quality control, John Wiley & Sons, 2020.

[20] R. G. Easterling, M. E. Johnson, T. R. Bement, C. J. Nachtsheim, *Statistical tolerancing based on consumer's risk considerations*, Journal of Quality Technology 23 (1) (1991) 1–11.

[21] N. Doganaksoy, *Assessment of impact of measurement variability in the presence of multiple sources of product variability*, Quality Engineering 13 (1) (2001) 83–89.

[22] G. A. Larsen, *Measurement system analysis in a production environment with multiple test parameters*, Quality Engineering 16 (2) (2003) 297–306.

[23] R. K. Burdick, Y.-J. Park, D. C. Montgomery, C. M. Borror, *Confidence intervals for misclassification rates in a gauge R&R study*, Journal of Quality Technology 37 (4) (2005) 294–303.

[24] F.-K. Wang, S. Yang, *Applying bootstrap method to the types I–II errors in the measurement system*, Quality and Reliability Engineering International 24 (1) (2008) 83–97.

[25] D. Cocchi, M. Scagliarini, *A robust approach for assessing misclassification rates under the two-component measurement error model*, Applied Stochastic Models in Business and Industry 26 (4) (2010) 389–400.

[26] N. Doganaksoy, *A simplified formulation of likelihood ratio confidence intervals using a novel property*, Technometrics 63 (1) (2021) 127–135.

[27] N. L. Johnson, S. Kotz, N. Balakrishnan, Continuous multivariate distributions, Vol. 7, Wiley New York, 1972.

Journal of Advanced Research in Natural and Applied Sciences
dergipark.org.tr/en/pub/jarnas
Open Access

ISSN: 2757-5195 | 11 (2) (2025) 144-155 | doi.org/10.28979/jarnas.1657419

Supervised Machine Learning Based Fake Profile Detection Using User Ratings and Reviews in Recommender Systems

Ümmügülsüm Mengutaycı[1], Selma Ayşe Özel[2]

Article Info
Received: 18 Mar 2025
Accepted: 28 Jun 2025
Published: 30 Jun 2025
Research Article

Abstract − Recommendation systems produce content based on user's interests and aim to increase user satisfaction. In this way, the system keeps the user constantly active. Therefore, the reliability and robustness of these systems are essential. However, in recent years, with the influence of popular culture, recommendation systems have been struggling with fake users to highlight a particular product more or, conversely, to reduce the popularity of the product. Fake accounts mimic real user data and provide misleading information to the systems. This affects the accuracy of recommendation algorithms. This paper proposes a novel approach to detect fake user profiles by combining two different data sources: rating data and product reviews by using machine learning techniques, such as Decision Trees, Logistic Regression, Support Vector Machines, k-Nearest Neighbors and Naive Bayes algorithms. We also test the impact of integrating ensemble learning techniques on classification success. The research results show that the ensemble learning method Stack Classifier model has the highest detection success with an F1-score of 81.11%. This highlights that the innovative approach using multiple data sources together provides a more robust and reliable solution for detecting fake profiles, thus improving the accuracy and efficiency of recommender systems.

Keywords **–** *Recommender system, fake profile detection, machine learning, robustness*

1. Introduction

With the development of technology and the internet, people have started to spend more time on social media today. In these social platforms, which can even be downloaded to mobile phones, users can easily express their feelings and thoughts, and users can influence each other. A user who wants to receive a service examines and analyzes the opinions of other users who have previously used the same service or product. For this reason, digital platform owners will aim to bring them together with the right service to avoid losing their customers. These platforms develop special content for their customers using recommendation algorithms. Recommendation systems are essential in increasing user satisfaction and participation by offering content adapted to personal preferences. Therefore, the accuracy of the data entered into these systems is crucial for their effectiveness and reliability. However, in the competitive market, especially in recent years, the number of fake user accounts on online platforms has increased. These fake accounts in the system use real user's data by imitating them and injecting misleading information into the system. This situation negatively affects the outputs of recommendation algorithms. As a result, user trust decreases, and customer dissatisfaction increases [1].

[1]mengutayci@tarsus.edu.tr (Corresponding Author); [2]saozel@cu.edu.tr
[1]Department of Computer Engineering, Faculty of Engineering, Tarsus University, Mersin, Türkiye
[2]Department of Computer Engineering, Faculty of Engineering, Çukurova University, Adana, Türkiye

Fake users evaluate and interpret the service/product in a way that suits their purposes to direct real user behavior to their desired goal. In this way, they mislead recommendation algorithms. Over time, a real user in the system may be matched with an unsuitable service, which may cause unpleasant situations. Consumers who are not satisfied with the service they receive will come to the point of completely stopping using the platform in the long run [1, 2]. The detection of fake users can often be assumed to be a binary classification problem. Binary classification divides users into fake and real users [1]. Supervised machine learning techniques effectively perform this detection, which is a binary classification problem.

Numerous traditional approaches [3 - 9] depend on only a single data source to detect fake users, for example, focusing only on analyzing products that users have rated. Given the ever-increasing mass of data [1], a more comprehensive analysis is required to identify fake profiles. In some recent studies [10-14] it has been observed that using ratings, user reviews, and user characteristics together improves the classification success in detecting fake users. Based on this inspiration, combining two different data sources, such as rating data and item reviews, can give a more effective solution to ensure the accuracy of recommendation systems and reduce the impact of fake users. Rating data reflects the user's rating and appreciation of the product, while product reviews reveal the user's thoughts and experiences. Based on these two different data sources, detecting fake users will be much more robust and reliable.

In this study, rating data and product reviews will be used together to distinguish fake users, and these attributes will be classified using machine learning algorithms. Machine learning is a powerful tool for detecting patterns in large and complex datasets. To detect fake users, inconsistencies between the ratings given by users and the comments they write or deviations from the norm can be highlighted by classification algorithms. In this context, support vector machines (SVM), decision trees (DT), logistic regression (LR), k-nearest neighbors (kNN) and naive bayes (NB) machine learning algorithms, which have shown high success in detecting fake users, will distinguish fake users from real users [15-18]. Unlike previous studies, this innovative approach combines data sources to ensure accurate and efficient detection of fake profiles. In addition, the research utilizes ensemble learning techniques and combines the outputs of machine learning algorithms. The outputs are given to a second model, the XGBoost algorithm and the classification success is tested. Thus, the effectiveness of the two methods in detecting fake users in the system is compared.

2. Related Works

Previous research on fake user attacks in recommender systems involves statistical and machine learning methods. The authors in [4] combined statistical and machine learning methods. Statistical techniques detect anomalies in user behavior, and machine learning is applied to classify them as real or fake users. In most recommender systems, the number of labeled users is limited, and the number of unlabeled users is usually large, and labeling large amounts of data will be costly. In [9], the authors proposed the Semi-supervised learning based Shilling Attack Detection (Semi-SAD) algorithm, a semi-supervised learning approach, to detect fake users. This algorithm initially trains a Naive Bayes classifier on labeled users. Then, it optimizes the classifier by including unlabeled users in the system using the weight factor λ added Expectation Maximization (EM-λ) algorithm. Experiments on the MovieLens dataset show that the proposed approach is more efficient than other methods.

In another research, the authors [19] emphasized the class imbalance problem in supervised detection methods and stated that the detection performance decreases when the number of attack profiles is small. Therefore, they proposed a new method, the Support Vector Machine-Target Item Analysis (SVM-TIA) model, to detect attacks. In the first stage, they solved the class imbalance problem using the Borderline - Synthetic Minority Over-sampling Technique (SMOTE) method. In the second stage, target product analysis is performed with a fine-tuning that examines attack profiles and reduces false positives. In this stage, the authors first used the user rating data in the rating matrix as feature data and performed classification with the SVM algorithm. In this way, the first detections were identified. Target item analysis was then performed on the data labeled as a

potential attack profile based on the classification result. In this way, incorrectly categorized users were weeded out. Since attack profiles will rate the target item according to the attack intent (min or max), the number of evaluations on the target item will be higher than other products.

Researchers [3] have used an ensemble learning approach to eliminate fake users in the system. They have used various classification algorithms, such as Quadratic Discriminant Analysis (QDA), Naive Bayes Classifier (NBC), and kNN, to identify fake profiles and combined these algorithms with the ensemble voting (VE) approach. They emphasized that the ensemble voting technique achieved high accuracy at the end of the study. The authors [20] proposed the Single-Class SVM (OCSVM) method, which is generally used to detect outliers in fake user detection. This new approach builds models using only real user data. In this way, the authors aimed to minimize the need for labeled data to detect attacks. The hyperparameters of the OCSVM algorithm were determined by the Quick Model Selection technique to ensure the model's optimal performance and speed up the selection process. The researchers concluded that OCSVM provides a more applicable method for detecting fake profiles and stated that their research differs from other methodologies in the existing literature on this subject. In [21], authors tried to find a general solution for recommender systems that can detect any attack regardless of its characteristics. For this purpose, they used feedback from verified real users and trained classifiers. The proposed new method is based only on the behavioral characteristics of legitimate users. The authors considered any abnormal behavior in the system as an attack. It was concluded that this innovative approach based on positive unlabeled learning (PU) and single-class SVM (OSVM) models successfully detected unknown attacks.

In the studies mentioned above, a single data source (rating) data was used to detect fake users. However, a user not only rates a product but also provides a review of the product. The authors [15] used machine learning techniques to detect fake reviews on the YELP dataset by incorporating the length of reviews, the maximum number of reviews per user per day, and the average review rating deviation rate into the review data. Another study [22] combines product reviews with some behavioral characteristics of users (total number of capital letters, punctuation marks and emoji) to detect fake users using machine learning techniques. The experimental results show that the XGBoost algorithm provides the highest detection rate. Chopra & Dixit [10] used ratings and reviews together to detect fake users in recommender systems. In the study, the authors labeled product reviews with a score of 1 and 5 as fake. The results of the classification using a recurrent neural network (RNN) and the Bald Eagle Search (BES) optimization algorithm showed that the combination of ratings and reviews increased the detection of fake users. They [11] proposed a new approach to detect fake users using product reviews, aspect ratings (especially ratings based on things like cleanliness, location, service) and overall ratings. After extracting features from product reviews with Bidirectional Encoder Representations from Transformers (BERT), the authors aimed to extract feature vectors with deeper meaning from text data using Convolutional Neural Network (CNN) and Long Short-Term Memory (LSTM) architecture. They used a fully connected layer to classify the product reviews, where they selected the most important features relevant to the aspect, then combined them with aspect rating and overall rating. The obtained F1 score of 96% shows that the combination of ratings and user reviews is successful in detecting fake users.

The authors [12] proposed a graph-based method to detect spam users. In this method, reviews form the nodes and edges are formed by reviews made by the same user on the same item, reviews made by users who gave the same rating for the same item, and reviews made on the same item in the same month. After the correlation between the comments was determined by using Graph Neural Network (GNN) and Multi-Layer Perceptron (MLP) together, the outputs were given to CNN and LSTM architectures respectively and fraud detection was achieved with high accuracy. Noting that rating data alone does not directly reflect user characteristics, the authors [13] used the information obtained from the user rating matrix, as well as user's rating biases, rating time intervals, review text lengths, and similarity of review texts, to detect spam users. To learn the relationships between users, they used a Graph Sample and Aggregate (GraphSAGE) based method to distinguish between real and fake users. They used an attention mechanism to calculate the contribution of

each node's neighbors. The experimental results show that the combination of the two data types improves the performance of fake user detection. Therefore, we use both rating and review data in our research. Since fake user detection is a binary classification problem, we will identify potential attack profiles using machine learning and ensemble learning methods used in the literature and perform adequately in this field.

3. Method

3.1. Dataset

We used the Yelp dataset [23] from Kaggle for this study. The dataset contains user-review data about restaurants on the Yelp platform related to products and services. The dataset comprises reviewID, reviewerID, rating, reviewContent, and flagged information that indicates whether the user is real or fake. The dataset contains 751232 real user data and 8301 fake user data. The ratings provided by users range from 1 to 5. In the dataset, one is the lowest, and five is the highest. The reviews are written in English.

The dataset consists of the following basic features:

i. reviewerID: A unique identifier assigned to each user in the dataset.
ii. reviewID: A unique identifier assigned for each product or service reviewed.
iii. rating: The rating given to restaurants by users, ranging from 1 to 5.
iv. reviewContent: The user's opinion about the service they received.
v. flagged: A label indicating whether the user is genuine or an attacker.

3.2. Dataset Preparation

In the dataset, fake users are a minority class. Due to class imbalance in the dataset, 9,300 real user data were used. Details of the users in the dataset are presented in Table 1. Around 36 percent of the users in the dataset have reviewed and rated only one restaurant. For this reason, the rating matrix is sparse. A rating matrix was created using user, item, and rating data in the classification performed on the rating data. In this matrix, since not all users can evaluate all products, the Nan rating values were replaced with 0.

Table 1. Dataset overview

Data count of real users	9300
Data count of fake users	8301
Number of unique real users	4233
Number of unique fake users	7114

Since we used product review and rating data for fake user profile detection in this study, preprocessing was performed on the textual part of the review data. During preprocessing steps, punctuation marks, special characters, and numeric values were removed from the text. Words that do not affect the meaning, such as prepositions and conjunctions, were filtered out, sentences were tokenized, and lemmatization was applied to the words. There may be more than one product purchased by existing users in the system. Hence, users may review varying numbers of products differently from each other. As textual data is highly dimensional, and each review may have varying words, it is difficult to represent reviews as a fixed-sized matrix as in the rating matrix. Word2Vec was used to overcome this difficulty for word-based vector representation in our research. We employed the Word2Vec model for word embedding and tokenization to handle the textual data in the reviews. Word2Vec [24] is a shallow, two-layer neural network model used to learn vector representations of words in a continuous vector space based on their surrounding context in the text. The idea behind Word2Vec is that words that appear in similar contexts have similar meanings, which are captured through dense vector representations, unlike traditional one-hot encoding that produces sparse vectors.

Word2Vec works on two main architectures:

i. Continuous Bag of Words (CBOW): This model looks at the words around the target word to predict it.
ii. Skip-gram: This model works in reverse to the CBOW model and predicts the surrounding words by looking at the target word.

Both models position similar words close together in vector space. These dense word embeddings capture semantic relationships; words with similar meanings or usages will have similar vector representations.

In this study, the vector of each word in the review is found using the Word2Vec model. Then, these vectors are averaged to find the vector of the review. All word vectors in a review were collected for the review vector representation, and their average value was taken to create a 100-dimensional review vector. In such a case, a user's comment about a product would be multidimensional (100-dimensional vector). In user-item review matrix notation where rows represent users and columns represent items, computing such a matrix would be costly and time-consuming, as each matrix element is a 100-dimensional vector. To overcome this problem, we first categorized the product reviews of each uniquely identified user separately and then stored the user information. When making predictions using the test data, we also considered which user the product review belonged to. For example, let's assume that user X in our test dataset has reviewed three different items, and the classification algorithm predicted that the first and second reviews of the user were fake while the third review was genuine. The probability of the classification algorithm for each class prediction was calculated and averaged over all predicted class labels.

The same training and test data were used in rating- and review-based classification. The dataset was split into 80% training and 20% test data. The division into training and test datasets was performed entirely at the user level. After checking that the training and test dataset did not contain the same user ID, the classification step was started.

3.3. Classification

In this section, we describe the algorithms used in classification. A decision tree is a framework that graphically displays the likelihoods and results of a sequence of events or choices. Within this framework, each node signifies an event or decision juncture, while the edges illustrate how these decisions are reached or the factors that affect these choices. In simpler terms, each node reflects an assessment of a scenario or characteristic, while the edges denote the alternatives or routes to pursue based on that scenario.

Naive Bayes is widely used in problems such as text classification. This algorithm calculates the probability between classes and features on training data. It then uses these probabilities on test data to predict which class the new data belongs to.

SVM is a method that establishes a boundary to identify the class to which the data is assigned. This boundary maximizes the margin between the data points, reducing classification mistakes. When the data can be separated linearly, SVM creates a simple linear boundary; however, if the data is intricate and cannot be separated linearly, the kernel trick is employed to convert the data into a higher-dimensional space, where linear boundaries can be applied for classification. This capability makes SVM a highly effective and adaptable classifier.

The kNN algorithm is one of the supervised machine learning algorithms. This algorithm is used in both classification and regression problems. It determines the class or value of a data point by looking at its k nearest neighbors where k is a specified integer value [25].

LR is a probability-based method used in classification and regression problems. LR is applied when the dependent (target) variable is binary and makes no assumptions about the distribution of independent variables [26].

Ensemble learning is a technique that uses multiple models together. By utilizing several models, it produces more accurate and robust predictions. In other words, instead of a single model, predictions from various models are used to provide more correct results. This technique mitigates the shortcomings of each model while striving to deliver more robust and trustworthy predictions. It proves particularly valuable in addressing the challenges posed by complex and demanding datasets.

Ensemble learning employs a variety of algorithms and processes the features derived from the dataset to formulate predictions. These predictions are aggregated through various voting methods to create stronger and more dependable results, particularly when dealing with high-dimensional or unbalanced data [27]. In this research, we use manually selected/default parameter values without hyperparameter optimization to measure the baseline performance of the algorithms. The chosen hyperparameter values are in line with common usage in the literature and in the Scikit-learn library [28]. The XGBoost algorithm [29] and the Word2Vec model [24] were used within the range of values recommended in the reference article. In the LR model, which is one of the traditional machine learning techniques, since the 'saga' method is recommended as the solver parameter for large data sets, this parameter was set to balanced, the class_weight parameter was set to 'balanced' to preserve the data classification distribution, and the number of iterations was first set to 1500 and the algorithm was run. However, since the algorithm run with this iteration value was insufficient for the size of the dataset, the problem was solved by increasing the number of iterations from 1500 to 2000. In the SVM algorithm, the parameters consist of the default values in Scikit-learn. However, in this library, the probability value is False by default, whereas in our research we set the probability value to True to find out how confident the model is for the ROC-AUC evaluation metrics and to get the probability values for each prediction. The parameter details of the algorithms used in the study are shown in Table 2.

Table 2. Parameter values used in the algorithms

Model Name	Parameters
Word2Vec	vector_size=100, window=5, min_count=2, workers=4, epochs=10
LR	C=1.0, solver='saga', max_iter=2000, class_weight='balanced'
kNN	metric='euclidean', n_neighbors=2
SVM	C=1.0, kernel='rbf', probability=True
DT	default
NB	default
XGBoost	n_estimators=100, learning_rate=0.1, random_state=42

3.4. Evaluation Metrics

In order to measure the performance success of the algorithms, accuracy, precision, recall, F1-score metrics provided in (3.1)-(3.4) as well as Receiver Operating Characteristic (ROC) curve were used.

$$\text{Accuracy} = \frac{\text{True Positive} + \text{True Negative}}{\text{True Positive} + \text{True Negative} + \text{False Positive} + \text{False Negative}} \tag{3.1}$$

$$\text{Precision} = \frac{\text{True Positive}}{\text{True Positive} + \text{False Positive}} \tag{3.2}$$

$$\text{Recall} = \frac{\text{True Positive}}{\text{True Positive} + \text{False Negative}} \tag{3.3}$$

$$\text{F1} - \text{Measure} = \frac{2 \times \text{Precision} \times \text{Recall}}{\text{Precision} + \text{Recall}} \tag{3.4}$$

The ROC curve was constructed using the real class labels and the estimated probabilities. Using the J-Index method [30], the threshold value at which the maximum difference between the true positive and false positive rates was determined as the optimum threshold value. The optimal threshold value was used as a decision mechanism to determine whether the user was spam. This approach ensures that rating-based and review-based classifications are performed on the same data, aiming for more accurate and reliable results.

$$J = \text{True Positive Rate} - \text{False Positive Rate}$$

3.5. Experiments and Results

In the research, fake user detection was performed using rating data and product reviews with kNN, SVM, NB, LR, and DT machine learning algorithms. At the same time, the research aims to utilize the advantages of ensemble learning methods. For this reason, machine learning techniques were used with two different approaches, Stack and Voting Classifier. In the Voting Classifier method, majority voting was performed based on the outputs of the machine learning algorithms used in the study. The final predictions were selected according to the majority vote. In the Stack Classifier method, the algorithm's predictions were given to the XGBoost algorithm as input, and this ensemble learning algorithm decided the final results. Figure 1 outlines the general framework of the study.

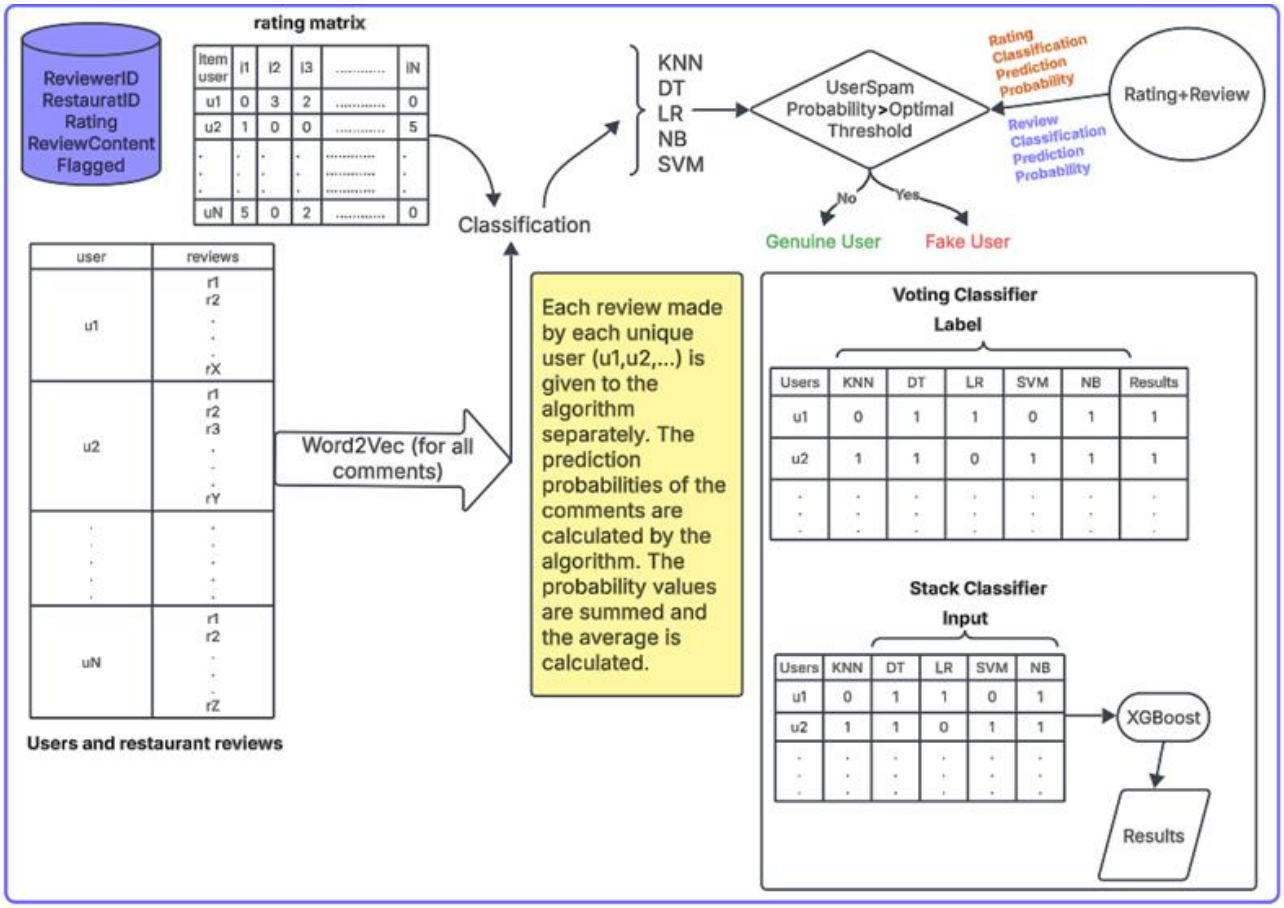

Figure 1. Process stages

Figure 2 shows the classification results based on rating data. When the curve is analyzed, it is seen that the model's performances are very close to each other. It can be said that classification success is not sufficient when only rating data is used.

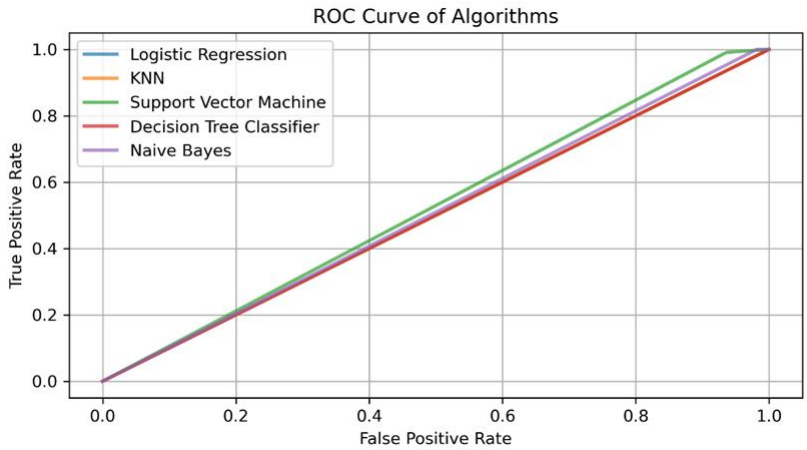

Figure 2. Classification performance of the algorithms using only rating data

Table 3, which presents the detailed classification results of the algorithms, shows that LR, kNN, and DT models have the same performance values with an F1 score of approximately 76.74%. The fact that these models have a recall of 100% indicates that they correctly classified all positive examples, but their precision is low. This suggests that the false positive predictions of the models are high. The NB algorithm outperforms these three models with an F1 score of 77.07%. The SVM algorithm has the highest F1 score of 77.47% among all algorithms. It can be concluded that the algorithms have an average performance in detecting fake users.

Table 3. Classification results using only rating data

Model Name	Accuracy	Precision	Recall	F1 Score
LR	62.26	62.26	100.0	76.74
kNN	62.26	62.26	100.0	76.74
SVM	64.12	63.59	99.1	77.47
DT	62.26	62.26	100.0	76.74
NB	62.95	62.69	100.0	77.07

Figure 3 shows the results of the review-based machine learning classification. Table 4 analyzes the classification results of all algorithms using product review data features against evaluation metrics. LR and SVM have the highest accuracy that are equal to 73.61% and 72.82%, respectively. The fact that kNN and LR models have the best recall value makes it possible to conclude that these algorithms are more successful in detecting fake users. The DT algorithm showed the lowest results. This method achieved 61.64% accuracy and 57.57% recall, suggesting the model may be overfitting. As a general analysis, it can be concluded that although the SVM algorithm has the highest precision, the LR model shows a more balanced success in all metrics.

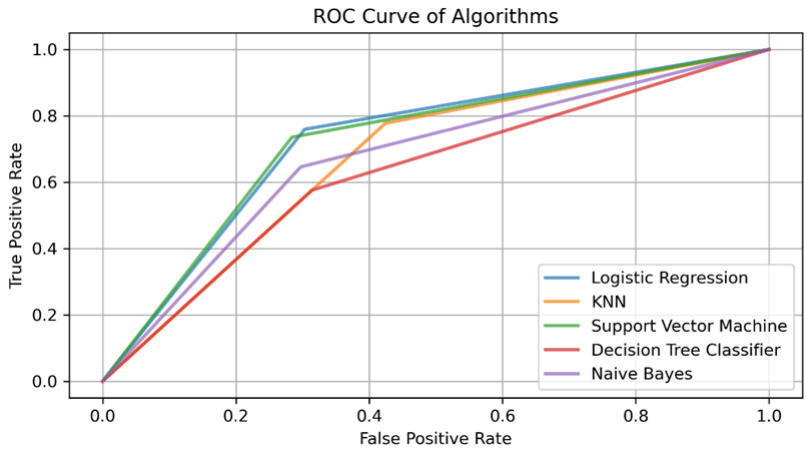

Figure 3. Classification performance of the algorithms using only user review data

Table 4. Classification results using product review data

Model Name	Accuracy	Precision	Recall	F1 Score
LR	73.61	81.01	75.93	78.39
kNN	70.29	75.74	77.76	76.74
SVM	72.82	81.51	73.54	77.32
DT	61.64	75.74	57.57	65.41
NB	66.70	78.73	64.60	70.97

As with the classification of review data, the prediction probabilities for rating data were given equal weighting values for the classification results obtained separately from rating and review data. The classification was performed separately for both data types. As a result of the classification, the prediction probability of the classification made according to both data types were averaged, and the final result was obtained. The obtained probability value was compared with the optimum threshold value (as in the case of review data classification only) to decide whether the user is real or fake. Finally, in Figure 4 and Table 5, we analyze and present our rating results and review data using the ensemble learning method, Stacking and Voting Classifier. The Stack Classifier model shows the best performance according to the ROC curve. Here, in the Stack Classifier model, machine learning techniques were used as the base model and the XGBoost algorithm as the meta-model. The prediction values of the machine learning techniques used herein were given as input values to the final classifier, the XGBoost algorithm. The VotingClassifier method takes the predictions of the machine learning algorithms used in the study and makes the final decision based on the prediction value labeled by the majority.

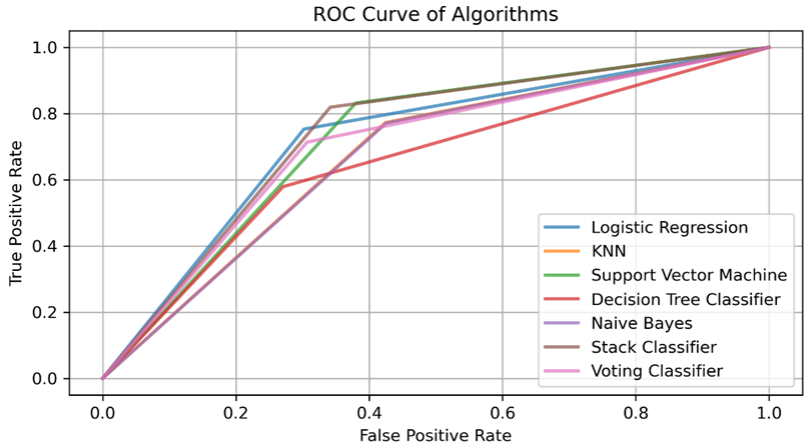

Figure 4. Classification performance of the algorithms when rating and review data are combined

When Table 5 is examined in detail, the highest accuracy rate is in the Stack Classifier model, with an F1 score of 81.11%. As a result of the LR and Stack Classifier models having the highest precision values of 80.94% and 80.33%, it can be said that the number of false positives is low. Thus, users can be prevented from being labeled as false users. Except for the DT, other algorithms also showed good and balanced performance. The NB algorithm showed relatively less performance.

Table 5. Classification results in machine learning and ensemble learning (using rating and review data)

Model Name	Accuracy	Precision	Recall	F1 Score
LR	73.26	**80.94**	75.30	78.02
kNN	69.98	75.62	77.27	76.44
SVM	75.34	78.85	**83.18**	80.96
DT	63.46	78.46	57.92	66.64
NB	69.84	75.53	77.13	76.32
Stack Classifier	**75.96**	80.33	81.91	**81.11**
Voting Classifier	70.60	79.84	71.36	75.36

Boldfaced values indicate the "best" performances.

It can be said that using the XGBoost algorithm as a meta-model contributes positively to the success of machine learning techniques. Using rating and review data in detecting fake users has positively affected the success. Only the kNN algorithm has shown relatively less success than the classification based on product reviews. The success has increased even more due to using machine learning algorithms with ensemble learning algorithms.

3.6. Performance Comparison with Previous Work

Supervised machine learning techniques have been used in previous work [15] to detect fake users on the YELP dataset. In their study, they used NB, SVM, LR algorithms to detect fake profiles on the review data. In the results of the study, the LR algorithm achieved 78%, the NB algorithm 65% and the SVM algorithm 77% F1- score success. In another study [22], fake user detection was performed on a different YELP dataset by combining product reviews with some behavioral characteristics of users (total number of capital letters, punctuation marks and emojis). Here, kNN, SVM, NB, LR algorithms achieved an F1-score of 82.40%, 82.17%, 81.86%, 82.20% respectively.

Different YELP datasets were used in both studies. In our research, we used the open-access YELP dataset available on kaggle.com, which is different from the above studies. Despite the differences in the dataset, fake user detection using only reviews achieved almost similar results. Although a direct comparison is not appropriate given the differences, it can be said that the proposed multi-data approach shows a significant and promising classification success on the used dataset.

4. Conclusion

In this study, the detection of fake users on digital platforms was carried out by combining the classification of two separate data sources: rating data and product reviews. Unlike traditional approaches, this method analyzes both the rating behaviors and textual comments of users, allowing for more effective identification of fake profiles. Two classifications were performed using machine learning algorithms to separate fake users from real ones. The dataset used in this study has sparse architecture. Although the dataset has much user information, the number of products these users evaluate is close to the minimum. This may cause less meaningful features to be extracted from users. However, the classification results showed that rating and review data overcame this disadvantage and increased detection success. In addition, the study combined machine learning techniques with ensemble learning techniques, and a second approach was proposed. The classification results obtained from this approach showed that ensemble learning methods further improved the classification success. The results of this research aim to increase the accuracy of recommendation systems, improve user satisfaction, and support the long-term success of the platforms. However, the small number of labeled data and unbalanced data distribution have partially limited the study. In future work, integrating additional data sources, such as behavioral features reflecting user and item interactions, can strengthen fake user detection. In this way, user behavior can be better analyzed, and more meaningful features can be extracted to improve classification success. In addition, using more advanced transformer models such as BERT, GPT and more advanced architectures for text data can significantly improve detection performance. Fake users are a minority class compared to real users. This leads to the problem of data imbalance. Using techniques to reduce class imbalance such as artificial data generation can improve the accuracy of the model. These enhancements could further strengthen the detection of fake users and improve the security and reliability of social platforms, especially e-commerce.

Author Contributions

All the authors equally contributed to this work. They all read and approved the final version of the paper.

Conflict of Interest

All the authors declare no conflict of interest.

Ethical Review and Approval

No approval from the Board of Ethics is required.

References

[1] C. Lin, S. Chen, M. Zeng, S. Zhang, M. Gao, H. Li, *Shilling black-box recommender systems by learning to generate fake user profiles*, IEEE Transactions on Neural Networks and Learning Systems 35 (1) (2022) 1305-1319.

[2] T. T. Nguyen, N. Quoc Viet Hung, T. T. Nguyen, T. T. Huynh, T. T. Nguyen, M. Weidlich, H. Yin, *Manipulating recommender systems: a survey of poisoning attacks and countermeasures*, ACM Computing Surveys 57 (1) (2024) 1-39.

[3] J. Suryawanshi, S. M. Abdul, R. P. Lal, A. Aramanda, N. Hoque, N. Yusoff, *Enhanced recommender systems with the removal of fake user profiles*, Procedia Computer Science 235 (2024) 347–360.

[4] R. A. Zayed, L. F. Ibrahim, H. A. Hefny, H. A. Salman, A. Almohimeed, *Using ensemble method to detect attacks in the recommender system*, IEEE Access 11 (2023) 111315-111323.

[5] Q. Zhou, J. Wu, L. Duan, *Recommendation attack detection based on deep learning*, Journal of Information Security and Applications 52 (2020) 102493.

[6] B. Mobasher, R. Burke, R. Bhaumik, C. Williams, *Effective attack models for shilling item-based collaborative filtering system*, In Proceedings of the 2005 WebKDD Workshop, held in conjuction with ACM SIGKDD, Chicago, Illinois, 2005.

[7] S. Shaw, A. Singh, *Using machine learning algorithms to alleviate the shilling attack in a recommendation system*, 11 (5) (2023) 1879-1883.

[8] S. Rani, M. Kaur, M. Kumar, V. Ravi, U. Ghosh, J. R. Mohanty, *Detection of shilling attack in recommender system for YouTube video statistics using machine learning techniques*, Soft Computing 27 (1) (2023) 377-389.

[9] J. Cao, Z. Wu, B. Mao, Y. Zhang, *Shilling attack detection utilizing semi-supervised learning method for collaborative recommender system*, World Wide Web 16 (5–6) (2013) 729–748.

[10] A. B. Chopra, V. S. Dixit, *An adaptive RNN algorithm to detect shilling attacks for online products in hybrid recommender system*, Journal of Intelligent Systems 31 (1) (2022) 1133–1149.

[11] R. A. Duma, Z. Niu, A. S. Nyamawe, J. Tchaye-Kondi, A. A. Yusuf, *A Deep Hybrid Model for fake review detection by jointly leveraging review text, overall ratings, and aspect ratings*, Soft Computing 27 (10) (2023) 6281–6296.

[12] Y. Cheng, J. Guo, S. Long, Y. Wu, M. Sun, R. Zhang, *Advanced Financial Fraud Detection Using GNN-CL Model*, 2024 International Conference on Computers, Information Processing and Advanced Education (CIPAE), Ottowa, ON, Canada, 2024, pp. 453–460.

[13] Z. Han, T. Zhou, G. Chen, J. Chen, C. Fu, *A Robust Rating Prediction Model for Recommendation Systems Based on Fake User Detection and Multi-Layer Feature Fusion*, Big Data Mining and Analytics 8 (2) (2025) 292–309.

[14] S. Rayana, L. Akoglu, *Collective opinion spam detection: Bridging review networks and metadata*, in: L. Cao, C. Zhang (Eds.) KDD '15: The 21th ACM SIGKDD International Conference on Knowledge Discovery and Data Mining, Sydney, NSW Australia, 2015, pp. 985–994.

[15] A. Sihombing, A. C. M. Fong, *Fake Review Detection on Yelp Dataset Using Classification Techniques in Machine Learning*, Proceedings of the 4th International Conference on Contemporary Computing

and Informatics, IC3I, Singapore, 2019, pp. 64–68.

[16] R. Barbado, O. Araque, C. A. Iglesias. *A framework for fake review detection in online consumer electronics retailers*, Information Processing and Management 56 (4) (2019) 1234-1244.

[17] Y. Jian, X. Chen, X. Wang, Y. Liu, X. Chen, X. Lan, W. Wang, H. Wang, *A metadata-aware detection model for fake restaurant reviews based on multimodal fusion*, Neural Computing and Applications 37 (1) (2024) 475–498.

[18] A. Mukherjee, V. Venkataraman, B. Liu, N. Glance, *Fake Review Detection: Classification and Analysis of Real and Pseudo Reviews,* Techical Report, Department of Computer Science (UIC-CS-2013-03) University of Illinois (2013) Chicago.

[19] W. Zhou, J. Wen, Q. Xiong, M. Gao, J. Zeng, *SVM-TIA a shilling attack detection method based on SVM and target item analysis in recommender systems*, Neurocomputing 210 (2016) 197–205.

[20] H. İ. Ayaz, Z. Kamışlı Öztürk, *Shilling attack detection with one class support vector machines*, Necmettin Erbakan University Journal of Science and Engineering 5 (2) (2023) 246-256.

[21] P. K. Singh, P. K. D. Pramanik, N. Sinhababu, P. Choudhury, *Detecting unknown shilling attacks in recommendation systems*, Wireless Personal Communications 137 (1) (2024) 259–286.

[22] A. M. Elmogy, U. Tariq, A. Ibrahim, A. Mohammed, *Fake Reviews Detection using Supervised Machine Learning*, IJACSA) International Journal of Advanced Computer Science and Applications 12 (1) 2021 601-606.

[23] A. Dheyaa, *YelpReviwsDB*, https://www.kaggle.com/datasets, Accessed 2 April 2025.

[24] T. Mikolov, K. Chen, G. Corrado, J. Dean, Efficient estimation of word representations in vector space, (2013), https://arxiv.org/pdf/1301.3781, Accessed 2 April 2025.

[25] B. Mahesh, *Machine learning algorithms - a review*, International Journal of Science and Research 9 (1) (2020) 381-386.

[26] I. H. Sarker, *Machine learning: algorithms, real-world applications and research directions*, SN Computer Science 2 (3) (2021) 160.

[27] X. Dong, Z. Yu, W. Cao, Y. Shi, Q. Ma, *A survey on ensemble learning*, Frontiers of Computer Science 14 (2) (2020) 241-258.

[28] Scikit-learn, *scikit-learn: Machine Learning in Python*, https://scikit-learn.org/stable, Accessed 28 June 2025.

[29] T. Chen, C. Guestrin, *XGBoost: A scalable tree boosting system*, Proceedings of the ACM SIGKDD International Conference on Knowledge Discovery and Data Mining, San Francisco, California, USA, 2016, pp. 785-794.

[30] W. J. Youden, *Index for rating diagnostic tests*, Cancer 3 (1) (1950) 32-35.

Journal of Advanced Research in Natural and Applied Sciences
dergipark.org.tr/en/pub/jarnas
Open Access

ISSN: 2757-5195 11 (2) (2025) 156-174 doi.org/10.28979/jarnas.1657826

A Comparative Anatomical Study on Two Endemic *Sempervivum taxa* (Crassulaceae) in Türkiye

Tuğba Şahin[1], Nezahat Kandemir[2]

Article Info
Received: 14 Mar 2025
Accepted: 11 Jun 2025
Published: 30 Jun 2025
Research Article

Abstract − This paper comparatively examines the anatomical features of *Sempervivum brevipilum* and *Sempervivum gillianiae* using cross-sections from roots, stems, rosette leaves, sepals, and petals, alongside surface sections from rosette leaves, sepals, and petals. It identifies key distinguishing characters including: root periderm and cortex layer numbers; periderm width and length; root tracheid diameter; cortex parenchyma cell diameter; root tannin density (dense/not dense); stem cuticle layer structure; micropapillae presence/absence; stem cortex layer count; xylem configuration (straight/wavy); stem epidermis cell diameter; pith parenchyma and xylem tracheid diameter; stem cuticle thickness; mesophyll parenchyma diameter; stomatal width and length; rosette leaf upper/lower epidermis cell length, shape, and anticlinal wall structure; mesophyll layer number and shape in rosette leaves and sepals; margin structure of irregular cells adjacent to stomata in sepals and rosette leaves; sepal upper epidermis cell length; sepal lower epidermis cell width and length; petal cuticle thickness (thick/thin); petal epidermis cell diameter; petal epidermis anticlinal wall structure; petal mesophyll layer number; and tannin quantity in vegetative organs. This study confirms statistically significant differences ($p<0.05$) in select anatomical features. It also establishes that these findings align with earlier anatomical research within Crassulaceae and the genus *Sempervivum*, validating the diagnostic utility of these characters.

Keywords − *Sempervivum taxa, endemic, anatomical features, Crassulaceae*

1. Introduction

The Crassulaceae family is nearly cosmopolitan, and its species are distributed in South Africa, Mexico, Macaronesia, the Mediterranean, and the Himalayas [1, 2]. Mort et al. [3] suggested that this family spread from Southern Africa to the Mediterranean, Eastern Europe, and Asia, while the North African species spread to Macaronesia and where they later diversified. Family members generally consist of herbs, shrubs, and succulent plants. They are remarkable plants because they have water-storage tissue in their leaves and stems [4]. The majority of members of the family are leaf succulents. Due to their biological characteristics, these plants adapt well to life in ecologically harsh conditions.

The closeness of the Crassulaceae family to other families has caused some problems distinguishing its subfamilies and genera. On the other hand, the species of the family have high similarities in vegetative and generative organs (especially flower and embryonic features) [5]. Ham and $'\tau$ Hart [6] conducted chloroplast DNA restriction-site variation analyses to eliminate the problems related to subfamilies. They identified four

[1]hftch40@gmail.com; [2]nezahatkndmr@gmail.com (Corresponding Author)
[1]Institute of Science, Amasya University, Amasya, Türkiye
[2]Department of Mathematics and Science Education, Faculty of Education, Amasya University, Amasya, Türkiye

subfamilies within the family: Cotyledonoideae, Sempervivoideae, Sedoideae, and Echeverioideae. Furthermore, Mort et al. [3] comprehensively studied the molecular phylogeny and evolution of the Crassulaceae family. Their research revealed that the family is divided into two subfamilies, Crassuloideae and Sempervivoideae, while Thiede and Eggli [2] divided this family into three subfamiles (Sempervivoideae, Crassuloideae and Kalanchoideae). Nevertheless, *Sempervivum* L., both according to Ham and $'\tau$ Hart [6] and Mort et al. [3] belong to Sempervivoideae subfamily.

The genus *Sempervivum* consists of approximately fifty species and seventeen hybrids [7-10]. The natural habitat of the species of this genus is the rocky and dry terrains of the high mountains of Central and Southern Europe, Southwest Asia, the Caucasus, and the Mediterranean [11, 12]. The endemism rate of the genus is 70% in the world and 87% in Türkiye. The first revision of the *Sempervivum* genus in Türkiye was made by Muirhead [13, 14], and eleven species and one variety were described. Since the publication of the Türkiye Flora, new taxa have been described from Türkiye, and the number of taxa has reached nineteen [7, 8, 15]. Thirteen of these are endemic to Türkiye. Besides, *Serpervivum minus* Turrill var. *glabrum* Wale was elevated to species level as *Sempervivum ekimii* by Karaer and Celep [16]. Detailed descriptions of taxa from Türkiye and information on ecology, distribution, and naturally occurring hybrids have been published by Neeff [15]. According to the Türkiye Flora [14], most *Sempervivum* species in Türkiye are local endemics, but differences between taxa are minimal.

Members of the Crassulaceae family (Orostachys L., *Sedum* L., *Hylotelephium* L., *Sempervivum*, etc.) have been preferred in the food industry, medicine, and ornamental plants for a long time. *Sempervivum* species (*Sempervivum marmoreum* Griseb.) are frequently used in landscape design and applications in home gardens, rock, and dry wall gardens as succulent ground covers [17, 18]. Additionally, some species (*Sempervivum davisii* Muirhead, *Sempervivum armenum* Boiss. Et Huet., *Sempervivum marmoreum,* and *Sempervivum tectorum* L.) are also preferred as folk medicine [19, 20]. Fresh juice obtained from the leaves of *Sempervivum* species treats skin complaints such as burns, wounds, and painful areas. Drinking tea prepared from *S. tectorum* leaves is recommended for ulcer treatment. The basal leaves of *Sempervivum sosnowskyi* Ter-Chatsch. are consumed as a salad by locals in NE Anatolia [21-23]. The biological activities and chemical composition of essential oils in fresh flowers, leaves, and stems of *Sempervivum brevipilum* Muirhead have been investigated. It has been reported that it has high antituberculostatic activity against *Mycobacterium smegmatis* [24].

Tannins are essential polyphenols found naturally in plants. They can be found in various plant structures such as wood, bark, root, leaf, fruit, and seed, and they regulate the development of these structures. They also protect vegetative organs against freezing, herbivores, pathogens, UV rays, and allelopathic and bactericidal effects [25]. Metcalfe and Chalk [26] suggested that tannins are widespread in non-woody stems, especially in the cortex, pith, and phloem of representatives of the Crassulaceae family. On the other hand, the presence of tannins has been detected in numerous members of representatives of this family, such as *Crassula multicava* Lemaira, *Echeveria venezuelensis* Rose, *Pachyphytum* sp., *Compactum* sp., *Kalanchoe* Adans. sp., *Bryophyllum daigremontianum* (Raym.-Hamet et perrier) A. Berger, *Sedum* sp., *Aeonium* sp. and *Sempervivum* sp. [27]. Although some morphological and palynological studies have been carried out on the *Sempervivum* genus, ecological, anatomical, and micromorphological studies on its species are insufficient. Therefore, this study aims to compare the anatomical features of the vegetative and generative organs and tannin content of the two aforementioned endemic *Sempervivum* taxa and evaluate whether any of the analyzed traits possess taxonomical significance.

The rest of the paper is organized as follows: Section 2 identifies plant specimens used in this study and the methods. Section 3 describes the anatomical features of the vegetative and generative organs of the examined taxa. Furthermore, the anatomical results obtained from this study were discussed in the literature, and the anatomical results of studies conducted with other members of the Crassulaceae family. In section 4, the study's conclusions are presented, and the future studies that need to be undertaken on taxa are mentioned.

2. Materials and Methods

Plant samples were taken from areas where taxa naturally spread, during flowering periods. Collection data related to plant materials are presented in Table 1. The identification of the collected taxa was conducted using the descriptions provided by Muirhead [14] and Eggli [28]. In *S. brevipilum*, sections were taken from 10 number of samples with a length of 20-22 cm in the summer season, while sections of *S. gillianiae* were taken from 10 number of samples with a length of 16-18 cm in the summer season. In anatomical examinations, cross-sections of the root, stems, rosette leaves, sepals, petals, and surface sections from the upper and lower surfaces of rosette leaves, sepals, and petals were taken and photographed. To enhance the visibility of tissues and cells in the vegetative and generative organs of the examined taxa, sartur reagent was applied to the cross and surface sections [29]. Width and length measurements of cells in each species' layers of stems, rosette leaves, sepals, and petals were made using an ocular micrometer. The means and standard deviations were determined according to the IBM SPSS Statistics 27.0 program. Similarities and differences in anatomical features of the examined taxa are given in Tables 2 and 3. Since the obtained data did not show normal distribution, the Mann-Whitney U test was used to reveal differences between similar groups more clearly. The test results are shown in Table 4. Tannin contents of taxa were determined by the Folin-Denis method [30, 31]. The measured absorbance value was converted to tannin amount in $GA_{mg}/extract_{mL}$ using the previously established standard curve (Figure 3).

Table 1. Locality information of the areas where *S. brevipilum* and *S. gillianiae* were collected

Taxa	Locality	Coordinates	Altitude	Collectors
S. brevipilum	Akdağ (Derebaşalan- Amasya) 07.08.2023	40°52'34.4"N 35°51'34.3"E	1500 m.	Tuğba Şahin
S. gillianiae	Sakarat Mountain (Yuva Village-Amasya) 02.07.2023	40°38'47.2"N 36°10'49.1"E	1100 m.	Tuğba Şahin

Table 2. Comparison of qualitative anatomical features of *S. brevipilum* and *S. gillianiae*

	Features of plant organs	*S. brevipilum*	*S. gillianiae*
ROOT	Periderm*	3-4 layered	4-5 layered
	Endodermis	Single-layered	Single-layered
	Cortex layer*	10-13 layered	19-22 layered
	Tannins in parenchyma cells*	Very dense	Sparse
	Xylem (trachea)	Chain shaped	Chain shaped
STEM	Epidermis cell*	Single-layered, quadrangular-shaped and large celled	Single-layered, quadrangular-shaped, and medium celled
	Cuticle layer*	Cuticle thick and densely micropapillated	Cuticle thick and without micropapillae
	Cortex layer*	20-23 layered, oval or hexagonal, large and small parenchymatic celled	20-22 layered, rounded shaped and large parenchymatic celled
	Pith region*	Wide area and large, oval, or hexagonal parenchyma celled	Wide area and large rounded parenchyma celled
	Vascular bundle elements*	Phloem narrow, xylem wide and straight	Phloem narrow, xylem wide and undulate
	Vascular bundle type	Open collateral	Open collateral
	Tannins in parenchyma cells	+	+
ROSETTE LEAF	Mesophyll structure	Unifacial	Unifacial
	Tannins in mesophyll	+	+
	Upper epidermis cell*	Rectangular-shaped and large-celled	Quadrangular-shaped and medium-celled
	Lower epidermis cell*	Rectangular-shaped and large-celled, anticlinal walls undulate	Quadrangular-shaped and large-celled anticlinal walls slightly undulate
	Margin structure of ordinary irregularly shaped cells next to the stomata *	Straight	Straight and slightly undulate
	Stomata type	Anisocytic	Anisocytic
	Tannins in ordinary irregularly shaped cells next to the stomata	+	+

*: different anatomical features between taxa

Table 2. (Continued) Comparison of qualitative anatomical features of *S. brevipilum* and *S. gillianiae*

SEPAL	Epidermis cell	Rectangular-shaped and large-celled, slightly undulate	Rectangular-shaped and large-celled, slightly undulate
	Mesophyll type*	7-8 layered, large oval parenchyma celled	5-6 layered, small parenchyma celled
	Tannins in the mesophyll	+	+
	Stomata type	Anisocytic	Anisocytic
PETAL	Epidermis cell*	Single layered, large, quadrangular-shaped, and dense undulate	Single layered, large, quadrangular-shaped, and slightly undulate
	Cuticle layer*	Thick and dense micropapillated	Medium thickness and micropapillated
	Mesophyll structure*	8-10 layered, oval-shaped, large and small parenchymatic celled	8-9 layered, oval-shaped, large and small parenchymatic celled
	Tannins in the mesophyll	+	+

*: different anatomical features between taxa

Table 3. Mean and standard deviation of the analyzed anatomical traits (µm) in the organs of *S. brevipilum* and *S. gillianiae*

	Features of plant organs	Number of samples	*S.brevipilum*	*S. gillaniae*
			Mean±Standard Deviation	
ROOT	Length of peridermal cell	10+10	28.40±5.48	47.50±5.89
	Width of peridermal cell	10+10	37.60±5.71	83.00±13.37
	Cortex parenchyma cell	10+10	35.20±6.47	63.00±11.59
	Phloem cell	10+10	18.20±2.20	-
	Xylem (Trachea cell)	10+10	18.08±1.99	14.30±2.11
	Cambium	10+10	9.90±1.52	-
	Pith parenchyma cell	10+10	106.00±20.11	76.00±12.64
STEM	Epidermis cell	10+10	39.00±6.58	30.20±2.04
	Cortex parenchyma cell	10+10	79.00±16.63	90.00±16.32
	Pith parenchyma cell	10+10	106.00±20.11	76.00±12.64
	Cambium	10+10	16.10±2.96	-
	Cuticle	10+10	12.60±1.89	12.00±1,16
	Phloem cell	10+10	16.60±3.06	-
	Xylem (Trachea cell)	10+10	28.80±3.15	11.20±1.75
ROSETTE LEAF	Upper epidermis cell width	10+10	64.00±8.43	70.50±8.23
	Upper epidermis cell length	10+10	43.50±3.37	31.20±4.77
	Lower epidermis cell width	10+10	58.50±10.55	54.00±5.67
	Lower epidermis cell length	10+10	44.00±4.59	26.70±2.31
	Mesophyll (Parenchyma cell)	10+10	202.00±52.02	154.00±20.65
	Stomata length	10+10	46.00±6.32	40.80±4.54
	Stomata width	10+10	37.60±3.86	21.36±2.10
FLOWER	Sepal cuticle	10+10	4.68±0.77	-
	Sepal upper epidermis cell length	10+10	34.00±3.94	24.80±4.13
	Sepal upper epidermis cell width	10+10	58.50±7.83	52.00±4.21
	Sepal lower epidermis cell width	10+10	58.50±7.83	38.40±4.29
	Sepal lower epidermis cell length	10+10	35.00±4.08	24.00±3.26
	Sepal mesophyll (parenchyma cell)	10+10	106.00±12.64	-
	Petal cuticle	10+10	7.20±1.03	-
	Petal upper epidermis cell diameter	10+10	50.40±13.62	40.00±5.96
	Petal lower epidermis cell diameter	10+10	46.40±7.82	28.40±3.97
	Petal mesophyll (parenchyma cell)	10+10	56.80±8.59	64.00±13.59

Table 4. Mann-Whitney U results of anatomical measurements of *S. brevipilum* and *S. gillianiae*

	Features of plant organs	Number of samples	Mann-Whitney U test	
			U	p (*p<0.05)
ROOT	Cortex parenchyma cell	20	0.000	0.000*
	Width of peridermal cell	20	0.000	0.000*
	Length of peridermal cell	20	0.000	0.000*
	Xylem-Trachea cell	20	8.000	0.001*
STEM	Cortex parenchyma cell	20	34.000	0.219
	Pith parenchyma cell	20	9.000	0.002*
	Epidermis cell	20	10.000	0.002*
	Xylem-Trachea cell	20	0.000	0.000*
ROSETTE LEAF	Cuticle	20	40.000	0.441
	Lower epidermis cell width	20	33.000	0.191
	Lower epidermis cell length	20	0.000	0.000*
	Upper epidermis cell width	20	28.500	0.096
	Upper epidermis cell length	20	2.000	0.000*
	Cuticle	20	17.500	0.012*
	Mesophyll (parenchyma cell)	20	20.500	0.025*
	Stomata width	20	0.000	0.000*
	Stomata length	20	24.500	0.047*
SEPAL	Upper epidermis cell width	20	25.000	0.056
	Upper epidermis cell length	20	4,000	0.000*
	Lower epidermis cell width	20	0.000	0.000*
	Lower epidermis cell length	20	0.000	0.000*
PETAL	Upper epidermis cell diameter	20	26.000	0.067
	Lower epidermis cell diameter	20	1.000	0.000*
	Mesophyll	20	33.500	0.208

3. Results and Discussion

In this study, the anatomical features of root, stem, rosette leaf, sepal, and petal, potantially important in distinguishing *S. brevipilum* and *S. gillianiae* distributed in Türkiye, are given in detail and comparatively. Since there are not many anatomical studies in the literature (only three anatomical studies were found) on the species of this genus, our findings were additionally compared with the findings of studies conducted with other members of the Crassulaceae family.

In the root cross sections of the two taxa, the periderm is 3-4 layered in *S. brevipilum* and 4-5 layered in *S. gillianiae* Muirhead. The cortical parenchyma cells are oval-shaped, and while parenchyma is 10-13 layered in *S. brevipilum*, it is 19-22 layered in *S. gillianiae* (Figures 1 A-C and Figures 2 A, B). More tannin was observed in the parenchyma cells in *S. brevipilum* than in the other taxa analyzed (Figure 3). In both analyzed

taxa, the xylem is large and clearly visible in the vascular bundles of the pith region, while the phloem occupies a much narrower area. The trachea is in the radial form in both taxa (Figure 1 D and Figures 2 C-E). Similar anatomical features were reported in the root of *Sedum telephium* L. ssp. *maximum* (L.) Krock., which is characterized by a thin periderm and numerous vascular tissue bundles [32]. Ulcay [33] found the periderm of *Sedum acre* L. to be 7-8 layered, *Sedum album* L. to be 3-4 layered, and *Sedum pallidum* M. Bieb. to be 2-3 layered. Kirilenko [34] saw radial conduction tissue bundles in the roots of *Crassula perforata* Thunbg and *Crassula socialis* Schonland. The root anatomical features observed in this study are consistent with the above-mentioned results regarding family members.

Shahrestani et al. [35] reported that the features that provide essential taxonomic evidence for the separation of genera are the presence or absence of trichomes on the stem epidermis, the presence or absence of tannin secretory cells in the stem cortex and pith region, the number of collenchyma layer, the presence or absence of endodermis, the presence or absence of xylem and stomata in the stem. Some researchers have suggested that anatomical characteristics in stems and leaves are important in distinguishing plant taxa [36, 37].

When the cross sections of the stems were examined, the cuticle of *S. brevipilum* was thick and micropapillated, and the epidermis was single layered, consisting of large, quadrangular cells. The cuticle of *S. gillianiae* was medium-thick, and the epidermis was single-layered, quadrangular cells, and consisting of medium large. The cortex was 20-23 layered in *S. brevipilum* and 20-22 layered in *S. gillianiae* (Figures 1 E, F and Figures 2 F, G, K). Tannins and large parenchyma cells were densely seen in the cortex of both taxa. In these taxa, contrary to phloem, the xylem occupied a large area (Figure 1G and Figure 2 H). In *S.gillianiae*, the xylem is wavy (Figure 2 F), while the xylem is straight in *S. brevipilium.* The pith region is wider in *S. brevipilium* (Figure 1 H). Anatomical features such as the structure of the cuticle layer in the stem, whether the epidermis cells are large or small, whether micropapillae are present or not, and whether the xylem is wavy or not can be used as useful characters in distinguishing these two taxa.

Kirilenko [38] determined that the outermost part of the stem of *S. tectorum* has a thick cuticle and a single-layered epidermis. The cortex is composed of large 17-22-layered parenchyma cells. 1-2-layered collenchyma was found immediately under the epiderma. Numerous vascular bundles were observed in the stem. The presence of large intercellular spaces in the cortex was detected. Similar features were seen in the stem of the examined taxa (except for large intercellular spaces).

Vorobojev et al. [39] examined, and compared, anatomical features of stem of *Sempervivum globiferum* L. (=*Jovibarba globifera* (L.) J.Parn.), *S. tectorum* and *Sempervivum ruthenicum* Schnittsp. & C. B. Lehm. distributed in Ukraine [39]. The anatomical differences between *S. globiferum* from *S. tectorum* and *S. ruthenicum* are the grooved shape of the two-layered epidermis on the stem. The circular shape of the vascular bundles on the stem, the poor development of the xylem and phloem tissues were reported to be similar features in these three *Sempervivum* taxa. The results of Vorobej et al. [39] are consistent with the findings of this study.

Ulcay [33] investigated the anatomical features of some *Sedum* species distributed in Türkiye. When the stem cross-section was examined, it was found that the epidermis was single-layered and round-shaped in *Sedum acre*, single-layered and epidermis cells rectangular or round-shaped in *Sedum album,* and single-layered, with rectangular or circular shaped epidermis cells in *Sedum pallidum.* The cortex is reported to be 13-14 layered in *S. album*, 10-11 layered in *S. pallidum,* and quite wide in *S. acre*. The vascular bundles in the stems were in the form of regular rings. The anatomical features of *S. acre*, which is distributed under different ecological conditions in Southern and Central Kazakhstan, were investigated by Akhmetzhanova et al. [40]. It has been found that the vascular bundles in the stem are in a regular ring, single-layered of the epidermis and 7-8 layered of cortex.

Shahrestani et al. [35] reported anatomical features of 22 taxa of *Sedum s.l.* (Crassulaceae) distributed in Iran that could provide useful data in solving the current problem regarding the taxonomy and nomenclature of *Sedum s.l.* Their study found that species belonging to the genera *Phedimus* Raf., *Prometheum* (A. Berger) H.

Ohba, and *Hylotelephium* H. Ohba could be readily distinguished from other *Sedum s.l.* taxa based on their anatomical characteristics. In addition, it was found that *Sedum* and *Epeteium* sections were close to each other regarding anatomical features. Tannins and starches with different sizes and densities were detected in the parenchyma cells of some species' cortex and pith region of the stem. With the exception of *Sedum caespitosum* (Cav.) DC., 1-3 layered collenchyma was observed beneath the stem epidermis in analyzed taxa. The parenchymatic cortex is found between collenchyma and endoderma. The pith region was observed in the stem of all examined taxa (except *Sedum callichroum* Boiss.). Stomata were observed only in the stem epidermis of *Phedimus obtusifolious* (C. A. Meyer) *'τ* Hart*, Sedum tenellum* M. Bieb., *Sedum subulatum* (C. A. Meyer) Boiss. and *Sedum annum* L. It was also emphasized that the xylem in the stem of the taxa differed, and this feature was important in distinguishing the taxa. The stem anatomy of *Sedum s.l.* taxa and examined *Sempervivum* taxa showed similarities, such as xylem structure and presence of tannins, but also differences, including the presence of collenchyma layers and starch.

Abdel-Raouf [41] studied the anatomical features of 15 *Kalanchoe* species and their taxonomic importance. It was observed that the cuticle on the stem was relatively thick in eight taxa, as in *Kalanchoe tubiflora* Raym.-Hamet, and thin in other taxa. Hypodermis was recorded in *Kalanchoe daigremontiana* Raym.-Hamet et H.Perrier, and cork tissue examined were found only in *Kalanchoe blossfeldiana* Poelln. and *Kalanchoe beharensis* Drake. The cortex was in a wide area in *Kalanchoe pumila* Baker, and a narrow area in *K. tubiflora*, among others. The cortex of most taxa has well-developed collenchymatic cells, as in *K. tubiflora*. There are vascular bundles in three taxa, as in *Kalanchoe roseleaf* Adans., secretory ducts in *K. beharensis* and some species, and druse crystals in some species. Similar results (the stem cortex is generally composed of succulent and strongly developed and watery parenchyma or contains weakly developed collenchyma, the cork tissue being in the epidermis or in the subepidermal layer as in members of *Kalanchoe* and *Sedum* genera) were also determined by Metcalfe and Chalk [26] in other members of the Crassulaceae family. Abdel-Raouf [41] reported several stem features in *Kalanchoe* taxa, including the presence of cork tissues and hypodermis layers, pigmented epidermis cells, collenchymatic and storage cells in the cortex, secretory channels, and druse crystals, that differed from those observed in the examined taxa in this study.

Comprehensive studies on the leaf anatomical features and epidermal structures of species in the genus *Sempervivum* are quite limited [38, 39, 42]. However, studies have been conducted on the leaf epidermal structures of genera such as *Kalanchoe, Crassula*, *Rhodiola, Echeveria*, and *Sedum*, etc. [33-35, 41, 43-48]. It has been determined that leaves are amphistomatic and stomata are mostly anisocytic [2, 32-34, 38-40, 42, 44, 45]. In addition, it has been reported that stomata are generally more numerous in the lower epidermis in many species of the Crassulaceae family [49].

In cross-section, the rosette leaves of taxa analyzed in this study exhibit upper and lower epidermis cells of nearly equal size (Table 3). In S. *brevipilum*, the epidermis cells are rectangular, whereas in *S. gillianiae*, they are quadrangular. The anticlinal walls of the lower epidermis cells in *S. gillianiae* are slightly undulated. In the surface sections of the rosette leaves, anisocytic stomata were found in the upper and lower epidermis of the two taxa (Tables 2 and 3, Figure 1N and Figure 2 N). In both taxa, stomata are denser in the lower epidermis than in the upper epidermis. Abundant tannins were found in both taxa's epidermis cells around the stomata. While the anticlinal walls of adjacent stomatal cells are mostly straight in *S. brevipilum*, they are slightly undulate in *S. gillianiae* (Figure 1N and Figure 2N). In both taxa, the rosette leaves are unifacial, with a mesophyll composed of cells that are relatively uniform in shape, showing no clear differentiation into palisade and spongy parenchyma (Figures 1 K, L, M, and Figures 2 L, M) and abundant tannins are found in the parenchyma cells. The mesophyll layer of *S. brevipilium* comprises of 15-17 layered, large, oval, or hexagonal-shaped parenchyma cells (Tables 2 and 3, Figures 1 K, L). The mesophyll layer of *S. gillianiae* is quite wide and consists of 17-19 layered, large, oval-shaped parenchyma cells (Figures 2 L and M). The vascular bundles in the middle of the mesophyll are smaller in *S. gillianiae*. The findings in the literature showed that both taxa preserved the characteristic leaf anatomical features of the *Sempervivum* genus.

Jovanović et al. [42] studied the epidermal structures of rosette leaves of yellow-flowered *Sempervivum* species distributed in the Balkan Peninsula and grouped under two complexes as *Sempervivum ciliosum* (*Sempervivum ciliosum* Craib*, Sempervivum jakucsii* Penzes*, Sempervivum klepa* Micevski*, Sempervivum octopodes* Turrill and *Sempervivum galicicum* (Sm.) Micevski) and *S. ruthenicum* (*Sempervivum ruthenicum, Sempervivum leucanthum* Pancic, *Sempervivum kindingeri* Adamovic and *Sempervivum zeleborii* Schott). Eighteen quantitative characters describing the lower and upper epidermal structures were analyzed. Differences between the species of the two complexes were observed in the anticlinal walls and the number and length of epidermis cells. Statistical analysis showed that the differences in quantitative characteristics of the epidermal structures were significant ($p<0.05$), supporting their relevance in the differentiation of the complexes. Furthermore, the epidermis cells of the leaves of species in the *S. ciliosum* complex (especially those on the abaxial surface) are mostly undulated, with anticlinal walls that are straight or rarely undulated (*S. ciliosum)*

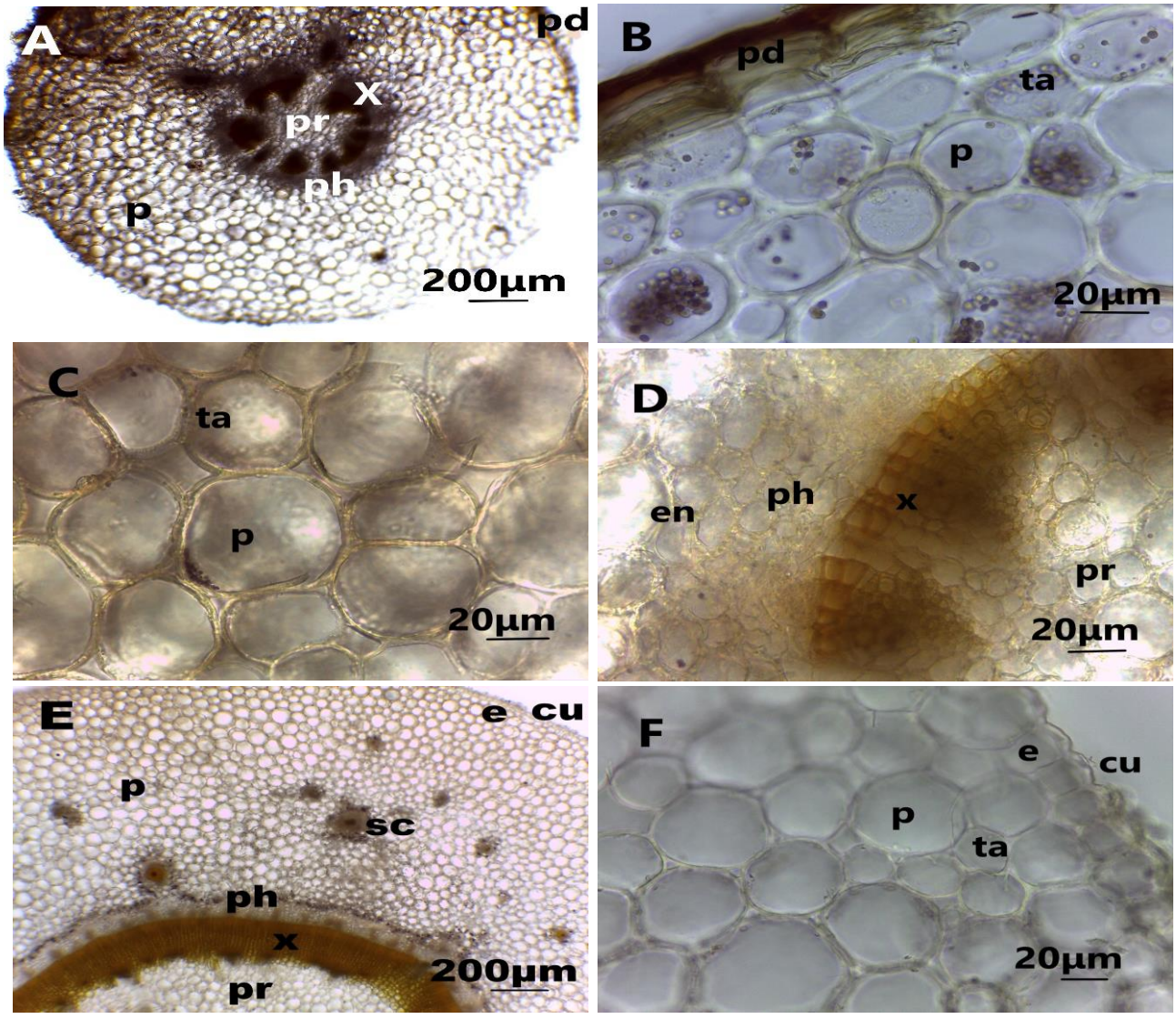

Figure 1. Anatomical structures of vegetative and generative organs of *Sempervivum brevipilum*. A. General structure of the root, B. Periderm and cortex regions of the root, C. Cortex region of the root, D. Phloem, xylem and pith regions of the root, E. General structure of the stem, F. Epidermis and cortex regions of the stem, pd: periderm; ph: phloem; x: xylem; p: parenchyma; ta: tannin; pr: pith region; en: endodermis; cu: cuticle; e: epidermis; sc: secretory channels.

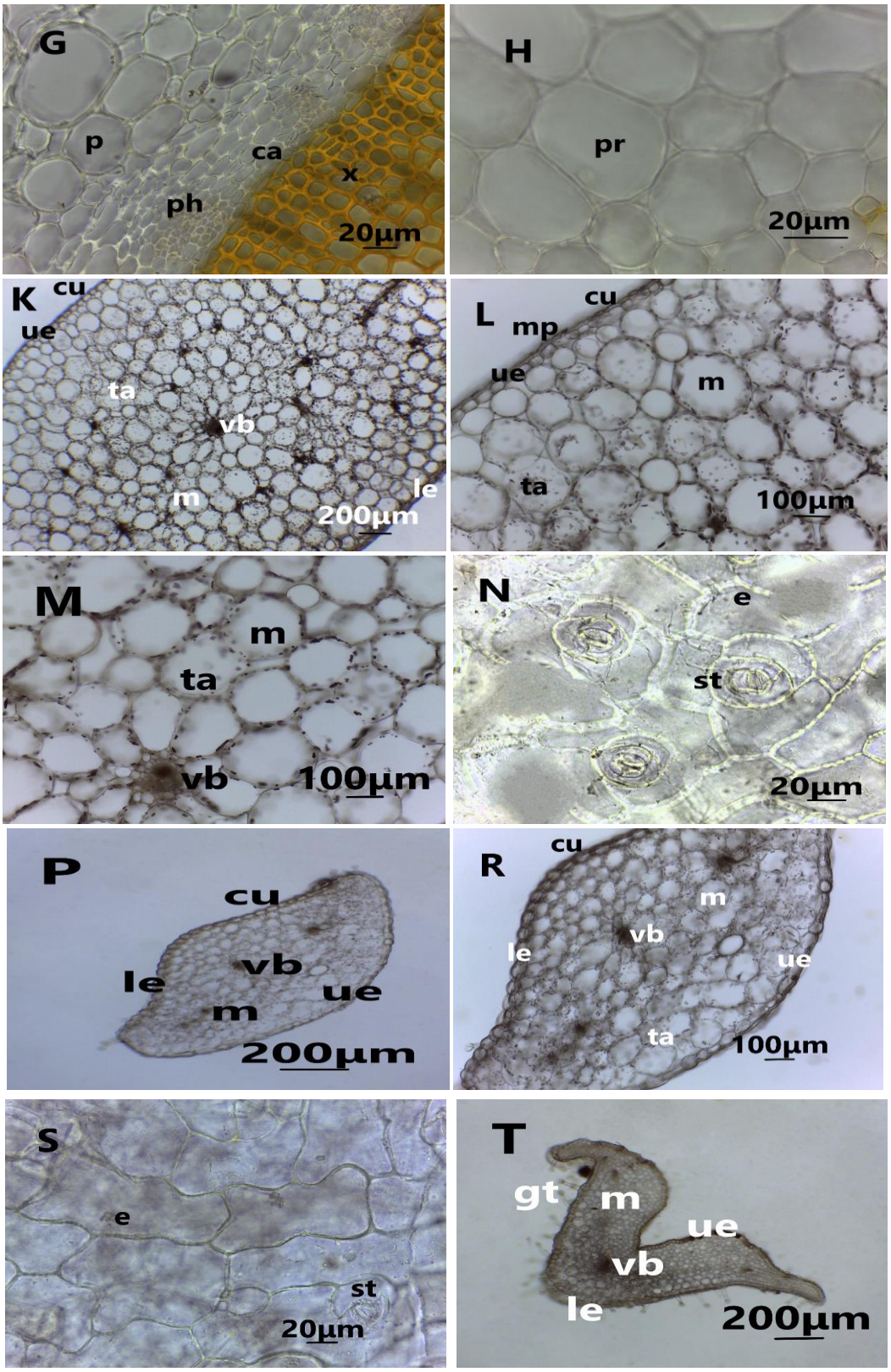

Figure 1. (Continued) Anatomical structures of vegetative and generative organs of *Sempervivum brevipilum*. G. Phloem and xylem regions of the stem, H. Pith region of the stem, K. General structure of rosette leaf, L. Mesophyll region of rosette leaf, M. Mesophyll region and vascular bundle, N. Stomata of rosette leaf, P and R. General structure of sepal, S. Epidermis and stomata cells of sepal, T. General structure of petal, ph: phloem; x: xylem; p: parenchyma; ta: tannin; pr: pith region; cu: cuticle; e: epidermis; ca: cambium; m: mesophyll; vb: vascular bundle; ue: upper epidermis; le: lower epidermis; st: stomata; mp: micropapillae; gt: glandular trichomes

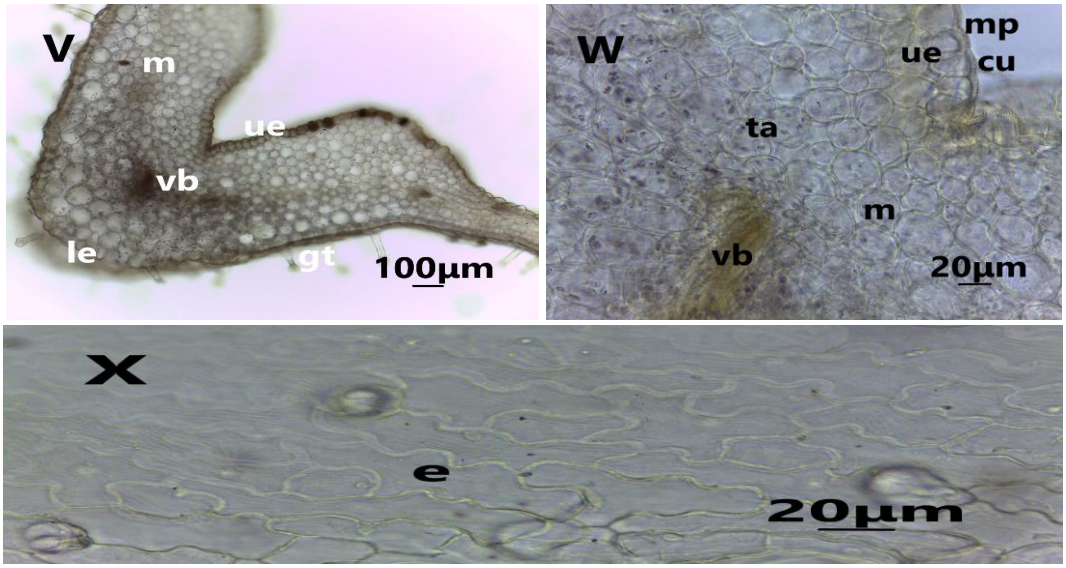

Figure 1. (Continued) Anatomical structures of vegetative and generative organs of *Sempervivum brevipilum*. V. General structure of petal, W. Epidermis and mesophyll region of petal, X. Epidermis cells of the petal, ta: tannin; cu: cuticle; e: epidermis; m: mesophyll; vb: vascular bundle; ue: upper epidermis; le: lower epidermis; mp: micropapillae; gt: glandular trichomes

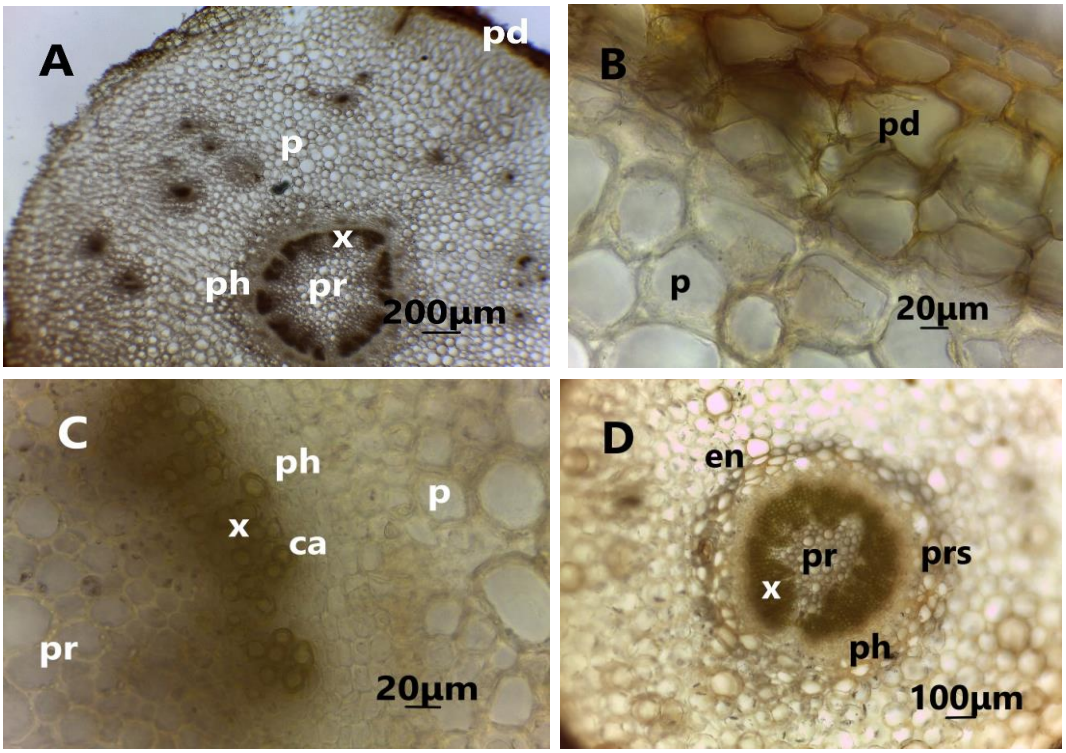

Figure 2. Anatomical structures of vegetative and generative organs of *Sempervivum gillianiae*. A. General structure of the root, B. Periderm and cortex regions of the root, C and D. Phloem, xylem, and pith regions of the root, pd: periderm; ph: phloem; x: xylem; p: parenchyma; pr: pith region; en: endodermis; prs: pericycle; ca: cambium.

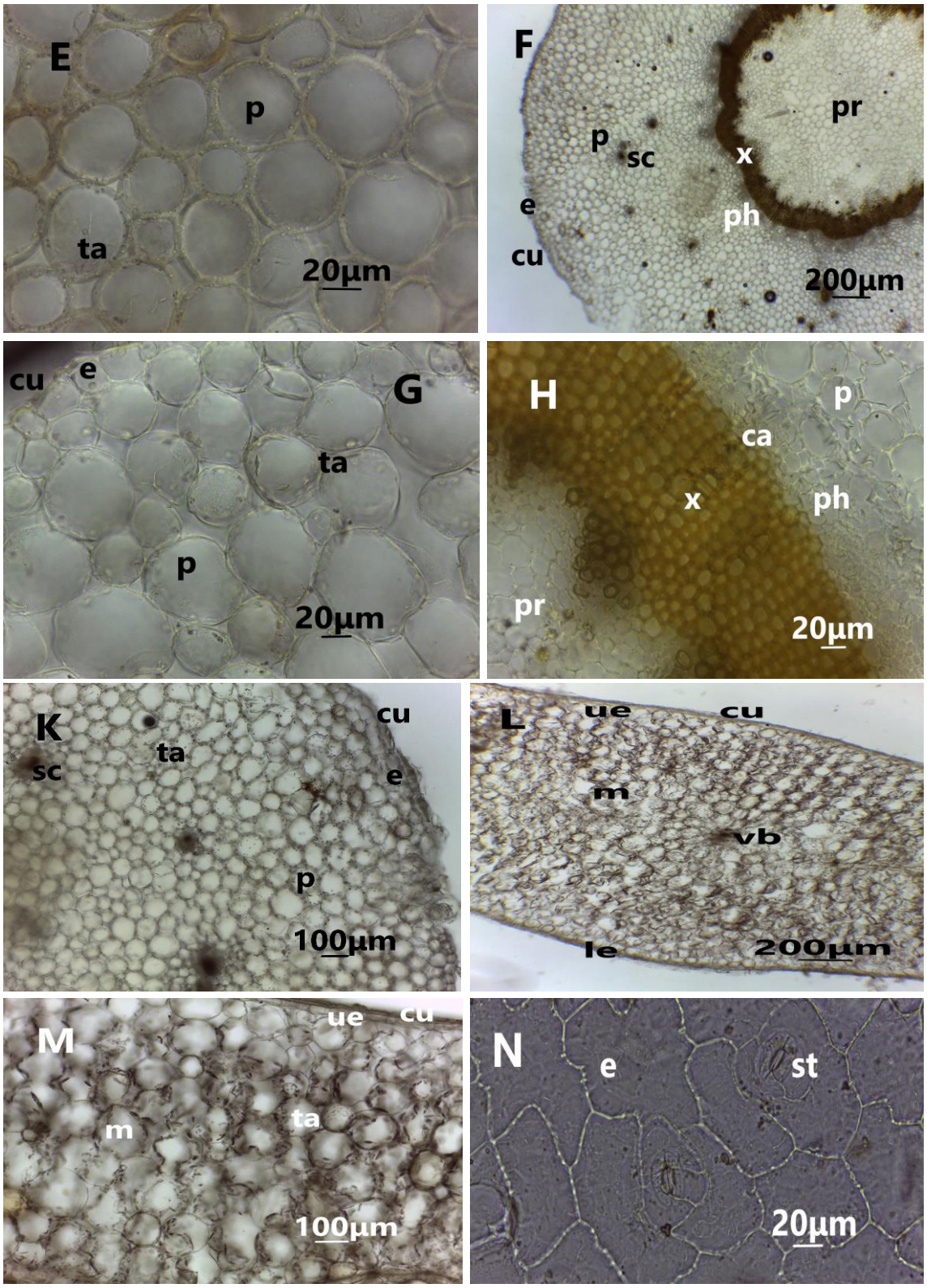

Figure 2. (Continued) Anatomical structures of vegetative and generative organs of *Sempervivum gillianiae*. E. Cortex region of the root, F. General structure of the stem, G and K. Epidermis and cortex regions of the stem, H. Phloem and xylem regions of the stem, L. General structure of rosette leaf, M. Mesophyll region of rosette leaf, N. Stomata of rosette leaf, ph: phloem; x: xylem; p: parenchyma; ta: tannin; pr: pith region; cu: cuticle; e: epidermis; ca: cambium; sc: secretory channels; m: mesophyll; vb: vascular bundle; ue: upper epidermis; le: lower epidermis; st: stomata.

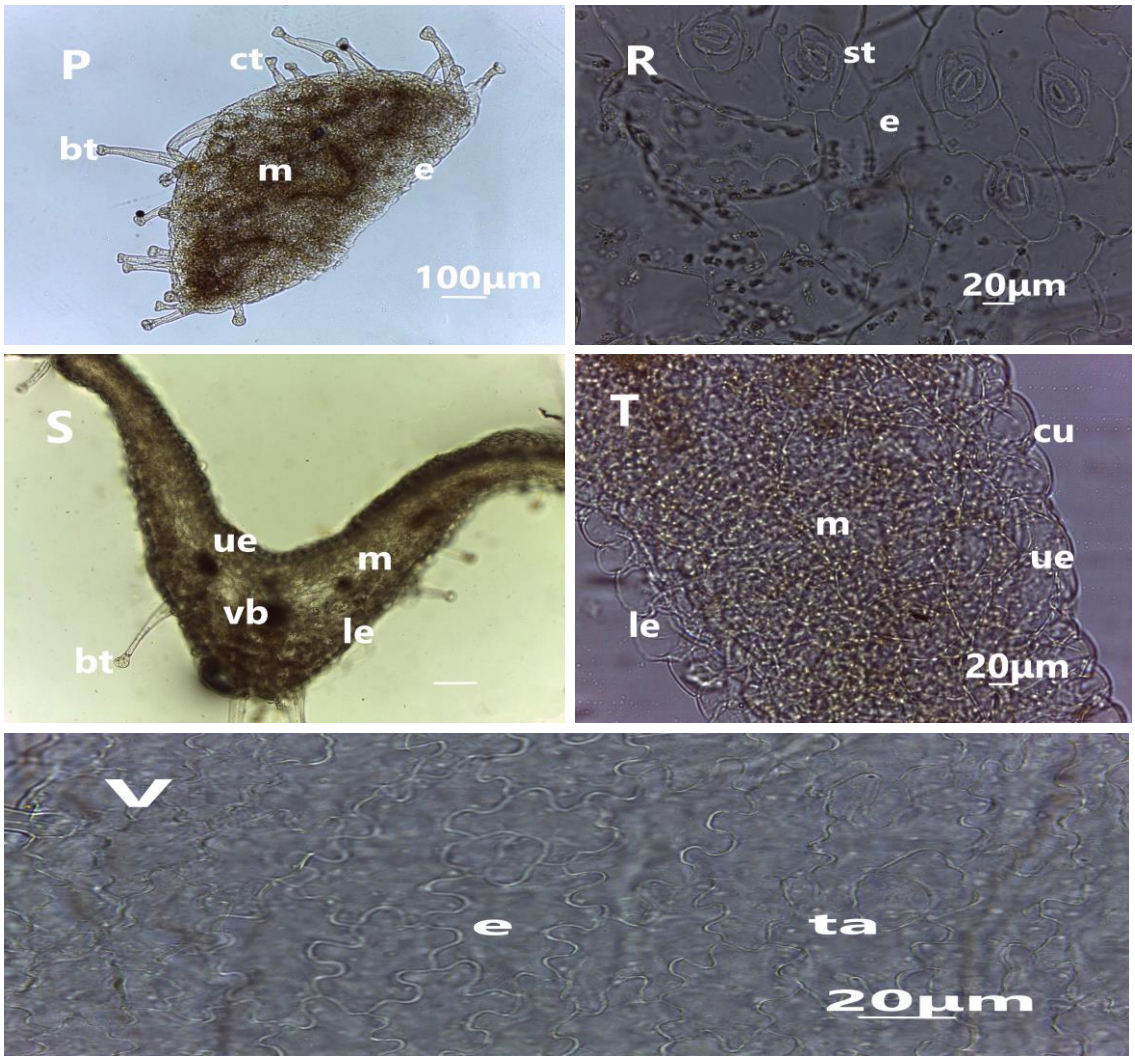

Figure 2. (Continued) Anatomical structures of vegetative and generative organs of *Sempervivum gillianiae*. P. General structure of sepal, R. Epidermis and stomata cells of sepal, S. General structure of petal, T. Epidermis and mesophyll region of petal, V. Epidermis cells of petals, ta: tannin; cu: cuticle; e: epidermis; m: mesophyll; vb: vascular bundle; ue: upper epidermis; le: lower epidermis; st: stomata; bt: multicellular biseriate trichome; ct: capitate trichome

In contrast, the anticlinal walls of the epidermis cells of species of the *S. ruthenicum* complex are straight and slightly undulate. Species of the *S. ciliosum* complex generally have longer and wider epidermis cells on both adaxial and abaxial surfaces. In the *S. ciliosum* complex, the highest number of epidermis cells was observed on the abaxial (lower) surface, while in the *S. ruthenicum* complex, the highest number of epidermis cells was observed on the adaxial (upper) surface. It was determined that the rosette leaves are amphistomatic, with anisocytic and scattered stomata in all species of analyzed complexes. However, there were differences in the length, width, and number of guard cells in stomata among species. It was reported that there is no significant difference in the length and width of the guard cells on the upper and lower surfaces of rosette leaves in individuals of the same species. The rosette leaves of species in the *S. ruthenicum* complex contain longer guard cells than those in the *S. ciliosum* complex. More numerous stomata were observed on the adaxial surface of the *S. ruthenicum* complex, while more stomata were observed on the abaxial surface of the *S. ciliosum* complex. In the examined taxa, the leaves are amphistomatic, and the stomata are anisocytic. It was determined that more stomata existed in the lower epidermis of the examined two taxa. Important distinguishing anatomical characters were detected between these two taxa in the length, shape, and wall structure of the upper and lower epidermis cells of the rosette leaf, the width and length of the stomata, and the wall structure of the neighboring cells of the stomata in the rosette leaves. These differences are also statistically significant

($p<0.05$). In this study, although the anticlinal walls of the cells adjacent to the stomata and the lower epidermis cells are slightly undulated in *S. gillianiae*, the edges of the cells adjacent to the stomata and the lower epidermis cells are straight in *S. brevipilum*. Thus, our data agrees with the data obtained by Jovanović et al. [42].

Vorobej et al. [39] determined the leaf anatomical structure of *S. globiferum* and reported that the leaves were amphistomatic, the stomata were anisocytic, and the leaves were unifacial regarding the mesophyll position, which is congruent with findings of this study.

Kirilenko [38] reported that the rosette leaves of *S. tectorum* have a single-layered epidermis on both the upper and lower surfaces, covered by a thin cuticle. Anisocytic stomata were also present on both surfaces but were more numerous on the lower epidermis. The rosette leaves were isolateral regarding the mesophyll structure. In other words, there was a weak differentiation between palisade and spongy parenchyma. The intercellular spaces in the mesophyll were quite large. The vascular bundles were quite small, and parenchymatic bundle sheaths were observed around them. Mucilage-containing cells were observed in the epidermis cells and mesophyll cells. Although some results of Krilenko [38] are compatible with our results (e.g., anisocytic type stomata), other results (e.g. isolateral mesophyll structure, large intercelluar spaces, mucilage-containing cells in the mesophyll) differ from our observations. This can be attributed to the distribution of taxa in habitats with different climates and soil conditions.

Shahrestani et al. [35] determined that the cells of the lower epidermis were larger compared to the ones in upper epidermis in *Sedum lencoranicum* Grossh., and *Sedum gracile* C.A. Mey. Hypodermis was observed in *Phedimus* sp., *Prometheum* sp., *Hylotelephium* sp., *S. lenkoranicum, Sedum rubens* L. and *Sedum annum*. The mesophyll was unifacial in all analyzed taxa. Large mucilaginous cells associated with parenchymatous cells were detected in *Sedum hispanicum* L., *Sedum pentapetalum* Boriss., *Sedum album*. Storage cells were found in the mesophyll (especially around the vascular bundles) in members of the *Phedimus* genus. Our findings (unifacial mesophyll) are parallel to the findings of Shahrestani et al. [35]. Although the taxa are in different genera, their similar anatomical features can be attributed to their growth in similar habitats and climatic conditions.

Ulcay [33] reported that the anticlinal walls of the epidermis cells were undulated in the leaf of *Sedum acre, S. pallidum* and *S. album*. The mesophyll tissue was undifferentiated and consisted of round-shaped parenchyma cells. In the center of the leaf of *S. acre*, the vascular bundles were regular, and the number of vascular bundles was 5-6. *Sedum album* exhibited 10–13 vascular bundles, whereas *S. pallidum* had 9–10 vascular bundles that were scattered. Anisocytic stomata was observed in all three taxa. It was determined that there were significant differences in the width and length of the stomata located in the upper and lower epidermis of the species. Similar leaf anatomical features mentioned above were also found in the examined *Sempervivum* species.

The leaf anatomical features of 15 *Kalanchoe* taxa were investigated by Abdel-Raouf [41]. The cuticle layer is thick in *Kalanchoe thrysiflora* Raym et Hamet, but the cuticle layer is thin in *K. beharensis* and most other examined species. Large epidermis cells were seen only in *K. beauverdii*, and hypodermis was seen in *K. beharensis* and *K. tubiflora*. Multicellular branched trichomes were also recorded in *K. tomentosa* and *K. beharensis*. Same author confirmed that mesophyll was generally homogenous in most analysed *Kalanchoe* species, with exception of *K. tomentosa* Baker and *K. beauveradii* that had heterogenous mesophyll. Storage cells were found in the mesophyll of *K. tubiflora*, secretory ducts in *K. marmorata* Baker, and druse crystals in some taxa of *K. beharensis*. The xylem is arranged in crescent-shaped in *K. tomentosa* and ring-shaped in other taxa. Although well-developed bundle sheaths are not found in CAM plants, collenchymatic bundle sheaths were found in the *Kalanchoe* taxa. In addition, Balsamo and Uribe [50] reported that the thickened cuticle, bundle sheath, and mesophyll are not differentiated as palisade and spongy parenchyma in the leaf of *K. dagremontiana.* Findings of this study are almost compatible with the results of Abdel-Raouf [41] and Balsamo and Uribe [50].

The leaf characters of succulent species *Crassula perforata, Crassula socialis* (Crassulaceae), *Senecio rowleyanus* H. Jacobsen, and *Senecio herreianus* Moritz Kurt Din. (Asteraceae) collected from extreme habitats were comparatively studied [34]. Many common features (characteristic features of the external structure, weak differentiation of the mesophyll, significant development of water-carrying tissue) and different features (type of leaf mesophyll, type of stomatal apparatus, degree of development of conductive system) resulting from adaptation to growth conditions were reported in taxa.

The structure of the leaf of *Kalanchoe pumila* was studied by Chernetskyy and Weryszko-Chmielewska [44]. In *K. pumila*, the amphistomatic leaf had a striated thick cuticle layer and a single-layered epidermis. Stomata were anisocytic. Vascular bundles were collateral, and bundle sheaths of parenchyma cells were seen around them. There was no palisade and sponge differentiation in the mesophyll layer. However, the mesophyll layer comprises large-celled (water-carrying, CAM-type) and small-celled mesophyll cells. Some of our findings (anisocytic stomata, unifacial mesophyll, collateral vascular bundles, amphistomatic leaves) are compatible with those of Chernetskyy and Weryszko-Chmielewska [44].

Moreira et al. [45] investigated the leaf anatomy of *Kalanchoe pinnata* Pers. and *Kalanchoe crenata* (Andrews) Haw. members growing in shade and sun. In *K. pinnata*, the anticlinal walls of the epidermis cells are undulate in both sun and shade members. However, these folds are more pronounced on the adaxial surface than on the abaxial surface in sun leaves. In sun leaves of *K. crenata*, the anticlinal walls of the epidermis cells are straight or slightly undulated on the adaxial surface while the anticlinal walls of the epidermis cells are undulated on the abaxial surface. In both species, stomata are anisocytic, and leaves are amphistomatic. It was observed that the rosette leaves of the studied *Sempervivum* species were amphistomatic, and the stomata were anisocytic. The members growing in shade and sun of both *Kalanchoe* species have more stomata on the abaxial surface than on the adaxial. Epidermis cells on the leaf margins are larger than those in other parts of the leaf. The epidermis is covered with a thin cuticle. The epidermis of the forms of *K. pinnata* growing in sun conditions was found to be thicker than those of shade plants. However, no significant differences were observed in epidermis thickness characteristics in members of *K. crenata* growing in sun and shade. The mesophyll of both species is homogeneous. The mesophyll thickness was determined to be greater in sun plants due to the collenchyma layer. Hydathodes were observed at the edges of the leaf lamina of both species. As a result, some differences were determined despite the similarities in the anatomical features of these two species (*K. pinnata* and *K. creneta*).

When the cross-sectional of sepals were examined, large, rectangular-shaped lower and upper epidermis cells were obtained in both taxa. The anticlinal walls of the epidermis cells in *S. brevipilium* were slightly undulate, while the anticlinal walls of the epidermis cells were straight in *S. gillianiae*. The mesophyll tissue of sepals was composed of 10-12 layered, ovoid, large parenchyma cells in *S. brevipilium* and 5-6 layered, small parenchyma cells in *S. gillianiae* (Figures 1 P, R and Figures 2 P, R). Vascular bundles were seen in the mesophyll tissue of both taxa. The stomata of both taxa are anisocytic (Figure 1 S and Figure 2 R).

Regarding the anatomical features of the petals, in *S. brevipilum* anticlinal walls of the epidermis cells are very undulate (Figure 1 X), cells are quadrangulary shaped, and the cuticle is thick and densely micropapillated, while in *S.gillianiae*, the anticlinal walls of the epidermis cells are undulate (Figure 2V), cells are quadrangulary shaped, the cuticle is of medium thickness and micropapillated. The mesophyll tissue between the two epidermis layers comprises of 8-10 layered, oval-shaped, large, and small parenchyma cells in *S. brevipilum* (Figures 1 T, V and W). In *S. gillianiae*, the mesophyll tissue comprises of 8-9 layered, large, and small, oval-shaped parenchymatic cells (Figures 2 S, T). In both taxa, there are vascular bundles in the mesophyll. The differences in epidermal traits of flower part were found to be smaller compared to differences in vegetative parts. This could be explained by the less pronounced phenotypic plasticity of generative organs

The number of tannins in the roots, stems, rosette leaves, and flowers of analyzed taxa were determined as gallic acid equivalent (GAE, mg/mL) using the Folin-Denis method. However, it was found that there were differences in tannin amounts between vegetative and generative organs. The highest tannin content was found

in flowers in both taxa. The amount of tannin in both *S. brevipilum* and *S. gillianiae* flowers was calculated as 0.45 ± 0.02 mg/mL GAE (Figure 3).

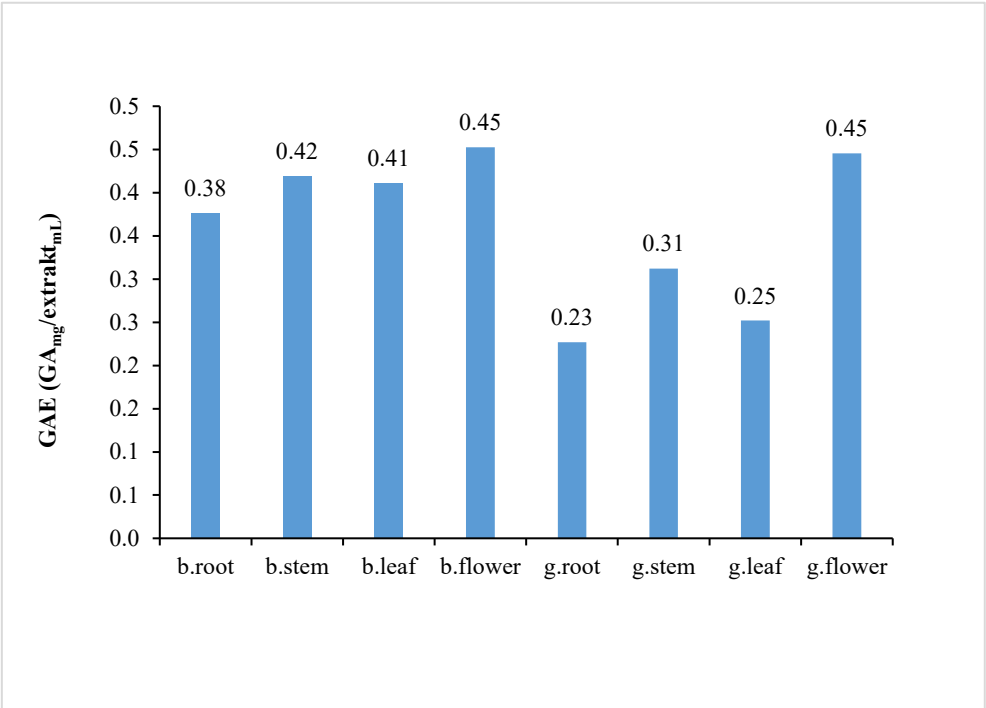

Figure 3. Tannin contents in vegetative and generative organs of *S. brevipilum* and *S. gillianiae*. b.root, b.stem, b.leaf, b.flower values of *S. brevipilum*. g.root, g.stem, g.leaf, g. flower values of *S. gillianiae*

Shahrestani et al. [35] reported that tannin storage cells in petioles and leaves provided important taxonomic evidence. In *K. pumila* leaves, anthocyanin pigments, tannin, epicuticular wax, and calcium deposits were seen. These structures serve to protect the leaves against harsh environmental conditions [44]. It was reported that there were differences in the distribution of phenolic compounds, especially in the subepidermal layer. It was stated that these different features could help identify species at the anatomical level and, therefore, the quality control of herbal medicines made by *K. pinnata* and *K. creneta* [45]. Tannins were found in all individuals of *Echeveria* aff. *gigantea* (a complex species) Rose and Purpus, especially in the epiderma, mesophyll, and vascular bundles of leaves. The distribution and amounts of tannins were essential in separating some forms of *E. gigantea* [48]. Metcalfe and Chalk [26] suggested that tannin cells were commonly found in non-woody stems, especially in the cortex, pith, and phloem of the Crassulaceae family. Proanthocyanidins (condensed tannins) are widely seen in the Crassulaceae family's herbaceous and woody taxa [2]. Stevens et al. [27] compared the alkaloid and tannin levels of 36 species of the Crassulaceae family. Tannins were found in *Crassula multicava*, *Echeveria venezuelensis, Pachyphytum* sp., *Compactum* sp., *Kalanchoe* sp., *Bryophyllum daigremontianum, Sedum* sp., *Aeonium* sp. and *Sempervivum* sp. Steven et al. [27] suggested that there is a dichotomy between the distribution of alkaloids and tannins, which is in good agreement with the major evolutionary trends within the family as inferred from chloroplast DNA restriction site variation. The distribution of tannins was reported as similar in the three *Sempervivum* taxa (S. *globiferum, S. tectorum,* and *S. ruthenicum*) [39]. Our findings regarding tannins support the tannin findings related to the family [26, 27, 35, 44, 45].

4. Conclusion

Consequently, the layer number of periderm, cortex layers in the root, the width and length of the periderm, the trachea diameter and the parenchyma cell diameter of the cortex, whether the tannins are dense or not, the cuticle layer structure in the stem and the presence or absence of micropapillae, number of cortex layers, straight or undulate xylem, epidermis cell diameter, pith parenchyma and xylem trachea diameter, cuticle

thickness, mesophyll parenchyma diameter, width and length of stomata, the length, shape and anticlinal walls structure of the upper and lower epidermis cells in the rosette leaves, the number of layers and shape of the mesophyll in the rosette leaf and sepal, the margin structure of ordinary irregularly shaped cells next to the stomata in the sepal and rosette leaves, length of upper epidermis cell in sepals, width and length of lower epidermis cell, the thickness or thinness of the cuticle layer in the petals, petal epidermis cell diameter, anticlinal walls structure of epidermis cell and the number of layers of the mesophyll in the petal, amount of tannin in vegetative organs were identified as important distinguishing anatomical characters between the two taxa. Moreover, differences in anatomical features were found to be statistically significant ($p<0.05$) (Table 4). At the same time, some important differences were reported in the morphological and trichomes characteristics of the vegetative and generative organs of these two taxa by Şahin and Kandemir [51, 52]. This study determined that the data on anatomical features obtained from the vegetative and generative organs of the *S. brevipilum* and *S. gillianiae* were congruent with the data obtained for other members of the Crassulaceae family and the *Sempervivum* genus. On the other hand, it has been emphasized in earlier studies that some anatomical features should be considered in solving some taxonomic problems between species and genera. Especially the anatomical features of stems and leaves are widely used as important distinguishing taxonomic characters in species classification [36, 37, 53-55]. It is recommended that detailed molecular (especially chloroplast DNA studies) and chromosome morphology studies be conducted on these two endemic taxa and other *Sempervivum* members in the future. Due to the tannin content in their vegetative and generative organs, the studied taxa are thought to have antioxidant and antimicrobial properties. Therefore, conducting antimicrobial and antioxidant studies on the taxa is deemed appropriate. The examined taxa have the potential to be used as ornamental plants (rock gardens and wall landscaping) due to their rosette structures and different colors of rosette leaves.

Author Contributions

All the authors equally contributed to this work. This paper is derived from the first author's master's thesis, supervised by the second author. They all read and approved the final version of the paper.

Conflict of Interest

All the authors declare no conflict of interest.

Ethical Review and Approval

No approval from the Board of Ethics is required.

References

[1] S. A. Sponberg, *The genera of Crassulaceae in the southeastern United States*, Journal of the Arnold Arboretum 59 (1978) 198–248.

[2] J. Thiede, U. Eggli, C*rassulaceae*, in: K. Kubitzki (Ed.), Families and Genera of Vascular Plants, Flowering Plants Eudicots, Springer, Hamburg, 2007, Ch. IX, pp. 83–118.

[3] M. E. Mort, D. E. Soltis, P. S. Soltis, J. Francisco-Ortega, A. Santos-Guerra, *Phylogenetic relationships and evolution of Crassulaceae inferred from matK sequence data,* American Journal of Botany 88 (1) (2001) 76–91.

[4] C. R. Metcalfe, L. Chalk, Anatomy of Dicotyledons, Claredon Press, Oxford 1972.

[5] L. C. Jensen, *Primary stem vascular patterns in three subfamilies of the Crassulaceae*, American Journal of Botany 55 (5) (1968) 553–563.

[6] R. C. Van Ham, H. ′τ Hart, *Phylogenetic relationships in the Crassulaceae inferred from chloroplast DNA restriction-site variation*, American Journal of Botany 85 (1998) 123–134.

[7] F. Karaer, F. Celep, *Taxonomic notes on Sempervivum armenum Boiss. and A. Huet (Crassulaceae) from Turkey with an amended description*, Bangladesh Journal of Botany 39 (2010) 103–105.

[8] F. Karaer, F. Celep, U. Eggli, *A taxonomic revision of the Sempervivum davisii complex (Crassulaceae)*, Nordic Journal of Botany 29 (2011) 49–53.

[9] J. T. Klein, J. W. Kadereit, *Phylogeny, Biogeography, and Evolution of Edaphic Association in the European Oreophytes, Sempervivum and Jovibarba (Crassulaceae)*, International Journal of Plant Sciences 176 (2015) 44–71.

[10] J. T. Klein, J W. Kadereit, *Allopatric hybrids as evidence for past range dynamics in Sempervivum (Crassulaceae), a western Eurasian high mountain oreophyte*, Alpine Botany 126 (2016) 119–133.

[11] H. ′τ Hart, B. Bleij, B. Zonneveld, *Sempervivum*. in: U. Eggli (Ed.), Illustrated handbook of succulent plants: Crassulaceae, Springer Verlag, Berlin, 2003, pp. 332–349.

[12] K. Topalov, M. E. Mort, P. Neeff, D. Lakušić, B. Zlatković, *Preliminary phylogenetic analyses of Sempervivum L. (Crassulaceae) inferred from DNA sequence data*, in: Botany 2006 Conference Abstract, Chico, 2006, pp. 300.

[13] C. W. Muirhead, Turkish species of *Sempervivum*, Notes from the Royal Botanic Garden Edinburgh 29 (1969) 15–28.

[14] C. W. Muirhead, *Sempervivum* L., in: P.H. Davis (Ed.), Flora of Turkey and East Aegean Islands, Edinburgh University, Edinburg, 1972, pp. 209–248.

[15] P. Neeff, *Neue Taxa der Gattung Sempervivum (Crassulaceae) in der Türkei*, Kakteen und andere Sukkulenten 56 (3) (2005) 71–72.

[16] F. Karaer, F. Celep, *Sempervivum ekimii nom. et stat. nov. for S. minus var. glabrum (Crassulaceae), with an amplified description,* Annales Botanici Fennici 45 (3) (2008) 229–232.

[17] Y. Kobiv, R. Kish, R. Hleb, *Sempervivum marmoreum Griseb. (Crassulaceae) in the Ukrainian Carpathians: distribution, morphology, coenotic conditions, population parameters, and conservation*, Ukrainian Botanical Journal 64 (1) (2007) 22–29.

[18] D. Sarı, *Investigation of some species from the Crassulaceae family distributed in the flora of Türkiye in terms of landscape and ornamental plant qualities*, in: I. Cengizler, S. Duman (Eds.), Research and Evaluations in Agriculture, Forestry and Aquatic Products–I, Night library, 2021, Ch. 19, pp. 292–313.

[19] R. Novaretti, D. Lemordant, *Plants in the traditional medicine of the Ubaye Valley*, Journal of Ethnopharmacology 30 (1) (1990) 1–34.

[20] Z. Giczi, B. Sik, V. Kapcsandi, E. Lakatos, A. Mrazik, R. Szekelyhidi, Determination of the health-protective effect of different *Sempervivum* and *Jovibarba* species, Journal of King Saud University-Science 36 (1) (2024) 102998.

[21] A. Alberti, S. Beni, E. Lacko, P. Riba, M. Al-Khrasani, A. Kery, *Characterization of phenolic compounds and antinociceptive activity of Sempervivum tectorum L. leaf juice*, Journal of Pharmaceutical and Biomedical Analysis 70 (2012) 143–150.

[22] D. Stojković, L. Barros, J. Petrović, J. Glamoclija, C. Santos-Buelga, I. Ferreira, M. Soković, *Ethnopharmacological uses of Sempervivum tectorum L. in southern Serbia: Scientific confirmation for the use against otitis linked bacteria*, Journal Ethnopharmacol 176 (2015) 297–304.

[23] E. Yeşilada, E. Sezik, G. Honda, Y. Takaishi, Y. Takeda, T. Tanaka, *Traditional medicine in Turkey IX: folk medicine in north-west Anatolia*, Journal Ethnopharmacol 64 (1999) 195–210.

[24] N. Kahriman, Z. Şenyürek, V. Serdaroğlu, A. Kahriman, N. Yayli, *Chemical composition and biological activity of essential oils of Sempervivum brevipilum Muirhead*, Records of Natural Products 9 (4) (2015) 603–608.

[25] N. Silanikove, A. Perevoltsky, F. D. Provenza, Use of tannin-binding chemicals to assay tannins and their negative post ingestive effects in ruminants, Animal Feed Science and Technology 91 (2001) 69–81.

[26] C. R. Metcalfe, L. Chalk, Anatomy of the Dicotyledons I, Oxford University, 1950.

[27] J. F. Stevens, H. T. Hart, R. C. Van Ham, E. T. Elema, M. M. Van Den Ent, M. Wildeboer, Z. H. Zwaving, *Distribution of alkaloids and tannins in the Crassulaceae*, Biochemical Systematics and Ecology 23 (2) (1995) 157–165.

[28] U. Eggli, Sukkulentenlexikon, Crassulaceae (Dickblattgewächse) (in German), Herausgegeben in Zusammenarbeit mit der Internationalen Organisation für Sukkulenten-Forschung (IOS), Eugen Ulmer Verlag, Stuttgart, 2003.

[29] S. Çelebioğlu, T. Baytop, A new reagent for microscopical investigation of plant, Publication of the Institute of Pharmacognosy, 1949.

[30] V. L. Singleton, R. Orthofer, R. M. Lamuela-Raventos, *Analysis of total phenols and other oxidation substrates and antioxidants by means of Folin-Ciocalteu reagent*, Methods in Enzymology 299 (1999) 152–178.

[31] F. Bärlocher, M. A. S. Graça, *Total Phenolics*, in: M. A. S. Graça, F. Bärlocher, M. O. Gessner (Eds.), Methods for Studying Litter Decomposition, Springer International Publishing, 2020, Ch.14, pp. 155–160.

[32] M. Ardelean, I. Stanescu, D. Cachita-Cosma*, Sedum telephium L. spp. maximum (L.) Krock. Histo-anatomical aspects on the vegetative organs*, Scientific Annals of Alexandru Ioan Cuza University of Lasi, New Series 55 (2009) 75–80.

[33] S. Ulcay, *Comparative anatomy of some Sedum species (Crassulaceae) in Turkey and distinguishing characteristics of these species*, Journal of Animal and Plant Sciences 33 (1) (2023) 95–102.

[34] N. A. Kirilenko, *Anatomical and morphological features of the vegetative organs of succulent plants regards growth conditions*, Ukrainian Journal of Ecology 8 (1) (2018) 509–515.

[35] M. M. Shahrestani, M. B. Faghir, M. Assadi, *Comparative anatomical studies in relation to taxonomy of Sedum sl. (Crassulaceae) in Iran*, Turkish Journal of Botany 44 (3) (2020) 281–294.

[36] N. Kandemir, A. Çelik, F. Ullah, *Comparative micro-anatomical features of endemic Fritillaria taxa growing in the Mediterranean region (Turkey)*, Flora 290 (2022) 152049.

[37] N. Kandemir, A. Çelik, S. N. Shah, G. Albasher, M. Iqbal, *Taxonomic relevance of stem and leaf anatomy in 10 endemic Fritillaria species from the Mediterranean Region*, Flora 310 (2024) 152444.

[38] N. A. Kirilenko, *Structural peculiarities of vegetative organs of Sempervivum tectorum L. (Crassulaceae) and Salicornia europaea L. (Chenopodiaceae) – residents of extreme habitats*, Journal of Education, Health and Sport 6 (9) (2016) 883–892.

[39] P. Vorobej, O. Futorna, I. Olshanskyi, S. Zhygalova, O. Bezsmertna, *Micromorphological study (anatomical structure of lamina surface, ultrastructure of seeds) of Sempervivum globiferum L*, Ecological Sciences 1 (28) (2020) 316–323.

[40] A. I. Akhmetzhanova, A. K. Auyelbekova, D. K. Kyzdarova, *The anatomic characteristic of a Sedum acre L, caustic from various ecological conditions of South and the Central Kazakhstan,* Bulletin of the Karaganda University Biology Medicine Geography Series 3 (83) (2016) 43–48.

[41] H. S. Abdel-Raouf, *Anatomical traits of some species of Kalanchoe (Crassulaceae) and their taxonomic value*, Annals of Agricultural Sciences 57 (1) (2012) 73–79.

[42] M. Jovanović, D. Lakušić, B. Lakušić, B. Zlatković, *Diversification of yellow-flowered Sempervivum (Crassulaceae) species from the Balkan Peninsula: evidence from the morphometric study of the epidermal structures of rosette leaves*, Botanica Serbica, 45 (2) (2021) 163–176.

[43] E. Weryszko-Chmielewska, M. Chernetskyy, *Structure of trichomes from the surface of leaves of some species of Kalanchoe Adans*, Acta Biologica Cracoviensia Series Botanica 47 (2) (2005) 15–22.

[44] M. Chernetskyy, E. Weryszko-Chmielewska, *Structure of Kalanchoe pumila Bak. leaves (Crassulaceae DC.)*, Acta Agrobotanica 61 (2) (2008) 11–24.

[45] N. S. Moreira, L. B. S. Nascimento, M. V. Leal-Costa, E. S. Tavares, *Comparative anatomy of leaves of Kalanchoe pinnata and K. crenata in sun and shade conditions, as a support for their identification*, Revista Brasileira de Farmacognosia 22 (5) (2012) 929–936.

[46] M. Chernetskyy, *The role of morpho-anatomical traits of the leaves in the taxonomy of Kalanchoideae Berg. Subfamily (Crassulaceae DC.)*, Modern Phytomorphology 1 (2012) 15–18.

[47] B. Zlatković, Z. S. Mitić, S. Jovanović, D. Lakušić, B. Lakušić, J. Rajković, G. Stojanović, *Epidermal structures and composition of epicuticular waxes of Sedum album sensu lato (Crassulaceae) in Balkan Peninsula*, Plant Biosystems-An International Journal Dealing with all Aspects of Plant Biology 151 (6) (2017) 974–984.

[48] E. Sandoval-Zapotitla, D. M. Martinez-Quezada, J. Reyes-Santiago, M. D. L. A. Islas-Luna, U. Rosas, *Leaf morpho-anatomical diversity in Echeveria aff. gigantea (Crassulaceae)*, Botanical Sciences 97 (2) (2019) 218–235.

[49] J. Thiede, *Quantitative phytogeography, species richness, and evolution of American Crassulaceae*, in: H. $'\tau$ Hart, U. Eggli (Eds.), Evolution and systematics of the Crassulaceae, Backhuys, Leiden,1995, Ch. 6, pp. 89–123.

[50] R. A. Balsamo, E. G. Uribe*, Leaf anatomy and ultrastructure of the Crassulacean-acid-metabolism plant Kalanchoe daigremontiana*, Planta 173 (1988) 183–189.

[51] T. Şahin, N. Kandemir, *Glandular trichomes on the vegetative and generative organs of endemic two Sempervivum taxa*, Journal of New Result in Science 14 (1) (2025) 48–61.

[52] T. Şahin, N. Kandemir, *Comparison of morphological characters in vegetative and generative organs of endemic two Sempervivum L. taxa (Crassulaceae) in Türkiye*, International Journal of Agricultural and Natural Sciences 18 (1) (2025) 19–32.

[53] N. Kandemir, A. Çelik, S. N. Shah, A. Razzaq, *Comparative micro-anatomical investigation of genus Heliotropium (Boraginaceae) found in Turkey*, Flora 262 (2020) 151495.

[54] K. V. Koçak, N. Kandemir, *Taxonomic importance of anatomical, ecological and trichome features of Marrubium astracanicum subsp. astracanicum Jacq*. (Lamiaceae), Black Sea Journal of Engineering and Science 6 (3) (2023) 199–209.

[55] K. V. Koçak, N. Kandemir, *Anatomical, ecological and trichome micro-morphological features of two Marrubium L. taxa (Lamiaceae)*, Black Sea Journal of Engineering and Science 7(1) (2024) 43–54.

Journal of Advanced Research in Natural and Applied Sciences
dergipark.org.tr/tr/pub/jarnas
Open Access

ISSN: 2757-5195 11 (2) (2025) 175-186 doi.org/10.28979/jarnas.1658029

Soft Sequences and Their Application to NC-Backgammon

Naim Çağman[1], Nizam Doğan Çınar[2]

Article Info
Received: 14 Mar 2025
Accepted: 03 Jun 2025
Published: 30 Jun 2025
Research Article

Abstract— Soft set theory was defined by Molodtsov in 1999 to model problems involving uncertainty. In this study, soft sequences are defined as a special case of soft sets. It is defined as a function from the set of positive integers to the power set of a universe. As a new concept, connected and disconnected soft sequences, chained soft sequences, centered soft sequences, increasing soft sequences, decreasing soft sequences, and ordered soft sequences are defined. Finally, soft sequences are applied to game theory. Using chained soft sequences, no chance (NC) backgammon —a zero-sum, strategic, and intelligence game — is played.

Keywords — *Soft set, soft sequence, connected soft sequence, NC-backgammon, game theory*

1. Introduction

The concept of soft sets was first introduced by Molodtsov in 1999 as a mathematical framework to model uncertainties [1]. Soft sets classify a given group of objects based on parameters that characterize these objects, with the classification being determined by decision-makers. The softness in soft sets arises from the fact that the classification depends on the discretion of the decision-makers. Due to this softness, the soft set defined by each decision-maker, even when using the same set of parameters and objects, will differ.

Aktaş and Çağman [2] laid the groundwork for exploring the algebraic structure of soft set theory by introducing the concept of soft groups. Following their work, several studies have contributed to the algebraic aspects of soft sets [3–5]. The application of soft sets to decision-making began with Maji and Roy [6], and since then, numerous studies have been conducted on soft decision-making methods [7–9]. Soft sets have since found applications in nearly all areas of mathematics, including topology [10–12] and analysis [13–15].

Recently, Reddy et al. [16] have proposed soft sequences. Afterward, subsequent studies on soft sequences have been conducted [17–21]. The soft sequences therein are based on soft numbers on real numbers. In this study, we define soft sequences as a special case of soft sets. A soft sequence is described as a mapping from the set of positive integers to the power set of a universe. As a new contribution, several types of soft sequences are introduced and defined, including connected and disconnected soft sequences, chained soft sequences, centered soft sequences, increasing soft sequences, decreasing soft sequences, and ordered soft sequences. Soft sequences are then applied to game theory,

[1]naim.cagman@gop.edu.tr; [2]nizamdogancinar@gmail.com (Corresponding Author)
[1]Department of Mathematics, Faculty of Arts and Science, Tokat Gaziosmanpaşa University, Tokat, Türkiye
[2]School of Graduate Studies, Tokat Gaziosmanpaşa University, Tokat, Türkiye

a branch of mathematics widely used in economics and decision-making processes to analyze strategic interactions. Game theory examines scenarios where individuals, groups, or organizations, referred to as players, attempt to determine the best strategy by considering the decisions of others. It has applications in various fields, including economics, political science, biology, psychology, and computer science. For an overview of game theory, its types, and application areas, [22] is recommended.

The dependence of soft sets on human discretion makes them particularly suitable for adaptation to game theory. Deli and Çağman [23, 24] were the first to adapt soft sets to game theory. They defined soft two-person games applicable to problems involving uncertainty, extended these games to n-person scenarios, and generalized them to fuzzy soft games. They introduced solution methods for these games, such as fixed-point, elimination, lower and upper value, dominant strategy, Nash equilibrium, and probabilistic solution methods based on soft sets.

Çağman defined no-chance (NC) backgammon [25] as a two-person, zero-sum, strategic game with perfect information and intelligence. For those interested in learning more about NC-backgammon and its rules, [25–27] are recommended for consultation.

Section 2 of the present study provides some notions to be required in the following section. Section 3 presents the definitions and properties of soft sequences. Section 4 introduces the definitions and properties of connected soft sequences. Section 5 defines the application of soft sequences to game theory through the utilization of chained soft sequences for the modeling of the NC-backgammon game. The final section discusses potential directions for future studies.

2. Soft Sets

Molodtsov first defined soft sets [1]. Considering the symbols and notations in the Çağman [28] source, this section has been prepared. Refer to [1, 28–30] for basic information about soft sets.

Definition 2.1. Let U be a universal set, $P(U)$ be the power set of U, and E be the parameters characterizing the elements of the universal set. F is called a soft set over U if and only if F is a mapping of E into the $P(U)$ as follows:

$$f : E \to P(U), \quad F = \{(e, f(e)) : e \in E\}$$

If $f(e) = \emptyset$, $(e, f(e))$ is not written as an element in the soft set F.

Here, the function f is called the approximation function of the soft set F. The set $f(e)$ for each $e \in E$ is called the e-approximation value set or e-approximation set. The softness of the soft set comes from the fact that e-approximation sets vary from person to person, that is, they depend on the decision makers.

Example 2.2. Let $U = \{u_1, u_2, u_3, ..., u_{30}\}$ be the set of students in a class, and $E = \{e_1, e_2, e_3, e_4\}$ be the set of parameters characterizing the students. Here, let be the students e_1, tall, e_2, hard-working, e_3, athletic, e_4, with glasses. For a A person: if tall students are $\{u_1, u_3, u_5\}$, then $f(e_1) = \{u_1, u_3, u_5\}$, if hard-working students are $\{u_1, u_4\}$, then $f(e_2) = \{u_1, u_4\}$, if the athletic students are $\{u_1, u_2, u_3\}$, then $f(e_3) = \{u_1, u_2, u_3\}$, if the students with glasses are $\{u_1, u_5\}$, then $f(e_4) = \{u_1, u_5\}$. In this case, the soft set F_A formed by person A is obtained as:

$$F_A = \{(e_1, \{u_1, u_3, u_5\}), (e_2, \{u_1, u_4\}), (e_3, \{u_1, u_2, u_3\}), (e_4, \{u_1, u_5\})\}$$

3. Soft Sequences

This section defines soft sequences and examines their basic properties. Throughout this study, U is a universal set and 2^U is the power set of U.

Definition 3.1. A soft sequence (a_n) over the universe U is defined by soft sets $(a_n) = (a_1, a_2, ..., a_n, ..)$ where $a_n : \mathbb{Z}^+ \to 2^U$.

Here, the set of positive integers $\mathbb{Z}^+$ is called the index set of the soft sequence, respectively the soft sets $a_1, a_2, ..., a_n, ...$ are called the first, second,..., n-th term of the soft sequence and the a_n term is called the general term of the soft sequence.

Example 3.2. Let $U = \{u_1, u_2, ..., u_n, ...\}$ be a universal set. Here, the general terms of some soft sequences over U are defined:

i. $a_n :=$ It is a set with n elements

ii. $b_n :=$ It is a set containing u_2

iii. $c_n :=$ It is a set with 3 elements

iv. $d_n :=$ It is a set containing at most two elements

v. $e_n :=$ It is a set with infinite elements

vi. $f_n := \{u_{i\times n} : i \in \mathbb{Z}^+\}$

Let the conditions of the (a_n) sequence be written here according to a decision maker. According to this decision maker:

Let the term a_1 be $\{u_7\}$, one of the elements of 2^U with 1 elements, the term a_2 be $\{u_1, u_{100}\}$, one of the elements of 2^U with 2 elements, the term a_3 be $\{u_9, u_{117}, u_{2059}\}$, one of the elements of 2^U with 3 elements, and let it continue like this. In this case, the soft sequence (a_n) over U is obtained as:

$$(a_n) = (a_1, a_2, a_3, ...) = \Big(\{u_7\}, \{u_1, u_{100}\}, \{u_9, u_{117}, u_{2059}\}, ...\Big)$$

Other soft sequences (b_n), (c_n), (d_n), (e_n) and (f_n) are obtained in a similar way.

Definition 3.3. Let U be the universal set, 2^U the power set of U, and A a finite subset of the set of positive integers. Defined from the set A to the set 2^U, where $|A| = k$

$$a_n : A \to 2^U$$

the soft set is called a finite soft sequence over U and it is represented as an ordered k-number

$$(a_n) = (a_1, a_2, ..., a_k)$$

Example 3.4. Let $U = \{u_1, u_2, ..., u_9\}$ be the set of contestants who will participate in a competition and let $A = \{1, 2, 3\}$ be the set of degrees the contestants will receive. General term of soft sequence (a_n) defined as:

$a_n :=$ It is the set of contestants who have the possibility of coming n-th in a competition

According to a juror: if the set of contestants who can come first is $\{u_3, u_4\}$, then $a_1 = \{u_3, u_4\}$, if the set of contestants who can come second is $\{u_2, u_7, u_9\}$, then $a_2 = \{u_2, u_7, u_9\}$, if the set of contestants who can comes third is $\{u_8\}$, it becomes $a_3 = \{u_8\}$. In this case, the finite soft sequence (a_n) is obtained as follows:

$$(a_n) = \Big(\{u_3, u_4\}, \{u_2, u_7, u_9\}, \{u_8\}\Big)$$

Definition 3.5. A soft sequence (a_n) over U is said to be an empty soft sequence, if $a_n = \emptyset$ for all $n \in \mathbb{Z}^+$.

Example 3.6. (a_n) is an empty soft sequence on $\mathbb{Z}$, whose general term is defined as $a_n = \{x : 2^{nx} < 0\}$.

Definition 3.7. A soft sequence (a_n) over U is said to be a constant soft sequence, if all terms of (a_n) are equal to each other.

Example 3.8. (a_n) is a constant soft sequence over $U = \{u_1, u_2, ...\}$, whose general term is defined as $a_n = \{u_1, u_2\}$.

Definition 3.9. A soft sequence (a_n) over U is said to be universal soft sequence, if $a_n = U$ for all $n \in \mathbb{Z}^+$.

Definition 3.10. Soft sequences (a_n) and (b_n) over U are said to be equal soft sequences, denoted by $(a_n) = (b_n)$, if $a_n = b_n$, for all $n \in \mathbb{Z}^+$.

Example 3.11. Let $U = \{-1, 1\}$ is the set of objects, $a_n = \{(-1)^n\}$ and $b_n = \{\cos n\pi\}$ defined over U, then $(a_n) = (b_n)$ since $(a_n) = (\{-1\}, \{1\}, \{-1\}, \{1\}, ...)$ and $(b_n) = (\{-1\}, \{1\}, \{-1\}, \{1\}, ...)$.

Definition 3.12. Let (a_n) and (b_n) soft sequences over U. Then, intersection of (a_n) and (b_n), denoted by $(c_n) = (a_n) \cap (b_n)$, is a soft sequence over U whose terms are defined by $c_n = a_n \cap b_n$.

Definition 3.13. Let (a_n) and (b_n) soft sequences over U. Then, union of (a_n) and (b_n), denoted by $(d_n) = (a_n) \cup (b_n)$, is a soft sequence over U whose terms are defined by $d_n = a_n \cup b_n$.

Definition 3.14. Let (a_n) be a soft sequence over U. Then, complement of the soft sequence (a_n) denoted by $(a_n)^\circ$, is a soft sequence over U whose terms are defined by $a_n^{'} = U - a_n$.

Here, $(\circ)$ is used for soft sequence complement, while $(')$ is used for set complement.

Example 3.15. Let the set of objects $U = \{u_1, u_2, u_3, u_4, u_5, u_6\}$, $A = \{1, 2, 3, 4\}$, and the soft sequences (a_n) and (b_n) defined over U. For $A = \{1, 2, 3, 4\}$, (a_n) and (b_n) are written as:

$$(a_n) = \Big(\{u_2, u_4, u_6\}, \{u_1, u_2, u_3\}, \{u_1, u_3, u_5\}, \emptyset\Big)$$

and

$$(b_n) = \Big(\{u_1, u_2\}, \{u_1, u_3, u_4, u_5, u_6\}, \{u_2, u_6\}, \{u_1, u_4\}\Big)$$

Terms of the soft sequence $(c_n) = (a_n) \cap (b_n)$ the intersection of the (a_n) and (b_n) is found as:

$$c_1 = a_1 \cap b_1 = \{u_2\}, \quad c_2 = a_2 \cap b_2 = \{u_1, u_3\}, \quad c_3 = a_3 \cap b_3 = \emptyset, \quad c_4 = a_4 \cap b_4 = \emptyset$$

And it is written as:

$$(c_n) = (a_n) \cap (b_n) = \Big(\{u_2\}, \{u_1, u_3\}, \emptyset, \emptyset\Big)$$

Terms of the soft sequence $(a_n) \cup (b_n)$ the union of the (a_n) and (b_n) is found as:

$d_1 = a_1 \cup b_1 = \{u_1, u_2, u_4, u_6\}$, $d_2 = a_2 \cup b_2 = U$, $d_3 = a_3 \cup b_3 = \{u_1, u_2, u_3, u_5, u_6\}$, $d_4 = a_4 \cup b_4 = \{u_1, u_4\}$

And it is written as:

$$(d_n) = (a_n) \cup (b_n) = \Big(\{u_1, u_2, u_4, u_6\}, U, \{u_1, u_2, u_3, u_5, u_6\}, \{u_1, u_4\}\Big)$$

Terms of the complement of the soft sequence (a_n) denoted by $(a_n)^\circ$ is found as:

$a_1^{'} = U - a_1 = \{u_1, u_3, u_5\}$, $a_2^{'} = U - a_2 = \{u_4, u_5, u_6\}$, $a_3^{'} = U - a_3 = \{u_2, u_4, u_6\}$, $a_4^{'} = U - a_4 = U$

And it is written as:

$$(a_n)^\circ = \Big(\{u_1, u_3, u_5\}, \{u_4, u_5, u_6\}, \{u_2, u_4, u_6\}, U\Big)$$

Definition 3.16. Let (a_n) and (b_n) soft sequences over U. Then, a soft subsequence of (b_n), denoted by $(a_n) \subseteq (b_n)$, if $a_n \subseteq b_n$ for all $n \in \mathbb{Z}^+$.

Example 3.17. Let the set of objects $U = \{u_1, u_2, u_3, u_4, u_5, u_6, u_7, u_8, u_9\}$ and $A = \{1, 2, 3, 4, 5\}$, the soft sequences (a_n) and (b_n) defined over U. For $A = \{1, 2, 3, 4, 5\}$, (a_n) and (b_n) are written as:

$$(a_n) = \Big(\{u_2, u_4, u_6\}, \{u_1, u_3, u_5\}, \{u_8, u_9\}, \{u_5, u_7, u_8, u_9\}, \emptyset\Big)$$

$$(b_n) = \Big(\{u_2, u_4, u_6, u_8\}, \{u_1, u_3, u_5, u_7, u_9\}, \{u_7, u_8, u_9\}, U, \{u_9\}\Big)$$

For all $n \in A$, $a_1 \subseteq b_1$, $a_2 \subseteq b_2$, $a_3 \subseteq b_3$, $a_4 \subseteq b_4$, $a_5 \subseteq b_5$ since the (a_n) is a soft subsequence of the (b_n) and written as; $(a_n) \subseteq (b_n)$. If $a_5 = \{u_3\}$, then $(b_n) \nsubseteq (a_n)$ since $b_4 \nsubseteq a_4$.

Proposition 3.18. Let (a_n), (b_n), and (c_n) be soft sequences over U. Then,

i. $(a_n) \cap (a_n) = (a_n)$

ii. $(a_n) \cap (a_\emptyset) = (a_\emptyset)$

iii. $(a_n) \cap (a_U) = (a_n)$

iv. $(a_n) \cap (a_n)^\circ = (a_\emptyset)$

v. $(a_n) \cap (b_n) = (b_n) \cap (a_n)$

vi. $(a_n) \cap \Big((b_n) \cap (c_n)\Big) = \Big((a_n) \cap (b_n)\Big) \cap (c_n)$

Proposition 3.19. Let (a_n), (b_n), and (c_n) be soft sequences over U. Then,

i. $(a_n) \cup (a_n) = (a_n)$

ii. $(a_n) \cup (a_\emptyset) = (a_n)$

iii. $(a_n) \cup (a_U) = (a_U)$

iv. $(a_n) \cup (a_n)^\circ = (a_U)$

v. $(a_n) \cup (b_n) = (b_n) \cup (a_n)$

vi. $\Big((a_n) \cup (b_n)\Big) \cup (c_n) = (a_n) \cup \Big((b_n) \cup (c_n)\Big)$

Proposition 3.20. Let (a_n) be a soft sequence over U. Then,

i. $\Big((a_n)^\circ\Big)^\circ = (a_n)$

ii. $(a_\emptyset)^\circ = (a_U)$

Proposition 3.21. Let (a_n), (b_n), and (c_n) be soft sequences over U. Then,

i. $\Big((a_n) \cap (b_n)\Big)^\circ = (a_n)^\circ \cup (b_n)^\circ$

ii. $\Big((a_n) \cup (b_n)\Big)^\circ = (a_n)^\circ \cap (b_n)^\circ$

Proposition 3.22. Let (a_n), (b_n), and (c_n) be soft sequences over U. Then,

i. $(a_n) \cup \Big((b_n) \cap (c_n)\Big) = \Big((a_n) \cup (b_n)\Big) \cap \Big((a_n \cup (c_n)\Big)$

ii. $(a_n) \cap \Big((b_n) \cup (c_n)\Big) = \Big((a_n) \cap (b_n)\Big) \cup \Big((a_n \cap (c_n)\Big)$

4. Connected Soft Sequences

This section first defines the concept of connected soft sequences based on the properties of soft sequences. Then, connected soft sequences, increasing soft sequences, decreasing soft sequences, and

chained soft sequences are defined and examined, along with their basic properties.

Definition 4.1. Let (a_n) be a soft sequence over U. For $i \in \mathbb{Z}^+$,

i. if $a_{i-1} \cap a_i \neq \emptyset$ for $1 < i$, then a_i term is called left connected term and if $a_i \cap a_{i+1} \neq \emptyset$, then a_i term is called right connected term,

ii. if $a_{i-1} \cap a_i = \emptyset$ for $1 < i$, the a_i term is called the left disconnected term and if $a_i \cap a_{i+1} = \emptyset$, the a_i term is called the right disconnected term,

iii. terms that are connected from both the left and the right are called connected terms, and terms that are disconnected from the left or the right are called disconnected terms,

iv. terms that are disconnected from the left and right are called disjoint terms.

Example 4.2. The first six terms of a soft sequence (a_n) over the set $U = \{u_1, u_2, ...\}$ defined as:

$$a_1 = \{u_1\},\ a_2 = \{u_1, u_2\},\ a_3 = \{u_3\},\ a_4 = \{u_4, u_6\},\ a_5 = \{u_2, u_3, u_4, u_5\},\ a_6 = \{u_2, u_3, u_4\}, ...$$

Hence,

$$a_1 \cap a_2 = \{u_1\},\ a_2 \cap a_3 = \emptyset,\ a_3 \cap a_4 = \emptyset,\ a_4 \cap a_5 = \{u_4\},\ a_5 \cap a_6 = \{u_2, u_3, u_4\}, ...$$

since a_1 is connected from the right and the left connect is not defined, it is a connected term,
a_2 is the disconnected term because it is connected from the left and disconnected from the right,
a_3 is a disjoint term because it is disconnected from the right and left,
a_4 is the disconnected term because it is connected from the right and disconnected from the left,
a_5 is the connected term because it is connected from the left and the right.

Definition 4.3. Soft sequences in which all connected terms are called connected soft sequences. A soft sequence (a_n) defined over U to be connected if and only if

$$\forall\ i \in \mathbb{Z}^+, a_i \cap a_{i+1} \neq \emptyset$$

Soft sequences with at least one disconnected term are called disconnected soft sequences.
A soft sequence (a_n) defined over U to be disconnected if and only if

$$\exists\ i \in \mathbb{Z}^+, a_i \cap a_{i+1} = \emptyset$$

Example 4.4. Let the general term of a soft sequence (a_n) over $U = \{u_1, u_2, ...\}$ be defined as $a_1 = 1^{U(1)}$ and $a_n = a_{n-1} \cup 1^{U(n)}$ for $1 < n$. Here $1^{U(n)}$ is a non-empty subset of the randomly selected set U for the n-th term of the soft sequence (a_n). In this case, the soft sequence (a_n) is a connected soft sequence. Because, if $1^{U(1)} = \{u_2\}$ is chosen, $a_1 = \{u_2\}$, if $1^{U(2)} = \{u_2\}$ is chosen, $a_2 = \{u_2\} \cup \{u_2\} = \{u_2\}$, if $1^{U(3)} = \{u_1, u_2, u_3\}$ is chosen, $a_3 = \{u_2\} \cup \{u_1, u_2, u_3\} = \{u_1, u_2, u_3\}$, if $1^{U(4)} = \{u_5\}$ is chosen, $a_4 = \{u_1, u_2, u_3\} \cup \{u_5\} = \{u_1, u_2, u_3, u_5\}$.

As can be seen in the terms obtained while continuing indefinitely, the intersection of each successive term is different from the empty one. But the soft sequence (b_n) over the same U, whose general term is defined as $b_n = \{u_i : \frac{n}{i} \notin \mathbb{Z}^+\}$, is an disconnected soft sequence. Because,

$$b_1 = \emptyset,\ b_2 = \emptyset,\ b_3 = \{u_2\},\ b_4 = \{u_3\},\ b_5 = \{u_2, u_3, u_4\},\ b_6 = \{u_4, u_5\}, ...$$

As seen in the terms, the intersection of multiple consecutive terms is an empty set.

Definition 4.5. Let (a_n) be a connected soft sequence over U. If $a_{i-1} \cap a_{i+1} = \emptyset$, where $i \in \mathbb{Z}^+$ and $1 < i$, then the term a_i is called a chained connected term. The Venn diagram of a chained connected term a_i where $x, y \in U$ is given in Figure 1.

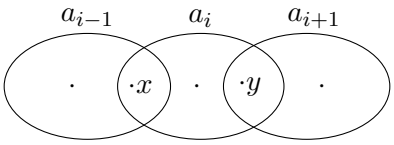

Figure 1. Chained connected term

Soft sequences with all terms chained connected are called chained soft sequences. The connected soft sequence (a_n) defined over U to be a chained soft sequence if and only if

$$\forall\ i \in \mathbb{Z}^+ \setminus \{1\}, a_{i-1} \cap a_{i+1} = \emptyset$$

where the dot, used in subsequent Venn diagrams without an element, indicates that this region may be empty or other than empty.

Example 4.6. All terms of the soft sequence (a_n), whose general term is $a_n = \{u_n, u_{n+1}\}$ defined over $U = \{u_1, u_2, ...\}$, are chain connected soft terms. Because,

$$a_1 = \{u_1, u_2\},\ a_2 = \{u_2, u_3\},\ a_3 = \{u_3, u_4\},\ a_4 = \{u_4, u_5\},\ ...,\ a_n = \{u_n, u_{n+1}\},\ ...$$

As seen in the terms, the intersections of all consecutive odd terms and all consecutive even terms are empty sets. Then, this soft sequence is a chained soft sequence.

Definition 4.7. Let (a_n) be a connected soft sequence over U. If $a_{i-1} \cap a_i \cap a_{i+1} \neq \emptyset$, where $i \in \mathbb{Z}^+$ and $1 < i$, then the term a_i is called a centered connected term. The Venn diagram of a centered connected term a_i where $x \in U$ is given in Figure 2.

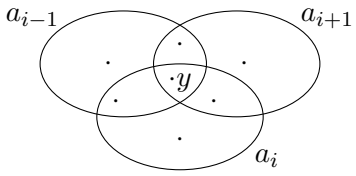

Figure 2. Centered connected term

Soft sequences with all terms centered connected are called centered soft sequences. The connected soft sequences (a_n) defined over U to be a centered soft sequences if and only if

$$\bigcap_{i \in \mathbb{Z}^+} a_i \neq \emptyset$$

The intersection of terms of centered soft sequences is called the center of this soft sequence, and it is shown as:

$$\text{cent}(a_n) = \bigcap_{i \in \mathbb{Z}^+} a_i$$

Example 4.8. All terms of the soft sequence (a_n), whose general term is $a_n = \{u_i : i|n\}$ defined over $U = \{u_1, u_2, ...\}$, are centered connected. Because,

$$a_1 = \{u_1\},\ a_2 = \{u_1, u_2\},\ a_3 = \{u_1, u_3\}, a_4 = \{u_1, u_2, u_4\},\ a_5 = \{u_1, u_5\},\ ....$$

As the terms show, u_1 is the common element of all consecutive terms. Then, this soft sequence is a centered soft sequence. In this case, the center of the soft sequence (a_n) is obtained as $\text{cent}(a_n) = \{u_1\}$.

Definition 4.9. Let (a_n) be a connected soft sequence over U. If $a_{i-1} \subseteq a_i \subseteq a_{i+1}$, where $i \in \mathbb{Z}^+$ and $1 < i$, then the term a_i is called increasingly connected term. The Venn diagram of an increasingly connected term a_i where $x, y \in U$ is given in Figure 3.

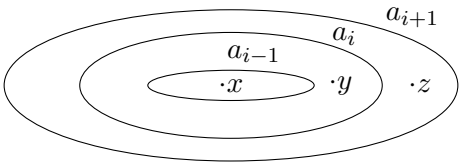

Figure 3. Increasingly connected term

Soft sequences with increasingly connected terms are called increasing soft sequences. The connected soft sequence (a_n) defined over U to be an increasing soft sequence if and only if

$$\forall\ i \in \mathbb{Z}^+, a_i \subseteq a_{i+1}$$

Proposition 4.10. Every increasing soft sequence is a centered soft sequence and $\text{cent}(a_n) = a_1$.

Proof. If (a_n) is an increasing soft sequence, $a_i \subseteq a_{i+1}$ for for all $i \in \mathbb{Z}^+$, in this case the terms of the soft sequence are $a_1 \subseteq a_2 \subseteq a_3 \subseteq ... \subseteq a_n \subseteq ....$ Since $a_1 \subseteq a_i$ for $1 < i$ in the increasing sequence, the term a_1 is a subset of all terms, that is, $\bigcap_{i\in\mathbb{Z}^+} a_i = a_1$. Then, $\text{cent}(a_n) = \bigcap_{i\in\mathbb{Z}^+} a_i = a_1$. □

Example 4.11. All terms of the soft sequences (a_n), whose general term is $a_n = \{u_1, u_2, ..., u_n\}$ defined over $U = \{u_1, u_2, ...\}$, are increasingly connected. Because,

$$a_1 = \{u_1\},\ a_2 = \{u_1, u_2\},\ a_3 = \{u_1, u_2, u_3\},\ a_4 = \{u_1, u_2, u_3, u_4\},\ a_5 = \{u_1, u_2, u_3, u_4, u_5\},\ ...$$

As seen in the terms, it inclusions each successive term as the index grows. Then, this soft sequence increases. From proposition 4.10, this increasing soft sequence is moreover, a centered soft sequence, with the center $\text{cent}(a_n) = a_1 = \{u_1\}$.

Proposition 4.12. The set of terms of increasing soft sequences is an order relation according to the subset relation $\subseteq$.

Definition 4.13. Let (a_n) be a connected soft sequence over U. If $a_{i+1} \subseteq a_i \subseteq a_{i-1}$, where $i \in \mathbb{Z}^+$ and $1 < i$, then the term a_i is called decreasingly connected term. The Venn diagram of the connected term a_i decreasing to $x, y, z \in U$ is given in Figure 4.

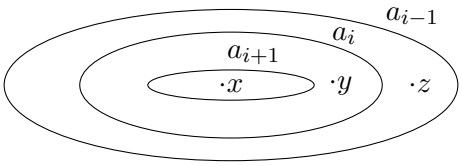

Figure 4. Decreasingly connected term

Soft sequences with decreasingly connected terms are called decreasing soft sequences. The connected soft sequence (a_n) defined over U to be a decreasing soft sequence if and only if

$$\forall\ i \in \mathbb{Z}^+, a_{i+1} \subseteq a_i$$

Proposition 4.14. Every decreasing soft sequence is a centered soft sequence and $\text{cent}(a_n) = \lim_{n\in\mathbb{Z}^+} a_n$.

Proof. A decreasing soft sequence (a_n) by definition satisfies the condition $a_{i+1} \subseteq a_i$ for all $i \in \mathbb{Z}^+$. In this case, the terms of the soft sequence are $a_1 \supseteq a_2 \supseteq a_3 \supseteq ... \supseteq a_n \supseteq ....$ Moreover, since it is a connected soft sequence, $a_{i-1} \cap a_i \neq \emptyset$ for for all $1 < i$. Then, $\bigcap_{i\in\mathbb{Z}^+} a_i \neq \emptyset$ since this will be a decreasing soft sequence, it is a soft sequence with a center, and its center is $\bigcap_{i\in\mathbb{Z}^+} a_i = a_i$ since the limit for the decreasing soft sequences will be the intersection of the terms, $\bigcap_{i\in\mathbb{Z}^+} a_i = \lim_{n\in\mathbb{Z}^+} a_n$ and from here $\text{cent}(a_n) = \lim_{n\in\mathbb{Z}^+} a_n$ is found. □

Example 4.15. All terms of the soft sequences (b_n), whose general term is $b_n = \left[0, \frac{1}{n}\right]$ defined over $U = [0, 1]$, are decreasingly connected. Because,

$$b_1 = [0, 1], \quad b_2 = \left[0, \frac{1}{2}\right], \quad b_3 = \left[0, \frac{1}{3}\right], \quad b_4 = \left[0, \frac{1}{4}\right], \quad ..., \quad b_n = \left[0, \frac{1}{n}\right], \quad ...$$

As seen in the terms, each term becomes a subset of the previous one as the index grows. Then, this soft sequence is a decreasing soft sequence. From Proposition 4.14, this decreasing soft sequence is furthermore, a centered soft sequence and its center is $\text{cent}(b_n) = \lim_{n\in\mathbb{Z}^+}[0, \frac{1}{n}] = [0, 0] = \{0\}$.

Proposition 4.16. The set of terms of decreasing soft sequences is an order relation according to the inclusion relation $\supseteq$.

Definition 4.17. Increasing or decreasing soft sequences are called ordered soft sequences.

5. Playing NC-Backgammon with Soft Sequences

In this section, the soft sequences are applied to the game theory. Using chained soft sequences, NC-backgammon, a zero-sum, strategic and intelligence game is played. Çağman defined NC-backgammon [25] as a two-person, zero-sum, strategic, perfect information, and intelligence game. For a detailed explanation of NC-backgammon and its gameplay, the reader is directed to [26, 27].

Herein, the utilization of chained soft sequences within the framework of NC-backgammon is systematically presented.

Let A and B be two players who will play NC-backgammon. Let player A be the first to start and select a number. Let $U = \{1, 2, 3, 4, 5, 6\}$ be a universe and $b_i \in U$, for all $i \in \mathbb{N}$. Then, a soft sequences (a_n) can be defined as

$$a_n : \mathbb{Z}^+ \to 2^U$$

$$a_n = \begin{cases} \{b_0, b_1\}, & n = 1 \ (b_0 \text{ and } b_1 \text{ are selected by } A \text{ and } B \text{ respectively, sucht that } b_1 \neq b_0) \\ \{b_{2k}, b_{2k-1}\}, & n = 2k \ (b_{2k} \text{ is selected by } A, \text{ sucht that } b_{2k} \neq b_{2k-1},\ b_{2k} \neq b_{2k-2}) \\ \{b_{2k}, b_{2k+1}\}, & n = 2k+1 \ (b_{2k+1} \text{ is selected by } B, \text{ sucht that } b_{2k+1} \neq b_{2k},\ b_{2k+1} \neq b_{2k-1}) \end{cases}$$

As shown in Figure 5, a_n is the general term of a chained soft sequence.

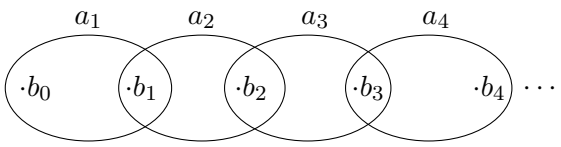

Figure 5. Chained soft sequence for NC-backgammon

In this case, the chained soft sequence (a_n) is used to specify the rules for players A and B in NC-backgammon. Let player A be the first to start the game.

In turn 0: If $n = 1$, then neither player moves any checkers with the $a_1 = \{b_0, b_1\}$.

In turn A: If $n \geq 2$, $n = 2k$, $k \in \mathbb{Z}^+$, then player A moves their checkers with number pair $a_{2k} = \{b_{2k}, b_{2k-1}\}$ as if the pair is obtained by rolling two dice.

In turn B: If $n \geq 3$, $n = 2k+1$, $k \in \mathbb{Z}^+$, then player B moves their checkers with number pair $a_{2k+1} = \{b_{2k}, b_{2k+1}\}$ as if the pair is obtained by rolling two dice.

This procedure continues until the game is finished.

Example 5.1. As it is above, player A starts the game first.

$n = 1$, in turn 0: If A choose a number $b_0 = 5$ and B choose a number $b_1 = 4$ among the six numbers. In this case, neither player moves any checkers with the $a_1 = \{5, 4\}$.

$n = 2$, in turn A: If A choose the number $b_2 = 1$, then A moves their checkers with the numbers $a_2 = \{1, 4\}$.

$n = 3$, in turn B: If B choose the number $b_3 = 6$, then B moves their checkers with the numbers $a_3 = \{1, 6\}$.

$n = 4$, in turn A: If A choose the number $b_2 = 4$, then A moves their checkers with the numbers $a_4 = \{4, 6\}$.

$n = 5$, in turn B: If B choose the number $b_3 = 2$, then B moves their checkers with the numbers $a_5 = \{4, 2\}$.

It continues until the game is over. These moves occur in Table 1.

Table 1. Game Moves

n	Players	a_n	Numbers
1.	A, B	$a_1 = \{b_0, b_1\}$	$\{5, 4\}$
2.	A	$a_2 = \{b_2, b_1\}$	$\{1, 4\}$
3.	B	$a_3 = \{b_2, b_3\}$	$\{1, 6\}$
4.	A	$a_4 = \{b_4, b_3\}$	$\{4, 6\}$
5.	B	$a_5 = \{b_4, b_5\}$	$\{4, 2\}$
$\vdots$	$\vdots$	$\vdots$	$\vdots$

In this example, the chained soft sequence (a_n) is obtained as follows:

$$(a_n) = (\{b_0, b_1\}, \{b_1, b_2\}, \{b_2, b_3\}, \{b_3, b_4\}, \{b_4, b_5\}, \{b_5, b_6\}, ...)$$

6. Conclusion

The study carried out in this paper, soft sequences were defined as a specialized of soft sets. It is determined from the set of positive integers to the power set of a universe. As a new concept, we defined connected and disconnected soft sequences, chained soft sequences, centered soft sequences, increasing soft sequences, decreasing soft sequences, and ordered soft sequences. Finally, the soft sequences are applied to game theory. Furthermore, NC-backgammon, a zero-sum, strategic, and intelligence game that uses chained soft sequences, was played. In the future, researchers can study the limits of soft sequences, which are not included herein due to their non-use. Soft sequences can be applied to other areas of game theory and social problems.

References

[1] D. A. Molodtsov, *Soft set theory-first results*, Computers and Mathematics with Applications 37 (4-5) (1999) 19–31.

[2] H. Aktaş, N. Çağman, *Soft sets and soft groups*, Information Science 177 (2007) 2726–2735.

[3] U. Acar, F. Koyuncu, B. Tanay, *Soft sets and soft rings*, Computers and Mathematics with Applications 59 (11) (2010) 3458–3463.

[4] D. Singh, I. A. Onyeozili, *On the ring structure of soft set theory*, International Journal of Scientific and Technology Research 2 (3) (2013) 96–101.

[5] Y. Yang, X. Xin, P. He, *Applications of soft union sets in the ring theory*, Journal of Applied Mathematics (1) (2013) 474890.

[6] P. K. Maji, A. R. Roy, R. Biswas, *An application of soft sets in a decision making problem*, Computers Mathematics with Applications 44 (8-9) (2002) 1077–1083.

[7] F. Fatimah, D. Rosadi, R. F. Hakim, J. C. R. Alcantud, *Probabilistic soft sets and dual probabilistic soft sets in decision-making*, Neural Computing and Applications 31 (1) (2019) 397–407.

[8] F. Feng, Y. Li, V. Leoreanu-Fotea, *Application of level soft sets in decision making based on interval-valued fuzzy soft sets*, Computers and Mathematics with Applications 60 (6) (2010) 1756–1767.

[9] Y. Liu, K. Qin, L. Martínez, *Improving decision making approaches based on fuzzy soft sets and rough soft sets*, Applied Soft Computing 65 (2018) 320–332.

[10] N. Çağman, S. Karataş, S. Enginoglu, *Soft topology*, Computers and Mathematics with Applications 62 (1) (2011) 351–358.

[11] S. Enginoğlu, N. Çağman, S. Karataş, T. Aydın, *On soft topology*, El-Cezeri Journal of Science and Engineering 2 (3) (2015) 23–38.

[12] Z. Li, T. Xie, *The relationship among soft sets, soft rough sets and topologies*, Soft Computing 18 (4) (2014) 717–728.

[13] Y. B. Jun, C. H. Park, *Applications of soft sets in Hilbert algebras*, Iranian Journal of Fuzzy Systems 6 (2) (2009) 75–86.

[14] P. Yadav, R. Singh, *El-Algebra in soft sets*, Journal of Algebraic Statistics 13 (2) (2022) 1455–1462.

[15] J. Zhan, Y. B. Jun, *Soft BL-algebras based on fuzzy sets*, Computers and Mathematics with Applications 59 (6) (2010) 2037–2046.

[16] S. S. Reddy, K. Yogesh, S. Jalil, *Some results on soft sequences*, International Journal of Mathematics And its Applications 3 (4-A) (2015) 37–44.

[17] V. Cafarli, Ç. Gunduz Aras, S. Bayramov, *Soft sequences in soft topological spaces*, in: V. Cafarli, Ç. Gunduz Aras, S. Bayramov (Eds.), Azerbaijan National Academy of Science Institute of Mathematics and Mechanics, Azerbaijan, 2017.

[18] A. A. Hamad, A. Babu, *Soft sequences in real analysis*, International Journal of Engineering and Technology 7 (4.19) (2018) 32–35.

[19] A. A. Hamad, R. A. Hameed, M. M. Khalil, A. A. M. A. Hamad, *On equality of infimum soft sequences*, International Journal of Mathematics Trends and Technology 55 (3) (2018) 223–225.

[20] A. H. Hameed, E. A. Mousa, A. A. Hamad, *Upper limit superior and lower limit inferior of soft sequences*, International Journal of Engineering and Technology 7 (4.7) (2018) 306–310.

[21] A. A. Hamad, A. A. Abdulrahman, A.A, *On the decreasing soft sequences*, American Journal of Research 5-6 (5-6) (2018) 20–24.

[22] T. S. Ferguson, A course in game theory, World Scientific, 2020.

[23] I. Deli, N. Çağman, *Fuzzy soft games*, Filomat 29 (9) (2015) 1901–1917.

[24] I. Deli, N. Çağman, *Application of soft sets in decision making based on game theory*, Annals of Fuzzy Mathematics and Informatics 11 (3) (2016) 425–438.

[25] N. Çağman, *Tahtasız, pulsuz ve zarsız tavla* (in Turkish), Bilim ve Teknik 430 (2003) 92–94.

[26] N. Çağman, *A new perfect information game no chance backgammon*, International Journal of Contemporary Mathematical Sciences 2 (18) (2007) 879–884.

[27] N. Çağman, U. Orhan, *A model transforming a problem based on chance problem into perfect information and its fuzzy application*, International Symposium on Innovations in Intelligent Systems and Applications, Istanbul, 2007.

[28] N. Çağman, *Contributions to the theory of soft sets*, Journal of New Results in Science 3 (4) (2014) 33–41.

[29] S. J. John, Soft sets: theory and applications, Springer, 2021.

[30] P. K. Maji, R. Bismas, A. R. Roy, *Soft set theory*, Computers and Mathematics with Applications 45 (1) (2003) 555–562.

Journal of Advanced Research in Natural and Applied Sciences
dergipark.org.tr/en/pub/jarnas
Open Access

ISSN: 2757-5195 | 11 (2) (2025) 187-196 | doi.org/10.28979/jarnas.1666819

Design and Evaluation of Nanoparticle-Reinforced Glass for Radiation Shielding in Angiography: An MCNP Simulation Study

Navid Kheradmand[1], Mustafa Çağlar[2]

Article Info
Received: 27 Mar 2025
Accepted: 03 Jun 2025
Published: 30 Jun 2025
Research Article

Abstract − Angiography is a widely utilized diagnostic and treatment method involving relatively high radiation doses for patients and personnel. Protecting radiation-sensitive organs, such as the eye lens, is crucial in this imaging modality. In this study, we employed the Monte Carlo N-Particle Transport (MCNP) code to design transparent shields incorporating metal nanoparticles (NPs). Two types of phosphate glass—one with lead and one with bismuth—were designed and simulated. ZnO-Bi_2O_3-P_2O_3 and ZnO-PbO-P_2O_3 were analyzed at six concentrations (0, 10, 20, 30, 40, 50 wt%). We calculated the linear attenuation coefficients, mass attenuation coefficients, and half-value layer for each sample across eight photon energies (50, 60, 80, 100, 120, 140, 150, and 200 kV), which are primarily used in angiography. A good agreement was observed between the simulated results and those from the XCOM database. The maximum mass attenuation coefficients were found for the PZBi 50 glass sample. The results suggest that the MCNP code can be a reliable alternative to experimental methods for other glass materials and systems, calculated for their photon attenuation characteristics. Among the studied samples, Bi-doped glasses demonstrated slightly better attenuation properties than Pb-doped ones, especially at lower photon energies. This superiority is mainly attributed to the higher atomic number of Bi and its enhanced photoelectric interaction probability. While the consistency between MCNP and XCom results reinforces the credibility of the simulation approach.

Keywords − *Monte Carlo simulation, angiography, glass shields, radiation shields, radiation protection*

1. Introduction

The increase in the use of ionising radiation in X-ray machines, particularly in angiography, is becoming more common for diagnosing a range of medical conditions. Currently, over ten million diagnostic radiology procedures involving ionizing radiation are performed daily worldwide, resulting in heightened radiation exposure for patients [1]. This increased exposure poses significant risks, especially to sensitive organs such as the lens, thyroid gland, and breast, which can elevate the risk of radiation-induced effects, including cancer [2]. This situation highlights the urgent need for effective protection against high-energy X-rays using non-toxic shielding materials [3]. Historically, lead has been the first choice for radiation shielding due to its high atomic number, effectively blocking ionizing radiation. However, lead has significant drawbacks. These include its inflexibility, excessive weight, toxicity, and limited mechanical and chemical stability [4]. Consequently, researchers are investigating alternative materials to enhance radiation protection. In this

[1]navid.kheradmand@medipol.edu.tr; [2]drmustafacaglar@gmail.com (Corresponding Author)
[1]Department of Health Physics, Graduate School of Health Sciences, İstanbul Medipol University, İstanbul, Türkiye
[1,2]Department of Radiotherapy, Vocational School of Health Services, İstanbul Medipol University, İstanbul, Türkiye

context, glass has emerged as a promising option because it is transparent to visible light, easy to fabricate, and can be modified through various compositional methods to improve its shielding effectiveness [5].

Researchers are developing protective glasses that incorporate nanoparticles (NPs) of bismuth (Bi), Lead (Pb), barium (Ba), and tungsten (W) [6, 7]. These materials, known for their high atomic numbers and beneficial properties such as flexibility, non-toxicity, and lightweight nature, enhance the glasses effectiveness in shielding against ionizing radiation. This innovative approach aims to improve safety for individuals exposed to radiation and opens new possibilities for protective gear in medical and industrial applications [8]. To optimize these materials, numerical modeling, especially through Monte Carlo (MC) simulations like Geant4 and MCNP, is used to assess their performance against X-rays and gamma rays [9].

For instance, in a study by Çağlar et al. [10], a glassy structured sodium silicate (Na2Si3O7) matrix was examined, with the presence of micro-sized and nano-sized silver (Ag) particles at varying weight percentages, to provide an example of the type of research that can be conducted. The findings revealed that adding NPs significantly enhances radiation shielding effectiveness compared to micro-sized particles, particularly at lower concentrations and photon energies. Studies have consistently shown that NPs, due to their larger surface-area-to-volume ratio, provide superior photon absorption capabilities [11]. For example, studies on Bi and gadolinium oxide (Gd2O3) NPs have demonstrated that nano-sized composites outperform their micro counterparts in shielding X-rays or gamma rays by approximately 28% [3]. In a separate study, Zaid et al. [12] conducted a theoretical analysis using XCom software to evaluate the radiation shielding effectiveness of Bi2O3–TiO2–V2O5–Na2O–TeO2 glasses designed to provide gamma-ray shielding. The glass composition containing Bi2O3 at 20% wt demonstrated the most effective gamma-ray shielding. In a different study, experimental and theoretical methods were used to determine the gamma-ray attenuation properties of metal oxide-doped glasses within a photon energy range of 53–383 keV. It was established that the sample of glass containing the highest concentration of heavy metals, which was found to consist of 5.05% Bi2O3, 5.05% MnO2, 4.5% ZnO, 1.7% Al2O3, and 67.65% SiO2, exhibited the optimal gamma shielding capacity [13].

In addition, Kebaili et al. [14] performed an MC simulation to investigate the radiation shielding performance of alkaliborate glasses with the substitution xTiO2/(10-x) V2O5 (referred to as LBZ-TV glasses), where x values ranged from 0 to 10%. They found that the LBZ-TV glasses developed in their study exhibited superior radiation shielding performance compared to conventional materials, including standard ordinary and barite concretes and lead-free glasses. In another study, Won-in et al. [15], utilizing Ba NPs, resulted in Pb-free radiation shielding glass fabrication. In the present study, the researchers fabricated lead-free glass specimens utilizing 40% by weight of local quartz sand, along with varying concentrations of $BaCO_3$ (20-40% by weight) as the base material. This experimental approach was employed for the purpose of examining the gamma attenuation characteristics at 662 keV. They suggested that a denser Pb-free glass with a high refractive index can improve attenuation properties, making it a viable alternative to lead for gamma-ray protection.

Given that, numerous studies have investigated protective materials against ionizing radiation, each highlighting unique advantages and disadvantages. While much research has focused on the effectiveness of various materials, there has been limited discussion on the role of NPs when combined with glass base materials to enhance radiation protection [16]. This gap underscores the need to further explore the protective capabilities of glasses reinforced with NPs, as these composites may offer improved shielding properties. Recent developments indicate that incorporating high atomic number NPs such as Bi and Pb into composite materials can significantly enhance their effectiveness against ionizing radiation. In this context, we evaluated the radiation shielding properties of glasses reinforced with NPs of Bi and Pb using MCNP simulation techniques. This research is particularly relevant in medical imaging, nuclear safety, and materials science, where effective radiation shielding is crucial for ensuring safety and efficacy. This study evaluates the radiation shielding performance of Bi- and Pb-doped phosphate glasses using MCNPX simulations. The aim is to support safer and more effective shielding solutions in medical imaging, particularly in angiography.

2. Materials and Methods

The current study is a fundamental and applied investigation utilizing the MCNP simulation code. Initially, research focused on various types of glasses and the potential for incorporating non-lead materials. Following preliminary studies, two glass types were selected for further examination: phosphate glass and normal glass. The study aimed to simulate and compare the radiation attenuation capabilities of these lead-free glasses when heavy non-lead materials were added.

2.1 Phosphate Glasses

This study designed and simulated two types of phosphate glass: one incorporating lead and bismuth, and the other without these materials. The specific compositions included ZnO-Bi_2O_3-P_2O_3 and ZnO-PbO-P_2O_3 glasses, which were examined at six varying concentrations (0, 10, 20, 30, 40, 50 wt%). The objective was to calculate each sample's linear and mass attenuation coefficients across eight photon energies (50, 60, 80, 100, 120, 140, 150, and 200 keV). Simulations were conducted at three different thicknesses for each energy level to achieve this. The mass attenuation coefficient was derived from the transmitted photon flux using the Beer-Lambert relation. The reduction coefficients related to these thicknesses were obtained to determine the mass attenuation coefficient using the Beer-Lambert relation. This theory postulates a correlation between the phenomenon of light absorption and the properties of the medium through which the light travels. Table 1 presents the physical characteristics of six types of bismuth-doped phosphate glass (ZnO-Bi_2O_3-P_2O_3) that were simulated.

Table 1. Physical characteristics and percentage of ZnO-Bi_2O_3-P_2O_3 phosphate glass components.

Sample	Element (wt%)			Density
	ZnO	Bi_2O_3	P_2O_3	(g/cm^3)
PZBi0	50	0	50	0.3126
PZBi10	40	10	50	0.3087
PZBi20	30	20	50	0.2984
PZBi30	20	30	50	0.2891
PZBi40	10	40	50	0.2798
PZBi50	0	50	50	0.2703

Similarly, Table 2 displays the physical characteristics of six types of phosphate glass with the presence of lead nanoparticles (ZnO-PbO-P_2O_3) that were also simulated.

Table 2. Physical characteristics and percentage of ZnO-PbO-P_2O_3 phosphate glass components.

Sample	Element (wt%)			Density
	ZnO	PbO	P_2O_3	(g/cm^3)
PZPb0	50	0	50	3.177
PZPb10	40	10	50	3.493
PZPb20	30	20	50	4.121
PZPb30	20	30	50	4.419
PZPb40	10	40	50	4.802
PZPb50	0	50	50	4.845

2.2 Theoretical Background

When X-rays of suitable energy traverse matter, they undergo attenuation through various interactions. The following phenomena are to be considered: the photoelectric effect (PE), Compton scattering (CS), and pair production (PP). These processes result in an exponential decrease in radiation intensity, which is influenced

by the thickness of the absorbing material. This relationship is mathematically described by Beer-Lambert law, represented by (2.1):

$$I = I_0 e^{-\mu x} \tag{2.1}$$

The parameters of relevance in this context are I_0 and I, representing the incident and transmitted X-ray intensities, respectively. To establish a comprehensive model of the process, it is necessary to include x, representing the absorbing medium's thickness. The fifth parameter required to establish a full process model is μ (cm^{-1}). This is known as the linear attenuation coefficient, and it is one of the most significant shielding parameters, the significance of which depends on the X-ray energy and the absorber composition. To remove the dependence of the attenuation coefficient (μ) on material density, the mass attenuation coefficient (μm = μ/ρ) is utilized, where ρ represents the density of the material.

In the present study, the MCNP and the XCom database have been used for modeling the radiation interaction of photons with material and the transportation with material. The difference between μm values of the methods (MCNP, XCom) is achieved from the following (2.2):

$$Diff\ (\%) = \left|\frac{\mu_1 - \mu_2}{\mu_1}\right| 100 \tag{2.2}$$

2.3 MCNP Code

This study employed the MC N-particle transport code MCNP version 2.6.0, developed at Los Alamos National Laboratory (LANL) in New Mexico. MCNP is a comprehensive code designed for transporting neutrons, photons, and electrons, allowing for simulations that combine these particle types. The input parameters for MCNP were carefully defined in the input files, detailing cell cards, material cards, surface cards, and energy source features. The simulation geometry was set up within a cylindrical space measuring 100 centimeters in height and 30 centimeters in diameter. A surface source with a diameter of 5 millimeters was specified using commands such as PAR, POS, ERG, RAD, AXS, VEC, and DIR. Additionally, lattice (LAT) and universe (U) cards were used to define the matrix and filler materials (Figure 1). To determine the μm for all samples, monoenergetic beams in the 60-200 keV energy range were simulated. This range was chosen for its significance in future experimental studies on X-ray machines commonly utilized in diagnostic radiology laboratories. The findings from these simulations will enhance our understanding of how different glass compositions attenuate ionizing radiation effectively.

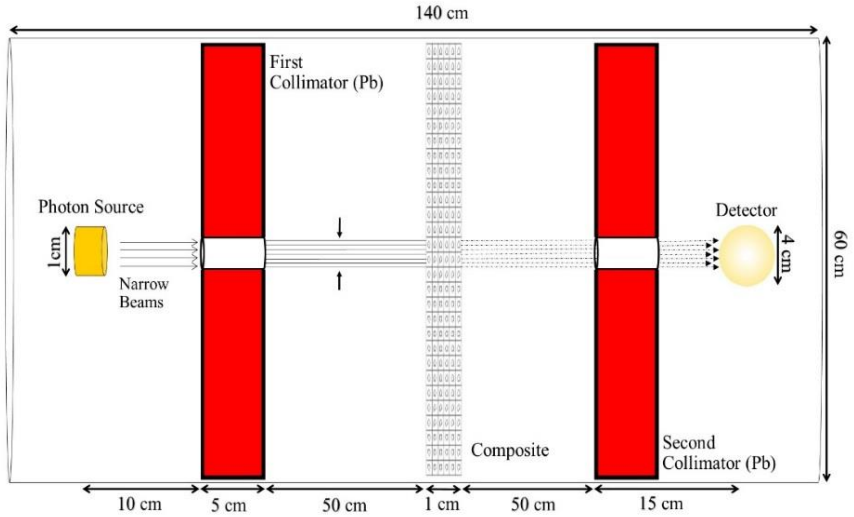

Figure 1. Representation of the geometry simulated in Monte Carlo software (no scale).

2.4 XCom Standard Database

The XCom database is essential for calculating photon cross-section data, specifically for interactions involving X-rays and gamma rays with various materials. Developed by the National Institute of Standards and Technology (NIST), XCom offers a comprehensive range of data, including partial and total cross sections, mass attenuation coefficients, and effective atomic numbers. It encompasses a range of interaction processes, including coherent and incoherent scattering, pair production, and photoelectric absorption. The energy range covered spans from 1 keV to 100 GeV. In this study, we utilized the XCom program in comparison with MCNP simulations.

2.5 Validation of MC Models Through XCom Database Comparison

The accuracy and reliability of the MC models were evaluated by comparing simulation results with data from the XCom database, focusing on a standard lead shield. This comparison ensured that the MC models accurately reflect real-world radiation interactions with shielding materials. Linear attenuation coefficients for lead were calculated from the MC simulations and compared to XCom reference values, allowing for a detailed analysis of discrepancies. Once the simulations were validated, the input codes were used to calculate mass attenuation coefficients for various samples, enhancing our understanding of material effectiveness in radiation protection.

3. Results and Discussion

3.1. Verification of Advanced Code

To verify the accuracy of the simulation code, we compared the results obtained from our code with data from the Xcom standard database. As illustrated in Figure 2, there is a strong correlation between the two datasets, confirming the reliability of the developed code. Figure 2(A) depicts the results for bismuth metal, while Figure 2(B) illustrates the shielding properties of pure silicon. This validation ensures that our simulation accurately reflects real-world radiation interactions with various materials.

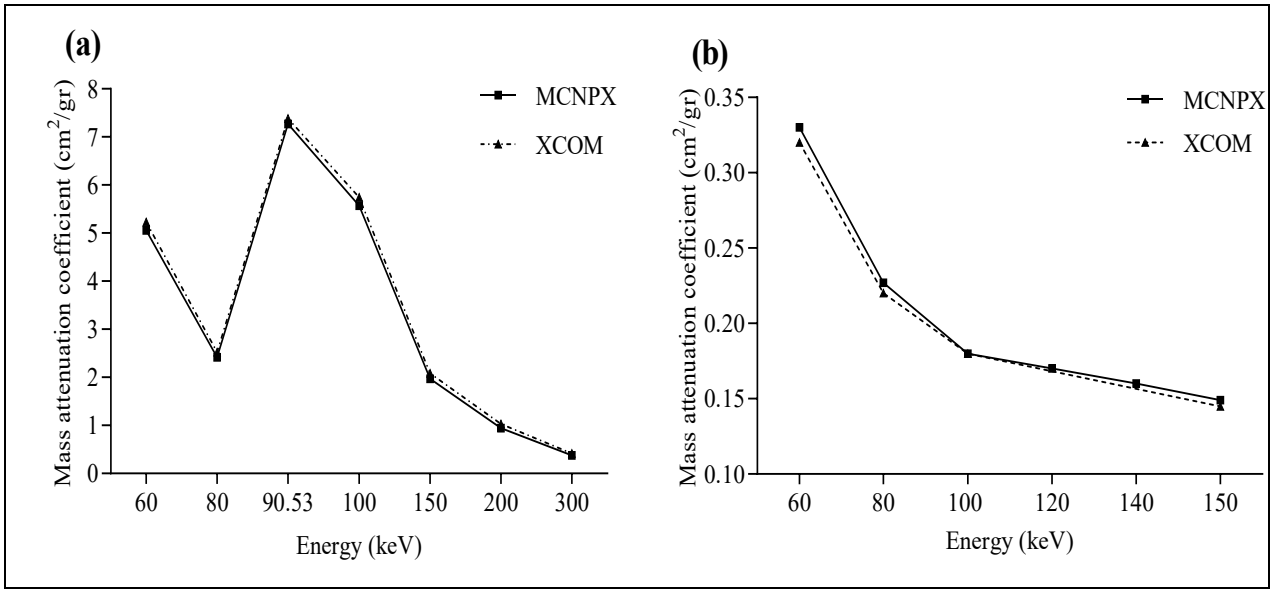

Figure 2. Comparison of mass attenuation coefficients of pure silicon shielding (a) and pure bismuth (b) at different energies obtained with the MCNP Monte Carlo code and Xcom standard data.

3.2 Mass Attenuation Coefficients of Phosphate Glass

In this section, the mass attenuation coefficients were calculated for twelve glass protectors containing varying percentages of bismuth oxide and lead, based on MC simulation data. Independent of material density, these coefficients are provided in figures for eight photon energies: 50, 60, 80, 100, 120, 140, 150, and 200 keV.

3.2.1 Lead Added Phosphate Glasses

The attenuation coefficients of lead-added phosphate glass with varying weight percentages (PZPb10, PZPb20, PZPb30, PZPb40, and PZPb50) at photon energies relevant to diagnostic radiology are presented in Figure 3. The data show a strong correlation between the simulation results and the Xcom standard database, indicating the reliability of the findings. Additionally, as the photon beam energy increases, there is a noticeable decrease in the radiation attenuation capability of the simulated glasses. As shown in Figure 3, the attenuation coefficients of Pb-doped phosphate glass samples decrease with increasing photon energy. The results confirm that higher Pb concentrations lead to better attenuation, particularly at lower energies.

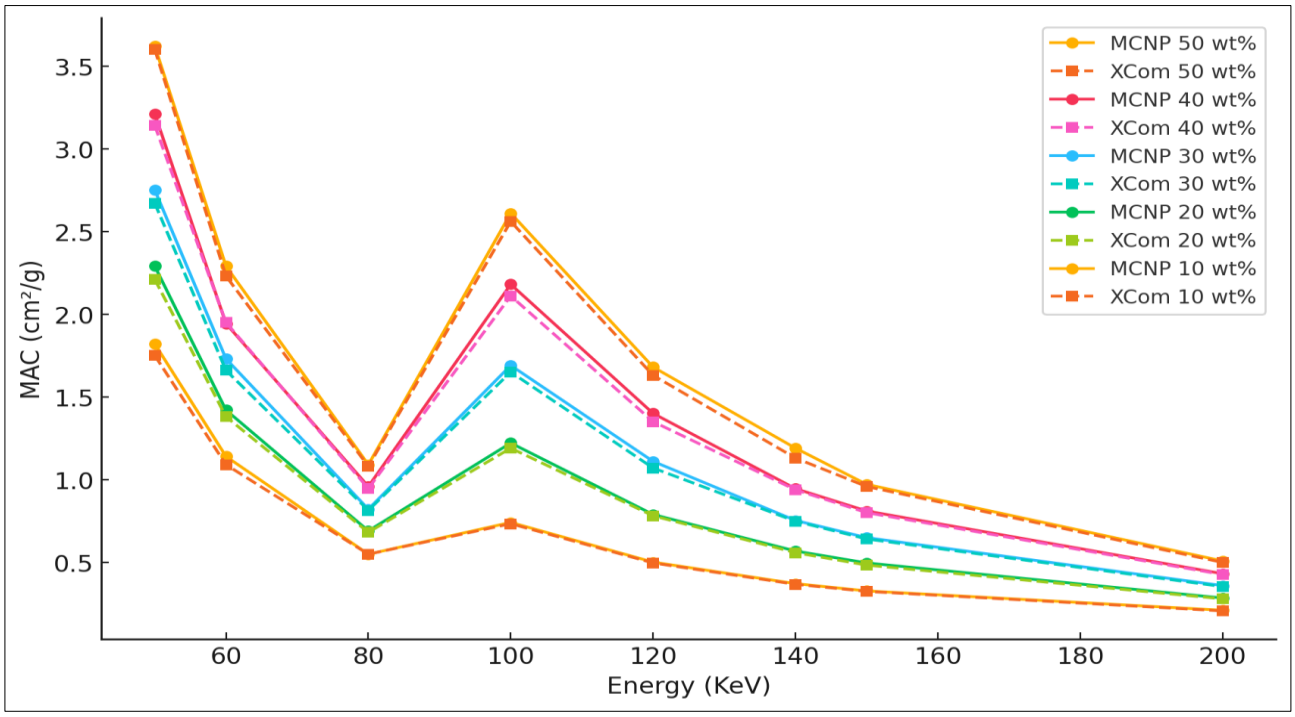

Figure 3. Mass attenuation coefficients of lead (Pb) added-phosphate glass PZPb10, PZPb20, PZPb30, PZPb40 and PZPb50 in the energies used in diagnostic radiology

3.2.2 Bismuth Added Phosphate Glasses

The attenuation coefficients of Bi added phosphate glass with varying weight percentages (PZBi10, PZBi20, PZBi30, PZBi40, and PZBi50) at photon energies pertinent to medical imaging applications are presented in Figure 4. Similarly, the data presented a robust correlation between the simulation results and the XCOM standard database, demonstrating the dependability of the findings. Furthermore, as expected, as the photon beam energy increases, there is a noticeable decrease in the radiation attenuation capability of the simulated glasses.

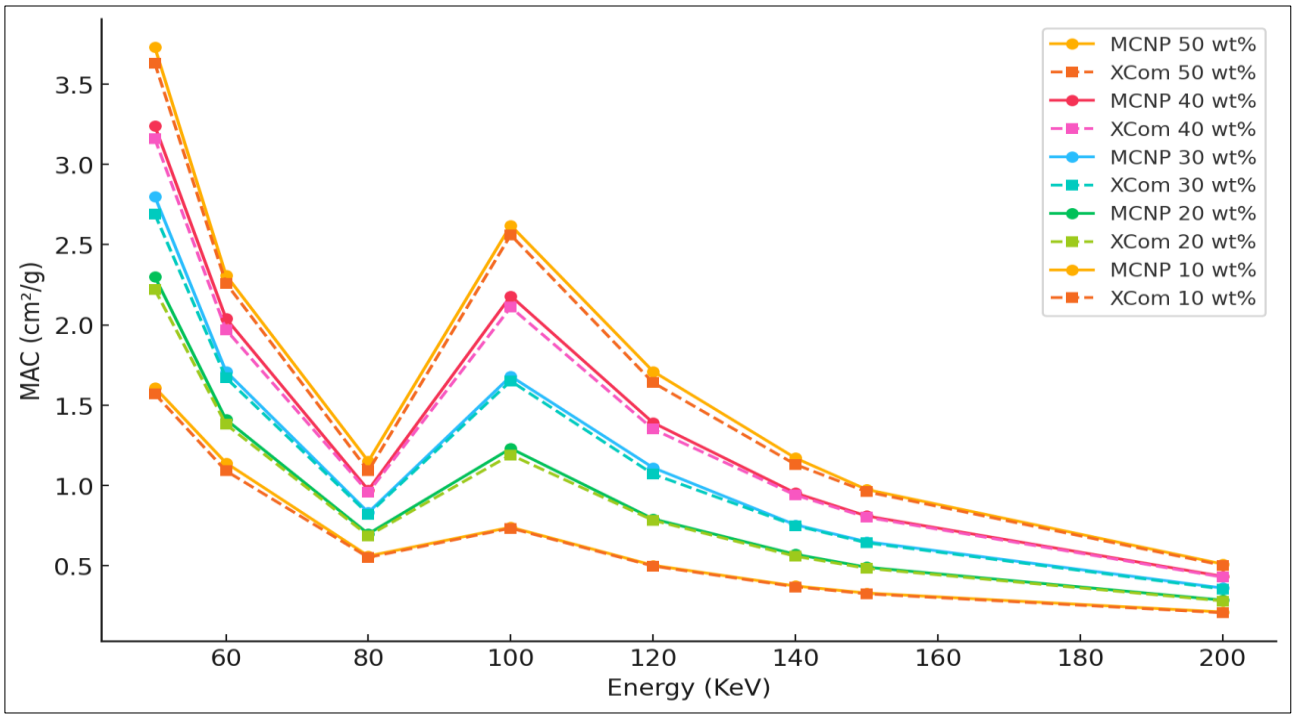

Figure 4. Mass attenuation coefficients of bismuth (Bi) added-phosphate glass PZBi10, PZBi20, PZBi30, PZBi40, and PZBi50 in the energies used in diagnostic radiology.

In this study, we developed and assessed the radiation shielding properties of glass doped with NPs of Bi and Pb to be used in radiology by an MCNP simulator. We compared the results with the data from the XCOM standard database. Figures 3 and 4 show that the attenuation coefficients of phosphate shields containing Pb and Bi fillers indicate that Bi shields are slightly more efficient than lead glass shields. For instance, at a constant concentration of 50%, Bi and Pb NPs exhibit mass attenuation coefficients of 1.15 and 1.09, respectively, at an energy of 80 keV. At a constant concentration of 40% by weight, the mass attenuation coefficients for Bi and Pb NPs are 0.971 and 0.958 at the same energy level. For a constant concentration of 30% by weight, the mass attenuation coefficients are 0.831 for Bi and 0.821 for Pb at the same photon energy. At a concentration of 20% by weight, the coefficients are 0.698 for Bi and 0.690 for Pb, respectively. For a weight percentage of 10%, these values are 0.560 for Bi and 0.549 for Pb. These results demonstrated that Bi fillers have superior attenuation capabilities compared to lead fillers, particularly at higher concentrations and lower energies. This enhanced attenuation can be attributed to the photoelectric effect, as Bi has a higher atomic number than lead, leading to more effective interactions with radiation.

In a related study by Karimi et al. [17], different glass shields were evaluated and compared against international standards. The study included one commercially available lead-based shield, four newly investigated shielding materials, four recently analyzed shields, and three new lead-free alternatives. The shielding factors for these materials were calculated, introducing three types of glass made from borate, phosphate, and silicate compounds, designated as Ir1, Ir2, and Ir3. Additionally, mass attenuation coefficients for all shields were obtained from the XCOM database, specifically within the diagnostic X-ray energy range of 40–120 keV. Ultimately, they found that Ir3 glasses emerged as the recommended lead-free transparent shielding materials within photon energies relevant to diagnostic imaging. In a study by Zakaly et al. [18], the influence of BaO incorporation on the optical, structural, mechanical stability, and nuclear radiation shielding properties of barium borosilicate glasses was examined. The linear attenuation coefficients for the glasses labeled Ba00, Ba05, Ba10, Ba20, and Ba30 were measured at energies of 81 keV and 2614 keV, yielding values of 0.4951, 1.0129, 1.5780, 2.8795, and 4.4203 at 81 keV, and 0.1030, 0.1084, 0.1148, 0.1278, and 0.1397 at 2614 keV, respectively. These results were compared with data from the XCOM program and the FLUKA MC simulation code across photon energies ranging from 81 to 2614 keV, and their findings are in line with our results.

In another study by Elsafi et al. [19], the influence of Bi_2O_3 concentration and particle size on the properties of Bi_2O_3 glass was assessed. The compositions examined included SiO_2- Bi_2O_3-CaO-MgO- Bi_2O_3 -K_2O-Na_2O-ZnO. The research compared plain glass with samples containing 10% bulk Bi_2O_3 NPs, 10% Bi_2O_3 NPs, 20% bulk Bi_2O_3, and 20% NPs. Results indicated that higher Bi_2O_3 content enhanced shielding effectiveness, with NPs demonstrating superior attenuation compared to bulk Bi_2O_3 at equivalent concentrations. Further analysis of the half-value layer showed that glasses with Bi_2O_3 NPs could attenuate the same photon levels at reduced thickness, highlighting the efficacy of NP shields. Our findings are in concordance with those reported by Karimi et al., who also observed improved shielding in phosphate-based glasses. However, our results emphasize the advantage of nanoparticle incorporation, which was less pronounced in their study. Similarly, compared to Elsafi et al. [19], our Bi2O3 nanoparticle-doped glasses showed higher attenuation at equivalent concentrations, likely due to optimized glass composition and particle size distribution.

4. Conclusion

This study tested the effect of adding two elements, lead and bismuth, to make X-ray shielding glass in phosphate glass. According to the figure of attenuation coefficients in shields, it was observed that μ/ρ decreases with the increase of beam energy. The mass attenuation coefficient at 50 keV energy is much higher than at other energies in all shields. μ/ρ decreases sharply when more energy is increased. Therefore, the lowest μ/ρ in all six shields is 200 keV energy. The observed jumps in attenuation coefficients around 90 keV and 92 keV are due to the K-absorption edges of Bi and Pb, respectively, where a sharp increase in photoelectric absorption occurs owing to the sudden availability of inner shell electrons for interaction. This phenomenon is attributed to the photon energy reaching the binding energy of the K-shell electrons in these elements. When this threshold is exceeded, the probability of photoelectric interaction rises significantly, leading to a peak in the mass attenuation coefficient (μ/ρ). Since bismuth and lead have high atomic numbers and strong electron binding energies, these materials' edge effect becomes highly pronounced.

The occurrence of the attenuation coefficient peak can be seen at the absorption edges if it is calculated, but in some shields, the increase of μ/ρ in the first energy after the absorption edge is also seen. For example, in shields containing bismuth oxide, μ/ρ is higher at 100 keV energy than at 80 keV energy, which is caused by the bismuth absorption edge effect. In some other shields, this mutation of the mass attenuation coefficient has occurred after the absorption edge of that metal, such as the effect caused by the lead absorption edge in lead shields at 80 kiloelectron volts energy. Because their absorption edges and as a result the μ/ρ jump occur at lower energies, which is not visible due to the larger μ/ρ and lack of calculation for the absorption edges, the increase in μ/ρ is not visible at the first energy after that. At lower energies, the main cause of beam attenuation is photoelectric reaction. So that at energies of 50 keV, the dominant interaction in the shields is photoelectric. With the increase in energy, the contribution of Compton scattering in the interaction of photons with matter increases, and as a result, the attenuation coefficient decreases. Bi-doped phosphate glass's attenuation performance was superior to that of Pb-doped glass at all comparable weight concentrations, particularly in the diagnostic X-ray energy range. This can be attributed to the higher atomic number of bismuths, which enhances photoelectric interactions at lower photon energies.

Author Contributions

They all read and approved the final version of the paper. The first author: Contributed to manuscript writing and critical review, performed language editing, and assisted in preparing figures and tables. The second author: Supervision and project administration; conducted the MCNP simulations, drafted the manuscript, prepared figures and tables, and provided overall oversight and guidance throughout the study.

Conflicts of Interest

All the authors declare no conflict of interest.

Ethical Review and Approval

Ethical approval was not required for this research.

References

[1] T. Srivastava, E. Chirikova, S. Birk, F. Xiong, T. Benzouak, J. Y. Liu, P. J. Villeneuve, L. B. Zablotska, *Exposure to ionizing radiation and risk of dementia: A systematic review and meta-analysis,* Radiation Research 199 (5) (2023) 490–505.

[2] N. Hamada, *Cancer and non-cancer effects following ionizing irradiation*, Cancers 16 (6) 1141 (2024) 1-5.

[3] E. Mansouri, A. Mesbahi, R. Malekzadeh, A. Mansouri, *Shielding characteristics of nanocomposites for protection against X- and gamma rays in medical applications: Effect of particle size, photon energy, and nano-particle concentration*, Radiat Environ Biophys 59 (4) (2020) 583–600.

[4] P. Mehnati, R. Malekzadeh, M. Y. Sooteh, *Use of bismuth shield for protection of superficial radiosensitive organs in patients undergoing computed tomography: A literature review and meta-analysis*, Radiol Phys and Technol 12 (1) (2019) 6–25.

[5] M. Kılıç, M. Çağlar, Y. Karabul, Z. Güven Özdemir, O. İçelli, *Dielectric and gamma shielding properties of sodium silicate glassy structure modified with tungsten*, Radiation Effects and Defects in Solids 174 (3–4) (2019) 229–247.

[6] P. Mehnati, R. Malekzadeh, M. Y. Sooteh, *Application of personal non-lead nano-composite shields for radiation protection in diagnostic radiology: A systematic review and meta-analysis*, Nanomedicine Journal 7 (3) (2020) 170–182.

[7] R. Malekzadeh, V. S. Zali, O. Jahanbakhsh, M. Okutan, A. Mesbahi, *The preparation and characterization of silicon-based composites doped with $BaSO_4$, WO_3, and PbO nanoparticles for shielding applications in PET and nuclear medicine facilities*, Nanomedicine Journal 7 (4) (2020) 324–334.

[8] S. Niksarlioglu, F. Akman, M. E. Pekdemir, S. Y. Kuzu, M. R. Kaçal, M. Yılmaz, *An extensive investigation on gamma shielding properties of PLA/Gd_2O_3 nanocomposites*, Radiation Physics and Chemistry 208 (2023) 110936.

[9] H. B. Kavanoz, Ö. Akcali, O. Toker, B. Bilmez, M. Çağlar, O. İçelli, *A novel comprehensive utilization of vanadium slag/epoxy resin/antimony trioxide ternary composite as gamma ray shielding material by MCNP 6.2 and BXCOM*, Radiation Physics and Chemistry 165 (2019) 108446.

[10] M. Çağlar, Y. Karabul, M. Kılıç, Z. G. Özdemir, O. İçelli, *$Na_2Si_3O_7$/Ag micro and nano-structured glassy composites: The experimental and MCNP simulation surveys of their radiation shielding performances*, Progress in Nuclear Energy 139 (2021) 103855.

[11] P. Mehnati, R. Malekzadeh, B. Divband, M. Y. Sooteh, *Assessment of the effect of nano-composite shield on radiation risk prevention to Breast during computed tomography*, Iranian Journal of Radiology 17 (1) (2020) 96002.

[12] M. H. M. Zaid, K. A. Matari, H. A. A Sidek, I. R. Ibrahim, *Bismuth modified gamma radiation shielding properties of titanium vanadium sodium tellurite glasses as a potent transparent radiation-resistant glass applications*, Nuclear Engineering and Technology 53 (4) (2021) 1323–1330.

[13] B. Aygün, E. Şakar, E. Cinan, N. Y. Yorgun, M. I. Sayyed, O. Agar, A. Karabulut, *Development and production of metal oxide doped glasses for gamma ray and fast neutron shielding*, Radiation Physics and Chemistry 174 (2020) 108897.

[14] I. Kebaili, I. Boukhris, M. I. Sayyed, M. B. Tonguc, M. S. Al-Buriahi, *Effect of TiO_2/V_2O_5 substitution on the optical and radiation shielding properties of alkali borate glasses: A Monte Carlo investigation*, Ceramics International 46 (16) (2020) 25671–25677.

[15] K. Won-In, N. Sirikulrat, P. Dararutana, *Radiation shielding lead-free glass based on barium-bearing glass using Thailand quartz sands*, Advanced Materials Research 214 (2011) 207–211.

[16] O. Bawazeer, K. Makkawi, Z. B. Aga, H. Albakri, N. Assiri, K. Althagafy, A. Ajlouni, *A review on using nanocomposites as shielding materials against ionizing radiation*, Journal of Umm Al-Qura University for Applied Sciences 9 (2023) 325–340.

[17] M. Karimi, K. Ghazikhanlou-sani, A. R. Mehdizadeh, H. Mostaghimi, *Lead-free transparent shields for diagnostic X-rays: Monte Carlo simulation and measurements*, Radiological Physics and Technology 13 (2020) 276–287.

[18] H. M. H. Zakaly, H. A. Saudi, S. A. M. Issa, M. Rashad, A. I. Elazala, H. O. Tekin, Y. B. Saddek, , *Alteration of optical, structural, mechanical durability and nuclear radiation attenuation properties of barium borosilicate glasses through BaO reinforcement: Experimental and numerical analyses*, Ceramics International 47 (4) (2021) 5587–5596.

[19] M. Elsafi, M. A. El-Nahal, M. I. Sayyed, M. I. Sayyed, I. H. Saleh, M. I. Abbas, *Effect of bulk and nanoparticle Bi_2O_3 on attenuation capability of radiation shielding glass*, Ceramics International 47 (14) (2021) 19651–19658.

Journal of Advanced Research in Natural and Applied Sciences
dergipark.org.tr/en/pub/jarnas
Open Access

e-ISSN: 2757-5195 | 11 (2) (2025) 197-209 | doi.org/10.28979/jarnas.1666819

Special Generalized Trigonometric and Hyperbolic Function Solutions of the Space-Time Fractional Nonlinear Dispersive Modified Benjamin-Bona-Mahony Equation

Sevil Çulha Ünal[1]

Article Info

Received: 25 Apr 2025
Accepted: 29 Jun 2025
Published: 30 Jun 2025
Research Article

Abstract − In mathematical physics, the nonlinear dispersive modified Benjamin-Bono-Mahony equation is an essential nonlinear evolution equation. This paper employs the Sardar sub-equation approach to derive the analytic solutions of the space-time fractional nonlinear dispersive modified Benjamin-Bona-Mahony equation with a conformable derivative. These solutions, obtained using the proposed approach, are presented in specialized generalized hyperbolic and trigonometric forms. The soliton solutions are also obtained using the presented approach. Additionally, some of these solutions are illustrated in both two- and three-dimensional graphs for visualization. Finally, the suggested approach is novel, easy, and productive for obtaining analytic solutions and is applicable to numerous nonlinear fractional partial differential equations.

Keywords *– Sardar sub-equation approach, fractional NDMBBM equation, soliton solutions, special generalized trigonometric and hyperbolic functions*

1. Introduction

In physics and mathematics, nonlinear evolution equations (NLEEs) are widely utilized to explain most real-world phenomena. These phenomena modeled by NLEEs can be better understood with the help of exact solutions. Therefore, researching travelling wave solutions of these equations is essential for studying nonlinear physical processes. One of the significant NLEEs in mathematical physics is the nonlinear dispersive modified Benjamin-Bona-Mahony (NDMBBM) equation. The NDMBBM equation in the form

$$\frac{\partial u}{\partial t}+\frac{\partial u}{\partial x}-cu^2\frac{\partial u}{\partial x}+\frac{\partial^3 u}{\partial x^3}=0$$

was initially developed using nonlinear dispersive media for surface long wave research [1]. Here, c is a nonzero constant. Additionally, this equation possesses a stable solitary wave solution and exhibits dispersive properties [2]. Numerous methods for solving the NDMBBM equation are presented in the literature [3-12].

In recent years, finding solutions to fractional partial differential equations has become a popular research topic. Fractional derivatives provide a more accurate and realistic representation of real systems and processes compared to integer derivatives [13]. The fractional partial equations are observed in numerous modern scientific fields, such as signal processing, plasma physics, turbulence, optical fibers, aerodynamics, nuclear physics, travelling waves, physical chemistry, fluid dynamics, elastic media, hydrodynamics, gravity, and

[1]sevilunal@sdu.edu.tr (Corresponding Author)
[1]Department of Avionics, School of Civil Aviation, Süleyman Demirel University, Isparta, Türkiye

electromagnetism [14-19]. The fractional NDMBBM equation is one of the significant fractional partial differential equations. The acoustic-gravity waves in compressible fluids, acoustic waves in anharmonic crystals, and hydromagnetic waves in cold plasma can be explained by this equation [20]. In 2017, Batool and Akram [20] found the solutions to the time-fractional NDMBBM equation using the extended Fan sub-equation method. Asaduzzaman and Jesmin [21] employed the extended modified simple equation technique to derive the time-fractional NDMBBM equation. Sribua-Iam and Chinviriyasit [22] applied the Riccati sub-equation method for solutions of the space-time fractional NDMBBM equation. However, solutions of the space-time fractional NDMBBM equation have not yet been obtained using the Sardar sub-equation approach in the literature. Therefore, the motivation of this study is to find the analytic solutions of the space-time fractional NDMBBM equation

$$D_t^{\alpha}u + D_x^{\beta}u - cu^2 D_x^{\beta}u + D_x^{\beta}D_x^{\beta}D_x^{\beta}u = 0, 0 < \alpha, \beta \leq 1 \tag{1.1}$$

utilizing the Sardar sub-equation approach. Here, D_t^{α} and D_x^{β} represent the conformable fractional derivative of u. In nonlinear optics, the Sardar sub-equation approach is considered a meaningful way to obtain solutions of NLEEs when combined with the symbolic computation package [23]. The proposed approach is also a powerful, novel, and productive for discovering various soliton solutions in the literature. Solitons arise as solutions to a wide range of weakly nonlinear dispersive differential equations that describe physical systems [2]. Applications of solitons have attracted the attention of scientists [24,25] in recent years. Numerous types of fractional partial differential equations have been recently investigated using the proposed approach [26-38].

The remainder of this study is structured as follows: In Section 2, the basic definition and theorems of the fractional derivative in the conformable sense are mentioned. In Section 3, a summary of the Sardar sub-equation approach is presented. In Section 4, the analytic solutions of the space-time fractional NDMBBM are obtained using the proposed approach. In Section 5, the efficiency of the presented approach is illustrated by two- and three-dimensional graphs of some solutions. In Section 6, the conclusions of the paper are given.

2. Basic Definition and Theorems of the Conformable Fractional Derivative

In the literature, various fractional derivative definitions, including Caputo, Grünwald-Letnikov, and Riemann-Liouville, are widely used by scientists. However, according to the definition of the Caputo derivative among these derivatives, the function needs to be differentiable. When the order of the derivative is not a natural number, the derivative of a constant function is not zero in the Riemann-Liouville derivative definition. Besides, numerous definitions of fractional derivatives do not provide the derivative formulas for the product and quotient of two functions, as well as the chain rule. To overcome these limitations, Khalil et al. [39] proposed a new basic definition of the fractional derivative, called the conformable fractional derivative, in 2014. This definition is the simplest among the other fractional derivatives because of its similarity to the definition of the usual derivative. Therefore, (1.1) is integrated with the conformable fractional derivative in this paper. The definition and properties of this derivative are presented below.

Definition 2.1. [39] Let $s: [0, \infty) \to \mathbb{R}$ be a function. The α-th order conformable fractional derivative of s is defined by

$$D^{\alpha}(s)(t) = \lim_{\varepsilon \to 0} \frac{s(t + \varepsilon t^{1-\alpha}) - s(t)}{\varepsilon}, \quad t > 0, \quad \alpha \in (0,1]$$

If s is α-differentiable in some $(0, \alpha)$ and $\lim_{t \to 0^+} s^{(\alpha)}(t)$ occurs, then $s^{(\alpha)}(0) = \lim_{t \to 0^+} s^{(\alpha)}(t)$.

Theorem 2.1. [39] Let $\alpha \in (0,1]$ and s, w are α-differentiable at a point t with $t > 0$. Then, the following properties are satisfied for all s and w:

i. $D^{\alpha}(d_1 s + d_2 w) = d_1 D^{\alpha}(s) + d_2 D^{\alpha}(w), \quad \forall\, d_1, d_2 \in \mathbb{R}$
ii. $D^{\alpha}(s) = 0$, if s is a constant function
iii. $D^{\alpha}\left(t^{\delta}\right) = \delta t^{\delta-\alpha}, \quad \forall\, \delta \in \mathbb{R}$
iv. $D^{\alpha}(sw) = sD^{\alpha}(w) + wD^{\alpha}(s)$
v. $D^{\alpha}\left(\frac{s}{w}\right) = \frac{wD^{\alpha}(s) - sD^{\alpha}(w)}{w^2}$
vi. If s is differentiable, then $D^{\alpha}(s)(t) = t^{1-\alpha}\frac{ds}{dt}(t)$

Theorem 2.2. [40] Assume that $s, w : (\alpha, \infty) \to \mathbb{R}$ are conformable differentiable functions of the order α, in which $0 < \alpha \leq 1$ and $z(t) = s(w(t))$. Then $z(t)$ is α-differentiable and for all t with $t \neq 0$ and $w(t) \neq 0$ we have

$$D^{\alpha}(z)(t) = D^{\alpha}(s)\big(w(t)\big)D^{\alpha}(w)(t)w(t)^{\alpha-1}$$

If $t = 0$, we get

$$D^{\alpha}(z)(0) = \lim_{t\to 0} D^{\alpha}(s)\big(w(t)\big)D^{\alpha}(w)(t)w(t)^{\alpha-1}$$

This theorem indicates that the fractional derivative in a conformable sense has a chain rule.

3. Description of the Sardar Sub-Equation Approach

This section presents an overview of the Sardar sub-equation approach [41]. Let us examine nonlinear fractional partial differential equations

$$F\left(u, u_x, u_t, D_x^{\beta}u, D_t^{\alpha}u, \dots\right) = 0, \qquad 0 < \beta, \alpha \leq 1 \tag{3.1}$$

where D_x^{β} and D_t^{α} symbolize the conformable fractional derivative of u. In order to get solutions of (3.1), the travelling wave transformation is considered as follows:

$$u = u(\eta), \qquad \eta = l\frac{x^{\beta}}{\beta} - k\frac{t^{\alpha}}{\alpha} \tag{3.2}$$

Here, arbitrary nonzero constants are k (wave speed) and l (wavelength). The transformation in (3.2) reduces (3.1) to an integer order ordinary differential equation (ODE) as

$$H(u, u', u'', u''', \dots) = 0 \tag{3.3}$$

The proposed approach aims to attain the solution of (3.1) formed as

$$u(\eta) = \sum_{i=0}^{M} a_i G^i(\eta) \tag{3.4}$$

where a_i are the coefficients to be determined later for $i \in \{1, 2, 3, \dots, M\}$. Here, $G(\eta)$ is the solution of the following nonlinear ODE

$$(dG/d\eta)^2 = \varphi + \nu G^2(\eta) + G^4(\eta) \tag{3.5}$$

in which φ and ν are real constants. This equation has the following solutions:

Case I. When $\nu > 0$ and $\varphi = 0$, then

$$G_1^{\pm}(\eta) = \pm\sqrt{-pq\nu}\,\mathrm{sech}_{pq}\left(\sqrt{\nu}\eta\right)$$

$$G_2^{\pm}(\eta) = \pm\sqrt{pq\nu}\,\mathrm{csch}_{pq}\left(\sqrt{\varphi\nu}\eta\right)$$

Case II. When $\nu < 0$ and $\varphi = 0$, then

$$G_3^{\pm}(\eta) = \pm\sqrt{-pq\nu}\,\mathrm{sec}_{pq}\left(\sqrt{-\nu}\eta\right)$$

$$G_4^{\pm}(\eta) = \pm\sqrt{-pq\nu}\,\mathrm{csc}_{pq}\left(\sqrt{-\nu}\eta\right)$$

Case III. When $\nu < 0$ and $\varphi = \frac{\nu^2}{4}$, then

$$G_5^{\pm}(\eta) = \pm\sqrt{\frac{-\nu}{2}}\tanh_{pq}\left(\sqrt{\frac{-\nu}{2}}\eta\right)$$

$$G_6^{\pm}(\eta) = \pm\sqrt{\frac{-\nu}{2}}\coth_{pq}\left(\sqrt{\frac{-\nu}{2}}\eta\right)$$

$$G_7^{\pm}(\eta) = \pm\sqrt{\frac{-\nu}{2}}\left(\tanh_{pq}\left(\sqrt{-2\nu}\eta\right) \pm \sqrt{-pq}\,\mathrm{sech}_{pq}\left(\sqrt{-2\nu}\eta\right)\right)$$

$$G_8^{\pm}(\eta) = \pm\sqrt{\frac{-\nu}{2}}\left(\coth_{pq}\left(\sqrt{-2\nu}\eta\right) \pm \sqrt{pq}\,\mathrm{csch}_{pq}\left(\sqrt{-2\nu}\eta\right)\right)$$

$$G_9^{\pm}(\eta) = \pm\sqrt{\frac{-\nu}{8}}\left(\tanh_{pq}\left(\sqrt{\frac{-\nu}{8}}\eta\right) + \coth_{pq}\left(\sqrt{\frac{-\nu}{8}}\eta\right)\right)$$

Case IV. When $\nu > 0$ and $\varphi = \frac{\nu^2}{4}$, then

$$G_{10}^{\pm}(\eta) = \pm\sqrt{\frac{\nu}{2}}\tan_{pq}\left(\sqrt{\frac{\nu}{2}}\eta\right)$$

$$G_{11}^{\pm}(\eta) = \pm\sqrt{\frac{\nu}{2}}\cot_{pq}\left(\sqrt{\frac{\nu}{2}}\eta\right)$$

$$G_{12}^{\pm}(\eta) = \pm\sqrt{\frac{\nu}{2}}\left(\tan_{pq}\left(\sqrt{2\nu}\eta\right) \pm \sqrt{pq}\,\mathrm{sec}_{pq}\left(\sqrt{2\nu}\eta\right)\right)$$

$$G_{13}^{\pm}(\xi\eta) = \pm\sqrt{\frac{\nu}{2}}\left(\cot_{pq}\left(\sqrt{2\nu}\eta\right) \pm \sqrt{pq}\,\mathrm{csc}_{pq}\left(\sqrt{2\nu}\eta\right)\right)$$

$$G_{14}^{\pm}(\eta) = \pm\sqrt{\frac{\nu}{8}}\left(\tan_{pq}\left(\sqrt{\frac{\nu}{8}}\eta\right) + \cot_{pq}\left(\sqrt{\frac{\nu}{8}}\eta\right)\right)$$

where

$$\mathrm{sech}_{pq}(\eta) = \frac{2}{pe^{\eta} + qe^{-\eta}}, \qquad \mathrm{csch}_{pq}(\eta) = \frac{2}{pe^{\eta} - qe^{-\eta}}$$

$$\mathrm{sec}_{pq}(\eta) = \frac{2}{pe^{i\eta} + qe^{-i\eta}}, \qquad \mathrm{csc}_{pq}(\eta) = \frac{2i}{pe^{i\eta} - qe^{-i\eta}}$$

$$\tanh_{pq}(\eta) = \frac{pe^{\eta} - qe^{-\eta}}{pe^{\eta} + qe^{-\eta}}, \qquad \coth_{pq}(\eta) = \frac{pe^{\eta} + qe^{-\eta}}{pe^{\eta} - qe^{-\eta}}$$

$$\tan_{pq}(\eta) = -i\frac{pe^{i\eta} - qe^{-i\eta}}{pe^{i\eta} + qe^{-i\eta}}, \qquad \cot_{pq}(\eta) = i\frac{pe^{i\eta} + qe^{-i\eta}}{pe^{i\eta} - qe^{-i\eta}}$$

They are special generalized hyperbolic and trigonometric functions. Here, $p > 1$ and $q > 1$ are any constants.

The generalized hyperbolic and trigonometric functions can be expressed by integrals. The inverse functions of $\sin_{pq}x$ and $\sinh_{pq}x$ are defined by

$$\sin_{pq}^{-1}x = \int_0^x (1-z^q)^{-1/p}\,dz$$

$$\sinh_{pq}^{-1}x = \int_0^x (1+z^q)^{-1/p}\,dz$$

The $\cos_{pq}x$ and $\cosh_{pq}x$ are also denoted by

$$\cos_{pq}x = \frac{d}{dx}\sin_{pq}x$$

$$\cosh_{pq}x = \frac{d}{dx}\sinh_{pq}x$$

These functions have relationships among themselves similar to the hyperbolic and trigonometric functions:

$$\left|\cos_{pq}x\right|^p + \left|\sin_{pq}x\right|^q = 1\,, \quad x \le \mathbb{R}$$

$$\left|\cosh_{pq}x\right|^p - \left|\sinh_{pq}x\right|^q = 1\,, \quad x \le \mathbb{R}$$

There are similar definitions and relations of other generalized trigonometric and hyperbolic functions in the literature. Details of them can be seen in some references [42-46].

The suggested approach starts by determining M with the help of the classic balance rule. When M is found, the predicted solution and its derivatives, along with (3.5), are placed into (3.3). After that, by setting all the coefficients of powers G equal to zero, a system of algebraic equations is gained and solved for the constants a_i and v. Then, the solutions of (3.1) can be obtained by substituting these constants with the solutions of (3.5).

4. Solutions for the Space-Time Fractional NDMBBM equation

In this section of the paper, the analytical solutions of the space-time fractional NDMBBM equation are obtained using the Sardar sub-equation approach. Using the wave transformation (3.2) into (1.1), we get

$$-k\frac{\partial u}{\partial \eta} + l\frac{\partial u}{\partial \eta} - clu^2\frac{\partial u}{\partial \eta} + l^3\frac{d^3u}{d\eta^3} = 0 \tag{4.1}$$

Balancing to the highest order of the nonlinear term and the highest order of the linear term in this equation, we find $M = 1$. Then, the solution has the following form

$$u(\eta) = a_0 + a_1 G(\eta) \tag{4.2}$$

Differentiating this solution three times and utilizing (3.5), the necessary derivatives are obtained as follows:

$$u' = a_1 G'$$

$$u''' = (a_1 v + 6a_1 G^2)G'$$

Substituting these derivatives into (4.1) and equating all the coefficients of G to zero, the following system of algebraic equations is found

$$-ka_1 + la_1 - cla_0^2 a_1 + l^3 v a_1 = 0$$

$$-2cla_0 a_1^2 = 0$$

$$-cla_1^3 + 6l^3 a_1 = 0$$

After that, solving this system of algebraic equations, we have

$$\nu = \frac{k-l}{l^3}, \qquad a_0 = 0, \qquad a_1 = \pm\frac{\sqrt{6}}{\sqrt{c}}l$$

Substituting the above values and the function G in (4.2), we obtain the following solutions:

Case I. If $\frac{k-l}{l^3} > 0$ and $\varphi = 0$, then

$$u_1^{\pm}(\eta) = \pm\sqrt{-pq\frac{k-l}{l^3}}\left(\pm\frac{\sqrt{6}\,l}{\sqrt{c}}\right)\operatorname{sech}_{pq}\left(\sqrt{\frac{k-l}{l^3}}\eta\right)$$

$$u_2^{\pm}(\eta) = \pm\sqrt{pq\frac{k-l}{l^3}}\left(\pm\frac{\sqrt{6}\,l}{\sqrt{c}}\right)\operatorname{csch}_{pq}\left(\sqrt{\frac{k-l}{l^3}}\eta\right)$$

Case II. If $\frac{k-l}{l^3} < 0$ and $\varphi = 0$, then

$$u_3^{\pm}(\eta) = \pm\sqrt{-pq\frac{k-l}{l^3}}\left(\pm\frac{\sqrt{6}\,l}{\sqrt{c}}\right)\operatorname{sec}_{pq}\left(\sqrt{-\frac{k-l}{l^3}}\eta\right)$$

$$u_4^{\pm}(\eta) = \pm\sqrt{-pq\frac{k-l}{l^3}}\left(\pm\frac{\sqrt{6}\,l}{\sqrt{c}}\right)\operatorname{csc}_{pq}\left(\sqrt{-\frac{k-l}{l^3}}\eta\right)$$

Case III. When $\frac{k-l}{l^3} < 0$ and $\varphi = \frac{1}{4}\left(\frac{k-l}{l^3}\right)^2$, then

$$u_5^{\pm}(\eta) = \pm\frac{\sqrt{-\frac{k-l}{l^3}}}{\sqrt{2}}\left(\pm\frac{\sqrt{6}\,l}{\sqrt{c}}\right)\tanh_{pq}\left(\frac{\sqrt{-\frac{k-l}{l^3}}}{\sqrt{2}}\eta\right)$$

$$u_6^{\pm}(\eta) = \pm\frac{\sqrt{-\frac{k-l}{l^3}}}{\sqrt{2}}\left(\pm\frac{\sqrt{6}\,l}{\sqrt{c}}\right)\coth_{pq}\left(\frac{\sqrt{-\frac{k-l}{l^3}}}{\sqrt{2}}\eta\right)$$

$$u_7^{\pm}(\eta) = \pm\frac{\sqrt{-\frac{k-l}{l^3}}}{\sqrt{2}}\left(\pm\frac{\sqrt{6}\,l}{\sqrt{c}}\right)\left(\tanh_{pq}\left(\sqrt{2}\sqrt{-\frac{k-l}{l^3}}\eta\right) \pm \sqrt{-pq}\operatorname{sech}_{pq}\left(\sqrt{2}\sqrt{-\frac{k-l}{l^3}}\eta\right)\right)$$

$$u_8^{\pm}(\eta) = \pm\frac{\sqrt{-\frac{k-l}{l^3}}}{\sqrt{2}}\left(\pm\frac{\sqrt{6}\,l}{\sqrt{c}}\right)\left(\coth_{pq}\left(\sqrt{2}\sqrt{-\frac{k-l}{l^3}}\eta\right) \pm \sqrt{pq}\operatorname{csch}_{pq}\left(\sqrt{2}\sqrt{-\frac{k-l}{l^3}}\eta\right)\right)$$

$$u_9^{\pm}(\eta) = \pm\frac{\sqrt{-\frac{k-l}{l^3}}}{2\sqrt{2}}\left(\pm\frac{\sqrt{6}\,l}{\sqrt{c}}\right)\left(\tanh_{pq}\left(\frac{\sqrt{-\frac{k-l}{l^3}}}{2\sqrt{2}}\eta\right) + \coth_{pq}\left(\frac{\sqrt{-\frac{k-l}{l^3}}}{2\sqrt{2}}\eta\right)\right)$$

Case IV. When $\frac{k-l}{l^3} > 0$ and $\varphi = \frac{1}{4}\left(\frac{k-l}{l^3}\right)^2$, then

$$u_{10}^{\pm}(\eta) = \pm\frac{\sqrt{\frac{k-l}{l^3}}}{\sqrt{2}}\left(\pm\frac{\sqrt{6}\,l}{\sqrt{c}}\right)\tan_{pq}\left(\frac{\sqrt{\frac{k-l}{l^3}}}{\sqrt{2}}\eta\right)$$

$$u_{11}^{\pm}(\eta) = \pm\frac{\sqrt{\frac{k-l}{l^3}}}{\sqrt{2}}\left(\pm\frac{\sqrt{6}\,l}{\sqrt{c}}\right)\cot_{pq}\left(\frac{\sqrt{\frac{k-l}{l^3}}}{\sqrt{2}}\eta\right)$$

$$u_{12}^{\pm}(\eta) = \pm\frac{\sqrt{\frac{k-l}{l^3}}}{\sqrt{2}}\left(\pm\frac{\sqrt{6}\,l}{\sqrt{c}}\right)\left(\tan_{pq}\left(\sqrt{2}\sqrt{\frac{k-l}{l^3}}\eta\right) \pm \sqrt{pq}\sec_{pq}\left(\sqrt{2}\sqrt{\frac{k-l}{l^3}}\eta\right)\right)$$

$$u_{13}^{\pm}(\eta) = \pm\frac{\sqrt{\frac{k-l}{l^3}}}{\sqrt{2}}\left(\pm\frac{\sqrt{6}\,l}{\sqrt{c}}\right)\left(\cot_{pq}\left(\sqrt{2}\sqrt{\frac{k-l}{l^3}}\eta\right) \pm \sqrt{pq}\csc_{pq}\left(\sqrt{2}\sqrt{\frac{k-l}{l^3}}\eta\right)\right)$$

$$u_{14}^{\pm}(\eta) = \pm\frac{\sqrt{\frac{k-l}{l^3}}}{2\sqrt{2}}\left(\pm\frac{\sqrt{6}\,l}{\sqrt{c}}\right)\left(\tan_{pq}\left(\frac{\sqrt{\frac{k-l}{l^3}}}{2\sqrt{2}}\eta\right) + \cot_{pq}\left(\frac{\sqrt{\frac{k-l}{l^3}}}{2\sqrt{2}}\eta\right)\right)$$

5. Graphical Representation

In this part of the study, we illustrate some of the analytic solutions of the space-time fractional NDMBBM equation using 2D and 3D graphs, which were chosen to provide appropriate values for the unknown parameters. These graphs play a crucial role in observing soliton behavior and understanding the physical significance of the obtained solutions. Additionally, all graphs are generated using the computer application Wolfram Mathematica.

Figure 1 demonstrates the solution u_4^+ for $0 \le x \le 200$ and $1 \le t \le 10$ when $c = 0.2$, $k = 0.2$, $l = 0.4$, $p = q = 1.3$, $\alpha = 0.2$, and $\beta = 0.3$. Figure 2 illustrates the solution u_4^+ with 2D plot for $0 \le x \le 200$ and and $t = 2$. This figure shows that the wave width decreases, and the wave frequency increases as x close to zero.

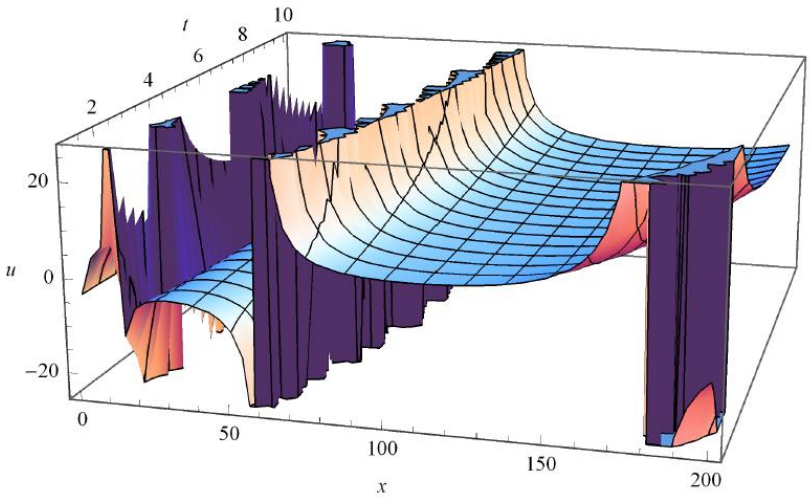

Figure 1. 3D graph of $u_4^+(x,t)$

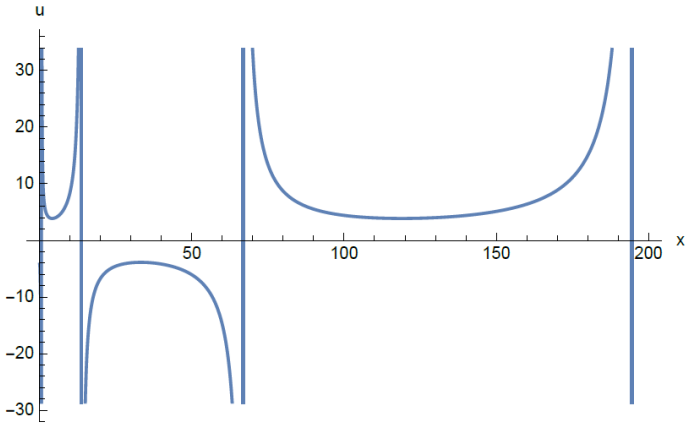

Figure 2. 2D graph of $u_4^+(x,t)$, for $t = 2$

Figure 3 demonstrates the solution u_5^- for $0 \le x \le 40$ and $1 \le t \le 6$ when $c = 0.3$, $k = 0.7$, $l = 0.9$ $p = 1.5$, $q = 1.1$, $\alpha = 0.1$, and $\beta = 0.6$. A soliton is a nonlinear wave packet that preserves its shape, amplitude, and velocity as it moves freely and at a constant speed. It retains shape after collisions with other localized wave packets [47]. The signs $(\mp)$ indicate localized soliton solutions traveling with opposing screw senses. These are the kink soliton and antikink soliton, respectively [48]. Therefore, Figure 3 exhibits the antikink soliton solution. Besides, Figure 4 illustrates the solution u_5^- with 2D plot for $0 \le x \le 40$ and $t = 3$. Similarly, it can be stated that the solution u_5^+ indicates the kink soliton solution.

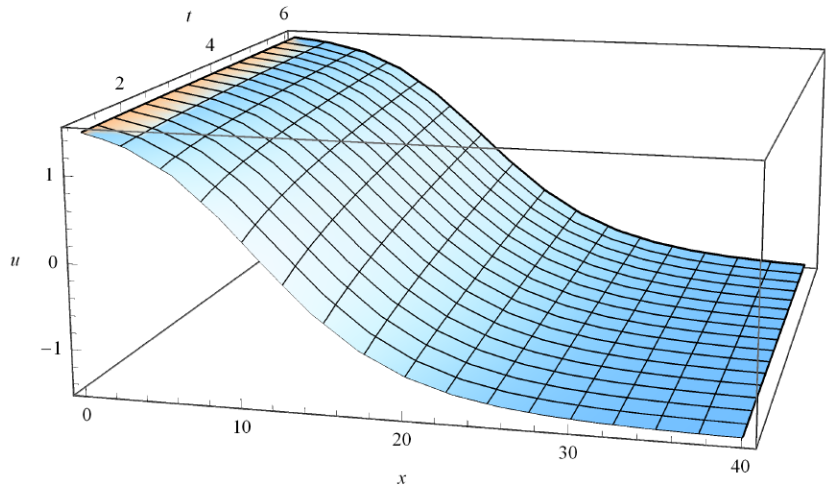

Figure 3. 3D graph of $u_5^-(x,t)$

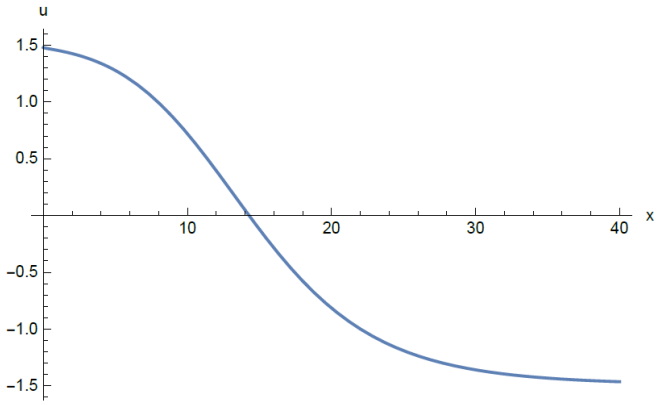

Figure 4. 2D graph of $u_5^-(x,t)$ for $t = 3$

Figure 5 demonstrates the solution u_{10}^- for $0 \le x \le 100$ and $1 \le t \le 5$ when $c = 0.5$, $k = 0.6$, $l = 0.3$ $p = q = 1.5$, $\alpha = 0.3$, and $\beta = 0.5$. This figure illustrates the antikink-type soliton solution. Besides, Figure 6

exhibits the solution u_{10}^{-} with 2D plot for $0 \leq x \leq 100$ and $t = 1$. This figure shows that as x approaches infinity, the inflection increases while the frequency decreases. Similarly, it can be stated that the solution u_{10}^{+} indicates the kink-type soliton solution.

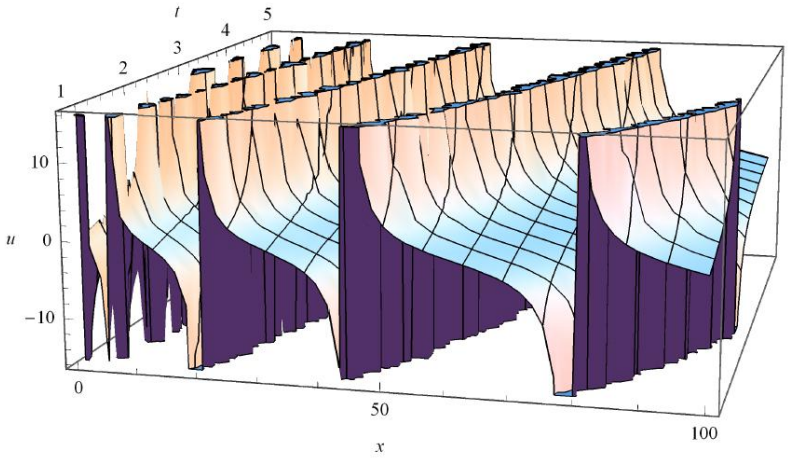

Figure 5. 3D graph of $u_{10}^{-}(x,t)$

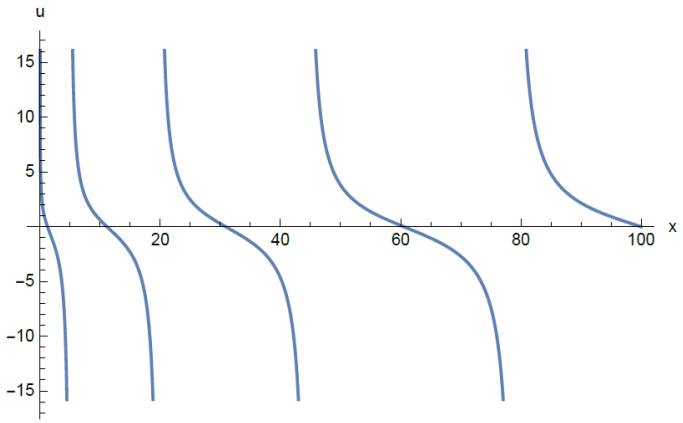

Figure 6. Two-dimensional graph of $u_{10}^{-}(x,t)$ for $t = 1$

Figures 7 and 8 illustrate the $u_{10}^{-}(x,1)$ solution for $0 \leq x \leq 100$ with the different values of α and β, respectively. From Figure 7, it can be seen that as the values of α increase and x approaches zero, the wave frequency increases. Besides, it is observed that the inflection increases as the values of β decrease in Figure 8. From these figures, it can be seen that the fractional parameters α and β play a crucial role in determining the shape and size of the solitons, depending on whether they are close to or far from 1.

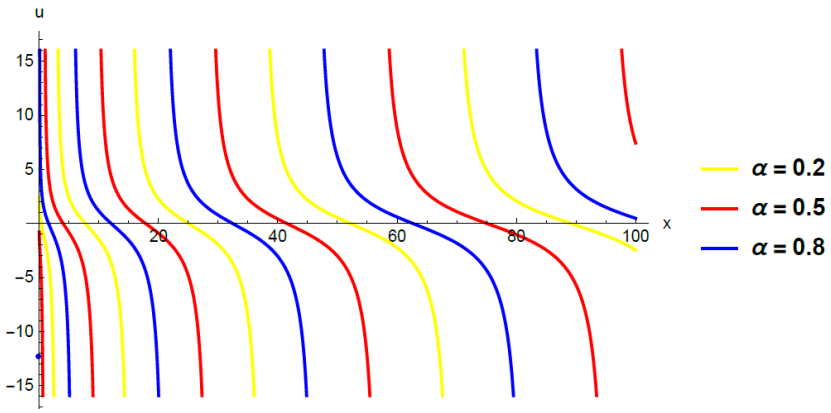

Figure 7. 2D graph of $u_{10}^{-}(x,1)$ for $\alpha = 0.2$ (yellow line), $\alpha = 0.5$ (red line), $\alpha = 0.8$ (blue line).

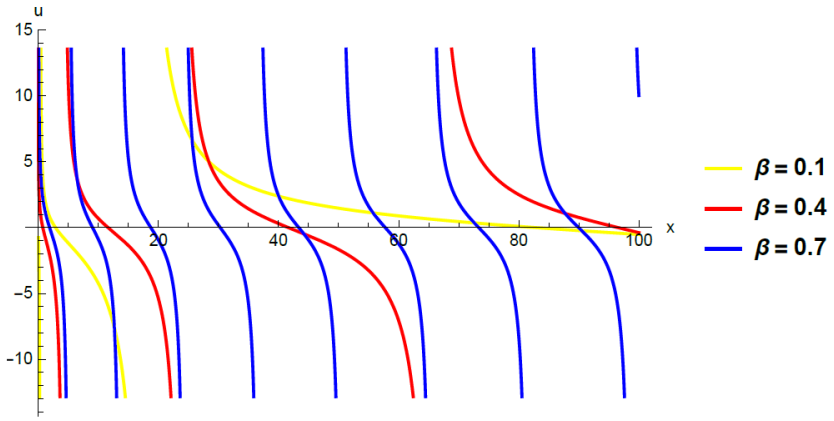

Figure 8. 2D graph of $u_{10}^{-}(x,1)$ for $\beta = 0.1$ (yellow line), $\beta = 0.4$ (red line), $\beta = 0.7$ (blue line).

6. Conclusion

This paper applies the Sardar sub-equation approach to gain the space-time fractional NDMBBM equation. The fractional derivatives in this equation are considered in a conformable sense. The proposed approach transforms the fractional partial differential equation into an ordinary differential equation by wave transformation. Utilizing the suggested approach, we present the obtained solutions in terms of the special generalized hyperbolic and trigonometric function forms. The proposed approach also yields soliton solutions. It can be stated that all the found solutions satisfy the presented equation as calculated by the Mathematica software. Two- and three-dimensional graphs of some of these solutions are illustrated by selecting appropriate values for the unknown parameters. Additionally, when the studies in the literature are examined, the space-time fractional NDMBBM equation is considered using the Riccati sub-equation method [20], and solutions are found in terms of special generalized trigonometric and hyperbolic functions. 15 solutions are obtained for three different cases using the Riccati sub-equation method, while 28 solutions are obtained for four different cases using the Sardar sub-equation approach. In (1.1), which is solved with the Riccati sub-equation method, the fractional parameters α and β are taken equal to each other. However, these parameters are selected differently in our paper. Moreover, the presented approach does not require linearization, perturbation, initial, and boundary conditions. Furthermore, the findings indicate that the Sardar sub-equation approach is satisfying, easy, and reliable when applied to various nonlinear fractional partial differential equations. The suggested approach can be applied to other definitions of fractional derivatives, such as the beta derivative and the truncated M-fractional derivative. As a result, researchers can use these findings in future applications. For future work, it is envisioned that the proposed approach can be used as an alternative to find analytical solutions for a wide range of nonlinear integer-order and fractional-order differential equations used in mathematics, physics, and engineering.

Author Contributions

The author read and approved the final version of the paper.

Conflict of Interest

The author declares no conflict of interest.

Ethical Review and Approval

No approval from the Board of Ethics is required.

References

[1] E. Yusufoğlu, *New solitonary solutions for the MBBM equations using exp-function method*, Physics Letters A 372 (2008) 442-446.

[2] A-M. Wazwaz, Partial differential equations and solitary waves theory, Nonlinear Physical Science, Springer, 2009.

[3] E. M. E. Zayed, S. Al-Joudi, *Applications of an extended* (G'/G)*-expansion method to find exact solutions of nonlinear PDEs in mathematical physics*, Mathematical Problems in Engineering (2010) 768573.

[4] K. Khan, M. A. Akbar, S. M. R. Islam, *Exact solutions for (1+1)-dimensional nonlinear dispersive modified Benjamin-Bona-Mahony equation and coupled Klein-Gordon equations*, SpringerPlus 3 (1) (2014) 724.

[5] A. Yokus, A. Sulaiman, M. T. Gulluoglu, H. Bulut, *Stability analysis, numerical and exact solutions of the (1+1)-dimensional NDMBBM equation*, ITM Web of Conferences 22 (2018) 01064.

[6] X-W. Yan, S-F. Tian, M-J. Dong, X-B. Wang, T-T. Zhang, *Nonlocal symmetries, conservation laws and interaction solutions of the generalised dispersive modified Benjamin-Bona-Mahony equation*, Zeitschrift für Naturforschung A 73 (5) (2018) 399–405.

[7] F. Taşcan, A. Akbulut, *Construction of exact solutions to partial differential equations with CRE method,* Communications in Advanced Mathematical Sciences 2 (2) (2019) 105–113.

[8] T. Alotaibi, A. Althobaiti, *Exact solutions of the nonlinear modified Benjamin-Bona-Mahony equation by an analytical method*, Fractal and Fractional 6 (7) (2022) 399.

[9] M. Shakeel, A. Ullah, E. R. El-Zahar, N. A. Shah, J. D. Chung, *Generalized exp-function method to find closed form solutions of nonlinear dispersive modified Benjamin-Bona-Mahony equation defined by seismic sea waves*, Mathematics 10 (7) (2022) 1026.

[10] B. Kopçasız, E. Yaşar, *μ-symmetries and μ-conservation laws for the nonlinear dispersive modified Benjamin-Bona-Mahony equation*, Journal of Mathematical Sciences and Modelling 6 (3) (2023) 87–96.

[11] H. M. Baskonus, H. Bulut, *Analytical studies on the (1+1)-dimensional nonlinear dispersive modified Benjamin-Bona-Mahony equation defined by seismic sea waves*, Waves in Random and Complex Media 25 (4) (2015) 576–586.

[12] S-W. Yao, K. U. Tariq, M. Inc, R. N. Tufail, *Modulation instability analysis and soliton solutions of the modified BBM model arising in dispersive medium*, Results in Physics 46 (2023) 106274.

[13] I. Podlubny, Fractional differential equations, Academic Press, New York, 1999.

[14] B. Ahmad, J. J. Nieto, *Existence of solutions for nonlocal boundary value problems of higher-order nonlinear fractional differential equations*, Abstract and Applied Analysis 2009 (2009) 494720.

[15] Y. Wang, S. Liang, Q. Wang, *Existence results for fractional differential equations with integral and multi-point boundary conditions*, Boundary Value Problems 2018 (2018) 4.

[16] M. Şenol, A. Ata, *Approximate solution of time-fractional KdV equations by residual power series method*, Journal of Balıkesir University Institute of Science and Technology 20 (1) (2018) 430–439.

[17] G. Akram, M. Sadaf, M. Abbas, I. Zainab, S. R. Gillani, *Efficient techniques for traveling wave solutions of time-fractional Zakharov-Kuznetsov equation*, Mathematics and Computers in Simulation 193 (2022) 607–622.

[18] M. M. A. Qurashi, Z. Korpinar, D. Baleanu, M. Inc, *A new iterative algorithm on the time-fractional Fisher equation: Residual power series method*, Advances in Mechanical Engineering 9 (9) (2017) 1–8.

[19] Z. Körpınar, *The residual power series method for solving fractional Klein-Gordon equation*, Sakarya University Journal of Science 21 (3) (2017) 285–293.

[20] F. Batool, G. Akram, *Application of extended Fan sub-equation method to (1+1)-dimensional nonlinear dispersive modified Benjamin-Bona-Mahony equation with fractional evolution*, Optical and Quantum Electronics 49 (2017) 375.

[21] Md. Asaduzzaman, F. Jesmin, *Construction of the closed form wave solutions for TFSMCH and (1+1) dimensional TFDMBBM equations via the EMSE technique*, Fractal and Fractional 9 (2) (2025) 72.

[22] N. Sribua-Iam and S. Chinviriyasit, *New analytical wave solutions of fractional order DMBBM and Bateman-Burgers equations*, Frontiers in Applied Mathematics and Statistics 11 (2025) 1568834.

[23] H. U. Rehman, A. Amer, A. Amer, *New solitary wave solutions of generalized fractional Tzitzèica-type evolution equations using Sardar sub-equation method*, Optical and Quantum Electronics 55 (13) (2023).

[24] H-D. Guo, T-C. Xia, B-B. Hu, *High-order lumps, high-order breathers and hybrid solutions for an extended (3+1)-dimensional Jimbo-Miwa equation in fluid dynamics*, Nonlinear Dynamics 100 (1) (2020) 601–614.

[25] H-D. Guo, T-C. Xia, B-B. Hu, *Dynamics of abundant solutions to the (3+1)-dimensional generalized Yu-Toda-Sasa-Fukuyama equation*, Applied Mathematics Letters 105 (2020) 106301.

[26] N. Ullah, M. I. Asjad, J. Awrejcewicz, T. Muhammad, D. Baleanu, *On soliton solutions of fractional-order nonlinear model appears in physical sciences*, AIMS Mathematics 7 (5) (2022) 7421–7440.

[27] M. I. Asjad, N. Ullah, H. Rehman, D. Baleanu, *Optical solitons for conformable space-time fractional nonlinear model*, Journal of Mathematics and Computer Science 27 (2022) 28–41.

[28] A. K. Alsharidi, A. Bekir, *Discovery of new exact wave solutions to the M-fractional complex three coupled Maccari's system by Sardar sub-equation scheme*, Symmetry 15 (8) (2023) 1567.

[29] M. Raheel, A. Zafar, A. Bekir, K. U. Tariq, *Exact wave solutions and obliqueness of truncated M-fractional Heisenberg ferromagnetic spin chain model through two analytical techniques*, Waves in Random and Complex Media (2023) https://doi.org/10.1080/17455030.2023.2173550.

[30] T. Rasool, R. Hussain, H. Rezazadeh, A. Ali, U. Demirbilek, *Novel soliton structures of truncated M-fractional (4+1)-dim Fokas wave model*, Nonlinear Engineering 12 (2023) 20220292.

[31] M. M. A. Khater, *Multi-vector with nonlocal and non-singular kernel ultrashort optical solitons pulses waves in birefringent fibers*, Chaos, Solitons and Fractals 167 (2023) 113098.

[32] C. Pleumpreedaporn, S. Pleumpreedaporn, E. J. Moore, S. Sirisubtawee, S. Sungnul, *Novel exact traveling wave solutions for the (2+1)-dimensional Boiti-Leon-Manna-Pempinelli equation with Atangana's space and time beta-derivatives via the Sardar subequation method*, Thai Journal of Mathematics 22 (1) (2024) 1–18.

[33] A. A. Altwaty, J. J. Amhalhil, A. E. Sakori, N. F. Meriki, *The Sardar sub-equation technique for obtaining some optical solitons of cubic nonlinear Schrödinger equation involving beta derivatives with Kerr law nonlinearity*, The Scientific Journal of University of Benghazi 37 (1) (2024) 28-36.

[34] M. Awadalla, A. Taishiyeva, R. Myrzakulov, J. Alahmadi, A. A. Zaagan, A. Bekir, *Exact analytical soliton solutions of the M-fractional Akbota equation*, Scientific Reports 14 (2024) 13360.

[35] D. Chou, H. U. Rehman, A. Amer, A. Amer, *New solitary wave solutions of generalized fractional Tzitzeica-type evolution equations using Sardar sub-equation method*, Optical and Quantum Electronics 55 (2023) 1148.

[36] Md. N. Hossain, M. M. Miah, M. Alosaimi, F. Alsharif, M. Kanan, *Exploring novel soliton solutions to the time-fractional coupled Drinfel'd-Sokolov-Wilson equation in industrial engineering using two efficient techniques*, Fractal and Fractional 8 (2024) 352.

[37] H. Qawaqneh, A. Altalbe, A. Bekir, K. U. Tariq, *Investigation of soliton solutions to the truncated M-fractional (3+1)-dimensional Gross-Pitaevskii equation with periodic potential*, AIMS Mathematics 9 (9) (2024).

[38] A. Said, A. Bakkar, H. Khan, C. Cattani, F. Tchier, *Construction of mechanically preserved optical travelling wave solution for fractional generalized reaction Duffing model*, Journal of Applied and Computational Mechanics (2025) https://doi.org/10.22055/jacm.2025.48049.4941.

[39] R. Khalil, M. A. Horani, A. Yousef, M. Sababheh, *A new definition of fractional derivative*, Journal of Computational and Applied Mathematics 264 (2014) 65–70.

[40] T. Abdeljawad, *On conformable fractional calculus*, Journal of Computational and Applied Mathematics 279 (2015) 57–66.

[41] H. Rezazadeh, M. Inc, D. Baleanu, *New solitary wave solutions for variants of (3+1)-dimensional Wazwaz-Benjamin-Bona-Mahony equations*, Frontiers in Physics 8 (2020) 332.

[42] H. Miyakawa, S. Takeuchi, *Applications of a duality between generalized trigonometric and hyperbolic functions*, Journal of Mathematical Analysis and Applications 502 (1) (2021) 125241.

[43] E. Neuman, *Inequalities for the generalized trigonometric, hyperbolic and Jacobian elliptic functions*, Journal of Mathematical Inequalities 9 (3) (2015) 709–726.

[44] H. Kobayashi, S. Takeuchi, *Applications of generalized trigonometric functions with two parameters*, Communications on Pure and Applied Analysis 18 (3) (2019) 1509–1521.

[45] S. Takeuchi, *Applications of generalized trigonometric functions with two parameters II*, Differential Equations and Applications 11 (4) (2019) 563–575.

[46] S. Takeuchi, *Multiple-angle formulas of generalized trigonometric functions with two parameters*, Journal of Mathematical Analysis and Applications 444 (2) (2016) 1000–1014.

[47] O. Büttner, M. Bauer, A. Rueff, S. O. Demokritov, B. Hillebrands, A. N. Slavin, M. P. Kostylev, B. A. Kalinikos, *Space- and time-resolved Brillouin light scattering from nonlinear spin-wave packets*, Ultrasonics 38 (2000) 443–449.

[48] M. Mossa Al-Sawalha, S. Mukhtar, A. S. Alshehry, M. Alqudah, M. S. Aldhabani, *Kink soliton phenomena of fractional conformable Kairat equations*, AIMS Mathematics, 10 (2) (2025) 2808–2828.